UNIVERSITÄT DES SAARLANDES

Fraunhofer IZFP

Examination of micro- and nanostructures of magnetic and piezoelectric materials in relation to their macroscopic properties by dynamic scanning force microscopy techniques

Dissertation

zur Erlangung des Grades des
Doktors der Ingenieurwissenschaften
der Naturwissenschaftlich-Technischen Fakultät III
Chemie, Pharmazie, Bio- und Werkstoffwissenschaften
der Universität des Saarlandes

von

Leonardo Batista

Saarbrücken

March 2014

Tag des Kolloquiums:	27.06.2014
Dekan:	Prof. Dr. Volkhard Helms
Berichterstatter:	Priv.-Doz. Dr.-Ing. Ute Rabe
	Prof. Dr. mont. Christian Motz
Vorsitz:	Prof. Dr.-Ing. Hans-Georg Herrmann
Akad. Mitarbeiter:	Dr.-Ing. Frank Aubertin

Acknowledgements

A Ph.D. thesis is a research work that results from an intense collaboration between different people. Therefore, I would like to express here my gratitude to all people that contributed from close or from far to its accomplishment.

I am extremely grateful to my academic supervisor, Priv.-Doz. Dr.-Ing. U. Rabe, for her constant guidance, support, patience, and for her inspiring and encouraging way to guide me to a deeper understanding of scientific work. Thanks to your support towards my very first experiments in the AFM-laboratory.

I would also like to express my sincere gratitude and thanks to Dr. rer. nat. S. Hirsekorn, for all supporting, patience, valuable comments, and giving me the chance to accomplish this work at the department NDT Fundamentals at Fraunhofer IZFP. I wish to thank her for everything she taught me, and for the friendly relationship we have had over the years.

I also thank Prof. Dr. mont. C. Motz for serving as the second reviewer of my thesis.

I would also like to thank all my colleagues of the department NDT Fundamentals, both past and present, for their constant help and meaningful contributions for this work. Thanks go to M.Eng. M. Heinrich, Dipl.-Ing. T. Helfen, Dipl.-Math. M. Weikert, Dr.-Ing. S. Lugin, Dr. rer. nat. U. Netzelmann, T. Schmeyer, M.Sc. K. Geng, Y. Gao, J. Schultz, T. Werner. I would like to express my gratitude to former master, bachelor, and internship students who I had the pleasure to guide during their accomplishments: M.Sc. S. Wust, Dipl.-Ing. B. Gronau, Dipl.-Ing. J. Sandström, M. Rank, and L. Behl.

I thank all colleagues at the IZFP for their interesting and helpful discussions, especially Dr.-Ing. I. Altpeter, Dr.-Ing. K. Szielasko, M.Sc. M. Amiri, and Prof. Dr.-Ing. Dr. rer. nat. G. Dobmann. I thank also Dipl.-Ing. M. Goebel for the help in preparation of some samples I used for this study. In addition, I would like to acknowledge support from people at different chairs at the Saarland University: MSc. M. Zamanzade helped with the nanoindentation measurements. I would like to thank Dipl. Phys. J. Schmauch for help with EBSD and TEM measurements, Dipl.-Ing. D. Britz and Dipl.-Ing. C. Pauly for help in with the FIB technique, and Prof. Dr. Hartmann with providing the coil which I used in the MFM.

My work was financially supported within the European FP7 project “Functionalities of Bismuth-based nanostructures (BisNano)”, grant No. 263878. I may not forget to say that during the project meetings I had a gratifying experience to get to know different people, some of them became even good friends. Thanks to Dr. P. Jagdale, Dr. M. Coisson, Dr. P. Tiberto, Dr. A. Zeinert, Dr. M. Bousquet, Dr. N. Lemée, Dr. R. Serna, Dr. S. Rodil, Dr. J. Oliveira, Dr.-Ing. R. Fernandes, Dr.-Ing. J. Muñoz-Saldaña and Dr. F. Espinoza-Beltrán.

I really would like to thank all my friends, mostly of them in Brazil, for their encouragement and friendship.

To my precious girlfriend Friederike I really have to say: Thank you so much for your love, patience, support and encouragement at all time.

Last but not least, I have no words in expressing my gratitude to my family: Mom, Dad, Lorena, Lisandra and Lelinho. Without their unconditional love, endless support and silent sacrifices, I would never have reached at this stage.

Leonardo Batista

Abstract

Dynamic scanning force microscopy techniques like magnetic force microscopy (MFM), ultrasonic piezoresponse force microscopy (UPFM), and atomic force acoustic microscopy (AFAM) were used for nanoscale imaging and characterization of magnetic, ferro- and piezoelectric, and mechanical properties in structural steels and functional ceramics. MFM coupled with an external coil providing a controllable external magnetic field was used to reveal magnetic domain dynamics and its interaction with the microstructure in bulk high purity iron and unalloyed pearlitic steel samples containing globular and lamellar cementite precipitates. The observations were interpreted with respect to macroscopic electromagnetic nondestructive testing signals like the magnetic Barkhausen noise. Using electron backscatter diffraction, the crystalline orientations in ferrite and cementite were determined and correlated to the magnetic domain structure. The surfaces of different lead-free bismuth-based bulk ceramics (BNT, BNT-BT, Mn-doped BNT-BT, Sr-doped BNT-BT) were imaged by UPFM and AFAM revealing the most stable ferroelectric domain structure in the Sr-doped BNT-BT sample. Large thickness coupling coefficients (0.37) and vibration amplitudes (18 nm maximum) were detected by an impedance measuring station and laser vibrometry, respectively. The testing of the Sr-doped BNT-BT sample as ultrasonic transducer material confirmed its high potential as alternative to lead-based piezoelectric materials.

Dynamische Rasterkraftmikroskopieverfahren wie Magnetkraft- (MFM), Ultraschall-Piezomode- (UPFM) und akustische Rasterkraftmikroskopie (AFAM) wurden zur Abbildung und Charakterisierung magnetischer, ferro- und piezoelektrischer sowie mechanischer Eigenschaften technischer Stähle und funktioneller Keramiken im Nanobereich genutzt. Mit MFM in Kombination mit einer Spule zum Aufbringen eines externen Magnetfelds wurden magnetische Domänenbewegungen und ihre Wechselwirkung mit der Mikrostruktur in Proben aus reinem Eisen und unlegiertem perlitischen Stahl mit kugelförmigen bzw. lamellaren Zementitausscheidungen beobachtet. Die Beobachtungen wurden in Korrelation mit makroskopischen, elektromagnetischen, zerstörungsfreien Verfahren wie dem magnetischen Barkhausenrauschen interpretiert. Mittels Elektronenrückstreubeugung wurden die Orientierungen der Ferrit- und Zementitkörner bestimmt und mit magnetischen Domänenstrukturen korreliert. Weiterhin wurden verschiedene bleifreie Bismuth-basierte Keramiken (BNT, BNT-BT, Mn- und Sr-dotiertes BNT-BT) untersucht. UPFM- und AFAM-Aufnahmen zeigten in der Sr-dotierte BNT-BT-Probe die stabilste ferroelektrische

Domänenstruktur. Mittels Impedanz-Messungen und Laservibrometrie wurden große Dickenschwingungskoppelfaktoren (0,37) und Schwingungsamplituden (18 nm maximal) nachgewiesen. Die Untersuchung der Sr-dotierten BNT-BT-Probe bestätigte das hohe Potential dieser Legierung, bleihaltige Keramikwerkstoffe im Ultraschallprüfkopfbau zu ersetzen.

List of Abbreviations

AFM	Atomic force microscopy
AFAM	Atomic force acoustic microscopy
BEMI	Barkhausen noise and eddy current microscopy
BFO	Bismuth ferrite ($BiFeO_3$)
BisNano	Functionalities of bismuth-based nanostructures
BNT	Bismuth sodium titanate ($Bi_{0.5}Na_{0.5}TiO_3$)
BNT-BT	Bismuth sodium titanate-barium titanate ($0.94Bi_{0.5}Na_{0.5}TiO_3$-$0.06BaTiO_3$)
BW	Bloch-wall
CINVESTAV	Centro de Investigación y de Estudios Avanzados
CR-FM	Contact resonance force microscopy
EBSD	Electron backscatter diffraction
EFM	Electrostatic force microscopy
IPF	Inverse pole figure
KPQ	Kikuchi pattern quality
LEM	Lorentz electron microscopy
LPFM	Lateral piezoresponse force microscopy
MAE	Magnetic acoustic emission (“acoustic Barkhausen noise”)
MBN	Magnetic Barkhausen noise
MFM	Magnetic force microscopy
MOKE	Magneto-optic Kerr effect
Mn-doped BNT-BT	Manganese-doped bismuth sodium titanate-barium titanate ($0.995(0.94(Bi_{0.5}Na_{0.5})TiO_3$-$0.06BaTiO_3)$-$0.005Mn$)
NDT	Nondestructive testing
NDT&E	Nondestructive testing and evaluation
OIM	Orientation imaging
OP	Optical microscopy

PFM	Piezoresponse force microscopy
PLD	Pulsed laser deposition
PZT	Lead zirconate titanate ($Pb[Zr_xTi_{1-x}]O_3$ $0 \leq x \leq 1$)
SEM	Scanning electron microscopy
SEMPA	Scanning electron microscopy with polarization analysis
SHPM	Scanning Hall probe microscopy
SFM	Scanning force microscopy
Sr-doped BNT-BT	Strontium-doped bismuth sodium titanate-barium titanate ($0.85(Bi_{0.5}Na_{0.5})TiO_3$-$0.12BaTiO_3$-$0.03SrTiO_3$)
SRO	Strontium ruthenate ($SrRuO_3$)
STO	Strontium titanate ($SrTiO_3$)
TEM	Transmission electron microscopy
TUHH	Technische Universität Hamburg-Harburg
TWIP	Twinning induced plasticity
UPFM	Ultrasonic piezoresponse force microscopy
UPJV	Université de Picardie Jules Verne
VPFM	Vertical piezoresponse force microscopy
XRD	X-ray diffraction
3MA	Micromagnetic multi-parameter microstructure and stress analysis

Table of content

I. INTRODUCTION

The development of new advanced materials and devices produced from nanostructural constituents requires measurement methods which are capable to probe material properties on the nanometer-length scale. One of the most promising approaches is based on the use of scanning force microscopy (SFM) techniques which has the ability to perform both imaging and also quantitative measurements of surface properties at a nanoscale. Since its invention in the mid 1980s SFM is going far beyond, and a variety of SFM-based techniques have been developed. Techniques such as magnetic force microscopy (MFM), atomic force acoustic microscopy (AFAM), ultrasonic piezoresponse force microscopy (UPFM), electrostatic force microscopy (EFM), Kelvin probe force microscopy (KPFM), scanning thermal microscopy (SThM), and others have arisen to assess local magnetic, mechanical, ferro- and piezoelectric, electric and thermal properties of materials on the nanometer scale.

In this thesis, different SFM-based techniques are used, especially dynamic modes such as MFM, AFAM and UPFM to nanoscale imaging and characterization of magnetic, mechanical and ferro- and piezoelectric properties in different materials, including structural steels and functional ceramics, the last in both thin films and bulk form. As it will be described in detail in the following, dynamic SFMs are employed here mostly in two distinct cases. First, the MFM technique is used for imaging and characterization of the magnetic microstructure in steels to support the understanding of their macroscopic magnetic properties which are used for nondestructive testing and evaluation (NDT&E). Second, the UPFM and AFAM techniques are used to nanoscale characterization of ferro- and piezoelectric and mechanical properties, respectively, in lead-free ferro- and piezoelectric ceramics with the objective to support the design and optimization of those new materials to be applied in the industry.

Nondestructive material characterization plays a crucial role on a wide range of industrial sectors because properties of materials, components or structures can be evaluated without causing damage. The strong demands for quality control and assurance require reliable nondestructive techniques capable of inspecting and monitoring microstructural changes during materials processing and materials degradation, and also the determination of mechanical material properties. Electromagnetic and specially micromagnetic techniques like the measurement of the magnetic Barkhausen noise, the incremental permeability and the harmonic analysis of the tangential magnetic field have the ability to fulfill most of the above mentioned requirements. Such techniques have been successfully applied for the

nondestructive characterization of the microstructure of ferromagnetic materials and also the determination of mechanical material properties like the yield strength, tensile strength, hardness, and also load-induced or residual stresses.

Because of the current strong demand for light-weight structures, as for example in the automotive sector, advanced high-strength steels containing different phases have been developed. Due to the complexity of their microstructures and also stress states, the interpretation of the nondestructive macroscopic electromagnetic measurement signals for microstructure characterization and determination of mechanical properties becomes extremely difficult. The observed macroscopic electromagnetic measurement signals rely on the phenomenological description of the interactions of the magnetic domains with the microstructure. There is therefore a need for local observation and characterization of the magnetic microstructure and the interactions between magnetic domain walls with microstructural features like grain and phase boundaries, dislocations, precipitations, etc. to support the interpretation and evaluation of the macroscopic nondestructive electromagnetic measurement signals. In line with this ultimate need, the work presented in the main and largest part of this thesis concerns the use of MFM to directly imaging and characterization of the magnetic microstructure and its dynamics in steels containing different phases at a micro- and nanoscale.

At present, $Pb(Zr,Ti)O_3$ and lead-based compounds constitute the best family of ferro- and piezoelectric materials. Because of their excellent properties, ease of processing, and low cost, lead-based piezoelectric materials are widely used as sensors, actuators, ultrasonic transducers, energy harvesting systems, etc. In thin film form, lead-based ferroelectrics have found many industrial applications, as e.g. in data storage devices. However, those materials contain a large amount of lead (more than 60 wt%) which creates hazards during processing and is environmentally toxic during disposal. As a result, legislations worldwide, as e.g. RoHS [1], restrict the use of lead due to health care and environmental problems. Therefore, lead-free materials with ferro- and piezoelectric properties comparable to lead-based compounds, as e.g. $Pb(Zr,Ti)O_3$, are in urgent demand.

The development of new lead-free ferro- and piezoelectric ceramics requires an understanding of the micro- and nanostructures and also the local ferroelectric, elastic and electromechanical coupling behavior at a micro- and nanoscale. Since the properties of ferro- and piezoelectric ceramics are related to their ferroelectric domain patterns, the imaging of the domains is also of particular interest. In the framework of a European-Mexican collaborative project (BisNano) with the overall objective of “adding value to mining at the nanostructure

level" [2], different lead-free bismuth based alloys were synthesized, in both bulk as well as thin films form, in order to discover new lead-free ferro- and piezoelectric materials for industrial applications. In this context, the second and shorter part of this thesis deals with mostly the characterization of lead-free ferro- and piezoelectric ceramic materials at a nanoscale using UPFM and AFAM techniques.

This thesis is organized as follows. Chapter I is divided into main four sections. Section 1 is devoted to the electromagnetic and micromagnetic nondestructive testing and evaluation (NDT&E) of steels at the macroscale and up to a micro- and nanoscale. Section 1.1 describes a brief history as well as the state of the art of electromagnetic and micromagnetic techniques. Problems and difficulties regarding interpretation of the output signals which are based not only on the microstructure and residual stress states of the investigated material, but also on the employed measurement setup, are discussed in section 1.2. In section 1.3, an approach to overcome some of the unsolved problems on the interpretation of the measured signals, and also to support further electromagnetic and micromagnetic techniques development is presented. This approach is based on the measurement signals at a macroscopic scale and also on the observation and characterization of the magnetic microstructure and its dynamics (micromagnetic events) at a micro- and nanoscale. At a macroscopic scale magnetic techniques like hysteresis loop and magnetic Barkhausen noise are used, and the physics background of these techniques is therefore discussed. A general overview of magnetic imaging techniques at a micro- and nanoscale which are relevant for NDT&E is first presented. A short review on magnetic imaging techniques, particularly in steels containing different phases, is also shown. MFM is chosen as the magnetic imaging technique when considering the correlation with macroscopic electromagnetic NDT&E methods.

The basic principles, the state of the art, and the experimental setups of the AFAM and UPFM techniques are discussed in section 2 and 3, respectively. In section 4 the research overview is presented.

The following chapters II-VIII show individual publications. The new findings are summarized after the individual publications in chapter IX.

1. ELECTROMAGNETIC AND MICROMAGNETIC NONDESTRUCTIVE TESTING AND EVALUATION (NDT&E) IN STEELS: FROM MACRO TO MICRO- AND NANOSCALE

1.1 Electromagnetic and micromagnetic techniques - brief history and state of the art

Magnetic measurement techniques like hysteresis loop and magnetic Barkhausen noise (MBN) have been widely applied for the characterization of the microstructure of ferromagnetic materials and their residual stress states. It is well known that the magnetic properties of steels depend on their chemical composition and the thermo-mechanical treatments to which the steel was subjected. Already in the early 1950s, magnetic Barkhausen noise and coercive force derived from the magnetic hysteresis loop measurements were employed with the objective to evaluate steels and other alloys with respect to their composition and microstructural state [3,4].

In Germany, electromagnetic nondestructive materials characterization started in the late 1970s during the nuclear safety research program with the goal of finding microstructure-sensitive NDT techniques to evaluate the quality of heat treatments. After a report [5] on MBN published in the United States revealing the use of the technique and its sensitiveness to microstructure changes as well as to load-induced and residual stresses, the European steel industry started a research using the MBN with the goal of determining residual stresses in large steel forgings [6].

Traditionally, microstructural parameters like precipitations, grain and phase boundaries, dislocation densities, etc. which directly influence the mechanical and magnetic properties of materials have been characterized using standard microscopy techniques like optical microscopy (OM), scanning electron microscopy (SEM), and transmission electron microscopy (TEM). With the objective to determine such microstructural parameters nondestructively, further micromagnetic techniques like incremental permeability measurement and harmonic analysis of the tangential magnetic field were later developed [7]. Such micromagnetic techniques require however calibration procedures and those are based on the observed micro- and nanoscopic data using microscopy techniques. At that time, due to the large scatter in the microscopy data and hence a strong propagation of errors in the calibration procedure, the research followed a more practical (businesslike) direction, i.e. a direct correlation between micromagnetic properties and mechanical properties like yield strength and hardness was proposed [6-9]. This correlation is based on microstructure interactions with both the domain walls as well as the dislocations [10]. An example of

hindering effects attributed to precipitates embedded in a matrix is shown in Figure 1. Figure 1a displays a TEM micrograph in which dislocations are being pinned by fine carbonitride precipitates in the Fe-22Mn-0.6C-0.2V alloy. Magnetic domain (Bloch-) walls which are pinned by large as well as small cementite precipitates in the unalloyed steel Fe-1.5%C are shown in the MFM image in Fig. 1b. Dislocations and magnetic domain walls are hindered by the same microstructural feature, i.e. precipitates, which gives rise to an increase of both the mechanical as well as the magnetic hardness of a ferromagnetic material.

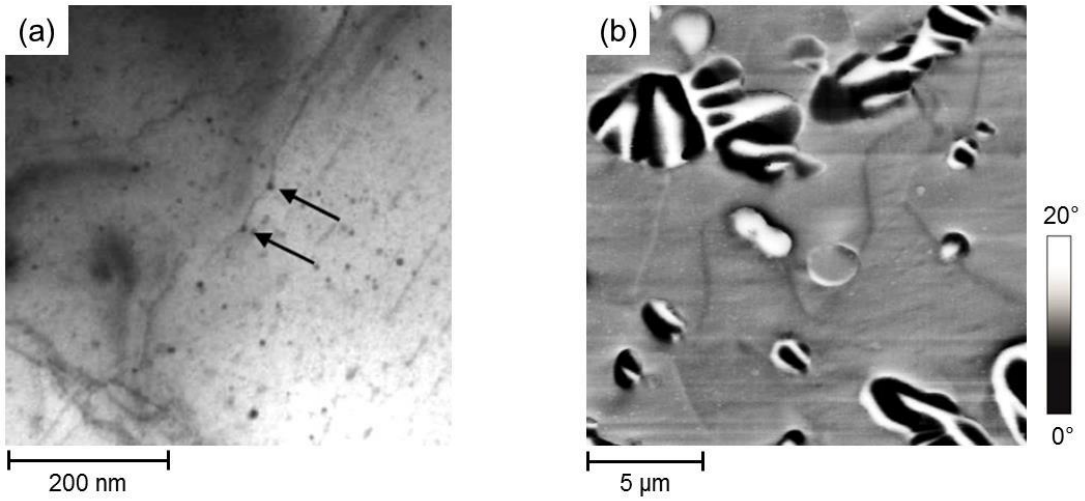

Figure 1. (a) TEM micrograph showing the hindering effect of dislocations by fine carbonitride precipitates as outlined by the two black arrows in the Fe-22Mn-0.6C-0.2V alloy [11]; (b) MFM image showing the hindering effect of domain (Bloch-) walls by large as well as small cementite precipitates in the unalloyed steel Fe-1.5%C [12, Publication A].

Microstructure interactions with both the domain walls as well as the dislocations allow therefore very often a correlation between mechanical and magnetic properties. By measuring some magnetic parameters nondestructively and using this correlation, some mechanical material properties like yield strength and hardness can be predicted. A schematic relationship which correlates the magnetic phenomena to material´s mechanical properties is shown in Fig 2.

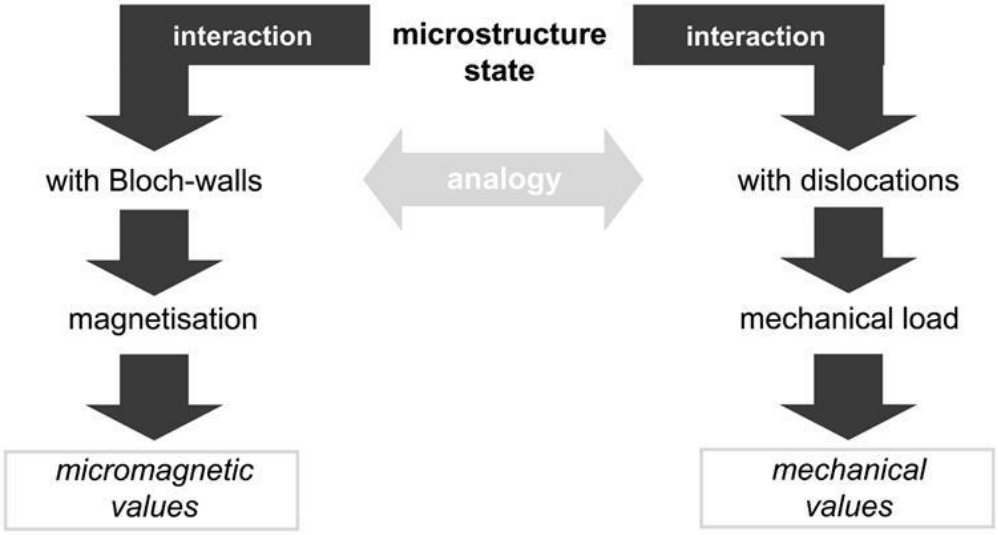

Figure 2. Correlations between micromagnetic and material mechanics [13].

However no micromagnetic parameters so far allow directly and universally valid quantitative determination of mechanical material properties like yield strength and hardness or load-induced and/or residual stresses. Due to the complexity of microstructures and the superimposed stress sensitivities the determination of such mechanical material properties becomes an extremly hard task. There was therefore a need to develop a robust multiple micromagnetic parameter approach. The Micromagnetic Multi-parameter Microstructure and stress Analysis (3MA) [14] is a methodology which was introduced into NDT by the Fraunhofer Institute for Nondestructive Testing (IZFP), Saarbrücken, where mechanical properties like yield and ultimate strength and hardness as well as residual stress states can be nondestructively evaluated. The 3MA method combines four micromagnetic techniques: Barkhausen noise, incremental permeability, harmonic of the tangential magnetic field, and multi-frequency eddy current (Fig. 3). By combining all these different micromagnetic techniques redundant and diverse information, i.e., "magnetic fingerprints", can be selected from microstructures of material states to be nondestructively analyzed. The magnetic fingerprints of the material consist of approximately 40 features derived from the measured signals. Together with magnetic fingerprints of calibration samples which are used as input for pattern recognition or regression analysis, mechanical material characteristics like hardness, yield strength, etc., or residual stress of the unknown sample can be predicted. The proper selection of the calibration specimen with well-defined values of the target quantity, e.g. Vickers hardness, is the most important task. Currently, there are more than a hundred 3MA installations worldwide in different industrial areas, including the steel industry,

mechanical engineering, etc.. For more details about the 3MA method the reader is referred to [7,14,15,16].

An electromagnetic monitoring principle at a microscopic scale was also developed by Fraunhofer IZFP. The Barkhausen noise and eddy current microscopy (BEMI) [17,18] allows surfaces to be monitored regarding their stress condition and material properties with a spatial resolution down to 10 µm. Furthermore, a new magnetic field sensor called "Point Probe" is beeing developed [19]. The Point Probe technique is based upon a needle-shaped ferromagnetic core which locally measures the strength of remnant magnetic fields and which can be applied for nondestructive hardness measurements, e.g. in parts with complex geometries.

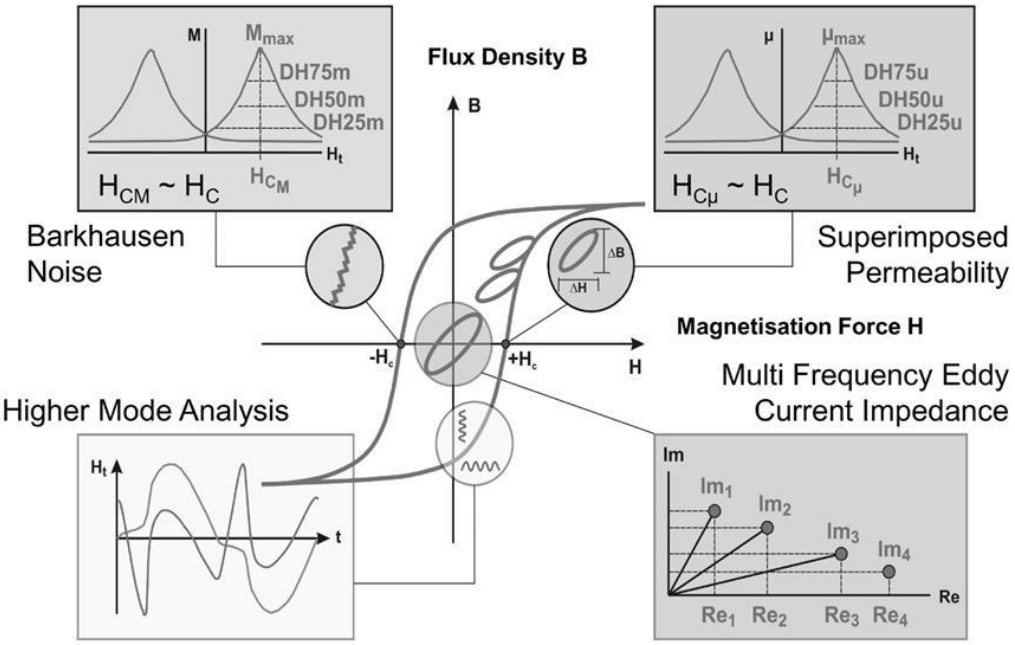

Figure 3. Micromagnetic Multi-parameter Microstructure and stress Analysis (3MA) approach [14].

1.2 Problems and difficulties of the electromagnetic and micromagnetic techniques

As previously described, electromagnetic and especially micromagnetic techniques have been successfully applied in the field of NDT&E because electromagnetic and micromagnetic intrinsic properties and mechanical properties are influenced very often by the same microstructure parameters. This correlation allows the inspection and monitoring of changes in microstructure states during material processing as well as materials degradation. Materials degradation can be understood with the onset of microstructural changes over time. A well-known example for this correlation is the connection between magnetic and

mechanical hardness. A material which shows high mechanical hardness usually exhibits a high coercivity, i.e. high "magnetic hardness" [20]. When a ferromagnetic metal is cold worked, both, mechanical and magnetic hardness, increases. When interstitial carbon atoms are added to iron to make steel, both, the magnetic and mechanical hardness increase with the carbon content [21]. However, the effect of the micro- and nanostructural features on the mechanical hardness may be completely different from those on coercivity ("magnetic hardness") and the use, for example, of the correlation between mechanical and magnetic properties is no longer valid. The addition of impurity atoms to a metal may result in the formation of a second phase which may have completely different properties compared to the matrix. The second phase may be softer than the matrix in terms of mechanical hardness which may lead to an overall decrease in the mechanical properties of the material. However, because of the magnetic anisotropy of the second phase, or due to its non-magnetic nature, the magnetic hardness of the material may increase due to the enhanced pinning of the domain walls [22]. In the case that impurity atoms are added to a metal to form a solid solution, the mechanical hardness increases because the solute atoms interfere with dislocation motion. However, the effect on the magnetic behavior is not to be foreseen. As discussed by *Cullity* [21], when silicon is added to iron the material becomes mechanically harder, but magnetically softer, because the addition of silicon decreases the crystal anisotropy K_1 and the magnetostriction γ. Additionally, magnetic oxides which are normally hard and brittle may be magnetically soft or hard depending on the crystal structure. With the new advances in materials processing, amorphous magnetic alloys are being developed which are mechanically hard, but magnetically soft, and which are therefore a strategic field for further NDT&E technology developments.

Further difficulties are also encountered as for example in the use of the MBN techniques. Such techniques are "not yet" regulated by a standard. Comparisons of MBN literature reveal considerable differences in experimental conditions such as magnetization set-up, signal pick-up, band width, sample surface condition, etc., which influence considerably the measured results. For example, large discrepancies between MBN results, i.e. number and shape of MBN peaks, are found in different studies of very similar materials [23,24,25]. First attempts into standardization of the MBN technique are initialized however by the German Engineering Society (VDE Guidelines) [26].

By combining multiple methods using statistical techniques as e.g. in the 3MA method [27,28], correlations are found between material degradation (e.g. by neutron irradiation), mechanical property changes, and micromagnetic signatures. Such techniques have been used

very often on monitoring hardening and recovery for example in reactor pressure vessel materials [29,30]. However, common embrittlement problems like phosphorus segregation cannot be detected using techniques based on micromagnetic methods when no hardening is involved [31]. On the other hand, when hardening is involved, embrittlement thresholds often can be determined. However, statistical regression methods and calibrated samples cannot distinguish between different hardening events [32].

It becomes clear that there is a critical gap on understanding the relationship between the magnetic NDT&E parameters and microstructural features. Some well-known case problems were addressed, in which the interpretation of the macroscopic electromagnetic NDT&E measurements becomes very difficult. Such problems become even more severe when the new advances in metallurgical technologies on new materials containing different microstructures and also stress states are considered, for example, multi-phase complex microstructure steels used in the automotive industry like dual-phase (DP), transformation-induced plasticity (TRIP), complex-phase (CP) steels, etc.. The development of practical electromagnetic and micromagnetic NDT&E technologies for microstructure and mechanical properties determination as well as early material degradation monitoring still lack in well understood interpretation of the resulting measurement signals. Therefore, fundamental scientific investigations at the micro- and nanoscale level are urgently required to support the electromagnetic and micromagnetic NDT&E technologies which are used for inspection and monitoring of component life assessment in industrial processes and also for future real-time monitoring of degradation in materials.

1.3 Development of an approach to support the electromagnetic and micromagnetic techniques

To support the understanding and further development of electromagnetic and micromagnetic techniques, an approach based on macro-scale measurement signals as well as the observation and characterization of the material at a micro- and nanoscale is proposed. At the macro-scale magnetic hysteresis loop and magnetic Barkhausen noise are used for materials characterization and evaluation. At the micro- and nanoscopic scale a relevant magnetic imaging technique for NDT&E is selected and used for microstructure imaging and determination of different micromagnetic events.

1.3.1 Macroscopic scale electromagnetic NDT&E measurements

In this section, the concept of magnetic domains and the basic characteristics of the magnetic hysteresis loop are first discussed. In the second part, the main principles of the Barkhausen noise method are described.

1.3.1.1 Hysteresis properties – the magnetic hysteresis loop

In 1907, *Weiss* [33] postulated that a ferromagnetic material is subdivided into uniformly magnetized regions called magnetic domains. Some years later, *Bitter* [34] using the so-called Bitter technique confirmed the Weiss' hypothesis by observing domain patterns on iron and iron-silicon alloys with large grains. The concept of magnetostatic energy, which supports the explanation of the formation of domains, was later proposed by *Landau and Lifshitz* [35]. Domain walls separate neighboring domains of different magnetization orientations. The magnetic domain structure results from the balance of several competing basic energy terms involved in ferromagnetism: exchange energy ($E_{exchange}$), magnetostatic energy ($E_{magnetostatic}$), magnetocrystalline anisotropy ($E_{magnetocrystalline}$), magnetoeleastic energy ($E_{magnetoeleastic}$), and domain wall energy (E_{wall}).

$$E = E_{exchange} + E_{magnetostatic} + E_{magnetocrystalline} + E_{magnetoeleastic} + E_{wall.} \quad (1)$$

The exchange energy ($E_{exchange}$) which originates from quantum mechanical exchange forces or spin-spin interactions favors uniform magnetization configurations. The magnetocrystalline anisotropy ($E_{magnetocrystalline}$) favors the orientation of the magnetization vector along preferred crystallographic directions, as for example <100> in iron. These directions are also termed axes of easy magnetization [36]. The magnetostatic energy ($E_{magnetostatic}$) favors the magnetization configurations giving a null average magnetic moment [37]. The magnetoeleastic energy ($E_{magnetoeleastic}$) describes the relation between the crystal lattice strains to the direction of domain magnetization. It reaches a minimum when the crystal lattice is deformed such that the domain is elongated or contracted in the direction of domain magnetization [38]. Domain walls have an energy E_{wall} which is proportional to its surface area. It is out of the scope of this work to revise all these energy terms in detail. For further information the reader is referred to [36,37,39,40]. The configuration of the final magnetic microstructure is the outcome of the minimization of the sum of these five energy terms.

A ferromagnetic material in the so-called virgin or demagnetized state consists of a large number of magnetic domains with arbitrary magnetic orientation (Fig. 4). The overall

magnetization (magnetic moment per unit volume) of a piece of material is the vector sum of the domain magnetizations. In an ideally demagnetized state, the overall magnetization is zero. An external magnetic field tends to align the individual magnetic moments of the domains allowing a net magnetization in the field direction. Domains with moments aligned most closely to the applied field increase their sizes at the expense of domains of other orientations. The process of magnetization is converting the multidomain state to a single domain magnetized in the direction of the applied field (Fig. 5). The process does not proceed continuously but by stepwise movements of the domain walls, and in case of strong applied fields also by rotation of the magnetization vectors in the domains towards the direction of the applied field [6]. For a sufficiently strong applied field, the total resultant magnetization reaches a saturation value. When the external magnetic field is decreased and reversed in sign, the magnetization does not retrace its original path of values, the material exhibits the so-called hysteresis [39].

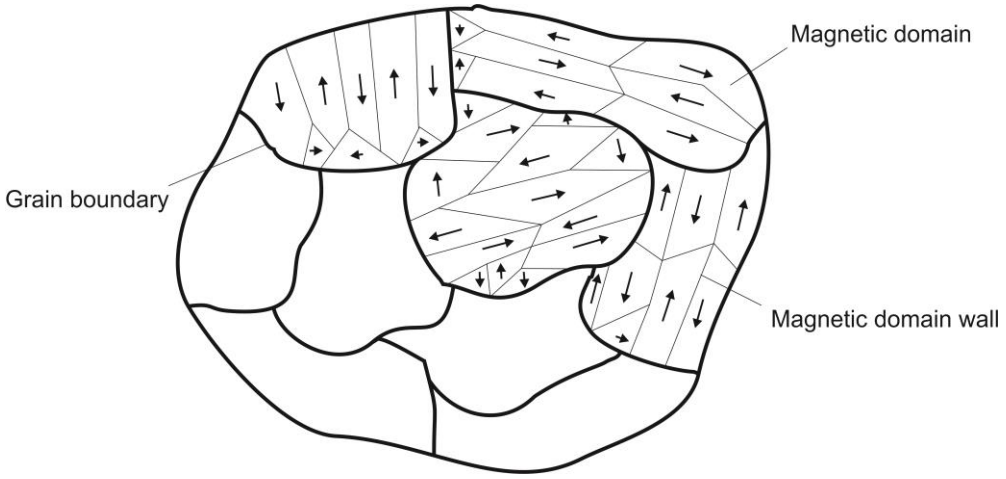

Figure 4. Schematic representation of magnetic domains with arbitrary magnetic orientation in a polycrystalline ferromagnetic material in the so-called virgin or demagnetized state. For better visualization, only some grains display magnetic domains.

In this work, the *SI system of units* is employed. The magnetization M and the magnetic field H are measured in amperes per meter (Am^{-1}), whereas the magnetic induction B is measured in Tesla (T). The permeability of the vacuum is given by $\mu_0 = 4\pi 10^{-7}$ Hm^{-1}. The magnetic hysteresis loop is obtained by applying a magnetic field $\mu_0 H$ to the specimen and measuring the ensuing change of the magnetization M or magnetic induction B in field direction (Fig. 5). Starting from the initial demagnetized state ($B = \mu_0 H = 0$ Tesla) the magnetic induction increases with increasing field and if a sufficiently large field is applied it reaches the saturation of the magnetic induction ($B = B_S$). By reducing the magnetic field

from the saturated state to zero, the specimen remains magnetized. The magnetic induction at zero external field is called remanence B_R. By applying a reverse magnetic field of strength $\mu_0 H_C$, known as the coercive field, the magnetic induction returns to zero. Further increase of the reversed applied field magnetizes the specimen in the opposite direction, and if a sufficiently large field is applied the specimen saturates in the opposite direction ($B = -B_S$).

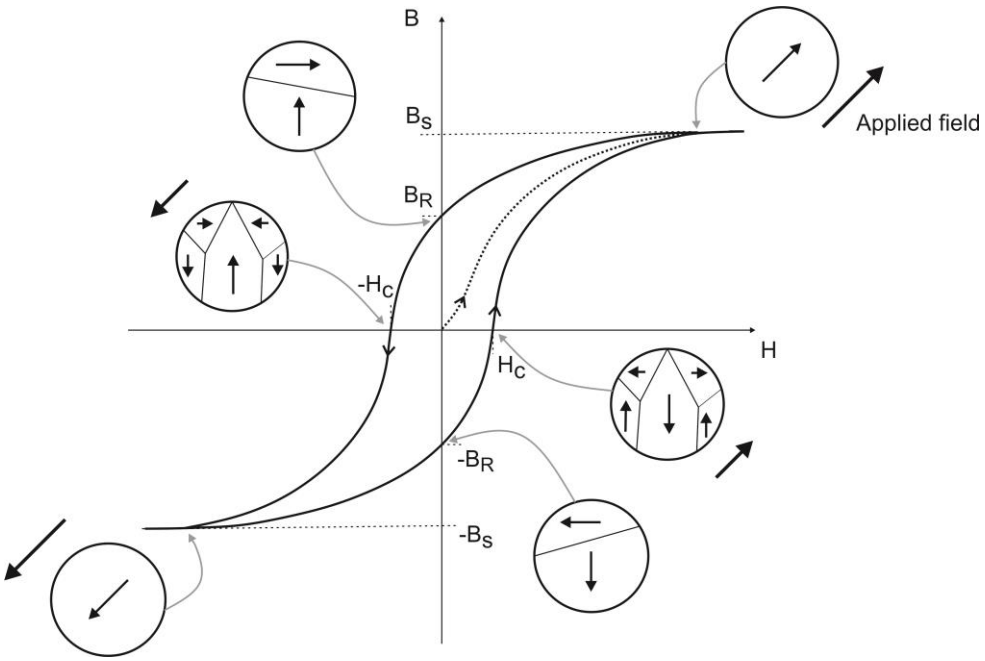

Figure 5. Schematic representation of hysteresis loop and ensuing evolution of magnetic domains.

The parameters most commonly used to characterize hysteresis are the coercive field H_C, the remanent magnetic induction B_R, and the hysteresis energy loss W_H, which is determined from the area enclosed by the loop. In general, the hysteresis parameters are considered as independent. However, many materials have shown linear relationships between, for example, W_H and H_C [8,41]. The basis of the magnetic hysteresis loop measurement system is an electromagnet to generate the alternating magnetic field, a pick-up coil wound around the sample to detect the change in the magnetic induction B, and a sensor, e.g. Hall probe, to measure the tangential magnetic field strength H. Fig. 6a shows a typical setup for the magnetic hysteresis loop (B-H) measurements in a rod specimen.

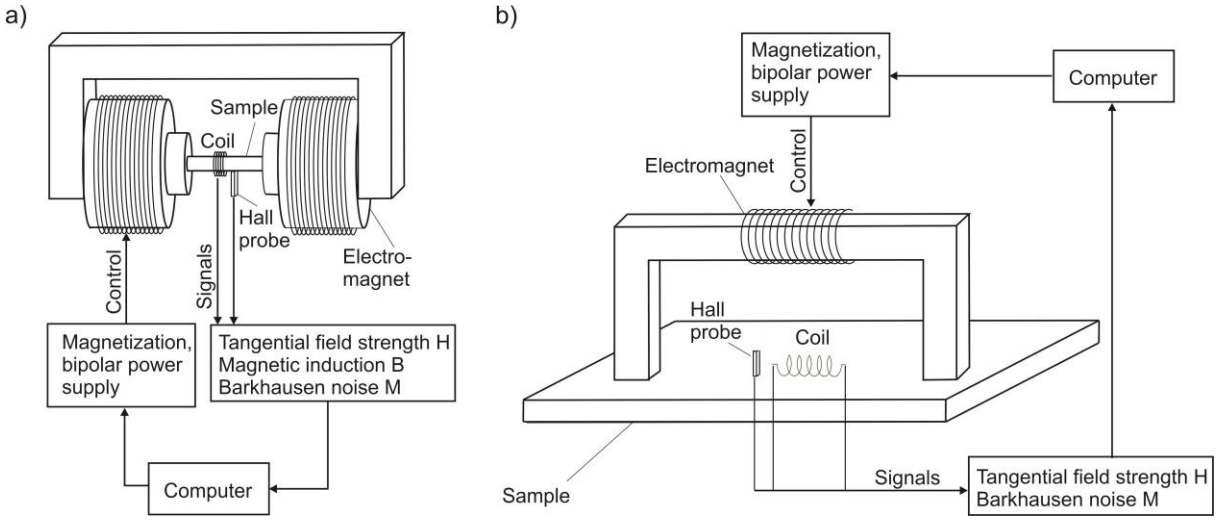

Figure 6. Typical measurement devices for magnetic Barkhausen noise measurements: encircling (a) and surface (b) Barkhausen noise detection.

1.3.1.2 Magnetic noise – the magnetic Barkhausen noise

In 1919, the German scientist Barkhausen [42] discovered that during the magnetization of a sample of ferromagnetic material many short-lived voltage pulses are induced in a coil wound around the sample. It was called "noise" because in the original experiment the short-lived voltage pulses were detected as audible clicks in a loudspeaker. The term "magnetic" for the magnetic Barkhausen noise is used to distinguish it from "acoustic Barkhausen noise" (MAE), the latter being based on magnetostrictively excited acoustic emission signals [43].

The magnetic noise is generated because during the magnetization process the movement of domain walls takes place discontinuously. The domain walls are temporarily pinned by microstructural obstacles like dislocations, precipitates, and phase or grain boundaries and their stepwise pull-out from these obstacles change the magnetization state locally inducing pulsed eddy currents into the sample. This noise phenomenon can give information on the interaction between domain walls and compositional microstructures and/or load-induced and residual stresses. By measuring the Barkhausen noise activity quantitative information about micromagnetic events occuring in the bulk sample can be obtained. In iron-based materials, while the MBN is generated by any sudden change in the magnetization state (movement of any domain wall), the MAE arises only from 90° domain wall motion. The MAE technique has never found widespread industrial application because of the need of very high signal amplification and because of its high sensitiveness to electrical interference noise. In a laboratory-scale, however, the combination of both MBN and MAE techniques can provide complimentary information.

The basis of a Barkhausen noise measurement system is similar to the one for the hysteresis loop measurement. The main components are an electromagnet to generate the alternating magnetic field, a pick-up coil to detect the noise pulses, and a magnetic sensor, e.g. Hall probe, to measure the tangential magnetic field strength H. There are mostly two types of Barkhausen noise experiments. The detection (pick-up) coil may be wound around the specimen (Fig. 6a), which gives the term encircling Barkhausen noise. This restricts the size and shape of the specimen and is therefore very often inconvenient for NDT. However, using this setup, the hysteresis loop can also be accurately measured (homogeneous magnetization and demagnetizing field) allowing a better understanding of the magnetization phenomena. The alternative method uses the electromagnet placed onto a flat surface and a detection (pick-up) coil on or near the surface of the specimen (Fig. 6b). This method can be called surface Barkhausen noise [44]. The MAE measurements are accomplished using an arrangement similar to the one in Fig. 6b, but instead of a detection coil, it uses a piezoelectric transducer bonded directly to the sample surface.

As mentioned above, during the magnetization process of a ferromagnetic material abrupt irreversible discontinuities in form of MBN emissions are observed (Fig. 7a). The detected raw magnetic noise data are a series of voltage pulses which can be plotted for example as a function of time (Fig. 7b). The root-mean-square (RMS) of the noise over several field cycles can be obtained. A typical plot of the inductive Barkhausen noise amplitude M versus applied field H is shown in Fig. 7c. Further plots are also often encountered in the literature. For example, to obtain the noise frequency content, Fourier analysis can be performed. The size distribution of noise pulses or the number of pulses can also be plotted as a function of time or applied field. Additionally, single parameters like the total number of pulses and the noise energy have been also used to characterize the noise signals [45].

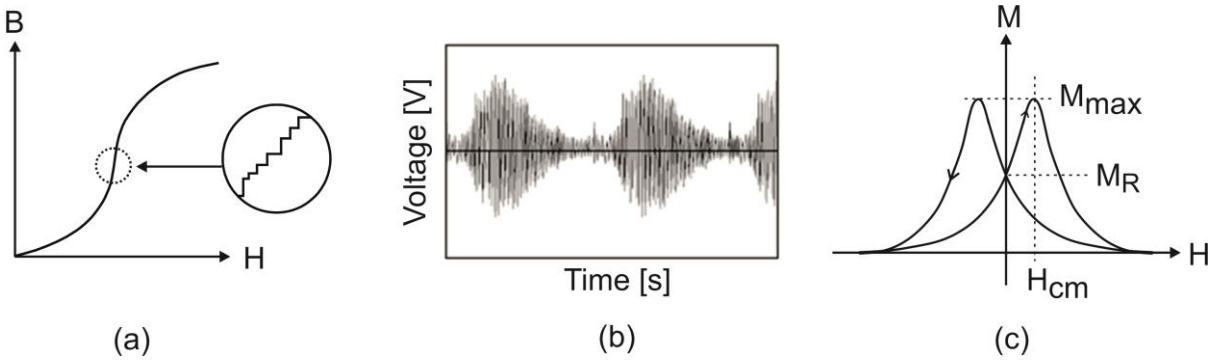

Figure 7. (a) B-H curve showing irreversible discontinuities in magnetization as the magnetic field is varied in the form of MBN emissions; (b) Magnetic Barkhausen noise plot showing the raw noise versus time and (c) the schematic Barkhausen noise curve versus applied field with the maximum of noise amplitude M_{max}, remnant noise amplitude M_R and coercive field H_{cm} deduced from noise curve.

1.3.2 Micro- and nanoscopic scale NDT&E imaging

The observation of the magnetic properties at a micro- and nanoscopic scale allows the identification of the microstructure changes which influence the macroscopic electromagnetic NDT&E methods. Section 1.3.2.1 discusses the magnetic imaging techniques which have most relevance when considering a correlation to and better understanding of macroscopic electromagnetic NDT&E methods. In section 1.3.2.2, a literature review on magnetic imaging in steels, particularly in those containing different phases, is presented. At the end of this section, a magnetic imaging technique which is suitable for imaging the magnetic micro- and nanostructure of multi-phase thick (bulk) steel samples as well as micromagnetic events is selected.

1.3.2.1 Magnetic imaging techniques – general overview

Different techniques can be used to image magnetic microstructures. This work is focused on the most relevant magnetic imaging techniques which have the potential to allow the correlation to and better understanding of macroscopic electromagnetic nondestructive methods. It is beyond the scope of this work to review all techniques in detail, but the reader is referred to a recent review [46].

The earliest magnetic microstructure images were obtained by depositing very fine magnetic powder on the specimen surface. The so-called Bitter technique [34] reveals domain walls which intersect the surface because the resulting stray fields attract the magnetic particles stronger than the surrounding regions [47]. The conventional Bitter pattern technique however has a low spatial resolution (~ 1 μm).

The magneto-optic Kerr effect (MOKE) technique [48,49] is a powerful and relatively cheap magnetic domain imaging method in which the contrast is obtained by the interaction between magnetic fields and polarized light. The surface reflected light may undergo a change in polarization state and intensity dependent on the relative orientation of the surface magnetization. Besides, the possibility of measuring local magnetization curves, the scanning Kerr microscopy [50] can perform very fast imaging within the nanosecond scale allowing to study the dynamics of domain pattern formation (micromagnetic events). However, the spatial resolution of the MOKE technique is limited by the wavelength of the used laser (few hundred nanometers).

A much higher spatial resolution can be achieved using methods based on electron microscopy. The domain observation using TEM in the so-called "Lorentz imaging mode" or Lorentz electron microscopy (LEM) [51] is based on the deflection of electron beams caused by the Lorentz force. Contrast in areas with different magnetization can be obtained because the electron beam trajectory deflects when it passes through a region of magnetic induction. Different variants as for example Fresnel and Foucault modes can be used. Using the Fresnel mode, domain walls can be visualized and distinguished from other features such as e.g. dislocations [52]. Using the new aberration-corrected microscopes, spatial resolution in the order of 1 nm can be achieved [46]. Besides the high cost of the TEM instrument, the LEM technique requires very special sample preparation (flat and electron transparent), and it is difficult to apply magnetic fields to the sample as this often changes the electron beam trajectory. It is thus challenging to apply an external magnetic field in LEM while imaging. SEM techniques for magnetic domain imaging have also been developed. The so-called scanning electron microscopy with polarization analysis (SEMPA) images surface magnetization distribution by measuring the spin polarization of secondary electrons emitted from a magnetic sample. The measurements are performed in a chamber of a SEM with the help of a Mott detector [53,54]. SEMPA can directly detect the sample magnetization component with a high spatial resolution of about 20 nm. The major limitation in application of SEMPA is the fact that the measurements must be performed in ultra-high vacuum on a well prepared clean conducting surface.

Magnetic domain imaging can also be performed using scanning probe techniques. The scanning Hall probe microscopy (SHPM) [55] employs a semiconductor Hall sensor which maps the magnetic induction associated with a sample. With the latest advances in the SHPM systems high magnetic field sensitivity (0.1 μT – 10 T) can be achieved. The drawback of this technique is the poor spatial resolution (~ 300 nm). MFM [56,57] is a

dynamic scanning probe technique which records the magnetostatic interaction between the sample surface and a microfabricated magnetic tip with a radius of curvature of nm dimensions. The main advantages of MFM is that it does not need special sample preparations and can work in ambient conditions with a spatial resolution down to 10 nm. MFM is suited to study multi-phase and relatively large thick (bulk) materials by measuring simultaneously the topography and the magnetic microstructure. The interpretation of the observed magnetic contrast is, however, not straightforward since MFM does not directly monitor the magnetization distribution but rather the stray field. In addition, the tip stray field may cause reversible and irreversible changes in the local magnetic state of the sample and vice-versa [58]. MFM is, however, the most commonly used magnetic imaging technique for studying nanomagnets due to its easy implementation and relatively low costs. Furthermore, MFM has the potential for studying local and collective magnetization switching behavior by performing large area scans (~ 100 μm^2) with in-situ magnetic fields [12,59].

All the previously mentioned magnetic imaging techniques are complimentary. Each technique has its advantages as well as drawbacks. A combination of these techniques allows one to reconstruct the complete magnetization distribution and also to understand the magnetization behavior of materials at the nanoscale.

1.3.2.2 Magnetic imaging in steels

The imaging of the magnetic microstructure of steels containing different phases is rarely encountered in the literature. The MFM technique has often been used to image domain structures in magnetic thin films [60-62]. Only a few studies used MFM to image domain structures in polycrystalline bulk materials [63]. In steel samples, MFM was used to image phase transformations caused by defects like strain-induced martensite forming at crack tips in 304 and 310S austenitic steels [64] and martensite formation along grain boundaries due to chromium depletion in 304 stainless steel [65]. Most relevant for the correlation to and understanding of macroscopic electromagnetic NDT&E methods is however the possibility of imaging the magnetic microstructure when an external magnetic field is applied. This enables the visualization and interpretation of the magnetic domain dynamics and of micromagnetic events. Most of the work of this type, i.e. high-resolution magnetic imaging of steels in combination with an external field, employs the LEM technique, which is based on the TEM, in both, Fresnel and Foucault modes. Using this technique, the configuration of the magnetic domains and their dynamics were observed in different steels containing different microstructures including high strength low-manganese pearlitic steels [66], low carbon

pearlitic steels [67,68], hypereutectoid pearlitic steels [69,70], and carbon-manganese steels with ferritic/pearlitic and martensitic/bainitic microstructures [71].

As described in section 1.3.2.1, the observation of micromagnetic events (magnetization dynamics) using LEM is however limited to samples which are transparent to the electrons (confined to specially prepared thin foils). Such thin foils face many problems during preparation. During the etching process in order to obtain thin areas transparent to electrons, often preferential etching occurs due to the different etching rates of the different phases. In addition to the laborious sample preparation, the TEM is complicated to handle and only small dimensions of the examined sample volume can be characterized. The application of an external magnetic field in the TEM is not an easy task. Furthermore, due to the strong ferromagnetic structural components and various electromagnetic lenses in the microscope column, accidental magnetization of the sample during sample insertion is possible [72].

Taking into account the inherent spatial resolution and instrumental constraints and also the possibility to perform the measurements directly on the surface of relatively thick and large (bulk) samples, the MFM is chosen in this work as the magnetic imaging technique when considering the correlation with macroscopic electromagnetic NDT&E methods. MFM with a superposed external magnetic field is used to observe local magnetization behavior as for example the individual magnetization of the different phases in steels. The choice of the magnetic probe plays a crucial role on the quality and reliability of the magnetic images. During MFM imaging, the stray field of the magnetic probe may cause reversible and irreversible changes in the local magnetic state of the sample and vice-versa. Therefore, an appropriate magnetic probe is chosen for each particular experiment. The observation of the magnetic microstructure and domain wall dynamics in the MFM is confined to the surface of the sample. Even though the magnetic microstructure of the surface does not correspond directly to the one of the volume, the characterization of different phases by their stray fields and their individual response to an external applied field provides information about the magnetic hardness of the individual phases and the different pinning mechanisms (micromagnetic events), which occur during the magnetization processes.

2. ATOMIC FORCE ACOUSTIC MICROSCOPY – PRINCIPLE, STATE OF THE ART AND EXPERIMENTAL SETUP

The atomic force acoustic microscopy technique [73-76] is a dynamic enhancement of atomic force microscopy (AFM) [77], which is used to determine qualitative, and also quantitative local elastic properties of sample surfaces at a nanoscale. A more recent name of

the technique is contact resonance force microscopy (CR-FM) [78]. The basic ideas of AFAM are demonstrated in Fig. 8. The AFM cantilever is driven to vibrate either by an actuator attached to the cantilever holder or by an ultrasonic transducer (piezoelectric element) coupled to one side of the sample. The response of the cantilever is composed of different vibration modes such as transverse and lateral flexural and torsional modes. When the tip of the cantilever is out of contact with the sample surface, i.e. free or in air, the resonant modes occur at specific frequencies which depend on the shape, the geometrical dimensions and the material properties of the cantilever Fig. 8(a). As soon the tip is brought into contact with the sample surface (Fig. 8(b)) the frequencies of the resonant modes increase because of the tip-sample forces which influence the mechanical boundary conditions of the cantilever (Fig. (8c)). This shift of resonance frequencies from "out of contact, free or in air" to "contact", is dependent on the sample's mechanical properties.

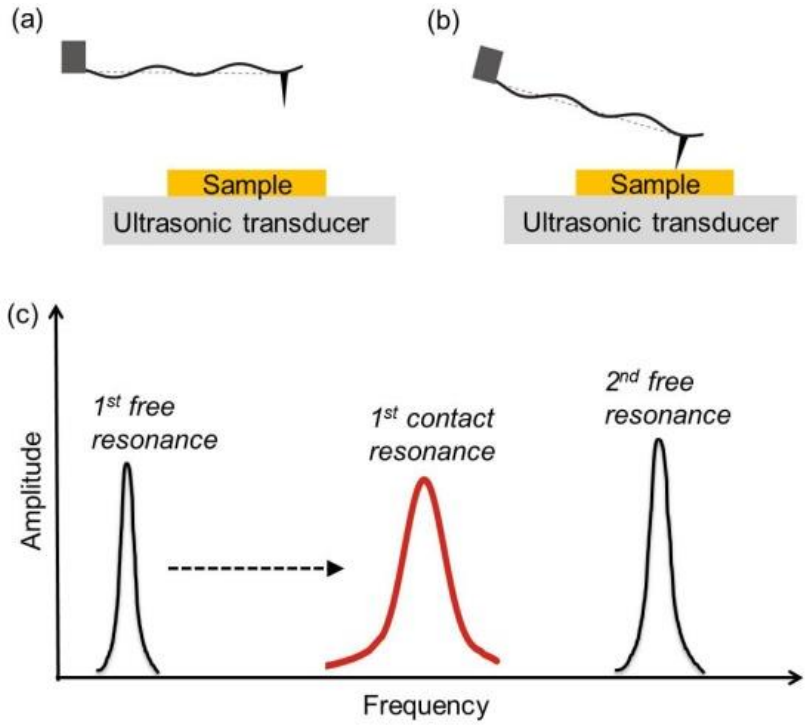

Figure 8. Basic ideas of AFAM. Transverse flexural resonant modes of the cantilever are excited by a piezoelectric actuator when the tip is (a) free or in air and (b) in contact with a sample surface under an applied static force. (c) Resonant spectra showing the first and the second free resonances as well as the first contact resonance. The first contact resonance is encountered between the first and the second free resonances.

The experimentally obtained transverse flexural contact resonance frequencies can be interpreted with an analytical model for cantilever dynamics [79,80]. One simple example of such a model to describe the tip-sample contact forces (contact stiffness) is shown in Fig 9.

The tip-sample interaction is entirely elastic and acts in a direction normal (vertical) to the sample surface. The lateral stiffness as well as the lateral and vertical damping constants are in this case neglected. The rectangular cantilever beam is coupled to the sample via the sensor tip by a spring of stiffness K^*. L_1 is the length between the tip and the cantilever base, L` is the length from the tip to the end of the cantilever with $L = L_1 + L`$ (Fig. 9). The analytical model for cantilever dynamics provides a characteristic equation (see for example [79-81]), which links the measured frequencies to the tip-sample contact stiffness K^*. However, the unknown effective tip position parameter L_1 of the cantilever influences the value of K^* obtained using the characteristic equation. If the free and contact resonances for at least two different transverse flexural modes are known, the unknown parameters L_1 and K^* can be resolved. In this case, the contact stiffness K^* is calculated and plotted as a function of the tip position parameter L_1 for each resonant mode. The cross-point of the two yields the value of the contact stiffness K^* and the effective tip position. A more detailed description of models of cantilever dynamics in AFAM can be found in [79,80].

Fig. 9. Transverse flexural beam-dynamics model for the AFM cantilever. The rectangular cantilever beam is clamped at one end and has a total length L. The tip-sample contact forces are represented by a spring of stiffness K (contact stiffness) located a distance L´ away from the free end of the cantilever. In this simple model, the lateral stiffness as well as the lateral and vertical damping constants are neglected.*

Using the values of K^* the elastic properties of the sample can be determined with the help of a second model for the tip-sample contact mechanics, such as for example Hertz or Maugis models [82,83]. The most used and simple contact mechanics model is the well-known Hertzian model, which describes the elastic interaction between two nonconforming bodies of general anisotropy [82]. Considering the sensor tip a hemisphere with radius R pressed against a flat surface with an applied force F_c, the contact stiffness K^* can be calculated from:

$$K^* = \sqrt[3]{6F_c R E^{*2}}. \quad (1)$$

E^* is the reduced Young´s modulus that combines the elastic properties of the tip and the sample, and can be represented by:

$$\frac{1}{E^*} = \frac{1-\nu_{tip}^2}{E_{tip}} + \frac{1-\nu_s^2}{E_s}. \quad (2)$$

where E_{tip}, E_s, ν_{tip}, ν_s, are the Young´s moduli and Poisson´s ratio of the AFM tip and the surface, respectively. The Hertzian model however holds only for isotropic bodies. AFM sensor tips made of single crystalline silicon and also individual grains in a polycrystalline material are not elastically isotropic. In special cases of symmetry, i.e. if there is a three or fourfold rotational symmetry axis perpendicular to the boundary, Eqs.1 and 2 remain valid if the reduced elastic modulus $E/(1-\nu^2)$ is replaced by an indentation modulus that is calculated numerically from single crystal elastic constants [84,85]. The definition of the reduced Young´s modulus E^* becomes:

$$\frac{1}{E^*} = \frac{1}{M_{tip}} + \frac{1}{M_s}. \quad (3)$$

where M_{tip} and M_s are the identation moduli of the AFM tip and the sample, respectively. For the [100] silicon AFM sensor tip the required symmetry holds, and M_{tip} = 165 GPa is used. For the calculation of the M_s in Eq. (3) one requires the reduced Young´s modulus of the unknown sample E^*_s. The tip radius R (Eq. 1) is difficult in practice to be determined, and it is therefore an unknown parameter. To circumvent this problem two different reference methods based on reference samples with known elastic properties have been developed: single reference method [86] and dual reference method [80,87]. For the single reference method the contact stiffness K^* of the reference (K^*_{ref}) and unknown sample (K^*_s) are determined at the same static load F_c and compared:

$$E_s^* = E_{ref}^* \left(\frac{K_s^*}{K_{ref}^*}\right)^n. \quad (4)$$

E^*_s and E^*_{ref} are the reduced Young´s moduli of the unknown and reference samples, respectively. The tip geometry factor *n* depends on the tip-sample geometry. For Hertzian contact (spherically shaped), *n* = 3/2; for a flat punch (flat tip), *n* = 1. The indentation modulus of the sample M_s can be therefore derived using Eqs.(1-3) without the need of the radius R of the tip. The measurements are usually performed by acquiring alternated contact resonance spectra, i.e. on the unknown sample and a reference sample the elastic properties of which are known.

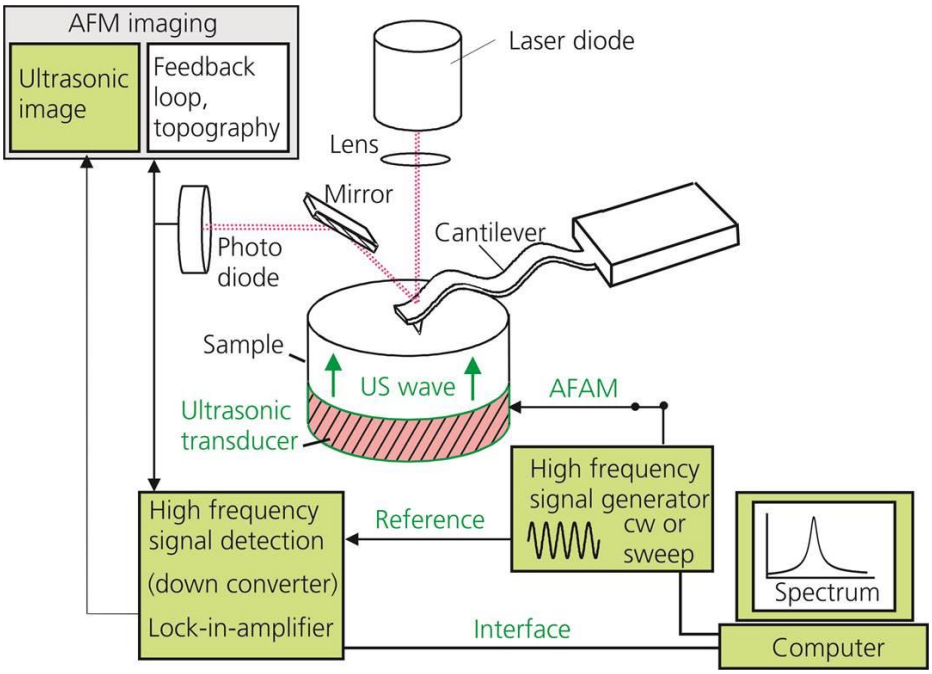

Figure 10. Experimental set-up for contact resonance spectroscopy and for acoustical imaging using AFAM. The AFM tip is scanned in contact over the sample surface.

Figure 10 illustrates the setup for AFAM measurements. AFAM is based on a combination of AFM and ultrasonic techniques. In standard AFM technique, the oscillation of the cantilever while it scans across the surface of a material is used to map the topography. The deflection of the reflected laser beam in the photodiode detector is used to measure the height differences. For the AFAM technique the sample is mounted on an ultrasonic transducer driven by a function generator which may be charged with either a sine (single frequency) or a sweep. The ultrasonic transducer emits longitudinal waves through the sample causing out-of-plane surface vibrations. The vibrations couple to the cantilever via its sensor tip forcing the cantilever into transverse flexural vibrations. The low frequency components of the cantilever vibrations are used for topographic imaging. The higher frequencies are evaluated by special electronics which provides the high frequency oscillation amplitude and phase of the cantilever which depends on the excitation frequency. A heterodyne downconverter (mixer) in combination with a lock-in amplifier, or a fast signal acquisition card in combination with fourier analysis, can be used [88].

As mentioned previously, the function generator can be programmed to send either a sine (single frequency) or a sweep signal. When the sweep signal is activated, the excitation frequency of the output signal is varied continuously over a fixed time interval to a maximum cut-off frequency, whereby the contact resonance spectrum of the system composed of the sensor with its tip and the sample can be found. The amplitude of the cantilever in contact

with the sample surface as function of the frequency can be also recorded in dependence of the applied force F_c. In the case that the tip has a geometry different from a flat punch, an increase in static load leads to an increase in the tip-sample contact area and therefore a larger value for the tip-sample contact stiffness K* is expected [89].

When the contact resonance frequency is found, one can take acoustic (also called AFAM amplitude) images by selecting a frequency close to a contact resonance of a particular mode while the sample surface is scanned. In this case, the lock-in output is connected to an auxiliary channel of the commercial AFM instrument, the signal is then digitized, and displayed as a color-coded image. The resulting image thus contains the relative amplitude of the cantilever vibration at the excitation frequency for each position on the sample. The acoustic image contrast depends on the difference between the excitation frequency and the local contact resonance. Therefore, acoustic images allow differences in the local tip-sample stiffness, as e.g. between phases and/or grains having different crystal orientations, to be detected. The topographic AFM image is acquired simultaneously with the acoustic image. Contrast inversion of acoustic images is observed if the frequency of excitation is varied between values below and above a contact resonance. Figure 11 presents a practical example of an unalloyed pearlitic steel containing two phases, lamellar cementite and ferrite. Figure 11a shows the topography image giving information about the sample microstructure and surface roughness. The topographic height variation is about 300 nm. Fig. 11b displays a single point contact resonance frequency spectrum. The red and blue curves represent the contact resonance frequencies for the cementite (745 kHz) and the ferrite (755 kHz) phases, respectively. Figurec 11c and d show acoustic images acquired at these two different frequencies. In the acoustic image taken at or close to the lower contact resonance frequency (Fig. 11c), the cantilever vibration amplitude is higher for the more compliant phase, here the cementite lamellae. Therefore, the cementite lamellae appear brighter. Increasing the excitation frequency so that it is at or close to the higher contact resonance frequency (Fig. 11d), the amplitude of the cantilever decreases on the more compliant phase and increases on the stiffer one. Hence, the stiffer phase, here the ferrite, appears now brighter. Thus, a contrast inversion is observed by varying the excitation frequency. If the excitation frequency is far away from a contact resonance, the contrast disappears completely. From acoustic images only qualitative information about the sample elastic properties is obtained. In order to obtain local quantative information, contact resonance frequency measurements in each image point are necessary. For faster acquisition of the contact

resonance spectra further methods like the dual resonance excitation [90], band excitation [91] and resonance tracking [92], were developed.

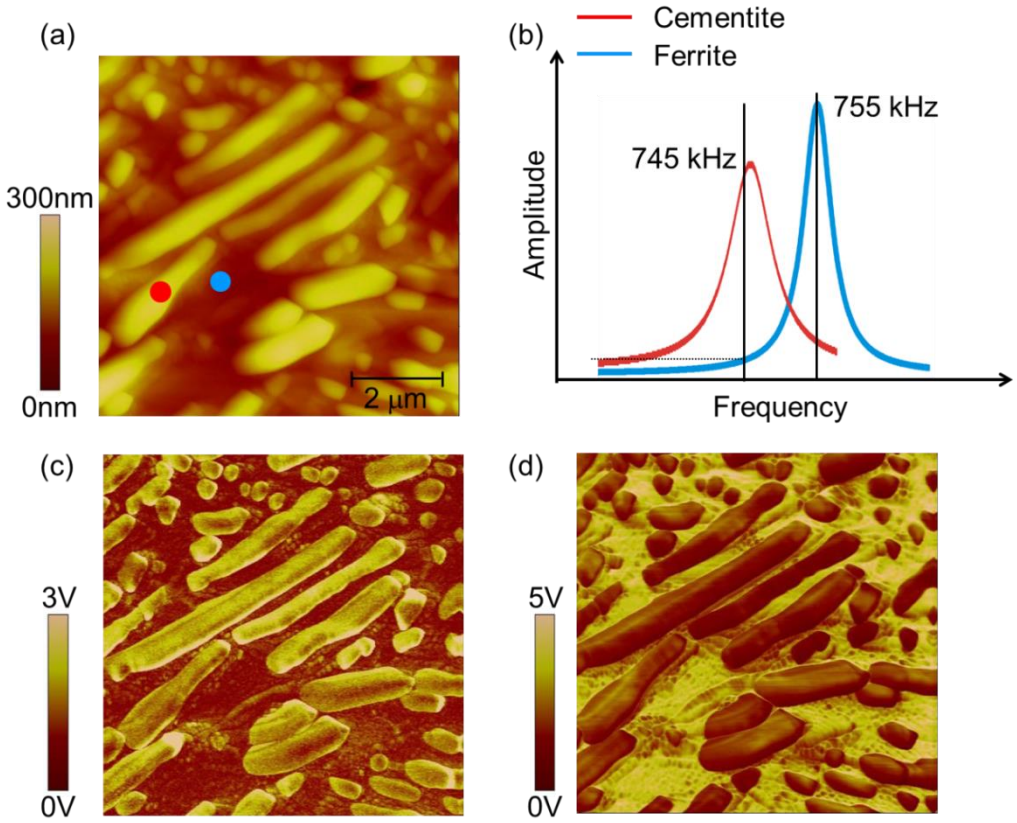

Figure 11. Principles of AFAM acoustic (amplitude) imaging showing contrast inversion. The sample is an unalloyed pearlitic steel containing lamellar cementite embedded in a ferrite matrix. (a) Contact-mode topography. (b) Single point contact resonance frequency spectra. Acoustic images acquired at different excitation frequencies, (c) f = 745 kHz and (d) 755 kHz. The first free transverse flexural resonance frequency of the cantilever is f_0 = 175.7 kHz.

As will be shown in the next section, contact resonances are also useful for signal enhancement in the piezo-mode AFM technique.

3. PIEZO-MODE – PRINCIPLE, STATE OF THE ART AND EXPERIMENTAL SETUP

The AFM-based dynamic technique called piezo-mode or piezoresponse force microscopy (PFM) is used for nondestructive high resolution (~ 20 nm) ferroelectric domain imaging and manipulation in thin films, single crystals, and polycrystalline ceramics. PFM is based on the detection of surface deformations induced by the electrically biased probing tip [93]. An ac voltage is applied between the electrically conductive sensor tip and the ground

electrode creating a localized electric field below the tip which interacts with the surface of a piezoelectric sample via the inverse piezoelectric effect. This voltage (peak-to-peak amplitude of ~ 10 V_{pp}) excites a sample vibration (expansion and contraction) locally which is detected by the cantilever via its sensor tip being in contact with the sample surface. The laser beam reflected from the cantilever is detected by the four quadrant laser diode of the commercial AFM microscope, and the signal is then further analyzed using a lock-in technique. Similarly to AFAM, PFM is carried out in contact mode, and using the low frequency components of the cantilever deflection with the electronic feedback loop of the AFM, the topography of the sample is simultaneously acquired. The frequency of the applied voltage is usually lower than the first transverse flexural resonance frequency of the cantilever (mostly between 10 and 60 kHz). First images at a nanoscale of piezoelectric materials using PFM were presented in 1992 by Güthner and Dransfeld [94]. To date, PFM has found a broad applicability to ferroelectric domain imaging, domain patterning and spectroscopy in many different materials such as ferroelectric perovskites [95], piezoelectric III-IV nitrides [96], and recently, biological systems such as tissues [97,98] and proteins [99].

One distinguishes between vertical (VPFM) and lateral PFM measurements (LPFM). In a VPFM measurement, the elongation or contraction of the surface (usually a single domain) is analyzed perpendicularly to the sample surface. Those so-called out-of-plane signals are obtained mostly via the transverse flexural vibrations of the cantilever and give information on the out-of-plane component of electromechanical surface response. In a LPFM measurement, the elongation or contraction of the surface is examined in the plane of the sample surface. The so-called in-plane signals are obtained mostly via the torsional movements of the cantilever and give information on the in-plane component of electromechanical surface response. As mentioned previously, the lock-in technique is used to analyze the detected signals by comparing those with the excitation signal in terms of amplitude and phase of the cantilever vibrations. The resulting amplitude is a measure of the local piezoactivity, and the phase indicates the direction of the domain polarization. Using the information of VPFM and LPFM signals, the domain polarization, as e.g. in $BaTiO_3$, can be completely reconstructed [100,101]. Additionally, as discussed by Jungk [102], besides the transverse flexural and torsional movements, the cantilever can suffer also an independent third movement called “buckling”. In this case the in-plane force acts perpendicularly to the tip but in axis with the cantilever (Fig. 12).

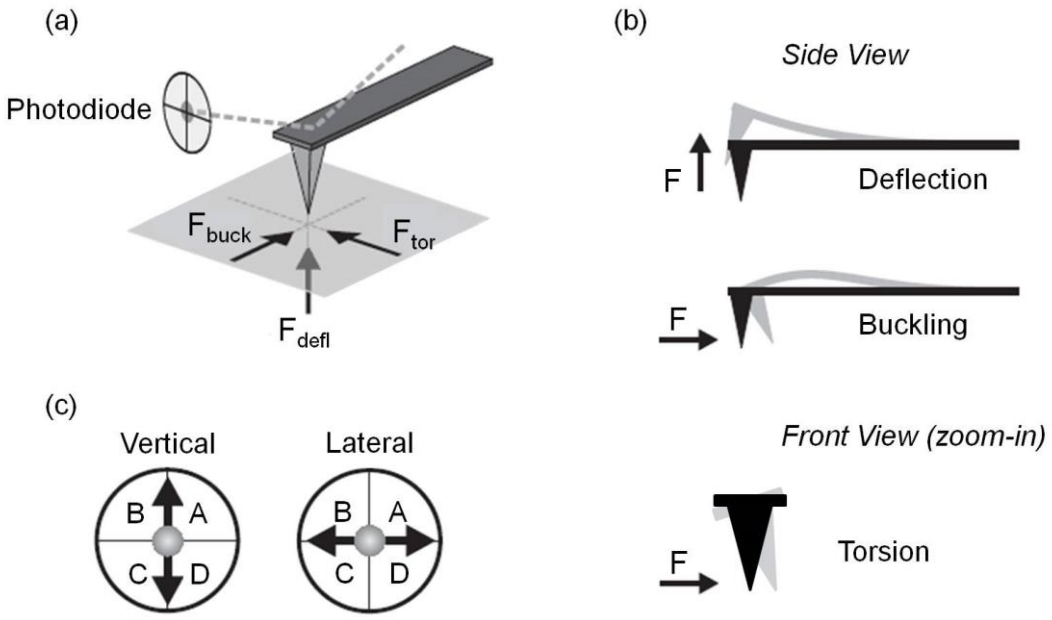

Figure 12. (a) Forces acting on the sensor tip in PFM mode. The three forces F_{defl}, F_{buck} and F_{tor} cause three movements of the cantilever: transverse flexural deflection, buckling and torsion, respectively (b). The vertical force F_{defl} causes a transverse flexural deflection of the cantilever which is independent of its orientation with respect to the surface normal. Already in the case of the in-plane forces F_{tor} and F_{buck}, the cantilever response is dependent on the direction of the driving force with respect to the cantilever axis. While transverse flexural deflection and buckling are detected as vertical signals, torsion results in a lateral signal on the photodiode (c). Modified representation according to [102].

Buckling cannot be easily distinguished from a deflection of the cantilever because both are detected as a vertical signal on the photodiode. Because of the symmetry of the cantilever, an additional LPFM measurement must then be performed by physically rotating the sample about 90° [103]. In this way, three components of the piezoresponse signal are obtained, which allows at least a semiquantitative reconstruction of the polarization orientation. A complete and precise determination of the polarization directions can be calculated only if all components of the piezoelectric tensor are known [93]. For further description of the method the reader is referred to [104-108].

The piezo-mode technique used in this work operates at much higher frequencies compared to the standard (low frequency) piezoresponse force microscopy technique. Because of the range of frequencies one operates with (few hundred of kHz to a few MHz) the technique is named ultrasonic piezo-mode or ultrasonic piezoresponse force microscopy (UPFM). As in the case of the AFAM technique, UPFM combines AFM with ultrasonics. The schematic setup used in this work is presented in Fig. 13. The idea to excite contact resonance

frequencies is similar, but the way to induce the sample vibrations differs considerably. In the AFAM mode, the high frequency signal of the function generator is connected to the ultrasonic transducer below the sample. Longitudinal waves are emitted which causes out-of-plane surface vibrations that are sensed by the cantilever via its sensor tip. As described earlier, contact resonance frequencies are excited. This can be used to measure local elastic properties. In the UPFM mode, the high frequency signal of the function generator is connected directly to the electrically conductive AFM-cantilever, and the tip-sample vibration is excited via the inverse piezoelectric effect. Like in the AFAM mode, the operation frequency is set close to a contact resonance frequency of the system. The piezo-mode signal is thus enhanced through resonance amplification [85]. For the vertical (out-of-plane) surface displacements, the excitation frequency is set close to a transverse flexural contact resonance of the cantilever. In the case for the lateral (in-plane) surface displacements, the excitation signal is set close to a torsional contact resonance of the cantilever. Similar to the standard (low frequency) PFM, amplitude and phase images are taken for information about the piezo activity of the sample. In order to allow local poling experiments with subsequent imaging of induced changes, a DC-power supply is also connected to the system (Fig. 13).

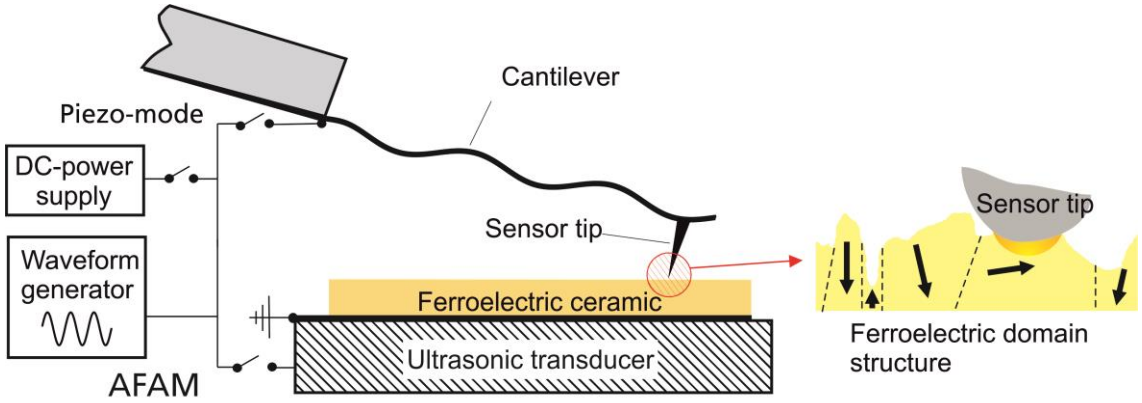

Figure 13. Schematic set-up showing the combined AFAM and UPFM techniques. The AFM cantilever is in contact with the piezoelectric sample surface. The contact resonance modes of the beam are excited by surface displacements caused by: (1) longitudinal waves emitted from an ultrasonic transducer (AFAM mode); (2) due to the inverse piezoelectric effect when an alternating electrical voltage is applied directly to the AFM cantilever and tip (piezo-mode). A connected DC-power supply allows also the manipulation of the ferroelectric domains. Modified representation according to [85,109].

Experiments are made in two steps. In a first step, a DC voltage of variable amplitude and poling direction is applied between the tip and the sample while the sample is scanned. In a second step, the same area is imaged in the UPFM mode to check whether the PFM contrast

is changed locally. An increased contrast in the UPFM amplitude image corresponds to an increased piezo activity.

4. RESEARCH OVERVIEW

4.1 Structural steels

The main objective of the first and largest part of this thesis is to identify the mechanisms governing and/or contributing to the magnetization process of steels containing different phases at the micro- and nanoscale in order to support the evaluation of macroscopic electromagnetic and micromagnetic nondestructive methods. Analysis and interpretation of the observed macroscopic electromagnetic and micromagnetic nondestructive output signals require an understanding of the underlying domains and their interactions with the microstructure. The observation and characterization of the magnetic microstructure and its dynamics is therefore crucial to reveal the mechanisms controlling the magnetization processes in multiphase steels.

In the work described in chapters II-VI (publications A-E), samples of a high purity polycrystalline iron and of two unalloyed pearlitic steels (Fe-0.8%C and Fe-1.5%C) containing globular and lamellar cementite embedded in a ferrite matrix have been chosen as model systems. To study the relative influences of the ferrite and cementite phases on the macroscopic electromagnetic and micromagnetic measurement signals an approach based on macroscopic measurement signals as well as the observation and characterization of the material in the micro- and nanoscale is applied. At the macroscopic scale, magnetic hysteresis loops and magnetic Barkhausen noise are used for materials characterization and evaluation. At the micro- and nanoscopic scale, a relevant magnetic imaging technique for NDT&E, namely MFM, is used for magnetic domains visualization and also for the detection of different micromagnetic events.

A setup based on an electromagnet, a pick-up coil, and a magnetic field sensor was used to measure magnetic hysteresis loops and magnetic Barkhausen noise of the high purity polycrystalline iron and unalloyed pearlitic steel samples, the latter containing different proportions of ferrite and cementite phases. A system composed of a commercial MFM microscope coupled with an external coil providing a controllable external magnetic field was built. Applying this setup, the influence of the cementite and ferrite phases on the magnetization processes and also on the detected Barkhausen signals was investigated. The characterization of local micromagnetic events in a thick (bulk) polycrystalline sample requires a surface in which the grains are suitably oriented with regard to their easy axes of

magnetization. Using the EBSD technique, the crystalline orientations of grains in both, the ferrite and the cementite phases, were determined. Local elastic properties of the ferrite and cementite phases were probed with a resolution down to the nm range using the AFAM technique. By combining the MFM, AFAM and EBSD techniques, the local magnetic, elastic, and crystallographic microstructure of the investigated unalloyed pearlitic steels were examined.

Chapter II (publication A, peer-reviewed paper) shows in detail the use of the MFM under a controllable external applied field to image the magnetic microstructures of the high purity polycrystalline iron and the Fe-0.8%C and Fe-1.5%C samples. Focus is given in the magnetization process in the ferrite, reversible and irreversible domain wall movements are observed, and different interactions of the domain walls in the ferrite matrix with the cementite precipitates are revealed.

Chapter III (publication B, peer-reviewed paper) shows how one can optimize the macroscopic measurement setup in order to identify the ferrite and the cementite phases in the Fe-0.8%C and Fe-1.5%C samples on the MBN profiles. MFM under a controllable external applied field is used to study the magnetic microstructure in the Fe-1.5%C sample with special emphasis to the process related to the magnetization of the cementite phase.

Chapter IV (publication C, paper submitted to Ultramicroscopy) proposes a new method to determine the magnetic easy axes of micro- and nanoscopic ferromagnetic precipitates embedded in a bulk material by combining the MFM and EBSD techniques. It also shows how different types of magnetic probes can influence the contrast in the magnetic images. As examples, the Fe-0.8%C and Fe-1.5%C samples which contain globular and lamellar cementite precipitates in a ferrite matrix are chosen.

Chapter V (publication D, conference paper) describes the dynamics of the magnetic microstructure imaged by MFM of the high purity polycrystalline iron and the Fe-1.5%C samples. Particular attention is given to the magnetization process of the high purity iron sample. The domain wall movements in this sample are initiated by much weaker applied field compared to those necessary on the Fe-1.5%C sample. It demonstrates how the crystalline orientation of the grains in the high purity iron sample influences their surface domain configurations.

Chapter VI (publication E, conference paper) presents the magnetic microstructure and the local elastic properties of the Fe-0.8%C sample. Additionally, the AFAM technique is used to image the microstructure and probe mechanical properties on the micro- and nanoscale of austenitic twinning induced plasticity (TWIP) steels. Quantitative indentation

modulus results were obtained as a function of the grain orientations and compared to the results obtained using the nanoindentation technique. Finally, important insights in the deformation mechanisms were examined via surface relief analysis obtained by AFM during plastic deformation.

4.2 Functional lead-free ceramics

The main objective of the second much shorter part of this thesis, carried out together with the BisNano project partners [2], is the evaluation of the functionalities of bismuth-based materials for a variety of industrial applications, as e.g. lead-free ferroelectrics and piezoelectrics. The design and engineering of new functional lead-free ferro- and piezoelectric materials requires a thorough understanding of the micro- and nanostructure related properties.

Chapter VII (publication F, peer-reviewed paper) describes ferroelectric epitaxial thin film samples of bismuth ferrite ($BiFeO_3$) which were grown in different crystallographic orientations (100), (110), and (111). The quality of the films was evaluated using X-ray diffraction (XRD) and AFM. To study the influence of the crystallographic orientation of the films on the ferroelectric domain patterns, low frequency (standard) PFM and UPFM were used. In order to examine local polarization switching, an additional dc-power supply was connected to the PFM/UPFM system. Finally, AFAM was employed to probe the local elastic properties of the films at a nanoscale by acquiring surface elasticity maps.

Promising candidates for lead-free piezoelectric materials were investigated at a macro-, micro- and nanoscale (chapter VIII, publication G, part of the EU-Mexico BisNano project report). Different lead-free bismuth-based bulk ceramics like $Bi_{0.5}Na_{0.5}TiO_3$ (BNT), $0.94Bi_{0.5}Na_{0.5}TiO_3$-$0.06BaTiO_3$ (BNT-BT), Mn-doped BNT-BT, and Sr-doped BNT-BT were synthesized via conventional mixed oxide route and sintering. Macroscopic properties like piezoelectric coupling coefficients and elastic constants were determined using impedance and ultrasound measurements, respectively. Laser vibrometry was used for the identification of sample resonances and also for the measurements of the maximal surface vibration amplitudes of the ceramic samples at their resonances. Micro- and nanoscopic investigations were performed using AFM, AFAM and UPFM. AFM contact mode was used to examine first the quality of the sample surfaces with regard to roughness and cleanliness. AFAM and UPFM were used to image at a nanoscale surface elastic properties and ferroelectric domains, respectively. Finally, the most promising lead-free bismuth-based bulk ceramic samples were successfully tested as ultrasonic transducer materials.

REFERENCES

[1] EU-Directive 2002/95/EC: Restriction of the Use of Certain Hazardous Substances in Electrical and Electronic Equipment (RoHS)“, *Official Journal of the European Union* **46** (2003) 19.

[2] EC-FP7 Call: NMP.2010.1.2-4 Adding Value to mining at the Nanostructure level, Project: Functionalities of Bismuth-based nanostructures (BisNano) 263878.

[3] D.I. Gordon, *Reviews of Modern Physics* **25** (1953) 56.

[4] A.H. Geisler, *Reviews of Modern Physics* **25** (1953) 316.

[5] G.A. Matzkanin, R.E. Beissner, E.M. Teller “The Barkhausen effect and its Application to Nondestructive Evaluation”, in: *Nondestructive Testing Information Analysis Center*, (San Antonio, Texas, NTIAC report 79-2, 1979).

[6] O. Kanji, G. Dobmann, “Nondestructive Testing, 5. Magnetic and Electromagnetic Engineering”, in *Ullmann's Encyclopedia of Industrial Chemistry*, (Weinheim, John Wiley & Sons, 2000).

[7] I. Altpeter, R. Becker, G. Dobmann, R. Kern, W. Theiner, A. Yashan, *Inverse Problems* **18** (2002) 1907.

[8] D.C. Jiles, *Journal of Physics D: Applied Physics* **21** (1988) 1186.

[9] H. Kronmüller, “Magnetisierungskurve der Ferromagnetika”, in: Moderne Probleme der Metallphysik, Vol. 2, ed. by A. Seeger (Springer, Berlin, 1966) 24-156.

[10] D.C. Jiles, *NDT & E International* **21** (1988) 311.

[11] A. Dumay, Dissertation, Ecole des Mines, Nancy, France (2008).

[12] L. Batista, U. Rabe, S. Hirsekorn, *NDT & E International* **57** (2013) 58.

[13] C. Boller, I. Altpeter, G. Dobmann, M. Rabung, J. Schreiber, K. Szielasko, R. Tschuncky, *Materialwissenschaft und Werkstofftechnik* **42** (2011) 269.

[14] G. Dobmann, R. Becker, W.A. Theiner, “Progress in the Micromagnetic Multi-parameter Microstructure and Stress Analysis (3MA)”, in *Non-Destructive Characterization of Materials*, vol 3, P. Höller, V. Hauk, G. Dobmann, C. Ruud, R. Green, Eds. (Berlin: Springer) (1989) 516.

[15] K. Szielasko, *Entwicklung messtechnischer Module zur merhparametrischen elektromagnetischen Werkstoffcharakteriesierung und prüfung*, Dissertation, Saarland University, Saarbrücken (2009).

[16] K. Szielasko , I. Mironenko , I. Altpeter, H.-G. Herrmann, C. Boller, *IEEE Transactions on Magnetics* **49** (2013) 101.

[17] I. Altpeter, W. Theiner, M. Gessner, Vorrichtung zum ortsaufgelösten zerstörungsfreien

Untersuchungen vom magnetischen Kenngrößen, European Patent Nr. EPO 595 117B1, 04.05. 1994.

[18] I. Altpeter, G. Dobmann, N. Meyendorf, H. Blumenauer, D. Horn, M. Krempe, *Proceedings of the International Symposium on Nondestructive Characterization of Materials* **8**, Boulder/Colorado, USA (1997) 659.

[19] M. Sheikh-Amiri, K. Szielasko, I. Altpeter, C. Boller, D. Fischer, J. Hahn, *IOP Conf. Series: Materials Science and Engineering* **31** (2012) 012021.

[20] E. Hanke, "Prüffung Metallischer Werkstoffe", (Leipzig,VEB Deutscher Verlag für Grundstoffindustrie, Band 2, 1960).

[21] B.D. Cullity, Introduction to magnetic materials, (London, Addison Wesley, 1972).

[22] D.K. Bhattacharya, Magnetic NDT for the Characterization of Industrial Materials, Materials Characterization Techniques – Principles and Applications, Eds.: G. Sridhar, S. Ghost Chowdhury & N.G. Goswami, NML, Jamshedpur-831007 (1999) 210-227.

[23] V. Moorthy, S. Vadyanathan, T. Jayakumar, B. Raj, *Journal of Magnetism and Magnetic Materials* **171** (1997) 179.

[24] O. Saquet, J. Chicois, A. Vincent, *Materials Science and Engineering A* **269** (1999) 73.

[25] M.J. Sablik, B. Augustyniak, "Magnetic methods of nondestructive evaluation", in: Wiley Encyclopedia of Electrical and Electronics Engineering Vol. 12, ed. by Wiley & Sons, (New York, 1999) 12-31.

[26] VDI/VDE – Richtlinie 2616, Blatt 1, Härteprüfung an metallischen Werkstoffen, Düsseldorf: VDI (2012) 30-35.

[27] G. Dobmann, I. Altpeter, M. Kopp, *Russian Journal of Nondestructive Testing* **42** (Compendex) (2006) 272.

[28] G. Dobmann, I. Altpeter, K. Szielasko, M. Kopp, *Journal of Theoretical and Applied Mechanics* **44** (Copyright 2006, The Institution of Engineering and Technology) (2006) 649.

[29] S. Takaya, I. Yamagata, S. Ichikawa, Y. Nagae, K. Aoto, *International Journal of Applied Electromagnetics and Mechanics* **33** (2010) 1335.

[30] D.-G. Park, I.-G. Park, W.-W. Kim, Y.-M. Cheong, J.-H. Hong, "*Nuclear Engineering and Design* **238** (Compendex) (2008) 814.

[31] L. Debarberis, B. Acosta, A. Zeman, S. Pirfo, P. Moretto, A. Chernobaeva, Y. Nikolaev, *International Journal of Microstructure and Materials Properties 2* (Copyright 2008, The Institution of Engineering and Technology) (2007) 326.

[32] J.S. McCloy, R.O. Montgomery, P. Ramuhalli, R.M. Meyer, S. Hu, C.H. Henager Jr., B.R. Johnson, "Materials degradation and detection (MD2): Deep Dive Final Report", *PNNL-22309* (2013).

[33] P. Weiss, *Journal de Physique* **6** (1907) 661.

[34] F. Bitter, *Physical Review* **38** (1931) 1903.

[35] L.D. Landau, E. Lifshitz, *Physikalische Zeitschrift der Sowjetunion* **8** (1935) 153.

[36] S. Chikazumi, "Physics of Magnetism", (New York, Wiley, 1964).

[37] G. Bertotti, "Hysteresis in Magnetism – For Physicists, Materials Scientists, and Engineers", (San Diego, CA, Academic Press, Inc., 1998).

[38] R. Becker, W. Döring, "Ferromagnetismus", (Berlin, Springer, 1939).

[39] R.M. Bozorth, "Ferromagnetism", (New York, IEEE Press, 1951).

[40] D.C. Jiles, "Introduction to Magnetism and Magnetic Materials (2nd Ed.)", (London, Chapman & Hall, 1998).

[41] D.C. Jiles, *Journal of Physics D: Applied Physics* **21** (1988) 1196.

[42] H. Barkhausen, *Physikalische Zeitschrift* **20** (1919) 401.

[43] A.E. Lord, "Acoustic Emission", in *Physics Acoustics*, Vol. XI, ed. by W.P. Mason, R.N. Thurston, (New York, Academic Press, 1975).

[44] K. Tiito, "Solving Residual Stress Measurement Problems by a New Nondestructive Magnetic Method", in: *Nondestructive Evaluation: Application to Materials Processing*, ed. by O. Buck, S.M. Wolf, (Ohio, ASM, Materials Park, 1984).

[45] V.A. Yardley, *Magnetic detection of microstructural change in power plant steels*, Dissertation, Cambridge University, Cambridge (2003).

[46] J.W. Lau, J.M. Shaw, *Journal of Physics D: Applied Physics* **44** (2011) 303001.

[47] C.A. Kittel, *Physical Review* **76** (1949) 1827.

[48] H. Ebert, *Reports on Progress in Physics* **59** (1996) 1665.

[49] Z.Q. Ziu, S.D. Bader, *Review of Scientific Instruments* **71** (2000) 1243.

[50] B.C. Choi, M. Belov, W.K. Hiebert, G.E. Ballentine, M.R. Freeman, *Physics Review Letters* **86** (2001) 728.

[51] H. Boersch, H. Raith, *Naturwissenschaften* **46** (1959) 574.

[52] M.E. Hale, H.W. Fuller, H. Rubinstein, *Journal of Applied Physics* **30(5)** (1959) 789.

[53] N.F. Mott, *Proceedings of the Royal Society A* **124** (1929) 425.

[54] J. Kessler, "Polarized Electrons", (Berlin, Springer, 1985).

[55] A.M. Chang, H.D. Hallen, L. Harriott, H.F. Hess, H.L. Kao, J. Kwo, R.E. Miller, R. Wolfe, J. van der Ziel, T.Y. Chang, *Applied Physics Letters* **61** (1992) 1974.

[56] Y. Martin, H.K. Wickramasinghe, *Applied Physics Letters* **50** (1987) 1455.

[57] J.J. Saenz, N. Garcia, P. Grütter, E. Meyer, H. Heinzelmann, R. Wiesendanger, L. Rosenthaler, H. R. Hidber, H. J. Güntherodt, *Journal of Applied Physics* **62** (1987) 4293.

[58] X. Zhu, P. Grütter, V. Metlushko, B. Ilic, *Journal of Applied Physics* **91** (2002) 7340.

[59] R. Proksch, E. Runge, P.K. Hansma, S. Foss, *Journal of Applied Physics* **78** (1995) 3303.

[60] A. Hubert, R. Schäfer, "Magnetic domains – the analysis of magnetic microstructures", (Berlin, Springer; 1998).

[61] H. Kronmüller, S. Parkin, "Handbook of magnetism and advanced magnetic materials", vol 2., Micromagnetism, (New York, Wiley & Sons, 2007).

[62] M. Coisson, F. Vinai, P. Tiberto, F. Celegato, *Journal of Magnetism and Magnetic Materials* **321** (2009) 806.

[63] S. Huo, J.E.L. Bishop, J.W. Tucker, M.A. Al-Khafaji, W.M. Rainforth, H.A. Davies, et al., *Journal of Magnetism and Magnetic Materials* **190** (1998) 17.

[64] L. Zhang, B. An, S. Fukuyama, T. Iijima, K. Yokogawa, *Journal of Applied Physics* **108** (2010) 063526.

[65] S. Takaya, T. Suzuki, Y. Matsumoto, K. Demachi, M. Uesaka, *Journal of Nuclear Materials* **327** (2004) 19.

[66] M.G. Hetherington, J.P. Jakubovics, J.A. Szpunar, B.K. Tanner, *Philosophical Magazine B* **56** (1987) 561.

[67] S.M. Thompson, B.K. Tanner, *Journal of Magnetism and Magnetic Materials* **123** (1993) 283.

[68] C.C.H. Lo, C.B. Scruby, *Journal of Applied Physics* **85** (1999) 5193.

[69] C.C.H. Lo, J.P. Jakubovics, C.B. Scruby, *Journal of Applied Physics* **81** (1997) 4069.

[70] C.C.H. Lo, J.P. Jakubovics, C.B. Scruby, *IEEE Transactions on Magnetics* **33** (1997) 4035.

[71] A.D. Beale, J.P. Jakubovics, M.G. Hetherington, C.B. Scruby, B.A. Lewis, K.J. Davies, *Journal of Magnetism and Magnetic Materials* **104-107** (1992) 365.

[72] J.W. Lau, M.A. Schofield, Y. Zhu, *Ultramicroscopy* **107** (2007) 396.

[73] U. Rabe, W. Arnold, *Applied Physics Letters* **64** (1994) 1493.

[74] U. Rabe, K. Janser, W. Arnold, *Review of Scientific Instruments* **67** (1996) 3281.

[75] D.C. Hurley, M. Kopycinska-Müller, A.B. Kos, R.H. Geiss, *Advanced Engineering Materials* **7** (2005) 713.

[76] K. Yamanaka, H. Ogiso, O.V. Kolosov, *Applied Physics Letters* **64** (1994) 178.

[77] G. Binning, C.F. Quate, C. Gerber, *Physics Review Letters* **56** (1986) 930.

[78] D.C. Hurley, “Contact Resonance Force Microscopy Techniques for Nanomechanical Measurements”, in: Applied Scanning Probe Methods Vol. XI, ed. by H. Fuchs, B. Bhushan, (Berlin, New York, 2009) 97-138.

[79] U. Rabe, “Atomic Force Acoustic Microscopy”, in: *Applied Scanning Probe Methods II*, ed. by H. Fuchs, B. Bhushan., (Berlin, Springer, 2006) 37-90.

[80] U. Rabe, M. Kopycinska-Müller, S. Hirsekorn, "Atomic Force Acoustic Microscopy", in: *Acoustic Scanning Probe Microscopy*, ed. by F. Marinello, D. Passeri, E. Savio, (Berlin, Springer, 2013) 123-153.

[81] U. Rabe, S. Amelio, E. Kester, V. Scherer, S. Hirsekorn, W. Arnold, *Ultrasonics* **38** (2000) 430.

[82] K.L. Johnson, “Contact Mechanics”, (Cambridge, U.K.,Cambridge University Press, 1985) 84-99.

[83] B. Cappella, G. Dietler, *Surface Science Reports* **34** (1999) 1.

[84] J.J. Vlassak, W.D. Nix, *Philosophical Magazine A* **67** (1993) 1045.

[85] U. Rabe, M. Kopycinska, S. Hirsekorn, J. Muñoz-Saldaña, G.A. Schneider, W. Arnold, *Journal of Applied Physics D: Applied Physics* **35** (2002) 2621.

[86] U. Rabe, S. Amelio, M. Kopycinska, M. Kempf, M. Göken, W. Arnold, *Surface and Interface Anal*ysis **33** (2002) 65.

[87] M. Kopycinska-Müller, *On the elastic properties of nanocrystalline materials and the determination of elastic properties on a nanoscale using the atomic force acoustic microscopy technique*. Saarbrücken: PhD thesis, Science and Technical Faculty III, Saarland University and IZFP report No. 050116-TW, 2005.

[88] B. Gronau, *Bandanregung in der Ultraschall-Kraftmikroskopie*. Saarbrücken: Diploma thesis, Science and Technical Faculty II, Saarland University and IZFP report No. 130107-TW, 2012.

[89] S. Amelio, A. V. Goldade, U. Rabe, V. Scherer, B. Bhushan, and W. Arnold, *Thin Solid Films* **392** (2001) 75.

[90] M. Kopycinska-Müller, A. Striegler, R. Schlegel, N. Kuzeyeva, B.Köhler, *Review of Scientific Instruments* **83** (2012) 043703.

[91] S. Jesse, S.V. Kalinin, R. Proksch, A.P. Baddorf, B.J. Rodriguez, *Nanotechnology* **18** (2007) 435503.

[92] A.B. Kos, D.C. Hurley, *Measurement Science and Technology* **19** (2008) 015504.

[93] A. Kholkin, S.V. Kalinin, A. Roelofs, A. Gruverman, “Review of Ferroelectric Domain Imaging by Piezoresponse Force Microscopy”, in: *Scanning Probe Microscopy: Electrical*

and Electromechanical Phenomena at the Nanoscale, ed. by S. V. Kalinin, A. Gruverman, (New York, Springer, 2007) 173-214.

[94] P. Güthner, K. Dransfeld, *Applied Physics Letters* **61** (1992) 1137.

[95] A. Gruverman, O. Auciello, H. Tokumoto, *Annual Review of Materials Science* **28** (1998) 101.

[96] B.J. Rodriguez, A. Gruverman, A.I. Kingon, R.J. Nemanich, O. Ambacher, *Applied Physics Letters* **80** (2002) 4166.

[97] C. Halperin, S. Mutchnik, A. Agronin, M. Molotskii, P. Urenski, M. Salai, G. Rosenman, *NanoLetters* **4** (2004) 1253.

[98] S.V. Kalinin, B.J. Rodriguez, S. Jesse, T. Thundat, V. Grichko, A.P. Baddorf, A. Gruverman, *Ultramicroscopy* **106** (2006) 334.

[99] A. Gruverman, B.J. Rodriguez, S.V. Kalinin, "Electromechanical Behavior in Biological Systems at the Nanoscale", in: *Scanning Probe Microscopy: Electrical and Electromechanical Phenomena at the Nanoscale*, ed. by S. V. Kalinin, A. Gruverman, (New York, Springer, 2007) 615-633.

[100] L.M. Eng, H.-J. Gütherodt, G.A. Schneider, U. Köpke, J. Muñoz-Saldaña, *Applied Physics Letters* **74**, (1999) 233.

[101] J. Muñoz-Saldaña, G.A Schneider, L.M Eng, *Surface Science Lett*ers **480** (2001) L402.

[102] T. Jungk, Á. Hoffmann, E. Soergel, in *Ferroelectric Crystals for Photonic Applications*, ed. by P. Ferraro, S. Grilli, P.D. Natale, (Berlin, Springer, 2014) 205-226.

[103] B.J. Rodriguez, A. Gruverman, A.I. Kingon, R.J. Nemanich, J.S. Cross, *Applied Physics A* **80** (2005) 99.

[104] L.M. Eng., *Nanotechnology* **10** (1999) 405.

[105] S. Hong, J. Woo, H. Shin, J.U. Jeon, Y.E. Pak, E.L. Colla, N. Setter, E. Kim, K. No, *Journal of Applied Physics* **89** (2001) 1377.

[106] C. Harnagea, A. Pignolet, M. Alexe, D. Hesse, *Integrated Ferroelectrics* **44** (2002) 113.

[107] S.V. Kalinin, R. Shao, D.A. Bonnell, *Journal of the American Ceramic Society* **88** (2005) 1077.

[108] S.V. Kalinin, D.A. Bonnell, "Electric Scanning Probe Imaging and Modification of Ferroelectric Surfaces", in: *Nanoscale characterization of Ferroelectric Materials*, ed. by M. Alexe, A. Gruverman, (Berlin, Springer, 2004) 1-39.

[109] U. Rabe, "Ultraschall-Kraftmikroskopie - Prinzip und Anwendung", in Fortschritte der Akustik (DAGA, Dresden, 2008).

II. MAGNETIC MICRO- AND NANOSTRUCTURES OF UNALLOYED STEELS: DOMAIN WALL INTERACTIONS WITH CEMENTITE PRECIPITATES OBSERVED BY MFM (PUPLICATION A)

L. Batista, U. Rabe, and S. Hirsekorn

NDT & E International (2013) Vol. 57; 58-68.

ABSTRACT. The morphology and content of a cementite phase controls the macroscopic mechanical and magnetic properties of steels. The influence of the cementite content on the bulk magnetic properties in unalloyed steels was observed in hysteresis loop and Barkhausen noise signals. Globular cementite embedded in a ferrite matrix is characterized by atomic force microscopy and magnetic force microscopy. Size, shape and orientation of the grains influence the domain configuration. When an external magnetic field is applied, the magnetization process occurs mainly in the ferrite matrix. The Bloch walls in the ferrite matrix move, and they are pinned by the cementite precipitates. This microscopic observation correlates with the macroscopic magnetic properties of the investigated material.

Keywords: Atomic force microscopy (AFM), Magnetic force microscopy (MFM), Steel, Magnetic domains, Barkhausen noise, Microstructure, Non-destructive testing

1. INTRODUCTION

Steels continue to be one of the most important structural material several millennia after their discovery. Two prominent phases in steels are ferrite and cementite (Fe_3C), a metastable narrow-composition-field intermetallic compound with an orthorhombic symmetry. Cementite is important because its morphology and volume fraction directly controls mechanical and magnetic properties of steels. For quality control and assurance the mechanical properties of steels as well as the morphology and content of the cementite phase can be monitored using electromagnetic non-destructive testing methods. These methods are based on a correlation between mechanical and magnetic properties and deliver parameters on a macroscopic scale.

The bulk macroscopic magnetic properties and Barkhausen noise profile curves of unalloyed steels have already been studied by many authors. It was shown that the carbon content influences the shape of the hysteresis loop and the Barkhausen noise signals generated by a microstructure containing globular cementite embedded in a ferrite matrix [1,2]. Amplitude and shape of the Barkhausen signal change with the addition of a small amount of carbon, i.e. solid solution in iron [3]. Thompson and Tanner [4] discussed the influence of the amount of pearlite phase on the magnetic and mechanical hardness. However, all these macroscopic observations rely on a phenomenological description of the interactions of the magnetic domains with the microstructure. Fundamental nano- and microscopic investigations are still researching theoretically and experimentally the phenomena associated to such interactions, e.g. the pinning effect of domain walls by magnetic inclusions.

The magnetic domain structures can be imaged by different techniques. For example, the Bitter technique was used to examine the configuration of the magnetic domains in magnetite [5]. Domains in high-permeability materials were imaged by Kerr microscopy [6], the domain configuration of a cementite thin foil was revealed by Lorentz electron microscopy [7], and recently a domain structure was imaged in three dimensions by Neutron diffraction tomography [8]. Magnetic force microscopy (MFM) has been widely employed to map magnetic structures of surfaces [9]. In addition to its outstanding local resolution of up to 10 nm MFM has other advantages [10]: Topography and magnetic structure can be simultaneously measured allowing the study of interaction between defects and magnetic properties, and MFM can be performed under various environmental conditions. Since magnetostatic interactions are long-range, MFM is less sensitive to surface contamination than other scanning probe techniques, and the surface preparation is relatively easy. Different reviews of the principles and methods of MFM were published [11-13]. Most studies of

domain structures with MFM focused on thin magnetic layers [14-16], and only few studies used MFM to image the domain structure of polycrystalline bulk materials [17].

In this paper, samples of a high purity polycrystalline iron and of two unalloyed steels (Fe-0.8%C and Fe-1.5%C) containing globular cementite embedded in a ferrite matrix have been chosen as model systems. In the first part of this work, the macroscopic magnetic quantities, i.e. saturation magnetization, coercive field and maximum Barkhausen noise amplitude were measured and interpreted with respect to the microstructural state. In the second part, the magnetic microstructures were observed using a magnetic force microscope. The MFM was coupled with an external coil providing a controlled in-plane magnetic field which allowed the observation of the dynamic behavior of the magnetic domains. Ferromagnetic domains were studied in the high purity polycrystalline iron sample and in the cementite and ferrite phases of the unalloyed steels. By means of electron backscatter diffraction (EBSD) the crystalline orientation of the cementite particles and the ferrite phase, respectively, was determined. The correlation between the macroscopic magnetic properties and the magnetic and crystallographic microstructure was examined.

2. BACKGROUND OF THE MEASUREMENT METHODS

2.1 Macroscopic magnetic methods

Ferromagnetic materials consist of small finite uniformly magnetized regions called magnetic domains. Each domain is spontaneously magnetized to the saturation value of the material. Domain walls separate neighboring domains of different magnetization orientations. The driving energy for formation of domains in a macroscopic ferromagnetic material is the stray field energy. The reduction of the stray field energy is accompanied by an increase of the total domain wall energy. The equilibrium state therefore is characterized by the minimum of the total energy, i.e. stray field plus domain wall energy [18,19]. In the magnetic structure of a bulk ferrous magnetic material only two kinds of domain walls are observed: 180° - Bloch walls (BWs) which are magnetostrictively inactive, have short range stress fields resulting in high mobility and sensitivity to external stress, and 90°-BWs which are magnetostrictively active, have long-range stress fields and therefore low mobility. The Bloch wall movement takes place discontinuously because BWs are temporarily pinned by microstructural obstacles like dislocations, precipitates and phase or grain boundaries in a polycrystalline material. The stepwise pull-out of the walls from the obstacles which changes the magnetization state locally is called “Barkhausen event” or “-jump”. These local magnetization changes induce pulsed eddy currents into the sample which are detected as

electrical voltage pulses in a pick-up coil near the surface, the so called Barkhausen noise [20]. Macroscopic magnetic properties including coercive field, permeability, residual induction and power loss derived from hysteresis loop and Barkhausen signals allow characterization of the microstructural state of ferromagnetic materials.

In the experimental set-up used here, the magnetic field for hysteresis loop and Barkhausen noise measurements was generated by an electromagnet which was connected to a computer-controlled bipolar power supply (Fig. 1). Cylindrical samples with a diameter of 8 mm and length of 50 mm were magnetized along their axial direction. A maximum magnetic field strength H of 130 A/cm was reached at an excitation frequency of 0.05 Hz. The magnetic tangential field strength H was measured by a Hall probe. The change in magnetic flux density B and the inductive Barkhausen noise amplitude M were measured by a pick-up coil surrounding the sample (Fig. 1). The envelope of the noise signals (analyzing frequency f_A = 200 Hz - 50 kHz) and the magnetic flux density were recorded as a function of the tangential field strength.

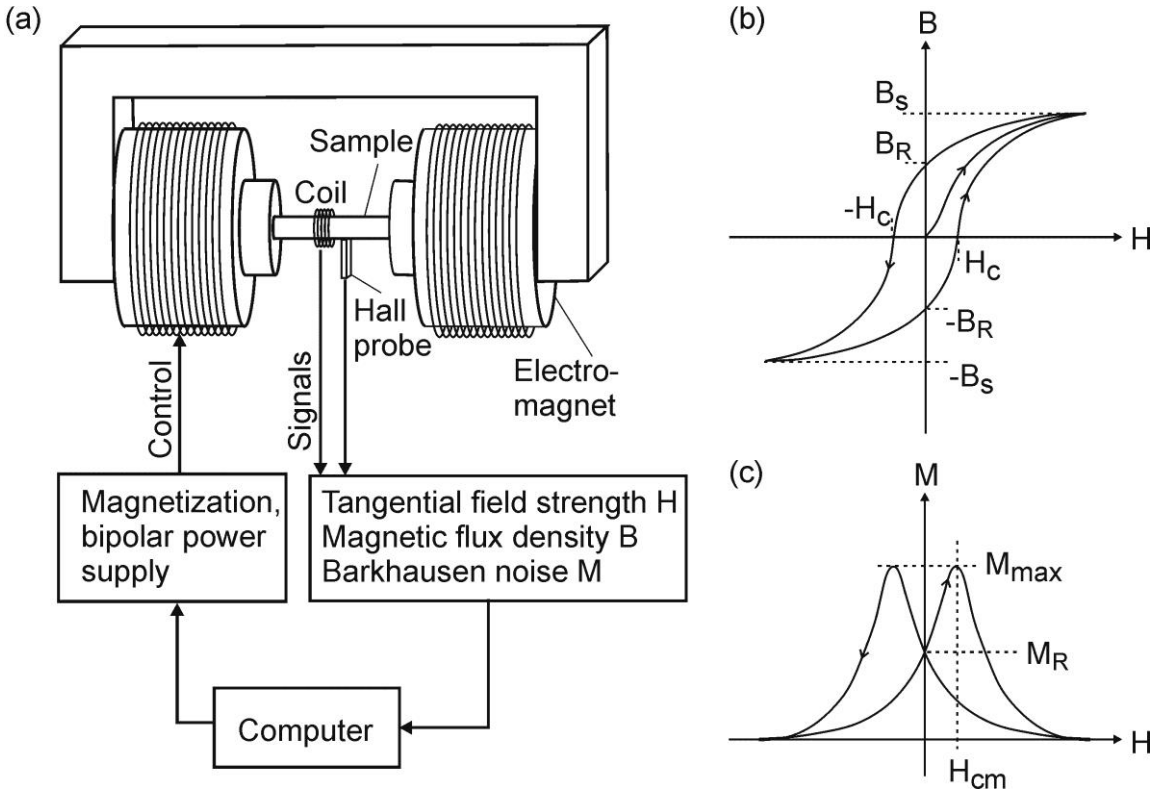

Figure 1. (a) Schematic sketch of the experimental set-up for hysteresis loop and Barkhausen noise measurements, (b) schematic hysteresis loop with coercive field H_C, Magnetic flux at saturation B_S, and remnant magnetic flux B_R, (c) schematic Barkhausen noise curve with maximum of Barkhausen noise amplitude M_{max}, remnant Barkhausen noise amplitude M_R, and coercive field H_{cm} deduced from Barkhausen noise curve.

2.2 Magnetic force microscopy with a superposed external magnetic field

Magnetic force microscopy [21,22] is a special dynamic mode of atomic force microscopy [23] in which a magnetic sample is scanned with a micro fabricated silicon cantilever coated with a thin layer (thickness < 50 nm) of ferromagnetic material (Fig. 2). A sharp sensor tip with an apex diameter in the nm range is attached to the cantilever. The cantilever is deflected by the magnetic interaction force *F* between the ferromagnetic tip and the stray field emanating from the sample surface:

$$F = (m \cdot \nabla) H_{Sam}, \qquad (1)$$

where *m* is the magnetic moment of the tip and H_{Sam} is the magnetic stray field of the sample. Since the magnetization of the tip is parallel to its axis, only the stray field component perpendicular to the sample surface is detected. Thus, the force F_z acting in the *z*-direction is

$$F_z = (m \cdot \nabla) H_{Sam} \approx m_z \frac{\partial H_{Sam}}{\partial z}. \qquad (2)$$

A beam deflection position detector measures the bending of the cantilever. MFM provides simultaneously an image of the topography and a map of the magnetic microstructure of the specimen surface. Every image line is scanned twice, and the cantilever is vibrated close to its resonance frequency during the scan. First the surface profile is recorded in the intermittent contact mode (Tapping mode) [24]. In the second run, the line is scanned once more at an adjustable distance above the previously measured topographic profile. Due to the magnetic force gradient the cantilever experiences a shift in amplitude and phase at its frequency of vibration. The topography and phase signals are displayed as color coded images in a computer. The advantage of the lifting procedure is the automatic subtraction of surface features from the total image leaving primarily magnetic information. The typical lift height ranges from 10 nm to 100 nm [25]. A lift height of 60-80 nm was chosen for all MFM measurements reported here. All magnetic images presented in this work are phase images, i.e. the local phase shift was recorded as a function of position.

A commercial MFM instrument (Nanoscope III® multimode, Digital Instruments, Santa Barbara, CA, USA) was used. The sensor tips were CoCr-coated with a coercivity of ~ 318.4 A/cm (~ 400 Oe) (MESP, Bruker AXS Inc., Madison, WI, USA). An external electromagnet was combined with the MFM (Fig. 2). The pole shoes of the electromagnet were adjusted such that the sample inside the AFM was magnetized parallel to its surface.

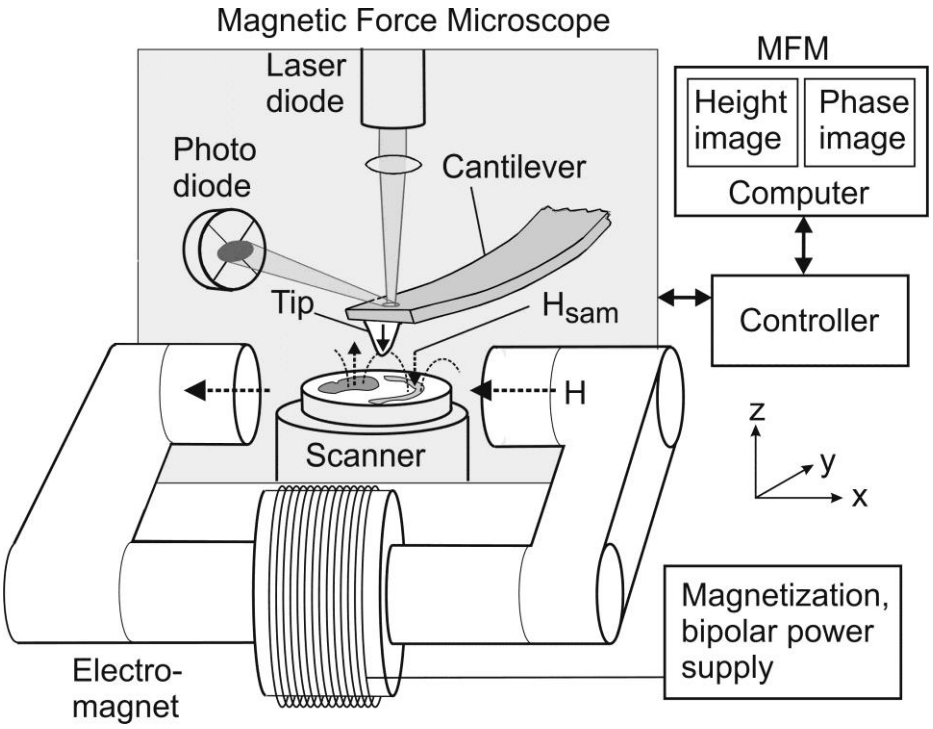

Figure 2. Experimental set-up for the MFM measurements coupled with an external coil providing a controlled in-plane magnetic field.

3. INVESTIGATED MATERIALS

Samples of high purity iron (99.99%) and of two unalloyed steels, Fe-0.8%C and Fe-1.5%C, containing globular cementite (Fe_3C) in a ferrite matrix were examined. The samples were provided as-cast and machined in a cylindrical shape of 8 mm diameter and 50 mm length. In order to remove all processing-induced residual stresses, the samples were vacuum annealed at 600°C for 4h. Scanning electron microscopy (SEM) images (Fig. 3) show the microstructure of the Fe-0.8%C and Fe-1.5%C samples. The size of the cementite precipitates ranges from a few hundred nanometers to about 10 μm in diameter. The average grain size is approximately 80 μm for all samples.

For AFM and MFM measurements small specimens (3 x 3 x 1 mm^3) were cut from the annealed cylindrical samples by spark erosion and mechanically polished by standard procedures. Directly before the measurements, the samples were slightly etched using Nital (95% ethanol + 5% nitric acid) in order to obtain suitably reproducible surface conditions.

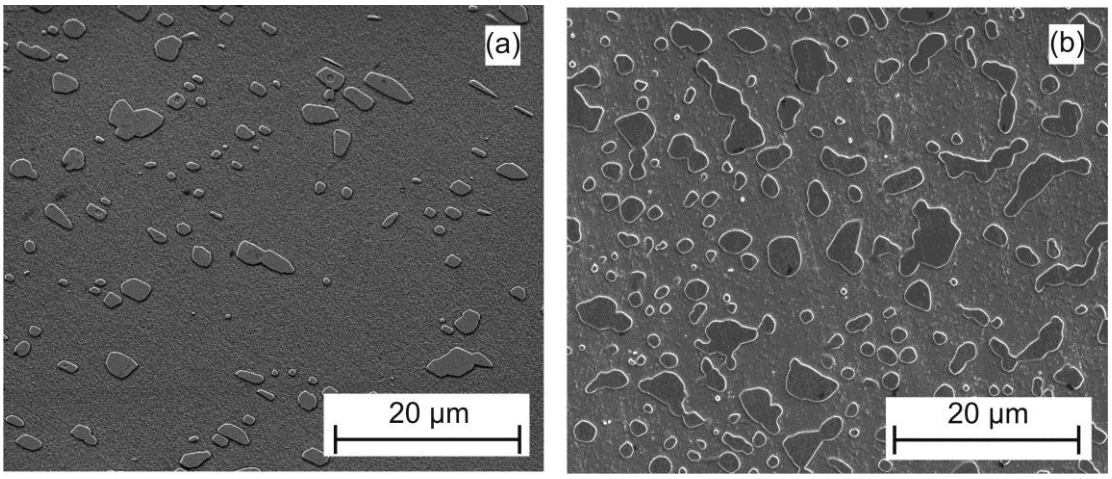

Figure 3. SEM images showing the microstructure of the investigated samples with cementite precipitates: (a) Fe-0.8%C and (b) Fe-1.5%C.

4. RESULTS AND DISCUSSION

4.1 Bulk magnetic properties

The magnetic hysteresis curves of the three samples are shown in Figures 4a-c (dotted lines). The coercivity H_c increases with carbon content, while the relative permeability at the coercive field H_c, the remanence B_R, and the saturation magnetization B_S at 100 A/cm decrease with increasing carbon content. In summary the magnetic hardness increases as the carbon content increases. A summary of the measured parameters is given in Table 1.

Table 1: Parameters deduced from the macroscopic measurements shown in figure 4.

Carbon content [wt%]	Coercive field H_C [A/cm]	Relative permeability at H_C	Remanence B_R [T]	Maximum Barkhausen noise amplitude M_{max} [mV]	Saturation magnetization B_S [T]
0 (Pure)	2.4	0.311	0.91	7.8	1.95
0.8	4.7	0.158	0.84	5.3	1.73
1.5	6.9	0.132	0.76	4.7	1.57

The Barkhausen noise curves (Figures 4a-c, continuous lines) give a further insight into the differences in the magnetization processes. A high maximum of Barkhausen noise (Fig. 4a) close to the coercive field H_C can be seen for the high purity iron sample. This is

attributed to the easy irreversible domain wall movement of the 180° BWs in pure iron. The addition 0.8 and 1.5 wt. % of carbon, respectively, results in a microstructure with globular cementite precipitates embedded in a ferrite matrix with less than 0.008 wt. % of carbon in solid solution. A broadening of the Barkhausen noise peak and a decreasing peak height can be observed as shown in the continuous curves of Figures 4b and c, respectively, which can be attributed to the interstitial carbon atoms in the ferrite matrix and the intra- and intergranular cementite precipitates.

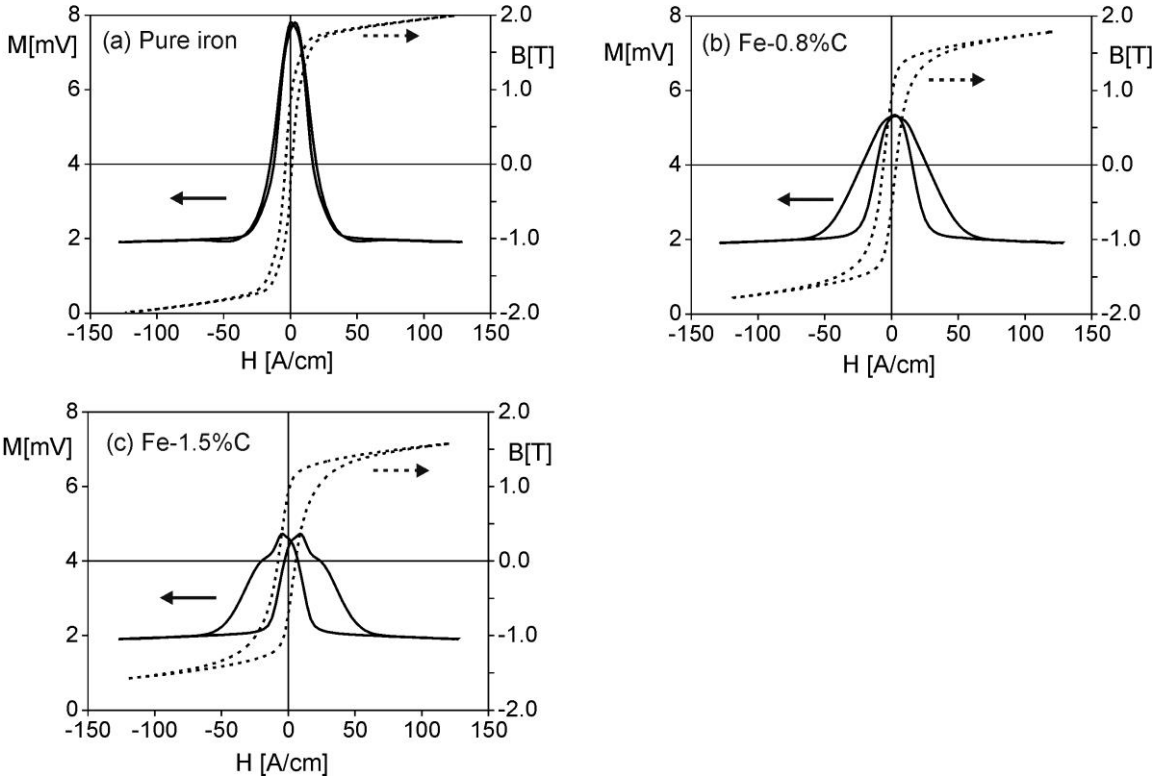

Figure 4. Hysteresis loop (dotted line) and Barkhausen noise (continuous line) curves for (a) pure Fe (99,99%) and two unalloyed steels containing different content of globular cementite (b) Fe-0.8%C and (c) Fe-1.5%C. The measurements were performed at 1.8 V and 0.05 Hz.

Interstitial atoms involve magnetic after effect phenomena [26]. This effect is associated with the diffusion of point defects, e.g. carbon atoms, within the crystalline lattice, e.g., ferrite. When BWs are moving under an ac magnetic field, carbon interstitial atoms are reoriented into energetically more favorable sites with regard to the spontaneous magnetization. Thus, after each reverse scan of the field, the domain walls which are interacting with the defects are hindered by the magnetic after effect pressure, and must overcome an additional residual stress within the material [27]. As a result a higher field is required to move all walls and to reach the saturation state. The direct effect is the lowering and broadening of the maximum in the envelope of the Barkhausen noise as shown in Fig. 4b

and c. Cementite precipitates embedded in the ferrite matrix, however, give rise to a much higher interaction with BWs than interstitial atoms [3]. Due to the very high anisotropy of the cementite its magnetic moments are not easily oriented by an applied magnetic field. The magnetostatic energy is very high creating magnetic poles around the precipitates enhancing the hindrance of the BWs. By increasing the amount of carbon (from 0.8 to 1.5 wt%), i.e. the amount of cementite precipitates, the pinning effect is enhanced requiring longer time to move all walls and reach the saturate state. For the sample containing 1.5 wt% C an additional peak starts to emerge at higher fields (Fig. 4c) which is attributed to the cementite phase [28,29]. It will be shown later that the magnetic microstructure of the ferrite matrix often appears to be unrelated to that one of the cementite phase.

4.2 Local magnetic properties – image contrast in magnetic force microscopy

Magnetic force microscopy monitors the magnetic force gradient between the tip and the sample, which is determined by the magnetic fields and moments of both, the tip and the sample. During MFM imaging, the tip and sample can be very close to each other. Therefore, the tip stray field may change the sample and vice-versa. Such distortion can be extremely severe if either the tip or the sample is magnetically soft. Depending on the nature of the sample different coating materials, e.g. cobalt-chromium, iron and Permalloy (Ni-Fe), can be used for the tip. In a series of preliminary experiments a suitable sensor type was chosen from a set of commercial tips with different coatings [30,31].

Fig. 5a shows the topography of the Fe-0.8%C sample revealing the cementite precipitates as higher, white areas in the ferrite matrix. Two magnetic images of the same surface area are shown in Fig. 5b and c. In both scans, the magnetization direction of the tip was perpendicular to the sample surface, but the tip was magnetized downwards and upwards along its axis, respectively. As can be observed by comparing Fig. 5b and c, the phase shift in the magnetic images shows contrast inversion for the opposite magnetization direction of the tip. We may therefore conclude that the chosen magnetic tip does not influence the magnetic microstructure of the sample and vice-versa, and that the observed contrast represents the z-component of the stray fields of the sample [30].

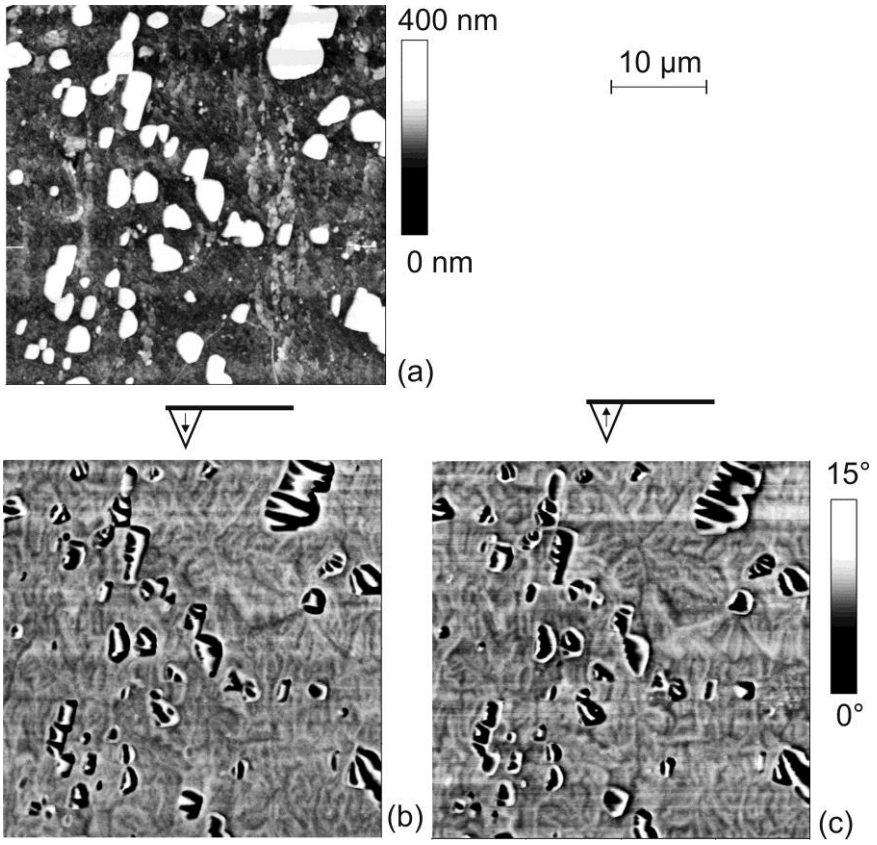

Figure 5. Topography (a) of the sample Fe-0.8%C containing globular cementite precipitates in a ferrite matrix, MFM images taken with the magnetic tip magnetized downwards (b) and upwards (c) along its axis [29].

4.3 MFM images of high purity iron

Fig. 6a-c demonstrate the evolution of the magnetic microstructure for the high purity iron sample in an external in-plane magnetic field. Fig. 6a shows the sample at the remanence state (no applied field) while Fig. 6b and c show the sample in an applied magnetic field of 190 A/cm and -190 A/cm, respectively. Arrow #1 in Fig. 6a points to a grain boundary separating two grains with different crystal orientation. The grain on the right side displays a multitude of small areas with different magnetic contrast, while the grain on the left side shows large areas with almost homogeneous grey level. The domain arrangement at the surface is primarily determined by the principle of flux closure which minimizes the total inner energy. Besides that, it is strongly dependent on the surface orientation relative to the easy directions. From the simplest case, a surface containing two easy axes, to surfaces strongly deviating from easy axes in their orientation, the domain patterns become progressively more and more complicated [14]. The <001> directions are the easy directions for iron and therefore the (100) surface contains two mutually perpendicular easy directions. This allows us to conclude that the orientation of the left grain is close to the plane (100), and

the orientation of the right grain strongly deviates from the plane (100), which contains two easy axes.

The grain on the left side displays a few domains clearly separated by Bloch walls which can be detected as bright or dark lines in the MFM image (arrows #2 and #3) in Fig. 6). At the remanence state, a domain wall will be in a position which minimizes the energy of the system formed by the wall itself and the adjoining domains and domain walls. In Fig. 6a, some walls are bulged possibly indicating the existence of defects and residual microstress which is caused by crystal imperfections as e.g. dislocations [18].

When the magnetic field is applied a change of position of the domain can be observed. For example a small domain wall indicated by arrow #3 in Fig. 6 moves to the right or left side when a positive or negative field is applied, respectively. In order to highlight the domain wall movements, the arrows were placed in exactly the same positions in all images by taking the immobile grain boundary (arrow #1) as a reference. All domain walls go back to their initial positions when the field is switched off, which means that the observed domain wall movements are reversible.

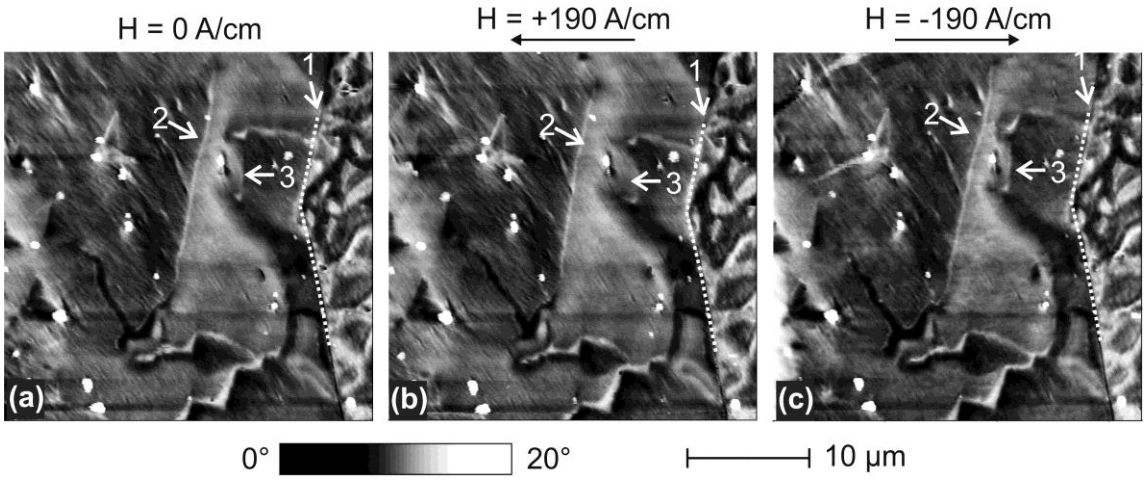

Figure 6. MFM images of the high purity iron sample (a) without external field and with an applied external field of (b) 190 A/cm and (c) – 190 A/cm, respectively. The direction of the in-plane field is indicated by black arrows.

4.4 MFM images of the samples containing globular cementite embedded in a ferrite matrix

Non-magnetic inclusions in a magnetic matrix are often discussed in literature [32,33], in contrast the unalloyed steels Fe-0.8%C and Fe-1.5%C investigated here consist of a soft ferromagnetic ferrite matrix with cementite precipitates which are magnetically harder than the matrix. The carbon content is higher in the Fe-1.5%C sample than in the

Fe-0.8%C-sample, but the basic behavior of the magnetic microstructure can be discussed by taking the Fe-1.5%C as an example.

Fig. 7 shows the microstructure of the Fe-1.5%C sample. The topography image obtained with the MFM (Fig. 7a) reveals the cementite precipitates as bright areas which are about 400 nm at maximum higher than the ferrite matrix. Three grains with different average height (numbered (1), (2), and (3)) are visible in the ferrite matrix. The corresponding electron backscatter diffraction maps taken with a scanning electron microscope, i.e. the Kikuchi pattern quality (KPQ) and the inverse pole figure (IPF), are shown in Fig. 7b and c, respectively. The color code of the inverse pole figure represents the crystallographic orientation in the ferrite matrix (nearly pure b.c.c. iron, lattice constant a = 2.87Å), and in the cementite particles (orthorhombic symmetry, length of the three perpendicular axes a = 5.09Å, b = 6.74Å, c = 4.52Å). Using an orientation imaging software the angles of inclination of the three ferrite grains (1), (2), and (3) relative to the (100) plane were obtained as 15°, 9° and 33°, respectively.

The inverse pole figure maps reveal that most of the large cementite precipitates observed in the topography image (Fig. 7a) are not single crystals, but have a polycrystalline structure with different grain orientations. The dark grey color of the cementite precipitates in the KPQ map corresponds to a low KPQ index (Fig. 7b). The decrease of the indexing rate is correlated with a strong lattice distortion induced by accumulation of dislocations in the cementite phase.

Fig. 8a-d displays the magnetic microstructure of the same sample area shown in Fig. 7 in the demagnetized state as well as with applied field strengths of 100 and 190 A/cm, respectively. Like in the Fe-0.8%C sample (Fig. 5), the cementite precipitates show mostly striped domains with a strong magnetic phase contrast, while the contrast in the ferrite matrix is weaker. This can be explained by the fact that cementite is magnetically harder than ferrite and thus causes stronger stray fields. Each cementite particle has its own domain structure, and no closure domains are observed. This probably is due to the high single crystal anisotropy of cementite (K_1 = 118.10^3 $J.m^{-3}$ and K_2 = 394.10^3 $J.m^{-3}$) [7]. The cementite domain structure in or around the (010) plane consists of parallel stripes directed alternately down- and upwards in relation to the surface. Since the MFM tip senses the component of the stray field emerging perpendicularly from the surface, we may conclude that the magnetic moments of these precipitates are more or less parallel to the tip axis, i.e. perpendicular to the sample surface plane. The observation that the long axis (here [010]- or b-axis) is the easy

axis in cementite agrees with the results of Keh and Johnson, obtained by transmission electron microscopy studies on cementite particles with 5-10 µm average dimension [7].

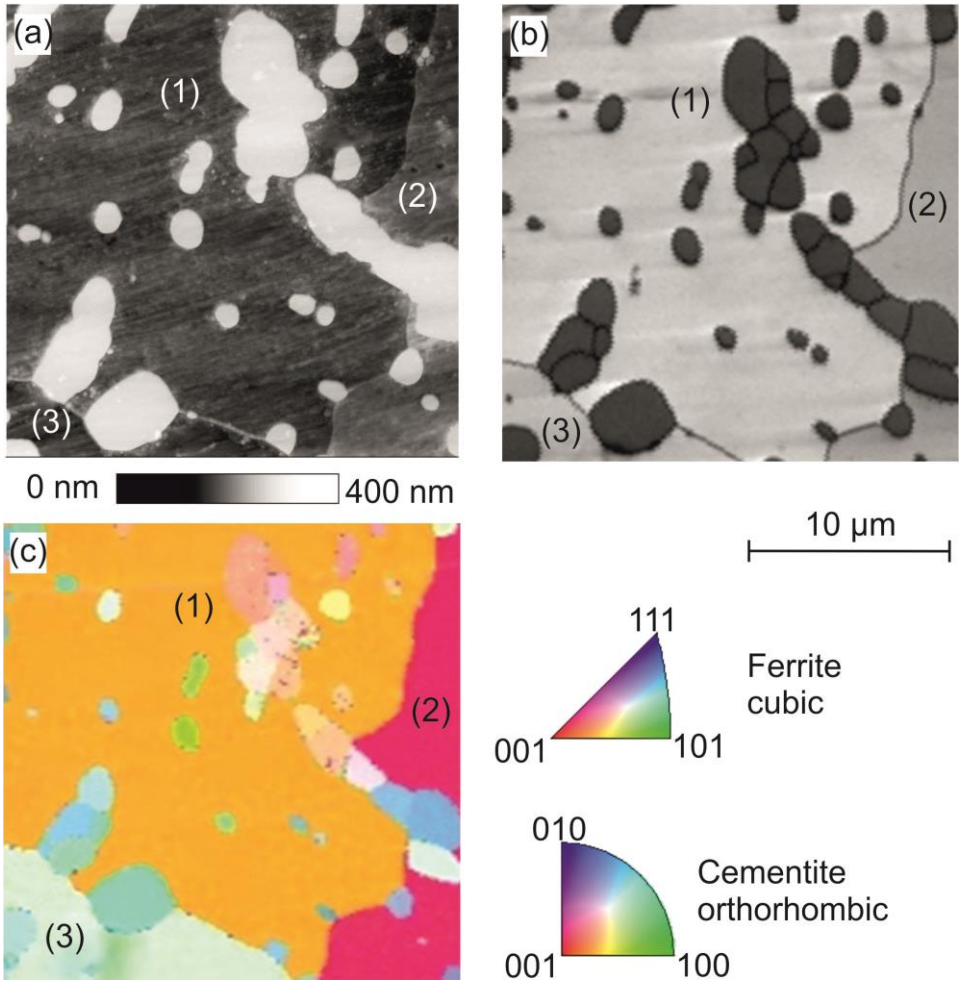

Figure 7. Topography (a) of the Fe-1.5%C sample taken with MFM. The corresponding KPQ (b) and IPF (c) maps taken with SEM show the crystals and their respective orientations. Three grains with different crystal orientation are marked as (1), (2), and (3) in the images.

Spike domains, first observed by Williams [42] in a Fe-Si alloy, are visible in the ferrite matrix on the grain boundary between the grains 1 and 3 as well as attached to the large precipitate (white arrow (S) in Fig. 8a). The formation of these spike domains may be explained by the reduction of the magnetostatic energy of the cementite and stress concentrations on the grain boundary and on the cementite/ferrite interface caused by differences in thermal expansion coefficient. Magnetostatic energy associated with an inclusion is proportional to its volume. Thus the probability to show attached spike domains in order to reduce magnetostatic energy increases with the size of the precipitates.

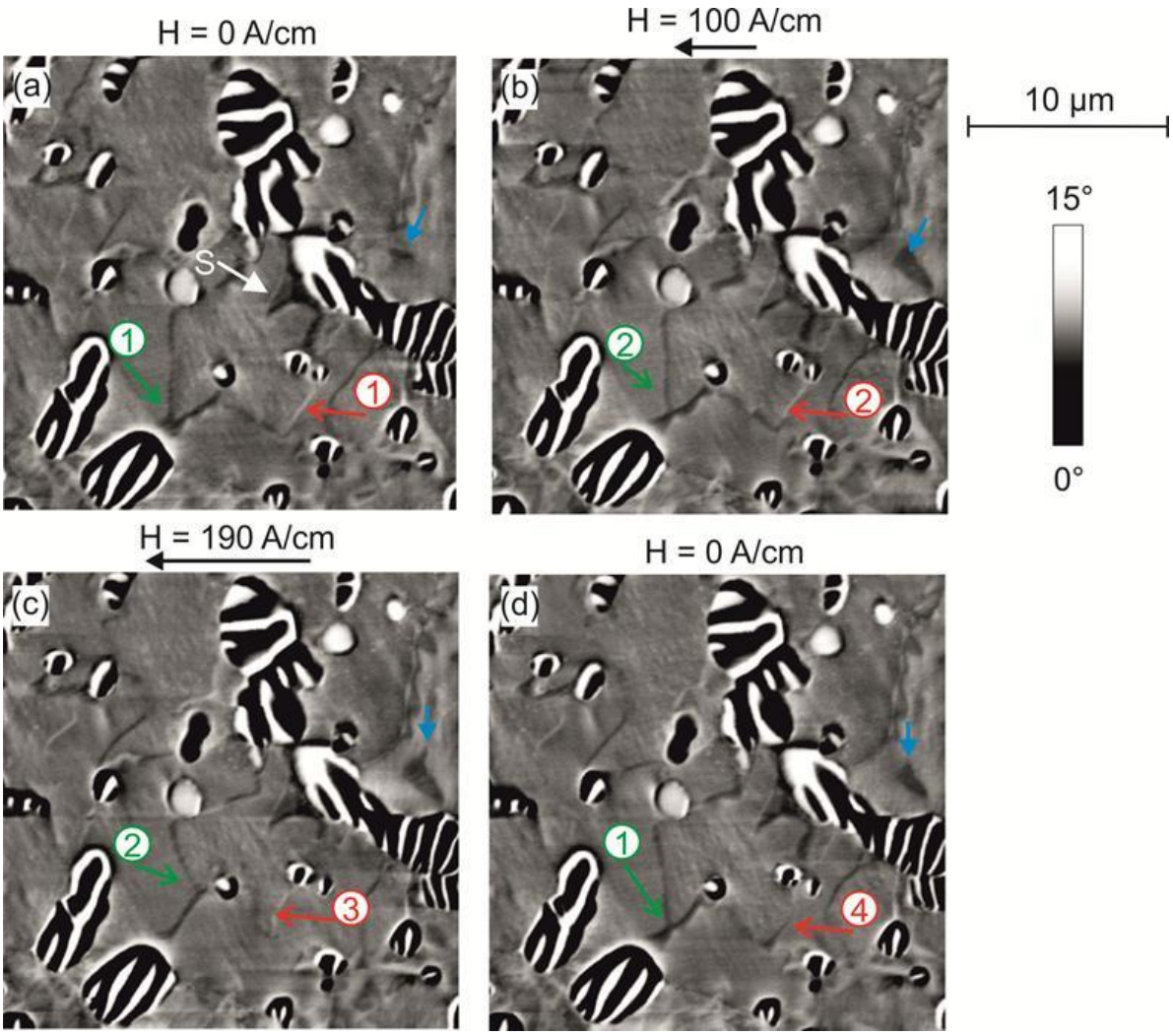

Figure 8. MFM images of the Fe-1.5%C sample taken after demagnetization of the sample without an external field (a) and with applied external fields of 100 (b) and 190 A/cm (c). In (d) the field was switched off again; the applied field direction is indicated by the black arrows. The white arrow (S) points to a spike domain in the ferrite matrix. The blue arrow shows a domain which changes its size, the red and green arrows indicate domain walls. The numbers in circles relate to the energy diagram (Fig. 9).

4.4.1 Reversible and irreversible domain wall movement in ferrite

Fig. 8a shows the sample after demagnetization without external field. The demagnetization process was done by applying alternating fields of slowly decreasing amplitude. Bright and dark lines are visible within the ferrite matrix in Fig. 8, which can be identified as domain walls. Two domain walls were marked in Fig. 8a with green and red arrows. These domain walls tend to intersect the cementite precipitates in order to minimize the magnetostatic and wall energy. When a magnetic field *H* is applied, it induces forces on the domain walls which cause growing of domains with orientation in the field direction at the

expense of the other domains. A supplementary domain can be observed in grain 2 (Fig. 8, blue arrows). When applying a field of 100 and 190 A/cm (Fig. 8b and c) respectively, the domain increases its size. When the magnetic field is switched off, the size of the domain decreases again (Fig. 8d).

At low fields, domain wall motion dominates the magnetization process rather than domain rotation. However, both domain wall bulging (a reversible process) and domain wall displacement (an irreversible process) are important in this region. Initially, if the magnetic field is smaller than the coercive field ($H < H_c$), the domain wall is attached to pinning points. As H increases, the wall bows between the pins as to be seen in Fig. 8b, red arrow. When $H > H_c$, the domain wall unpins and propagates (Fig. 8c, red arrow).

In order to explain such a displacement as observed by the domain wall marked by red arrows in Fig. 8, one can use a well-known model (Fig. 9) [18]. The domain wall displacement x can be described as a function of a single energy term E which stands for all types of energies involved such as wall energy and magnetostatic energy. The energy E varies with x as shown schematically in Fig. 9a. The magnetic field H causes a driving force on the domain wall which acts against the restoring force of energy gradient dE/dx (Fig. 9b). One can assume that the driving force is cH, where the proportionality constant c depends on the kind of wall and on the orientation of the field. At $H = 0$, the wall "rests" in an energy minimum (upon a cementite precipitate) (Figs. 8a and 9①). If a small field is applied, with cH lower than the maximum of the energy gradient, the wall moves reversibly to point ② and back to point ①, if H is switched off again (Figs. 8d and 9①). If a larger field H is applied such that cH is equal or larger to the maximum of the energy gradient, the wall jumps irreversibly to point ③ (Figs. 8c and 9③). If H is now switched off again, the wall will move to point ④, which then is the nearest minimum in energy (Figs. 8d and 9④). Note that for the same external applied in-plane magnetic field both reversible (green arrows in Fig. 8) and irreversible (red arrows in Fig. 8) domain wall movements are observable, because the shape and the gradient of the energy curve in Fig. 9 depend on the domain wall and on its microstructural neighborhood.

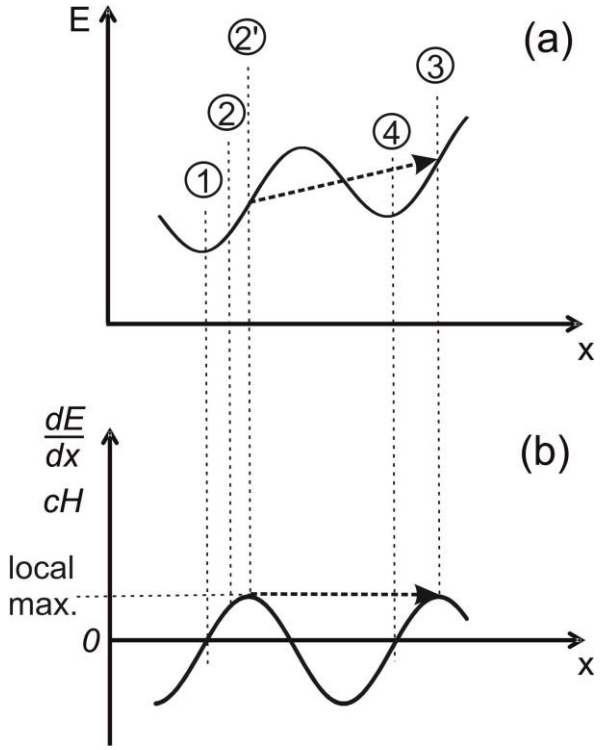

Figure 9. Energy model for reversible and irreversible domain wall movements in x-direction. The external force on the domain wall acting against the internal force dE/dx is proportional to the applied external field H. The wall will move back from ② to the energy minimum ① as long as cH is smaller than the local maximum of dE/dx. If cH is equal or larger than the maximum, the wall will jump from ②' to ③ and back to a new minimum ④ upon removal of the external field.

It is clearly visible that the magnetic microstructure of ferrite and the evolution of its domain configuration under an applied magnetic field are strongly influenced by the cementite. Domain walls are hindered in their movement by large as well as by small precipitates. For large precipitates, this is mainly due to interactions with attached subsidiary domains which tend to stick to the walls, whereas small precipitates reduce the energy of any wall that contains them. In relation to their volume density, inclusions with a diameter approximately equal to the wall thickness should cause the strongest effect [18]. The pinning sites cause a decrease in the initial permeability of a ferromagnetic material and an increase in its coercive force. Hence, increasing the amount of carbon, i.e. cementite, the macroscopic initial permeability decreases and the coercivity increases. Irreversible changes in magnetization are caused during wall displacement by the pinning process [35]. A wall jump generates an eddy current pulse which propagates in all directions and arrives at the surface of the sample according to a dispersion law [43]. The average of all local Barkhausen jumps can be detected by a suitable macroscopic set-up as shown in Fig. 1.

Fig. 10 shows the evolution of the magnetic microstructure of a section of grain (1) in Fig. 7. The magnetic microstructure is slightly different from the structure in Fig. 8 because the sample was removed from the MFM, demagnetized in a strong macroscopic field, and replaced into the MFM between the measurements. Fig. 10a is recorded at the remanence state of the sample while Fig. 10b and c display the results with an applied magnetic field of 190 A/cm and -190 A/cm, respectively. The walls (arrows in Fig. 10) are anchored at the precipitates. Fig. 10a (arrow #1) shows a wall which is already bent between two cementite precipitates without an applied external field. When applying a field of 190 A/cm to the right (Fig. 10c) the wall becomes nearly straight. Contrarily, the wall marked with arrow #2 is nearly straight when no external field is applied (Fig. 10a), but it clearly bends into the direction of the field of 190 A/cm (Fig. 10c). This confirms the predictions [34] that domain walls should be flexible rather than rigid. An irreversible domain wall movement (Barkhausen jump) is also visible as marked by arrow #3 in Fig. 10a-c. One Bloch wall shows a sharp kink (Fig. 10c, arrow K). The kink in a 180° Bloch wall has also been observed in magnetite using the Bitter method [5]. Bloch wall segments with different polarities do not form a straight line, but are kinked at the point where the direction of the interior rotation of spins in the wall reverses. This reduces the magnetostatic (stray field) energy of the wall.

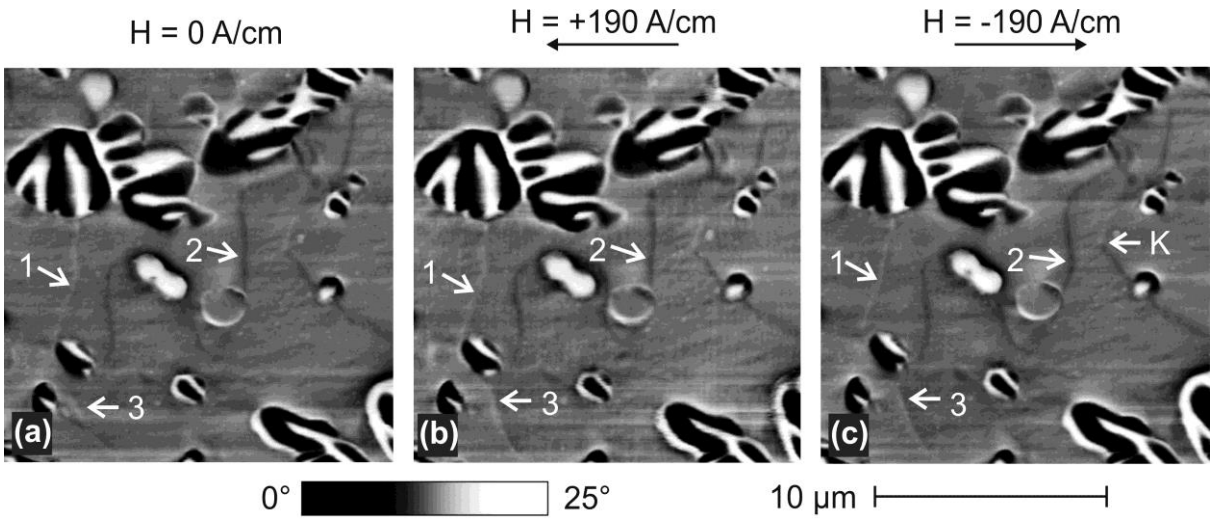

Figure 10. MFM images taken on the Fe-1.5%C sample (a) without external field and with external fields of (b) 190 A/cm and (c) – 190 A/cm, respectively. The applied field direction is indicated by the black arrows [29].

4.4.2 Bowing of domain walls in ferrite

Residual stresses in the ferrite phase as well as lattice mismatch in both phases may produce microstresses, which can cause bowing of 180° walls even without applied field.

Fig. 11a shows a sketch of a 180° Bloch wall which is bowed into a circular arc of radius *r*. The dotted line gives the position of the unflexed wall; *2y* is the distance between pinning sites and *x* the linear displacement [35]. The linear displacement *x* is obtained by a simple geometrical calculation (Fig. 11a):

$$x = r - \sqrt{r^2 - y^2}. \quad (3)$$

The average internal stress $<\sigma>$ responsible for the observed domain wall bowing can be estimated as [36]:

$$\left(x/2y\right)^2 \approx \left(\lambda_s < \sigma > / 2\mu_0 M_s^2\right). \quad (4)$$

Here, $\lambda_s = 22.2 \times 10^{-6}$ is the saturation magnetostriction constant for iron [100] [19], $\mu_0 = 1.256 \times 10^{-6}$ N/A^2 is the magnetic permeability in vacuum, and $M_s = 1.739 \times 10^6$ A/m [19] is the saturation magnetization of iron. Taking the measured values r = 48.1 μm, x = 0.1 μm and y = 3.1 μm, the estimated value of the average internal stress is $<\sigma>$ = 88.9 MPa (Fig. 11b, white arrow).

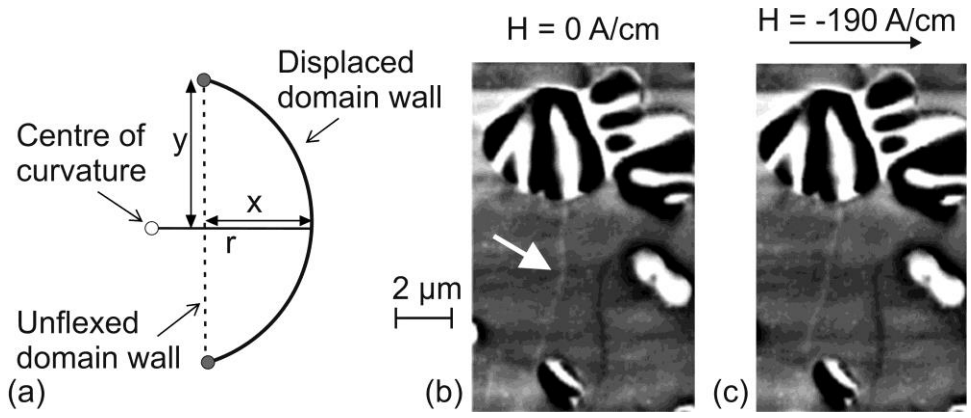

Figure 11. Bending of a magnetic domain wall between two pinning sites: (a) schematic sketch showing the geometry of the curved domain wall [37], (b) and (c) enlarged section of Fig. 10 showing the Fe-1.5%C sample at the remanence state and with an applied field of 190 A/cm to the right, respectively.

The amount of domain wall bending before breaking away from the pinning sites depends directly (but inversely) on the strength of the pinning sites and on the domain wall surface energy [35]. The domain wall undergoes more bending for a wall having low surface

energy and high pinning site strength. Furthermore the bending depends on an extrinsic factor which depends on the magnetic field *H*.

4.4.3 Contrast and width of domain walls in ferrite

Bloch walls in the ferrite matrix are visible as bright and dark lines in the scanned area. Fig. 12 shows once more an enlarged section of an MFM image of grain 1. MFM line scans across both walls are shown in Fig. 12b and c. The line scans clearly show the positive and negative phase shifts in the bright and dark walls, respectively. For a wall moment direction opposite to the tip moment direction, the tip will feel a repulsive force and the cantilever suffers a positive phase shift resulting in a bright line in the image. Vice versa, for a magnetic moment direction in the wall parallel to the moment of the tip, it will feel an attractive force creating a negative phase shift and a dark line in the image. The average magnetic moments inside the walls are perpendicular to the plane pointing out of or into it. We can conclude that on both sides of a wall, the magnetic moments are most likely antiparallel to each other and aligned in the plane. The BWs are transition areas in which the moment direction gradually rotates by 180°. As a consequence, the MFM tip feels an attractive or a repulsive force on the walls depending on their polarities.

Depending on the magnetic anisotropy value, the domain wall width δ_w can vary from a few inter-atomic distances in hard magnetic films with perpendicular anisotropy to several hundred nanometers in films with weak in-plane anisotropy [38]. The width of a BW in iron is around 100 nm [39,40]. In this work, the wall width measured in the ferrite phase ranges from 140 nm to about 500 nm. The larger value found in this work can be explained by limited local resolution of the MFM instrument caused by the finite horizontal and vertical dimensions of the tip apex and corresponding averaging over the local stray-field variation [41].

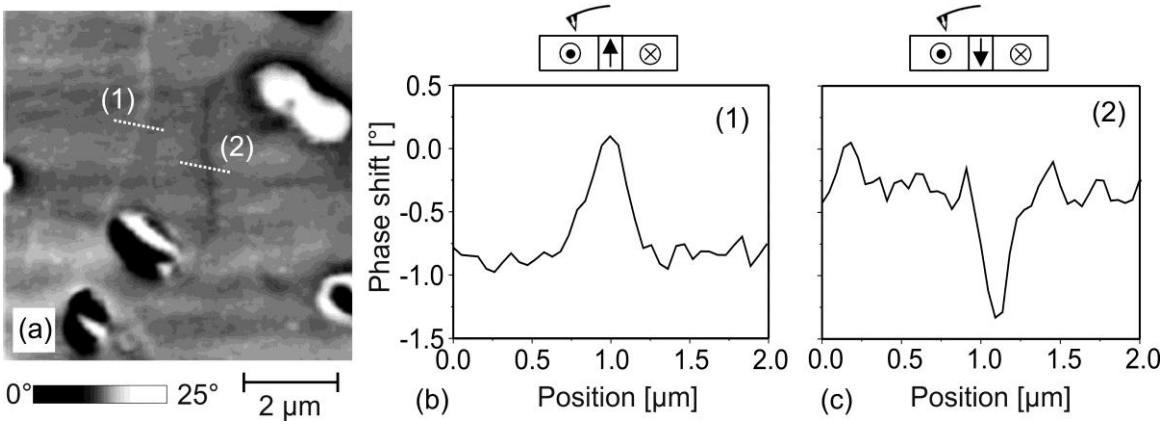

Figure 12. (a) Enlarged section of Fig. 10a showing Bloch walls in the Fe-1.5%C sample; (b) and (c) line scans across the Bloch walls, lines indicated in (a). The measured wall thickness in the line scans (1) and (2) is 500 nm and 340 nm, respectively.

4.5 Correlation between microscopic and macroscopic magnetic measurements

With increasing amount of cementite in the ferrite matrix the macroscopic magnetic hardness increases. As has been shown in sections 4.2, 4.3, and 4.4, the domain structure of the pure iron sample is completely different from the domain structure of the material with the cementite phase. The cementite particles show a magnetic stray field which is in generally stronger than the stray field of the ferrite, and the magnetic microstructure of ferrite is strongly influenced by the cementite. An interaction between the domain walls in ferrite with the precipitates becomes very well visible when an external magnetic field is applied. Observation of the position change of the domain walls at different external magnetic fields indicated clearly that the domain walls of the ferrite matrix are hindered in their movement by large as well as by small cementite precipitates.

The analysis of the magnetic microstructure of the investigated samples suggests that the field of 190 A/cm is not strong enough to reach saturation. However, the macroscopic measurements have shown that a field of 190 A/cm is strong enough to saturate all three samples. This disagreement may be explained by the fact that the macroscopic hysteresis loop measurements were made with cylindrical samples while the samples for MFM measurements were small square plates cut from the macroscopic cylinders. Shape anisotropy and demagnetization probably led to different magnetic fields in the completely different experimental geometries. Furthermore the MFM analysis of the domains and their dynamics relies on the behavior of the surface domains. Surface residual stress built up during mechanical polishing as well as the special electromagnetic boundary conditions of surface domains may hinder the movement of domain walls on the surface and thus a stronger

magnetic field may be required to reach the same magnetization level compared to the volume interior.

5. SUMMARY

Samples of highly pure iron and the unalloyed steels Fe-0.8%C and Fe-1.5%C were characterized macroscopically by measuring hysteresis loops and Barkhausen noise signals. With increasing amount of carbon in form of globular cementite precipitates in the ferrite matrix the magnetic hardness increases and the Barkhausen noise amplitude decreases.

The local resolution of most magnetic imaging techniques is not sufficient to observe individual domains in technical steels. Interpretations therefore are based on simulation, macroscopic experiments and on observations in materials with a coarser micro structure. The combination of AFM, MFM, and EBSD techniques opens a new field for material research and development enabling the direct observation of magnetic micro- and nanostructures including the corresponding single crystal grain orientations. The surface of bulk samples can be studied, the comparison to macroscopic data of the samples is therefore possible, and the sample preparation is simpler compared to sample preparation for transmission electron microscopy.

In this work, MFM images with a local resolution of 50 nm, recorded with different external fields reveal how the magnetization process takes place via domain wall displacement and domain wall nucleation. Ferromagnetic domain structures in highly pure iron and in cementite precipitates as well as their interaction were studied. Domain walls in the ferrite phase tend to intersect the cementite precipitates in order to minimize the magnetostatic and wall energy. Spike domains have been observed mostly in the grain boundaries of the ferrite phase as well as attached to large cementite precipitates. The cementite domain structure in or around the (010) plane was found to consist of parallel stripes directed alternately down- and upwards in relation to the surface without direct correlation to the ferrite domain structure of the matrix.

By applying an external in-plane magnetic field the dynamic behavior of the magnetic domains and the interaction between domain walls and the cementite precipitates was observed. In the ferrite matrix, bending of domain walls occurs at weak external magnetic fields. For stronger applied magnetic fields reversible and irreversible break-free of domain walls was observed, which can be interpreted as a local Barkhausen event or -jump. The microscopic observation that the cementite precipitates represent an obstacle to the domain wall movement correlates qualitatively with the increase of magnetic hardness with increasing

amount cementite, and with the broadening of the maximum in the envelope of the Barkhausen noise in the macroscopic measurements.

REFERENCES

[1] I. Altpeter, *Journal of Nondestructive Evaluation* **15** (1996) 45.

[2] I. Altpeter, G. Dobmann, M. Kröning, M. Rabung, S. Szielasko, *NDT&E International* **42** (2009) 283.

[3] C. Gatelier-Rothea, J. Chicois, R. Fougeres, P. Fleischmann, *Acta Materialia* **46** (1998) 4873.

[4] S.M. Thompson, B.K. Tanner, *Journal of Magnetism and Magnetic Materials* **123** (1993) 283.

[5] Ö. Özdemir, D.J. Dunlop, *Journal of Geophysical Research* **102** (1997) 20,211.

[6] R. Schäfer, *Journal of Magnetism and Magnetic Materials*, **215-216** (2000) 652.

[7] A. S. Keh, C. A. Johnson, *Journal of Applied Physics* **34** (1963) 2670.

[8] I. Manke, N. Kardjilov, R. Schäfer, A. Hilger, M. Strobl, M. Dawson, C. Grünzweig, G. Behr, M. Hentschel, C. David, A. Kupsch, A. Lange, J. Banhart, *Nature Communications* **1** (2010) 125.

[9] P. Grütter, T. Jung, H. Heinzelmann, A. Wadas, E. Meyer, H.R. Hidberand, H.J. Güntherodt, *Journal of Applied Physics* **67** (1990) 1437.

[10] U. Hartmann, *Journal of Magnetism and Magnetic Materials*, Volumes **157–158** (1996) 545.

[11] E. Dan Dahlberg, Jian-Gang Zhu, *Physics Today* **48** (1995) 34.

[12] U. Hartmann, T. Göddenhenrich, C. Heiden, *Journal of Magnetism and Magnetic Materials*, **101** (1991) 263.

[13] P. Grütter, H. J. Mamin, D. Rugar, in *Scanning Tunneling Microscopy, Vol. II*, ed. by H.J. Güntherodt, R. Wiesendanger, Springer, Berlin, Heidelberg, New York (1992) 845.

[14] A. Hubert, R. Schäfer, *Magnetic Domains - The Analysis of Magnetic Microstructures*, Springer, Berlin (1998).

[15] H. Kronmüller, S. Parkin, *Handbook of Magnetism and Advanced Magnetic Materials*, Vol 2: Micromagnetism, Wiley & Sons, New York (2007).

[16] M. Coisson, F. Vinai, P. Tiberto, F. Celegato, *Journal of Magnetism and Magnetic Materials* **321** (2009) 806.

[17] S. Huo, J. E. L. Bishop, J. W. Tucker, M. A. Al-Khafaji, W. M. Rainforth, H. A. Davies, M. R. J. Gibbs, *Journal of Magnetism and Magnetic Materials* **190** (1998) 17.

[18] B. D. Cullity, *Introduction to magnetic materials*, Addison Wesley, London (1972).

[19] H. Kronmüller, M. Fähnle, *Micromagnetism and the Microstructure of Ferromagnetic Solids*, Cambridge University Press, Cambridge (2003).

[20] E. Kneller, *Ferromagnetismus*, Springer, Berlin (1962).

[21] Y. Martin, H.K. Wickramasinghe, *Applied Physics Letters* **50** (1987) 1455.

[22] J.J. Saenz, N. Garcia, P. Griitter, E. Meyer, H. Heinzelmann, R. Wiesendanger, L. Rosenthaler, H.R. Hidber, H.J. Güntherodt, *Journal of Applied Physics* **62** (1987) 4293.

[23] G. Binning, C.F. Quate, C. Gerber, *Physical Review Letters* **56** (1986) 930.

[24] Q. Zhong, D. Inniss, K. Kjoller, V.B. Elings, *Surface Science*, **290** (1993) L688.

[25] A. Thiaville, J. Miltat, J. M. García, *Magnetic Force Microscopy: Images of Nanostructures and Contrast Modeling*, in: NanoScience and Technology, No. XVIII, Eds. H. Hopster, H. P. Oepen, Springer Berlin Heidelberg (2005) 128.

[26] P. Brissonneau, *Journal of Physics and Chemistry of Solids* **7** (1958) 22.

[27] J. M. Lopez, *Caractérisation de la précipitation du carbone dans les alliages Fe–C par des mesures magnétiques et magnétomécaniques*, Thèse, Université P. Sabatier, Toulouse (1986).

[28] G. Dobmann, *private communication*.

[29] I. Altpeter, *Spannungsmessung und Zementitgehaltsbestimmung in Eisenwerkstoffen mittels dynamischer magnetischer und magnetoelastischer Meßgrößen*, Dissertation, Saarland University, Saarbrücken (1990).

[30] S. Wust, *Untersuchung der magnetischen Domänen in Stahlproben mittels Magnetkraftmikroskopie unter Anlegen eines externen Magnetfeldes*, Diploma thesis, Saarland University, IZFP report No.110126-TW, Saarbrücken (2011).

[31] L. Batista, U. Rabe, S. Hirsekorn, "Micro- and Nanostructure Imaging and Characterization of Advanced Steels", *38th Annual Review of Progress in Quantitative Nondestructive Evaluation (QNDE)*, July 17-22, 2011, Burlington, Vermont, USA.

[32] L. Néel, *Cahiers de Physique* **25** (1944) 21.

[33] M. Kersten, *Grundlagen einer Theorie der ferromagnetischen Hysterese und der Koerzitivkraft*, S. Hirzel, Leipzig (1943).

[34] M. Kersten, *Zeitschrift für Angewandte Physik* **7** (1956) 313.

[35] D. C. Jiles, D.L. Atherton, *Journal of Magnetism and Magnetic Materials* **61** (1986) 48.

[36] S. Xu, R.T. Merril, *Journal of Geophysical Research*, **97** (1992) 4321.

[37] A. Globus, P. Duplex, M. Guyot, *IEEE Transactions on Magnetics* MAG-**7** (1971) 617.

[38] V. Zablotskii, J. Ferré, A. Maziewski, *Journal of Physics D: Applied Phys*ics **42** (2009).

[39] A.E. Berkowitz, E. Kneller, *Magnetism and Metallurgy, Vol. 1,* Academic Press New York, London (1969).

[40] C. Kittel, *Review of Modern Physics*, **21** (1949) 541.

[41] U. Hartmann, *Annual Review of Materials Science* **29** (1999) 53.

[42] H. J. Williams, *Physical Review* **71** (1947) 646.

[43] G. Dobmann, "NDT – Do we have the potential to predict material properties as yield strength, tensile strength and fracture toughness on the component? A state of the art survey", 18th European Conference on Fracture, Dresden, 30.08.-03.09.2010.

III. ON THE MECHANISM OF NONDESTRUCTIVE EVALUATION OF CEMENTITE CONTENT IN STEELS USING A COMBINATION OF MAGNETIC BARKHAUSEN NOISE AND MAGNETIC FORCE MICROSCOPY TECHNIQUES (PUBLICATION B)

L. Batista, U. Rabe, I. Altpeter, S. Hirsekorn, and G. Dobmann

Journal of Magnetism and Magnetic Materials (2014) Vol. 354; 248-256.

ABSTRACT. The influence of the carbon content in form of globular cementite precipitates in unalloyed steels was macroscopically characterized by means of magnetic hysteresis loop and Barkhausen noise techniques. The choice of the frequency of the applied field has a strong influence on the Barkhausen noise profiles. At sufficiently high frequency (0.5 Hz) there are two peaks, one at lower field, the amplitude of which corresponds to the amount of ferrite and one at higher field, the amplitude of which corresponds to the amount of the cementite phase, respectively. Magnetic force microscopy and electron backscattered diffraction techniques were used to determine the magnetic and crystallographic microstructures of the steels. Cementite has its own domain structure and stray fields which influence the magnetization process of the steel by its own magnetic contribution. When an external magnetic field is applied, the magnetization process in ferrite occurs mainly at lower fields through the 180° and 90° domain walls. A higher field is required for the observation of 180° domain wall movements in cementite.

Keywords: Magnetic force microscopy (MFM), Electron backscatter diffraction (EBSD), Steel, Magnetic domains, Barkhausen noise, Non-destructive testing

1. INTRODUCTION

In most steels, among all the phases or constituents that can be obtained by choosing the chemical composition and thermo-mechanical treatments, two are frequently encountered: ferrite and cementite. Ferrite shows high ductility and low strength values and therefore low mechanical and also - very often - magnetic hardness in terms of coercivity. Cementite on the other hand shows high mechanical and magnetic hardness and is much more brittle. Thus, the relative volume fraction of the ferrite and cementite phases gives rise to the final mechanical and magnetic properties of the steel. The knowledge of the amount of cementite in steels is thus crucial.

Hysteresis loop and magnetic Barkhausen noise (MBN) evaluations are widely used magnetic measurement techniques for the microstructural characterization of ferromagnetic materials and determination of residual stress states. In physics, regular hysteresis measurements providing reproducible and reliable results can only be performed by using special hystrometer measurement devices asking for specially shaped test specimens like spheres and cylinders with well-designed geometry combined with encircling coils to measure the magnetic induction. As a consequence the technique can not be applied to real components, as for instance vessel shells or pipes or high speed running steel sheets in a cold rolling mill [1], and is therefore destructive. All techniques based on magnetic circuit approaches [2] suffer from influence of lift-off on absolute value, ensuing value fluctuations, and shearing of the hysteresis curve [3]. Only in case of transformer steel sheets industrial consensus standards exist (i.e. Epstein frame measurements [4]) based on destructive batch tests. In contrast to these facts MBN-analysis can be performed with sensors positioned locally on top of the surface of a component, which means that MBN is non-destructive. However, the use of the magnetic Barkhausen noise techniques is “not yet” regulated by a standard. This makes the comparison of results published by different authors extremely difficult, especially as the side influences of different experimental conditions such as magnetization set-up, signal pick-up, band width, etc. are often insufficiently described. First attempts into standardization are initialized by the German Engineering Society (VDE Guidelines) [5].

During the magnetization process the domain structure of a ferromagnetic material is altered which involves different movements of the domain walls. There are exclusively 90°- and 180°- domain walls in case of iron materials. In the case considered here, the domain wall movement takes place in a microstructure consisting of a ferrite matrix with cementite precipitates. In basic physics the precipitates are either assumed acting as nonmagnetic

foreign bodies [6,7] in the ferromagnetic matrix, or they are considered to interact with the domain walls of the matrix via their residual stress fields [8]. Domain walls tend to cling to nonmagnetic inclusions in order to minimize the magnetostatic and the wall energy. It was considered in the literature in a first approach that cementite behaves as a nonmagnetic inclusion in a ferrite matrix [9] or even as a nonmagnetic phase at all [10]. However, cementite is a ferromagnetic phase [11,12], and therefore – depending on its size, shape, crystalline orientation and amount of defects - it has its own domain structure and stray fields. The stray fields of inclusions, which are a source of magnetostatic energy, may also interact with the domain walls within the matrix. In order to reduce the magnetostatic energy, supplementary domains (closure domains) are built close to the inclusions which in turn interact with the domain walls in the matrix [13,14]. The other source of interaction of the cementite precipitates with the domain walls in the ferrite phase are – as mentioned above - the residual stresses which are built-up due to different thermal expansion coefficients of the two phases during the solidification process of the material, and lattice defects, e.g. dislocations, which are created on the interface between ferrite and cementite.

Several studies have been done on the individual influence of different microstructural parameters, e.g. second phase particles, on the generation of the magnetic Barkhausen noise. For example, the observed MBN activity profile in a microstructure containing cementite in a ferrite matrix showed either a single [15] or a double peak [8,16]. The description of a double peak for a Barkhausen noise profile has also encountered divergences in the literature. The weaker field peak was attributed to the pinning of 180° walls in the matrix by secondary particles and the stronger field peak was explained by annihilation of 90° domain walls at grain boundaries [17]. Contrarily, Moorthy et al. [16] stated that the weaker field peak is caused by irreversible domain walls in the ferrite and the stronger field peak by irreversible movement of domain walls overcoming second phase particles. By measuring the MBN signal as a function of temperature of a compact cementite and unalloyed white cast iron samples, Altpeter [18] demonstrated that the cementite actively produces its own MBN signal. With increasing temperature the ferromagnetic coordination decreases, and consequently the MBN signal intensity decreases. The Curie temperature of cementite (~ 210°C) is lower than the Curie temperature of ferrite (~ 770°C). Altpeter observed a Barkhausen noise amplitude of the compact cementite specimen, which decreased with increasing temperature and disappeared at the Curie temperature of cementite [18]. Furthermore, the MBN amplitude of white cast iron showed qualitatively the same behavior, i.e. it decreased strongly towards the Curie temperature of cementite and remained at a low almost constant level above this value.

In addition, the MBN decrease of white cast iron was stronger with increasing amount of cementite.

In this work, we investigate the opportunity of assessing the relative proportion and contributions of the cementite and ferrite phases in unalloyed steels by optimizing the measured hysteresis loop and Barkhausen noise parameters. The evolution of the magnetic microstructure is directly correlated to the macroscopic measurement quantities by means of a superposed magnetic field applied to a magnetic force microscope (MFM).

2. MATERIALS AND METHODS

Three different materials were examined in this study, a high purity iron (99.99%) and two unalloyed steels, Fe-0.8%C and Fe-1.5%C, containing globular cementite (Fe_3C) embedded in a ferrite matrix. The samples were provided as-cast and machined in a cylindrical shape of 8 mm diameter and 50 mm length. In order to remove all processing-induced residual stresses the samples were vacuum annealed at 600°C for 4h. The resulting microstructure has an average grain size of 80 μm for all samples. The size of the cementite precipitates ranges from a few hundred nanometers to about 10 μm in diameter.

The hysteresis loop and Barkhausen noise measurements were performed inside an electromagnet with a computer-controlled bipolar power supply (Fig. 1). The magnetic tangential field strength H was measured by a Hall probe. The cylindrical samples were magnetized along their axial direction up to a maximum magnetic field strength of 11000 A/m at different excitation frequencies of 0.05 Hz, 0.1 Hz and 0.5 Hz, respectively. The change in magnetic flux density B and the magnetic Barkhausen noise amplitude M were measured by a pick-up coil with 300 turns (wire diameter: 0.1 mm, resonance frequency: 710 kHz) surrounding the sample (Fig. 1). The envelope of the noise signals (analyzed frequency range f_A = 200 Hz - 50 kHz) and the magnetic flux density were recorded as a function of the tangential field strength.

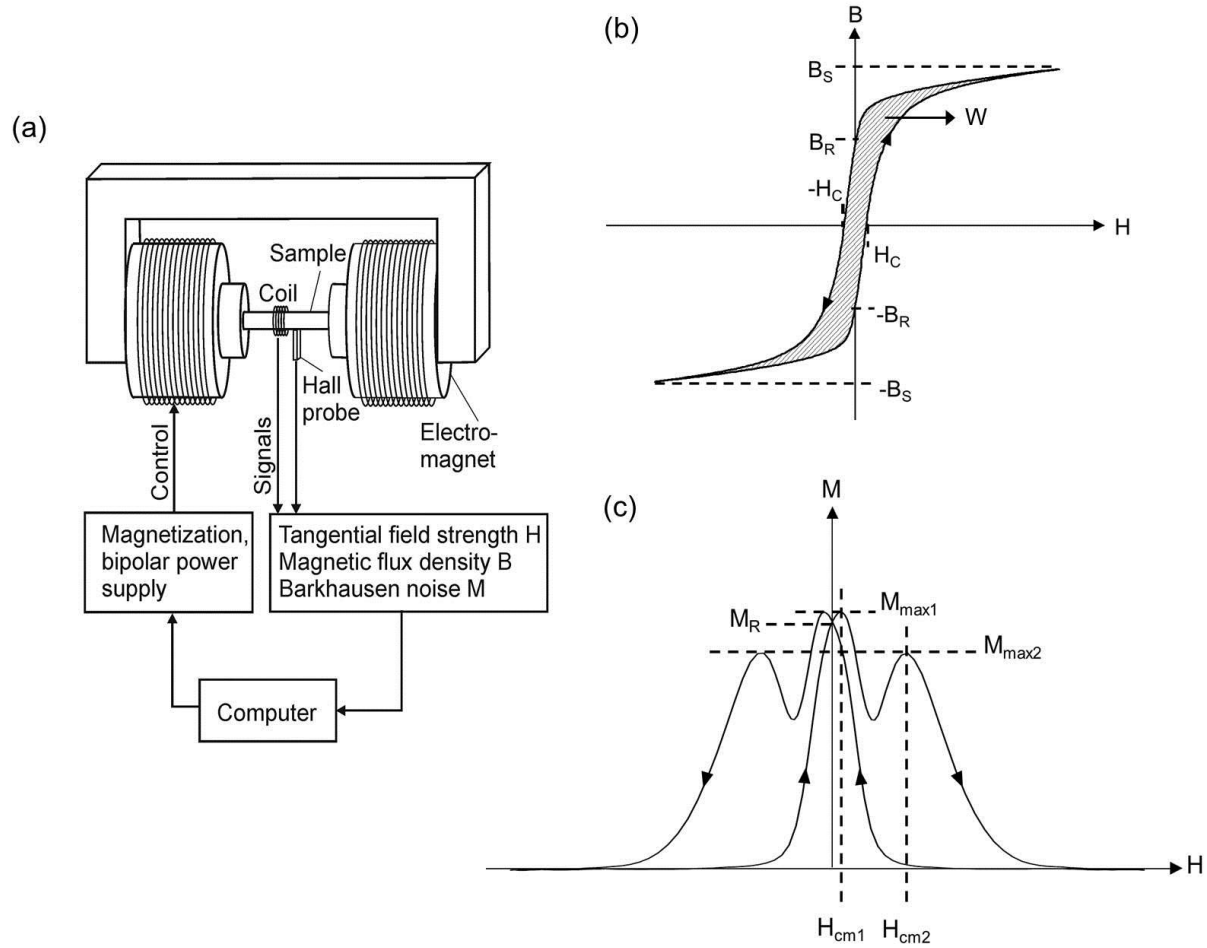

Figure 1. (a) Schematic sketch of the experimental set-up for hysteresis loop and Barkhausen noise measurements, (b) schematic hysteresis loop with coercive field H_C, magnetic flux at saturation B_S, remnant magnetic flux B_R, and loss per cycle W, (c) schematic Barkhausen noise curve with maximum amplitudes $M_{max1,2}$, remnant Barkhausen noise amplitude M_R, and coercive field $H_{cm1,2}$ deduced from Barkhausen noise curve.

Small specimens (3 x 3 x 1 mm^3) were cut by spark erosion from the annealed cylindrical samples for the atomic force microscopy (AFM) and magnetic force microscopy investigations. The specimens were mechanically polished using standard procedures and slightly etched using Nital (95% ethanol + 5% nitric acid). The AFM and MFM techniques were used to image the topography and the magnetic microstructure of the samples, respectively. The measurements were performed in tapping-lift mode using a commercial AFM/MFM instrument (Nanoscope III® multimode, Bruker AXS Inc. (formerly Digital Instruments/Veeco), Madison, WI, USA). The sensor tips were CoCr-coated with a coercivity of ~ 32000 A/m (MESP, Bruker AXS Inc., Madison, WI, USA). The topography images show the local height of the sample surface displayed in grey scales. The magnetic images are taken by vibrating the AFM sensor at its resonance frequency at a predefined lift height above

the sample surface. The gradient of the magnetic interaction forces cause a phase shift in the cantilever vibration which is displayed in gray scales. A lift-height of 60-100 nm was chosen for all measurements reported here. In order to investigate the evolution of the magnetic microstructure and the resulting domain configuration, an external electromagnet was combined with the MFM as shown in Fig. 2. The pole shoes of the electromagnet were adjusted such that the sample inside the AFM was magnetized parallel to its surface.

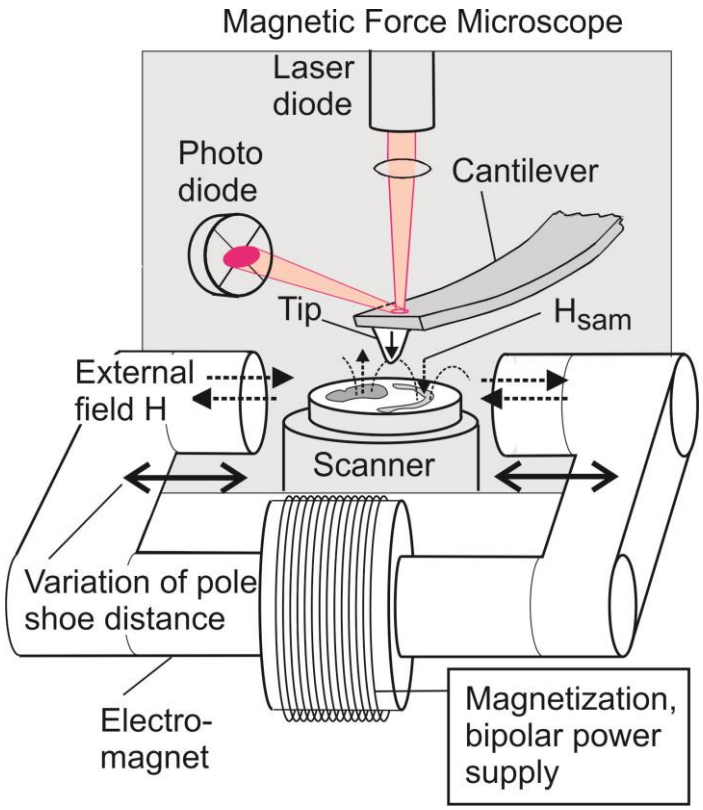

Figure 2. Experimental set-up for the MFM measurements coupled with an external coil providing a controlled external in-plane magnetic field. The strength of the field can be adjusted by the current applied to the coil and/or the distance of the pole shoes with respect to the sample.

3. RESULTS AND DISCUSSION

3.1 Bulk magnetic properties

The unalloyed steels investigated here consist of a relatively hard ferromagnetic phase (cementite) embedded in a soft ferromagnetic phase (ferrite). The different microstructural states lead to characteristic changes of the hysteresis loops and Barkhausen noise profiles as shown in Fig. 3.

Magnetic hysteresis curves of the three samples for three different frequencies *f* (0.05 Hz, 0.1 Hz, and 0.5 Hz, respectively) of the applied external field are shown as dotted lines in Fig. 3. The coercivity H_c and loss per cycle *W* increase with frequency and carbon content, while the relative permeability μ_r and the saturation magnetization B_S at 10000 A/m decrease with increasing frequency *f* of the applied magnetic field. This means that the material reacts magnetically harder with increasing frequency of the external magnetic field. In addition, the magnetic hardness increases as the carbon content increases. A summary of the measured parameters is given in Table 1.

Table 1. Parameters deduced from the macroscopic measurements shown in figure 3.

Measured parameter	**Magnetization frequency [Hz]**	**Carbon content [wt%]**		
		0 (Pure Fe)	**0.8**	**1.5**
Coercive field H_C [A/m]	0.05	240	470	660
	0.1	270	510	690
	0.5	420	680	820
Relative permeability μ_r	0.05	1700	1050	341
	0.1	1245	900	312
	0.5	746	490	294
Saturation magnetization B_S [T]	0.05	1.99	1.79	1.58
	0.1	1.99	1.78	1.57
	0.5	1.96	1.75	1.55
Loss per cycle *W* [mJ/kg]	0.05	2.76	5.08	6.38
	0.1	2.82	5.53	6.71
	0.5	4.40	6.33	7.18

With increasing amount of carbon in form of globular cementite precipitates in the ferrite matrix the pinning of the domain walls in the ferrite matrix is enhanced due to the presence of the cementite which acts as a foreign body, and by its stress fields. Furthermore, the cementite phase contributes to the increase of the magnetic hardness of the steel because cementite is magnetically harder than the ferrite [12]. The increase of the magnetic hardness with increasing frequency observed through the widening of the hysteresis loops is a well-known phenomenon in the case of conductive magnetic materials and it is attributed to eddy current losses [19,20,21], which depend not only on the excitation frequency but also on the

material electrical conductivity σ, amplitude of the magnetic induction B, sample dimensions, and the size and arrangement of the domains [22,23].

The Barkhausen noise profiles for the three samples measured at the same three frequencies are shown as continuous lines in Fig. 3. The curves are remarkably different in their shape (single peak and double peak) and in their maximum amplitude values. In case of a double peak of the MBN one observes a higher maximum at a low excitation field value ($H_{cm,1}$) and a lower peak ($H_{cm,2}$) at a higher excitation field value, as shown schematically in Fig. 1c. The Barkhausen noise amplitude M_{max} increases with the magnetizing frequency for all three samples because the overlapping of random pulses increases as the number of pulses per unit time increases. The Barkhausen noise amplitude M_{max} of the high purity iron sample is significantly larger (for all measured frequencies) than the values of the Fe-0.8%C and Fe-1.5%C samples, respectively. In general, the addition of carbon causes a broadening of the Barkhausen noise peak and a decreasing peak height. This fact can be explained by the influence of interstitial carbon atoms in the ferrite matrix and the intra- and intergranular cementite precipitates as already discussed in a previous work [12].

At very low magnetization frequency (0.05 Hz) the sample containing the higher amount of carbon (1.5 wt%) shows already the emergence of an additional peak $M_{max,2}$ at higher fields (Fig. 3g). By increasing the frequency to 0.1 Hz the emergence of an additional peak $M_{max,2}$ can also be seen for the sample containing less carbon, i.e. Fe-0.8%C, and for the sample Fe-1.5%C the additional peak becomes more evident (Fig. 3e and h). At 0.5 Hz, the signals obtained for the samples containing carbon become clearly double-peak (Fig. 3f and i) while for the high purity iron still a single peak is observed (Fig. 3c). For the Fe-0.8%C and Fe-1.5%C samples where a double peak is observed, the amplitudes of the peaks seem to be proportional to the amount of carbon. With increasing amount of carbon, the peak amplitude $M_{max,1}$ decreases and the peak amplitude $M_{max,2}$ increases (Fig. 4). The results confirm that the weaker field peak $H_{cm,1}$ corresponds to the ferrite and that the emergence of a second stronger field peak $H_{cm,2}$ is related to the presence of the second (cementite) phase.

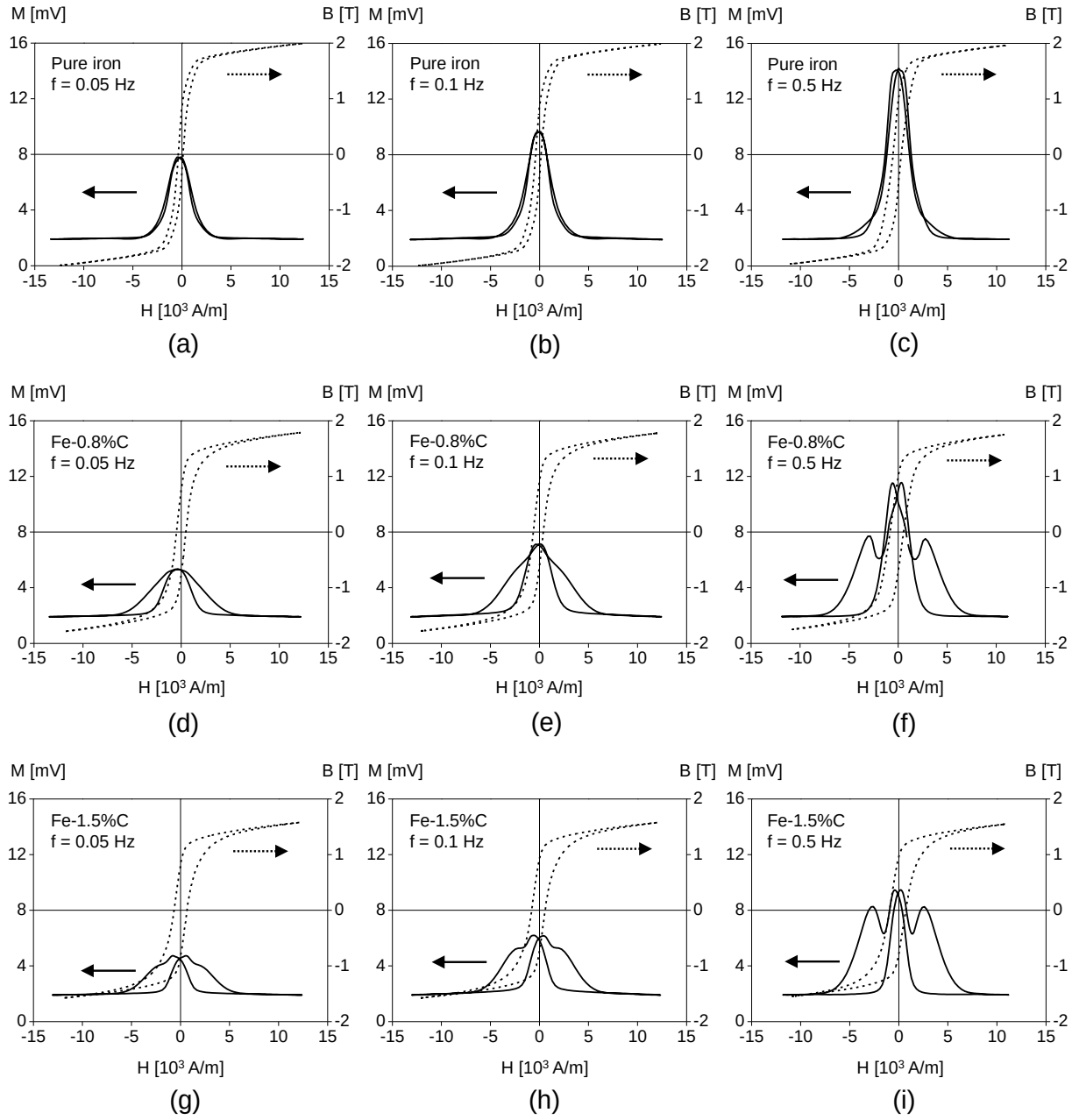

Figure 3. Hysteresis loop (dotted line) and Barkhausen noise (continuous line) curves for different oscillation frequencies of the applied external field recorded at pure Fe (99.99%) (a), (b) and (c) and at two unalloyed steels containing a different content of globular cementite, i.e. Fe-0.8%C (d), (e) and (f) and Fe-1.5%C (g), (h) and (i), respectively. The measurements were performed at 1.8 V and at frequencies of 0.05 Hz, 0.1 Hz and 0.5 Hz.

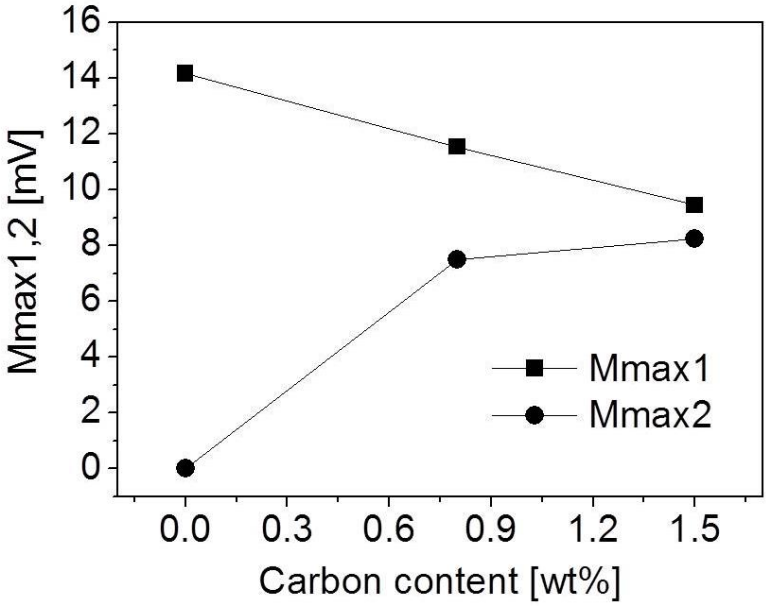

Figure 4. Maximum Barkhausen noise amplitude $M_{max1,2}$ as a function of carbon content for the pure Fe (99.99%), Fe-0.8%C and Fe-1.5%C samples. The measurements were performed at an excitation amplitude of 1.8 V and an excitation frequency of 0.5 Hz.

It is evident that the Barkhausen noise amplitude M_{max} increases with magnetizing frequency f due to the faster transition between magnetic states, i.e., there is an increase of the number of pulses per unit time. Cementite is in a minor relative proportion compared to the ferrite in the unalloyed steel samples. To observe the contribution of the cementite on the MBN signal a minimum excitation frequency of the applied field and/or minimum cementite content are required. This explains the reason why for the sample containing higher amount of carbon (1.5 wt%) the signal of the cementite phase can already be observed at very low magnetizing frequency (0.05 Hz), while for the sample containing less carbon (0.8 wt%) a higher magnetizing frequency is necessary for the observation of the signal of the cementite phase.

The larger Barkhausen noise amplitude M_{max} found for the high purity iron sample at all measured frequencies is attributed to the easy irreversible motion of domain walls (mostly 180° BWs) in the annealed pure iron with its low dislocation density and generally low density of lattice defects. In contrast, within the Fe-0.8%C and Fe-1.5%C samples, the 180° and 90° BWs in the ferrite interact with the cementite precipitates and with the interstitial carbon atoms in the ferrite matrix - as already mentioned above.

It was also reported [24] that the appearance of a second peak can be attributed to a uniaxial compressive stress. In our case, this argument can be excluded, because residual stresses, if still present in the investigated annealed samples, should be rather tensile stresses

which would be built up during solidification due to the higher thermal expansion coefficient of ferrite in comparison to cementite. Another observation that supports the assumption that the stronger field peak $H_{cm,2}$ is a signature of the cementite phase, is provided by the measurement of the temperature dependence on the MBN signal for example in the reactor pressure vessel steel DIN 22 NiMoCr 37 (ASTM A 508 Grade 2) containing globular and rod-shaped cementite. At room temperature, a double peak was observed in the MBN signal. After heating the sample up to the Curie temperature of the cementite (~ 200°C), the stronger field peak $H_{cm,2}$ of the MBN signal disappeared [8].

It is well known that, in addition to the excitation frequency f, the analyzed noise frequency range f_A can strongly influence the amplitude of the Barkhausen noise signal. Altpeter [8] reported that the higher noise signal is obtained at high analyzing frequency, i.e. at f_A = 50 kHz, for a compact cementite sample and at lower analyzing frequency, i.e. f_A = 1 kHz, for an alloyed soft iron (AME1) sample, respectively. In order to obtain the highest noise signal for both phases, ferrite and cementite, all noise signals in this work were analyzed in a frequency range from 0.2 kHz to 50 kHz.

3.2 MFM images of the unalloyed steel samples containing globular cementite embedded in a ferrite matrix

A detailed investigation of the magnetic microstructure while an external magnetic field is applied, allows a better understanding of the correlation of domain wall dynamics and magnetic hysteresis loop and Barkhausen noise profiles. The microscopic observation of easy reversible and irreversible domain wall movements in bulk pure iron [25,26] as well as the observation of pinning of domain walls by cementite precipitates in unalloyed steels [12,27] were previously reported. In this work the basic behavior of the magnetic microstructure with special emphasis to the processes related to the cementite is discussed by taking Fe-1.5%C as an example.

3.2.1 Domain wall dynamics in ferrite

Fig. 5a shows the topography obtained with the MFM of the Fe-1.5%C sample revealing three ferrite grains (numbered (1), (2), and (3)) with different average height and crystalline orientation. The evolution of the magnetic microstructure under influence of a superposed external magnetic field is shown in Fig. 5b-d. Fig. 5b is recorded in the demagnetized state of the sample while Figs. 5c and d display the results with an applied magnetic field of 19000 A/m and -19000 A/m, respectively. The cementite precipitates show

a much stronger magnetic image contrast than the ferrite matrix because cementite is magnetically harder than ferrite and thus causes stronger stray fields.

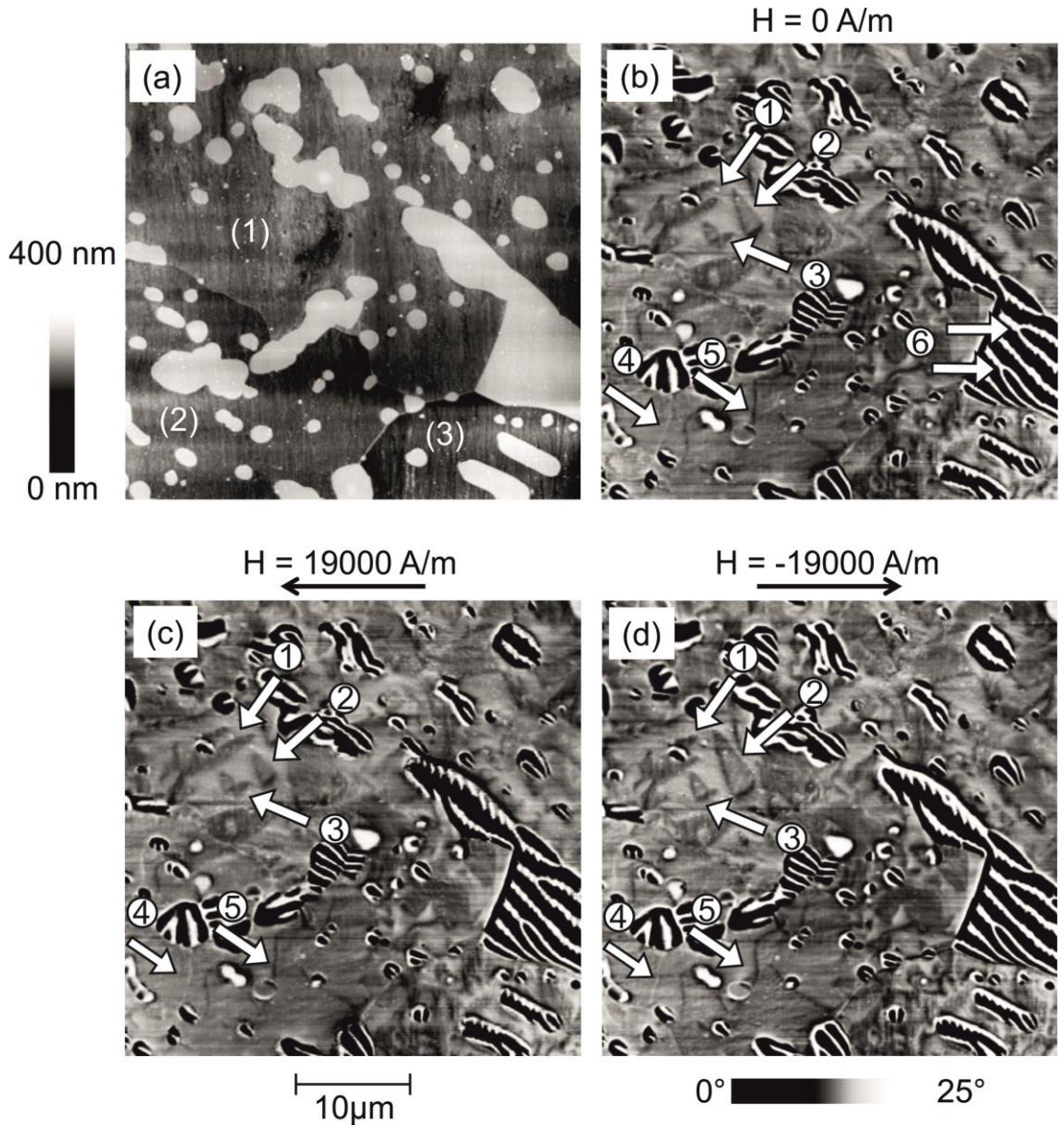

Figure 5. Topography (a) of the sample Fe-1.5%C containing globular cementite precipitates in a ferrite matrix. The gray scale covers a height range of 0 nm (black) to 400 nm (white). (b) MFM images taken without external magnetic field and with an applied field of (c) 19000 A/m and (d) – 19000 A/m, respectively. The direction of the in-plane field is indicated by black arrows. The gray scale of the MFM images covers a relative variation of the phase shift of 0° (black) to 25° (white).

Within the ferrite matrix, bright and dark lines which can be identified as domain walls are visible. In ferrite, the directions of easy magnetization [100] induce two types of walls: 90° and 180° Bloch walls. Curved 180° Bloch walls (arrows #4 and #5) are visible on grain (2). Branch domains [14] (arrow #3) and spike domains [13,28,29] (arrow #1) are

observed in grain (1). Such domains are typically enclosed by 90° walls. They are often bounded by main domains as for example the spike domains (arrow #1), which are bounded by the domains within a cementite precipitate. A supplementary domain [30] (arrow #2) is observed on grain (1). When applying a field of 19000 A/m to the left (Fig. 5c), the supplementary domain (#2) decreases its size, while the spike domain attached to the precipitate (#1) increases its size. The opposite is observed when a field of 19000 A/m is applied to the right (Fig. 5d), i.e. the supplementary domain increases its size at the expense of the area enclosed by the spike domain attached to the precipitate. Additionally, the two-arms branch domain (arrow #3) becomes nearly a single arm and the 180° BWs marked with the white arrows #4 and #5 are moved and bent, respectively, oppositely and into to the direction of the field. The results show that in ferrite both, the 90° and 180° BWs, move at relatively low applied fields while the domain structure in cementite remains unmodified.

3.2.2 Domain wall dynamics in cementite

Fig. 6a shows the topography obtained with the MFM and the corresponding electron backscatter diffraction map (Fig. 6b) taken in the same area with a scanning electron microscope, i.e. the inverse pole figure (IPF), of a section of grain (1) and (2) in Fig. 5. The color code of the inverse pole figure represents the crystallographic orientation in the ferrite matrix (nearly pure b.c.c. iron, lattice constant a = 2.87Å), and in the cementite particles (orthorhombic symmetry, length of the three perpendicular axes a = 5.09Å, b = 6.74Å, c = 4.52Å). The IPF map reveals that some cementite precipitates observed in the topography image (Fig. 6a) are not single crystals, but have a polycrystalline structure with different grain orientations. The cementite precipitate (Figs. 6b and 8) oriented in or around the (010) plane displays a domain structure composed of parallel stripes having opposite phase contrasts. This configuration suggests that the magnetic moments are positioned alternately down- and upwards in relation to the surface and separated by 180° domain walls. It is also observed that the parallel stripes in the magnetic microstructure of the cementite oriented in or around the (010) plane are often branched, i.e. individual domains terminate within the cementite particle (as shown for example in Fig. 5b, arrows #6). The formation of the branched magnetic structure may be explained due to the accumulation of dislocations. In order to analyze the dislocation density in cementite, a thin foil of the Fe-0.8%C sample was examined by transmission electron microscopy (TEM). Using the focused ion beam technique, the thin foil was prepared such that a cementite precipitate was in the field of view of the TEM. The TEM micrograph in Fig. 7 visualizes dislocations in the cementite precipitate some of which seem

to nucleate at the edge of the interface boundary between the cementite and ferrite. It was reported [31,32] that the domain wall configurations can be affected by the presence of dislocations. This occurs mainly because their internal stresses may cause a local deflection of the spins which leads to significant deviations from the saturated configuration.

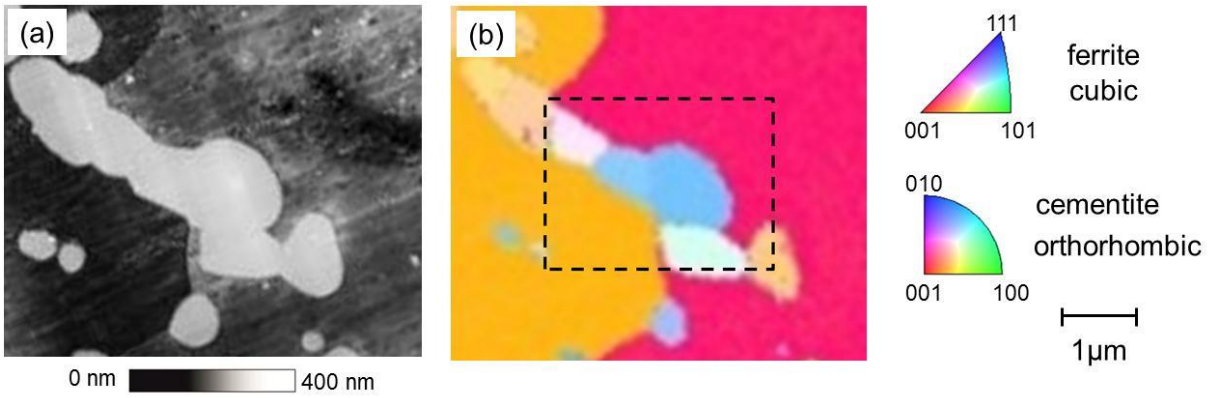

Figure 6. Enlarged section of Fig. 5a showing the topography (a) taken with the MFM. The corresponding IPF map taken in the same area with SEM shows the crystals and their respective orientations. The selected area was further measured by MFM, see Fig. 8.

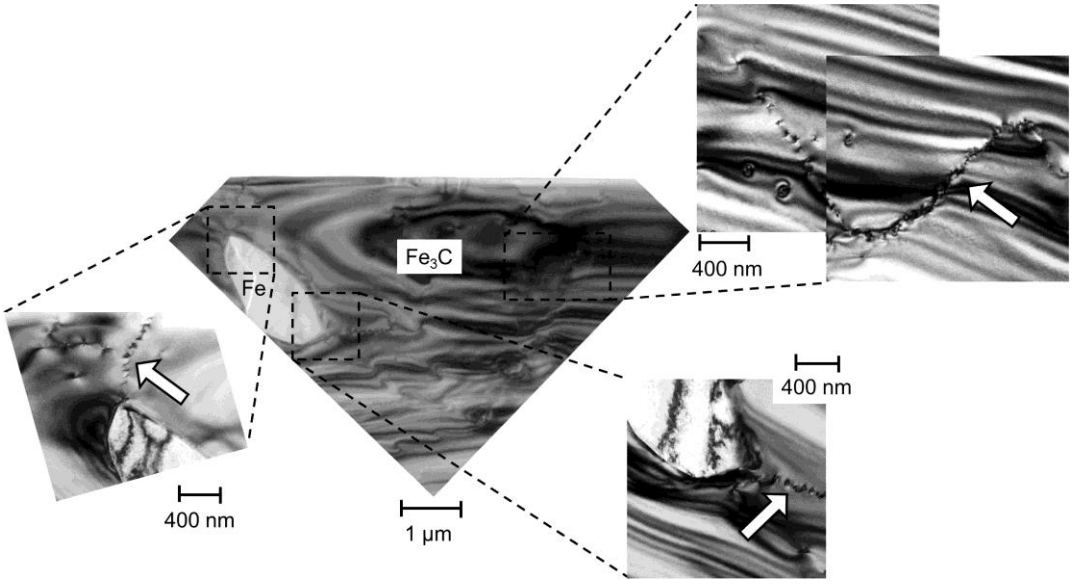

Figure 7. TEM images taken on a thin foil which was obtained from the Fe-0.8%C sample by cutting a cementite precipitate using the Focused Ion Beam (FIB) technique. A ferrite grain (in light gray) surrounded by cementite is visible. The TEM micrographs show a rippled background contrast, which is probably due to the inhomogeneous thin foil thickness. The contrast obtained from the dislocations (see e.g. white arrows) is still clearly visible.

Due to the very high anisotropy of the cementite its magnetic moments are not easily oriented by an applied magnetic field. Therefore, a higher magnetic field must be applied in

order to observe domain wall movement in cementite. A higher field was reached by placing the pole shoes of the external electromagnet which is combined with the MFM (Fig. 2) closer to each other.

A cementite precipitate (selected area, Fig. 6b) oriented close to the (010) plane and therefore having the magnetic moments more or less positioned alternately down- and upwards in relation to the surface was chosen for further investigation using MFM with a strong superposed magnetic field. The evolution of the magnetic microstructure in the selected area (Fig. 6b) is shown in Figs 8. The weaker contrast compared to the MFM images in Figs. 5 is due to an increased lift-height during the MFM scanning process. Fig. 8a is recorded in the demagnetized state while Fig. 8b and c display the results with an applied magnetic field of 22000 A/m and 24000 A/m, respectively. The MFM line scans highlighted by white dotted lines in Fig. 8 and a respective qualitative model describing the interaction between the magnetic tip and the magnetic moments of the cementite are shown in Fig. 9.

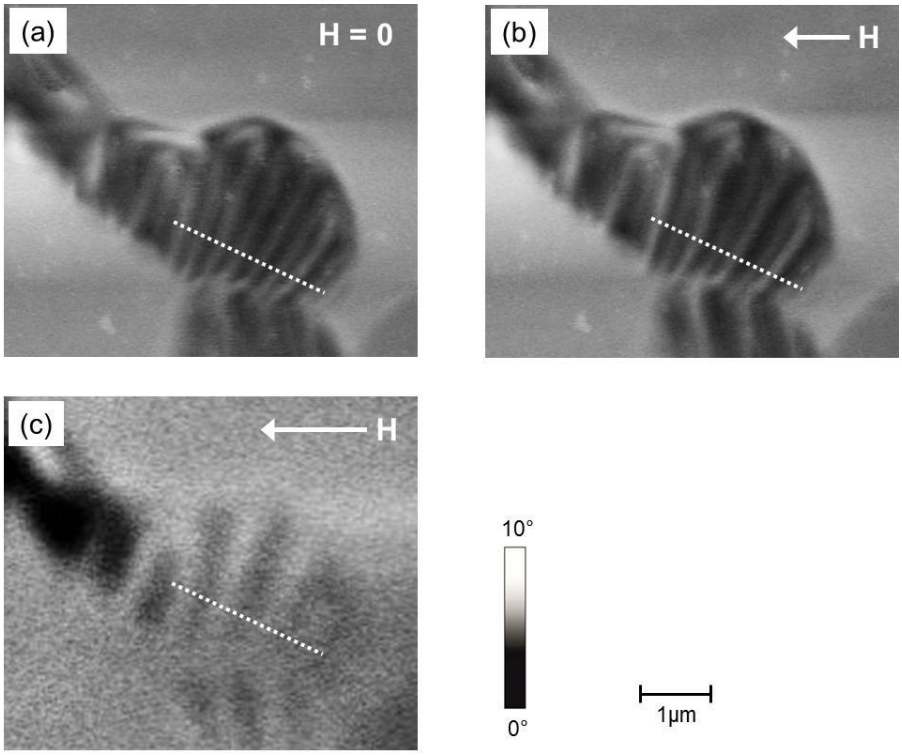

Figure 8. MFM images taken on the cementite precipitate in the selected area of Fig. 7b; (a) without external field; (b) and (c) with external fields of (b) 22000 A/m and (c) 24000 A/m, respectively. The applied field direction is indicated by the white arrows.

Since the MFM tip senses the component of the stray field emerging perpendicularly from the surface, we may conclude that in the demagnetized state the magnetic moments of the precipitate are more or less parallel to the tip axis, i.e. perpendicular to the sample surface

plane (Figs. 8a and 9a). When applying a field of 22000 A/m to the left, the domains become wider because the magnetic moments start to rotate into the direction of the field, i.e. into the surface plane (Figs. 8b and 9b). By increasing the field to 24000 A/m the domains become even wider as shown in Figs. 8c and 9c. At this point, the magnetic moments are already almost aligned to the direction of the field in the surface plane. This results in a very weak image contrast in MFM comparable to that one in the ferrite matrix. In order to prove that when applying an external field the change in the contrast of the MFM images is due to the change in the magnetic state of the cementite precipitates and not due to changes in the magnetic tip, the experiment was repeated using a commercial hard disc sample with high in-plane coercivity (about 135000 A/m). When applying a field of 24000 A/m no change in the magnetic contrast was observed which confirms that there was no modification in the magnetic state of the tip due to the external field.

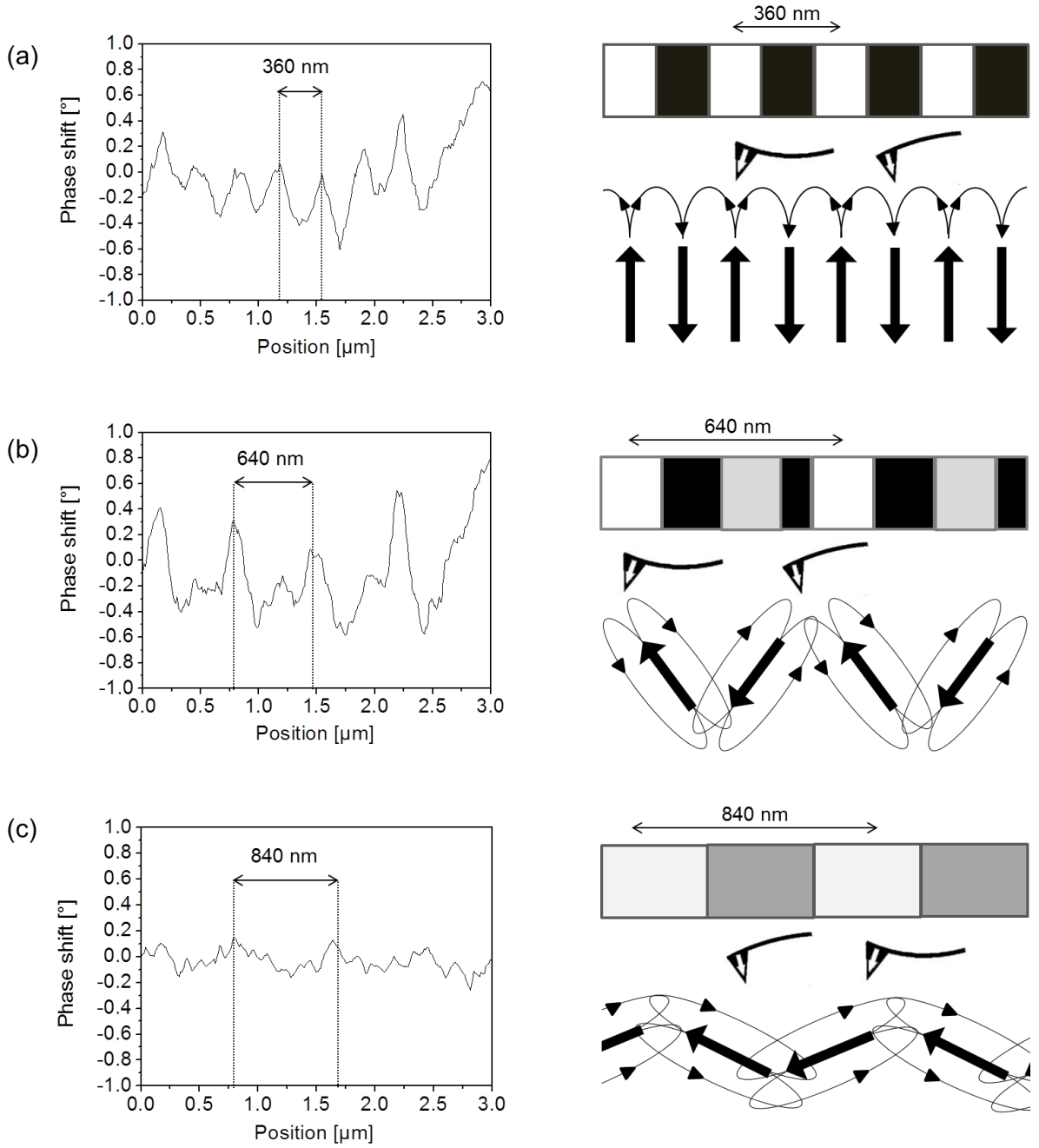

Figure 9. MFM line scans across the cementite precipitate (lines indicated in Fig. 8) together with a schematic model showing the interaction of the magnetic tip with the stray fields of the magnetic moments of the cementite and the respective obtained image contrasts (a) without external field and with external fields of (b) 22000 A/m and (c) 24000 A/m, respectively.

4. SUMMARY AND CONCLUSIONS

The dependence of the amount of carbon in form of globular cementite precipitates in unalloyed steels was macroscopically characterized by measuring hysteresis loops and Barkhausen noise signals. The magnetic hardness increases with the carbon content and the frequency of the applied magnetic field, which is explained by the enhanced pinning effect of

the cementite precipitates and their stress fields, and by increasing eddy current losses at higher frequency, respectively.

For the magnetic Barkhausen noise the choice of the frequency of the applied field plays a crucial role in the detection of the cementite phase and for the nondestructive evaluation of its proportion in the unalloyed steels. With increasing amount of cementite, the Barkhausen noise profile exhibits a second maximum $M_{max,2}$, however the emergence of the second peak becomes clearer with increasing frequency. Cementite is in a minor relative proportion compared to the ferrite phase, therefore a minimum excitation frequency of the applied field and/or a minimum cementite content are necessary to separate the contribution of the cementite in the MBN signal. The ferrite and cementite phases in the Fe-0.8%C and Fe-1.5%C samples were clearly recognized on the Barkhausen noise profiles measured at 0.5 Hz. The weaker field peak $H_{cm,1}$ corresponds to the ferrite and the stronger field peak $H_{cm,2}$ to the cementite phase.

The combination of AFM, MFM, and EBSD techniques enables the direct observation of magnetic micro- and nanostructures including the corresponding single crystal grain orientations. The AFM and MFM techniques were shown to be a powerful tool for topography imaging and magnetic micro- and nanostructure characterization of steels. The crystalline orientation of the cementite phase was determined by EBSD and correlated to the domain structure. Furthermore, using the TEM technique, dislocation structures were observed mostly in the cementite phase and in the interface between ferrite and cementite.

In this work, MFM images with a local resolution of 50 nm reveal that the cementite is ferromagnetic and that its stray fields are generally stronger compared to the ones of ferrite. The cementite has its own domain structure, and in order to reduce its magnetostatic energy, supplementary domains are often observed at the interface between the cementite precipitates and the ferrite matrix.

When an external field of 19000 A/m is applied, the position of the 180° and 90° DWs in the ferrite matrix change, while the domains in the cementite remain unmodified. This means that both, 180° and 90° BWs in ferrite, are moved at relatively low applied field. The 180° domain walls are mainly situated in the center of the grains whereas the 90° domain walls are mainly observed in connection with the closure domains in proximity to the phase and grain boundaries. A change in the domain configuration of the cementite phase is observed only when a higher external magnetic field (22000 A/m) is applied. A larger field is required to move the domain walls in cementite due to its very high anisotropy and high density of defects, e.g. dislocations, which make the cementite magnetically harder than

ferrite. The macroscopic measurements have shown that a field of 11000 A/m is strong enough to saturate all three samples. In our case the macroscopic magnetic measurements were performed with cylindrical samples, while the samples for MFM measurements were small square plates cut from the macroscopic cylinders. The different sample geometries and the fact that the MFM analysis relies on the behavior of surface domains, may explain the fact, that the field which had to be applied to move the domain walls in cementite was larger compared to the field which was necessary the reach saturation in the macroscopic measurements. The microscopic observation that a higher magnetic field is required to magnetize the cementite precipitates compared to ferrite correlates qualitatively with the increase of magnetic hardness with increasing amount of cementite and with the emergence of a second peak $M_{max,2}$ in the Barkhausen noise signal at higher field which corresponds to the cementite phase.

REFERENCES

[1] G. Dobmann, "*State of the art to NDT for characterizing properties in the production of flat steel products*". In: Joint Seminar of the German Iron and Steel Institute (VDEh) and the German Society for NDT (DGZfP) in Düsseldorf to "Material Properties Determination", *Proceedings (in German)* DGZfP Berlin (1999).

[2] G. Bosse, *Grundlagen der Elektrotechnik II – Das magnetische Feld und die elektromagnetische Induktion*; Manheim: Hochschultaschenbücher (1967).

[3] D.C. Jiles, J.B. Thoelke, Theory of ferromagnetic Hysteresis: Determination of Model Parameters from Experimental Hysteresis Loops, *IEEE Transactions on Magnetics* **25** (1989).

[4] H. Czichos, T. Saito, L. Smith (Eds.), *Springer Handbook of Materials Measurement Methods*; Springer, Leipzig, (2006).

[5] VDI/VDE – Richtlinie 2616, Blatt 1, *Härteprüfung an metallischen Werkstoffen*, Düsseldorf: VDI (2012) p. 30-35.

[6] M. Kersten, *Grundlagen einer Theorie der ferromagnetischen Hysterese und der Koerzitivkraft*, S. Hirzel, Leipzig, 1943.

[7] E. Kneller, *Ferromagnetismus*, Springer, Berlin, 1962.

[8] I. Altpeter, *Spannungsmessung und Zementitgehaltsbestimmung in Eisenwerkstoffen mittels dynamischer magnetischer und magnetoelastischer Meßgrößen*, Saarland University, Saarbrücken, 1990. (dissertation).

[9] L. J. Dijkstra and C. Wert, *Physical Rev*iew **79** (1950) 979.

[10] D.W. Kim and D. Kwon, *Journal of Magnetism and Magnetic Materials* **257** (2003) 175.

[11] A. S. Keh, C. A. Johnson, *Journal of Applied Physics* **34** (1963) 2670.

[12] L. Batista, U. Rabe, S. Hirsekorn, "*Magnetic micro- and nanostructures of unalloyed steel: Domain wall interactions with cementite precipitates observed by MFM"*. NDT&E Int (2013), http://dx.doi.org/10.1016/j.ndteint.2013.03.004.

[13] L. Néel, *Cahiers de Physique* **25** (1944) 21.

[14] B. D. Cullity, *Introduction to magnetic materials*, Addison Wesley, London, 1972.

[15] M. Blaow, J.T. Evans, B.A. Shaw, *Acta Materialia* **53**, (2005) 279.

[16] V. Moorthy, S. Vadyanathan, T. Jayakumar, B. Raj, *Journal of Magnetism and Magnetic Materials* **171** (1997) 179.

[17] J.A. Pérez-Benitez, J. Capó-Sánchez, J. Anglada-Rivera, L.R. Padovese, *Journal of Magnetism and Magnetic Materials* **288** (2005) 433.

[18] I. Altpeter, *Journal of Nondestructive Evaluation* **15** (1996) 45.

[19] G. Bertotti, *J. Appl. Phys.* **54** (1983) 5293.

[20] G. Bertotti, *J. Appl. Phys*. **55** (1984) 4339.

[21] D. C. Jiles, *J. Appl. Phys.* **76** (1994) 5849.

[22] D. Goll, *Handbook of Magnetism and Advanced Magnetic Materials*, in: H. Kronmüller, S. Parkin (Eds.), Micromagnetism, Vol 2, Wiley & Sons, New York, 2007, p.1047.

[23] G. Bertotti, in: K.H.J. Buschow, R.W. Cahn, M.C. Flemings, et al., (Eds), Magnetic losses, In Encyclopedia of Materials: Science and Technology, Elsevier, Amsterdam, 2001, p. 4798.

[24] A. Vincent, L. Pasco, M. Morin, X. Kleber, M. Delnondedieu, *Acta Materialia* **53** (2005) 4579.

[25] W. Drechsel, *Zeitschrift für Physik*, **164** (1961) 324–329.

[26] L. Batista, U. Rabe, S. Hirsekorn, "Characterization of the magnetic micro- and nanostructure in unalloyed steels by Magnetic Force Microscopy", *39th Annual Review of Progress in Quantitative Nondestructive Evaluation (QNDE)*, Denver, Colorado, USA, July 16-20, 2012.

[27] S. Wust, *Untersuchung der magnetischen Domänen in Stahlproben mittels Magnetkraftmikroskopie unter Anlegen eines externen Magnetfeldes*, Diploma thesis, Saarland University, IZFP report No.110126-TW, Saarbrücken (2011).

[28] H. J. Williams, *Physical Review* **71** (1947) 646.

[29] H. Träuble, Moderne Probleme der Metallphysik, Bd. 2; Ed. by A. Seeger, Berlin-eidelberg-New York (1966), p. 238-255.

[30] A. Hubert, R. Schäfer, *Magnetic Domains - The Analysis of Magnetic Microstructures*, Springer, Berlin, 1998.

[31] Ö. Özdemir, D.J. Dunlop, *Journal of Geophysical Research* **102** (1997) 20,211.

[32] J. N. Chapmann, *Journal of Physics D: Applied Physics*, **17** (1984) 623-647.

IV. DETERMINATION OF THE EASY AXES OF SMALL FERROMAGNETIC PRECIPITATES IN A BULK MATERIAL BY COMBINED MAGNETIC FORCE MICROSCOPY AND ELECTRON BACKSCATTER DIFFRACTION TECHNIQUES (PUBLICATION C)

L. Batista, U. Rabe, and S. Hirsekorn

Submitted to Ultramicroscopy

ABSTRACT. A method to determine the magnetic easy axes of micro- and nanoscopic ferromagnetic precipitates embedded in a bulk material is proposed and applied to globular cementite (Fe_3C). The method combines magnetic force microscopy (MFM) with electron backscattered diffraction (EBSD) measurements. Magnetic domain structures in globular and in lamellar cementite precipitates embedded in a ferrite matrix in unalloyed pearlitic steels were imaged using MFM. The domain structure of the precipitates was analysed in dependency of their size, shape and crystallographic orientation. It was found that the magnetic moments of the cementite precipitates are highly geared to their crystalline axes. The combined MFM and EBSD studies allow the conclusion that the cementite easy direction of magnetization is the long [010] axis. For fine lamellae cementite the determination of their crystallographic orientations using electron diffraction techniques is very difficult. With the previous knowledge of the behavior of the domain structure in globular cementite, the crystalline orientations of the fine lamellae cementite can be estimated by simply observing the magnetic microstructures and the topographic profiles.

Keywords: Magnetic force microscopy (MFM), Electron backscatter diffraction (EBSD), Magnetic easy axis, Magnetic domains, Precipitate, Microstructure

1. INTRODUCTION

Ferromagnetic materials exhibit intrinsic ‘easy’ and ‘hard’ magnetization directions, i.e., the energy required to magnetize a crystal depends on the direction of the applied field relative to the crystal axes. Magnetic anisotropy is an important property [1] and has therefore been exploited in the design of most magnetic materials of commercial importance, including e.g. grain-oriented electrical steels [2,3] or thin films for ultra-high density magnetic recording [4,5]. On the other hand, the magnetic micro- and nanostructure of the grains or phases of structural materials such as steels are of interest because the magnetic properties can be exploited for non-destructive testing.

The magnetic easy axis is usually found by measuring the magnetic anisotropy of single crystals using techniques like superconducting quantum interference device (SQUID) [6], torsion oscillating magnetometry (TOM) [7], alternating field gradient magnetometry (AFGM) [8], vibrating sample magnetometry (VSM) [9], or ferromagnetic resonance (FMR) [10]. The signal intensity of all these techniques is proportional to the total magnetic moment and hence to the volume of the sample. However, some ferromagnetic compounds, as e.g. Fe_3C, Fe_3Al, γ'-Fe_4N, are encountered as a second phase embedded in a polycrystalline matrix material. Techniques which are sensitive to the whole sample volume are not suitable to determine the magnetic easy axes of such phases separately. On the other hand, such second phases are usually not available as larger single crystal specimens that are pure, void-free, homogeneous, texture-free, and stoichiometric. Therefore techniques are required which provide local magnetic and crystallographic information in bulk materials.

The magneto-optic Kerr effect (MOKE) technique [11,12] is a magnetic domain imaging method in which the contrast is obtained by the interaction between magnetic fields and polarized light. In addition, the MOKE technique provides local magnetization curves, however, its spatial resolution is limited by the wavelength of the used laser (a few hundred nanometers) [13]. A much higher spatial resolution can be achieved using methods based on electron microscopy. Scanning electron microscopy with polarization analysis (SEMPA) can directly detect the sample magnetization component with a spatial resolution of about 20 nm [14]. The major limitation in application of SEMPA is the fact that the measurements must be performed in ultra-high vacuum on a well prepared clean conducting surface. Lorentz electron microscopy (LEM) [15] is based on the deflection of electron beams caused by the Lorentz force in transmission electron microscopy. Using the LEM technique, Keh and Johnson [16] studied the domain structure on cementite thin foils of approximately 200 nm thickness. Even though modern aberration-corrected microscopes achieve spatial resolution in

the order of 1 nm, the transmission electron microscopes are expensive, and the LEM technique is limited to thin foils which are transparent to the electrons. Especially in the case of multiphase materials, differences in the etching rates of the different phases impede smooth thin foil preparation.

In contrast to the techniques discussed above, magnetic force microscopy (MFM) [17,18,19] is suitable for measurements on thick (bulk) samples and can therefore be used to study micro- and nanoscopic embedded magnetic materials in a matrix by measuring simultaneously the topography and the magnetic microstructure with a relatively easy sample preparation. MFM is a scanning probe technique based on sensing the long-range magnetostatic interaction between the sample surface and a microfabricated tip with nm radius of curvature. A lateral resolution of about 10 - 20 nm can be achieved with optimized imaging conditions.

In this paper we examine the magnetic domains of micro- and nanoscopic ferromagnetic precipitates embedded in a bulk material using MFM. Local crystallographic information of the microstructure is provided by the electron backscatter diffraction (EBSD) technique, the recent developments of which allow a spatial resolution of about 10 nm [20]. The correlation between the magnetic and crystallographic microstructure is used to determine the magnetic easy axis of globular cementite precipitates in a ferrite matrix.

2. EXPERIMENTS

Two different unalloyed steels were examined in this study, Fe-0.8%C containing lamellar cementite, and Fe-1.5%C containing globular cementite embedded in a ferrite matrix, respectively. Scanning electron microscopy (SEM) images (Fig. 1) show the microstructure of the samples. Lamellar pearlite composed of alternating plates of ferrite (soft α-Fe) and cementite (hard Fe_3C) is a typical microstructure of Fe-0.8%C (Fig. 1b). Globular cementite precipitates (Fig. 1a) were obtained by heat treating an unalloyed pearlitic Fe-1.5%C sample in vacuum at 720°C during 20 hours and slowly cooling at the rate of 10°C/h in the furnace. The surfaces of all samples were mechanically polished and afterwards vacuum annealed at 600°C for 4h in order to remove residual stresses. Two micro-hardness indents were placed within the center region of the specimens as a reference to ensure that the EBSD and MFM measurements were taken in the same area. Directly before the measurements the specimens were demagnetized and etched using Nital (95% ethanol + 5% nitric acid). The demagnetization process was done by applying alternating fields of slowly decreasing amplitude.

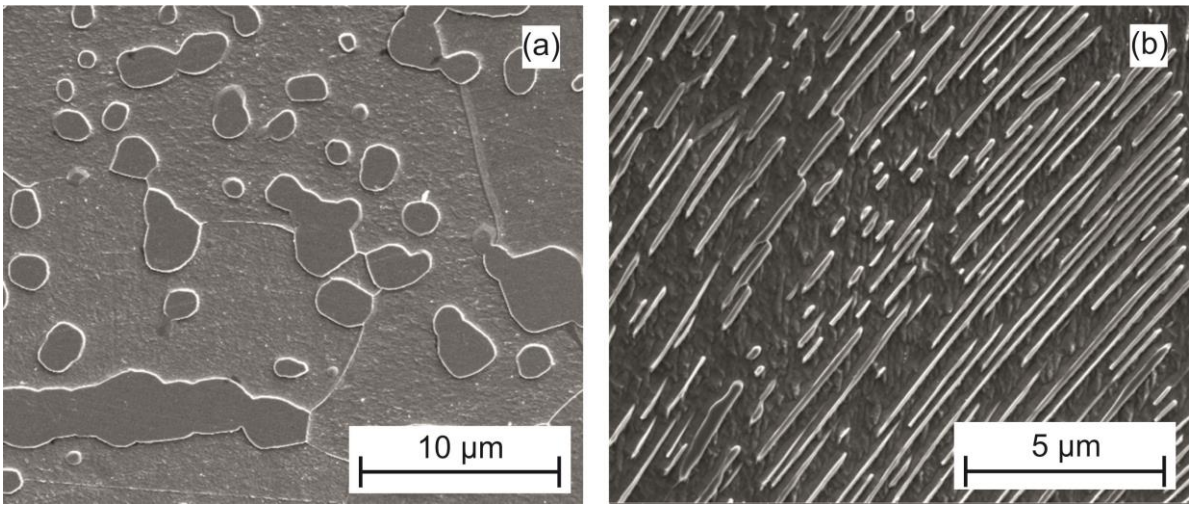

Figure 1. SEM images showing the microstructure of the investigated unalloyed pearlitic steel samples: (a) Fe-1.5%C with globular cementite and (b) Fe-0.8%C with lamellar cementite.

Electron backscatter diffraction maps were obtained on a JEOL JSM-7000F scanning electron microscope (Jeol Ltd., Tokyo, Japan) equipped with an EDAX Trident EBSD analysis system (EDAX Inc., Mahwah, USA). An acceleration voltage of 15 kV and an emission current of around 100 mA were used for all scans. Data was recorded and analyzed using the EDAX/TSL OIM software package [20]. The step size was between 20 and 100 nm for all EBSD maps reported here.

Magnetic force microscopy measurements were performed under ambient conditions using a commercial MFM instrument (Nanoscope III® multimode, Bruker AXS Inc. (formerly Digital Instruments / Veeco), Madison, WI, USA). The topographic and magnetic images were obtained using the two-pass (Tapping/lift® mode) technique. Within the first pass the surface profile is recorded in the intermittent contact mode (Tapping mode) [21]. Magnetic forces are mapped in the second pass whereas the magnetic sensor tip scans the previously measured topographic profile at an adjusted distance (lift-height) in the range of 10 nm to 100 nm above the surface. The cantilever is excited to forced vibration at a frequency close to its first flexural resonance. The gradient of the magnetic tip-sample interaction forces shifts the resonance frequency of the cantilever. As this frequency shift is usually small compared to the half-width of the resonance, the magnetic image is obtained by measuring the phase shift at the frequency of excitation as a function of position.

3. RESULTS AND DISCUSSION

3.1 Choice of a suitable MFM probe and general observations

It is well known that the contrast of MFM images depends on the imaging parameters and on the choice of the sensor tip, because the local tip-sample interaction forces are a result of the magnetic fields and moments of the tip and the sample [19]. During MFM imaging, the tip stray field may cause reversible and irreversible changes in the local magnetic state of the sample and vice-versa [22,23,24]. Therefore, it is very important to choose the appropriate kind of magnetic probe for each particular experiment.

Table 1. Data of the tested MFM probes [25] (Bruker AXS Inc., Madison, WI, USA).

Probe	R_c (nm)	M (emu)	H_c (A/cm)
MESP-LM	25-35	3×10^{-14}	< 318.4
MESP	35-50	1×10^{-13}	~ 318.4
MESP-HM	80-100	$> 3 \times 10^{-13}$	~ 318.4

The data of the three different types of commercial CoCr coated magnetic probes which were tested are shown in table 1, and MFM images taken with these sensors at the same region of the Fe-1.5%C steel sample with globular cementite are shown in Figs. 2a-f. The magnetic probes consist of micro-fabricated silicon cantilevers of the dimensions 225 µm × 28 µm × 2.75 µm (length × width × thickness). Both sides of the cantilever and the sensor tip are coated with CoCr layers. The radius R_c of the sensor tip, the magnetic moment M of the tip, and the coercivity H_c depend on the coating thickness. The measurements were performed maintaining the same lift height of 70 nm and the cantilever oscillation amplitude was kept between 30 and 32 nm. The probe tips were magnetized downwards along their axes and perpendicular to the sample surface.

In the topography images in Fig. 2a-c the cementite precipitates are visible as white islands, because they are several 100 nm higher than the ferrite matrix after the etching with Nital mentioned above. As can be seen by comparing the magnetic images in Figs. 2d-f, the local variation in phase shift, i.e. the magnetic contrast, is higher within the cementite precipitates than within the ferrite matrix. This general trend is independent of the choice of the magnetic probe [26]. However, using the probe with the low magnetic moment (MESP-LM), hardly any substructures are detected within the precipitates and especially in the ferrite matrix (Fig. 2d). The strongest magnetic contrast is obtained with the probe with the highest magnetic moment (MESP-HM) (Fig. 2f), but a lower spatial resolution is achieved.

Furthermore a crosstalk between the magnetic image and the topography image is visible, i.e. a spurious magnetic contrast appears in the intermittent contact-mode topography image (Fig. 2c). In addition, an irreversible change in the magnetic microstructure of the ferrite matrix was observed. The probe with the intermediate moment (MESP) (Fig. 2b and e) can clearly image the magnetic microstructure of both, ferrite and cementite phases, and the topography image is free of crosstalk with the magnetic image. Therefore, MESP probes were used for all further MFM images reported here.

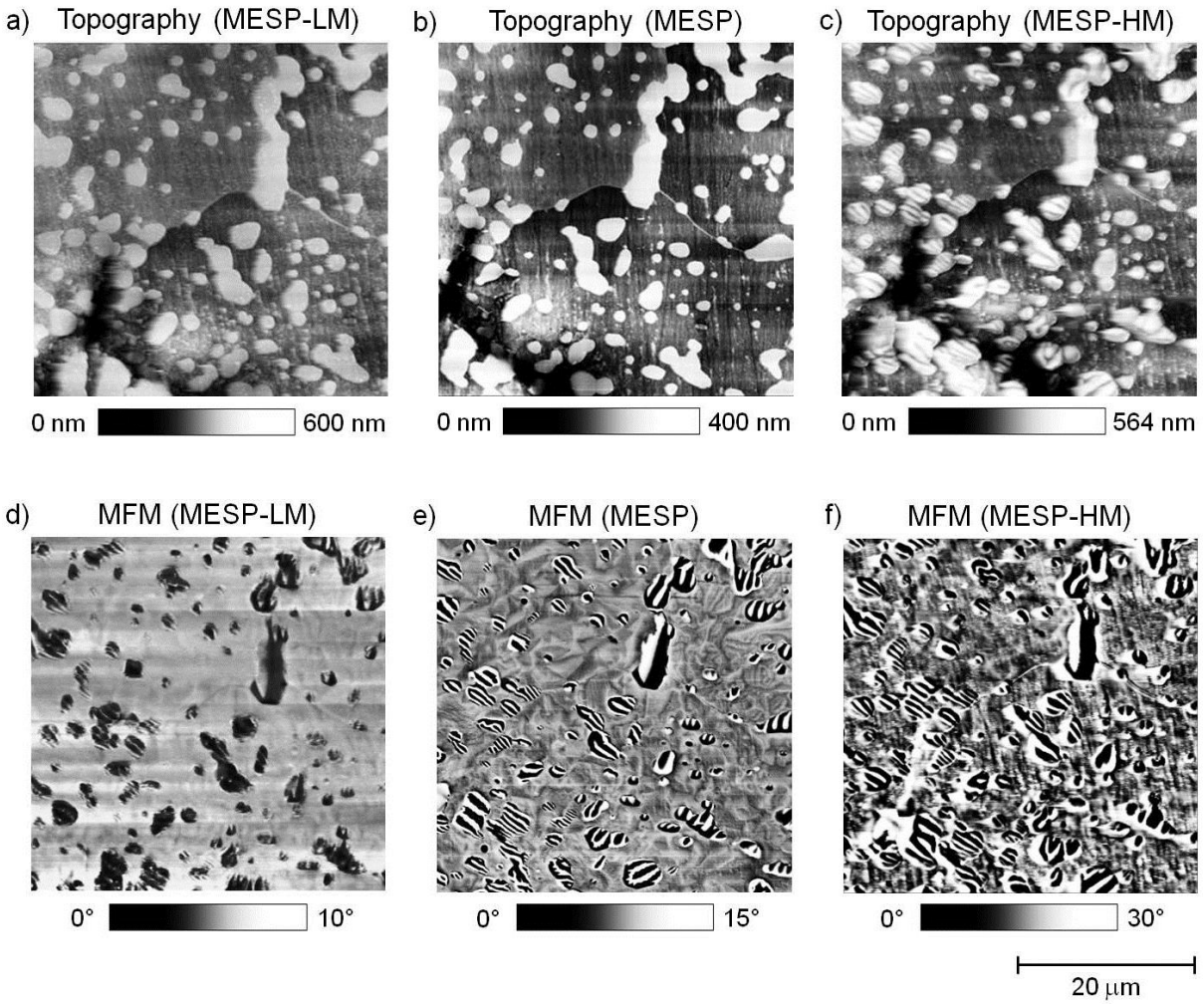

Figure 2. Topography (a-c) and MFM (d-f) images taken at almost the same area of the Fe-1.5%C sample with globular cementite using the co$\mu\mu$ercial MFM probes listed in Table 1: (a,d) tip with low moment, MESP-LM, (b,e) tip with intermediate moment, MESP, and (c,f) tip with high moment, MESP-HM [26].

An inverse pole figure (IPF) map taken with the EBSD of the same surface region as imaged in Fig. 2 is shown in Fig. 3a. The color codes of the IPF represent the crystallographic orientation in the ferrite matrix (nearly pure b.c.c. iron, lattice constant a = 2.87Å) and in the

cementite precipitates (orthorhombic symmetry, length of the three perpendicular axes a = 5.09Å, b = 6.74Å, c = 4.52Å). The orientation imaging (OIM) software of the EBSD instrument provides quantitative values of the misorientation angle of each area relative to the surface, and it is possible to map the ferrite and the cementite phases as shown in Fig. 3b. In spite of a slight drift in the MFM images, it is possible to correlate the MFM and EBSD data of each individual particle or area by comparing the images in Figs. 2 and 3.

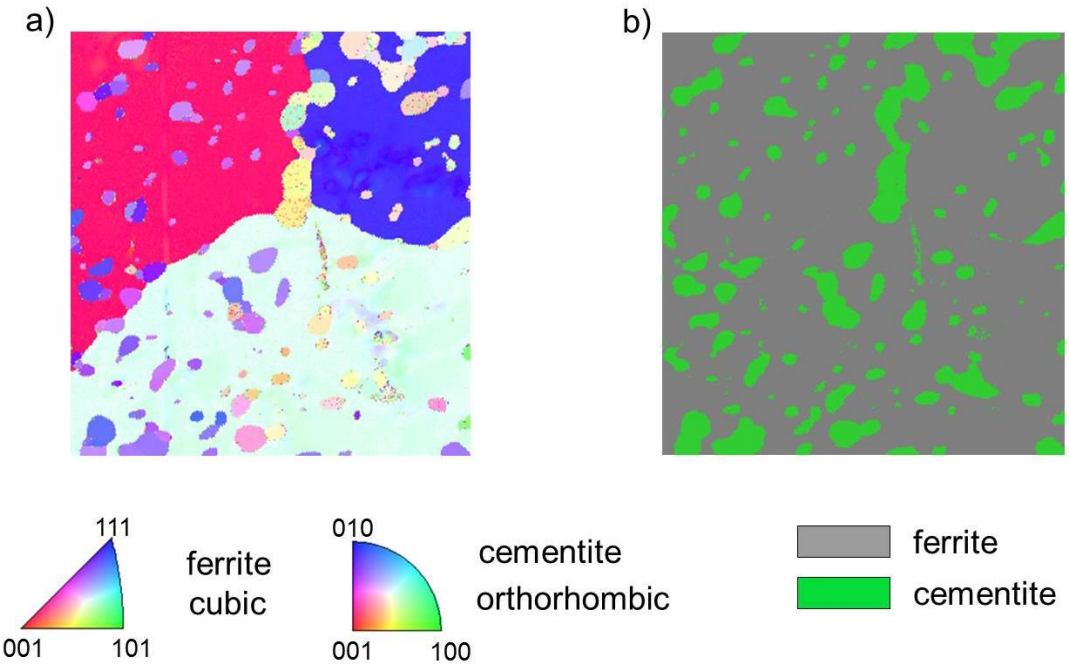

Figure 3. EBSD maps of the Fe-1.5%C sample with globular cementite: (a) inverse pole figure (IPF) map, displaying the crystal orientations and (b) phase distribution map displaying ferrite (gray) and cementite (green) phases.

In the particular area shown here, three different ferrite grains of different orientation are present. The angles of inclination of the three ferrite grains relative to the (100) plane are 9°(red), 33.7° (light blue), and 49.7°(dark blue), in this case.

Fig. 4 shows the orthorhombic crystalline structure of the cementite as visualized with the diamond software [27]. The cementite unit cell is formed by sixteen atoms (12 Fe atoms and 4 C atoms). The Fe atoms are distributed between two distinct lattice sites: the special FeI sites (Wyckoff position 4c) and general FeII sites (Wyckoff position 8d) [28]. Here, the longer axis is the [010]- or b-axis while the shorter one is the [001]- or c-axis. The crystalline planes are colored in accordance to the stereographic triangle for the cementite in the IPF maps.

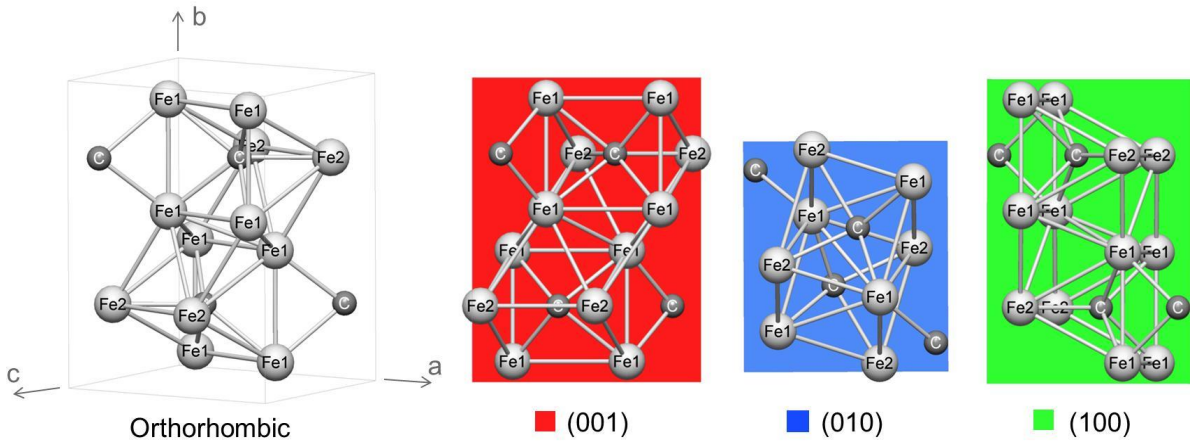

Figure 4. Cementite crystalline structure showing the crystalline planes and directions. The colors of the different planes correspond to the crystallographic orientations displayed in the stereographic triangle for the cementite phase in the EBSD measurements.

The size of the cementite precipitates in fig. 3 ranges from 300 nm to a few μm. It becomes furthermore clear that some of the precipitates which appear to be one particle because of their uniform white color in the MFM topography image, are in fact polycrystals.

3.2 Magnetic domain structure of globular cementite precipitates

Each of the cementite precipitates has its own domain structure, but as will be shown, the domain structure depends on the size of the precipitates and on their crystalline orientation. As already mentioned in the previous chapter, the observed magnetic contrast is generally stronger within the cementite precipites than within the ferrite matrix. The MFM phase shift is mainly proportional to the magnetic force gradient in vertical direction, i.e. normal to the sample surface. The domains show therefore a strong bright and dark contrast in cases where strong stray field with orientation normal to the surface are present (Fig. 5a). For a sample surface in which the magnetic moments lie parallel to the surface plane (Fig. 5b) and perpendicular to the tip axes, mainly the stray field of the domain walls is detected. The individual domains have a weaker contrast. This kind of weaker contrast predominates on the ferrite matrix. The details of the domain contrast and the domain wall movements in ferrite were discussed in a previous publication [29,30].

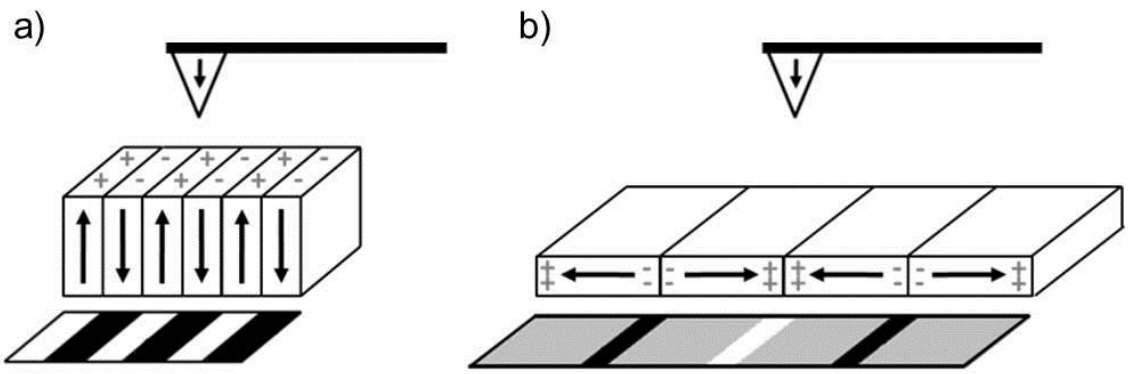

Figure 5. Image contrast formation in the MFM: (a) magnetic moment oriented perpendicular to the sample surface and parallel to the tip axes; (b) magnetic moment oriented parallel to the sample surface and perpendicular to the tip axes.

Fig. 6a shows the topography image of another area of the Fe-1.5%C sample revealing again the cementite precipitates as bright areas which are about 320 nm at maximum higher than the ferrite matrix. In addition, three ferrite grains with different average height (numbered (1), (2), and (3)) are visible. The corresponding magnetic microstructure in the demagnetized state is shown in Fig. 6b. Note that the small grain (2, white arrow) has about the same size as the cementite precipitates, but the magnetic contrast in Fig. 6b demonstrates that it is a ferrite grain with a similar magnetic microstructure as grain (3). The IPF map taken in the same area is shown in Fig. 6c. The angles of inclination of the three ferrite grains (1), (2), and (3) relative to the (100) plane were obtained as 40°, 7°, and 9°, respectively. The grains (2) and (3) have almost the same crystalline orientation relative to the sample surface and consequently almost the same color in the IPF map.

Even though some of the cementite precipitates which are visible in Figs. 6 are polycrystals, they are mainly oriented in or around the (010) plane (Fig. 6c). The domain structure of most of the precipitates (Fig. 6b) consists of parallel stripes with strong opposite magnetic contrast, and no closure domains are observed. Since the MFM tip senses the component of the stray field emerging perpendicularly from the surface, we may conclude that the magnetic moments of these precipitates are positioned alternately down- and upwards relative to the surface and are separated by 180° domain walls as indicated schematically in Fig. 5a. The width of the observed striped domains ranges from some tens of nanometers up to 800 nm depending on the orientation of the cementite particle relative to the sample surface.

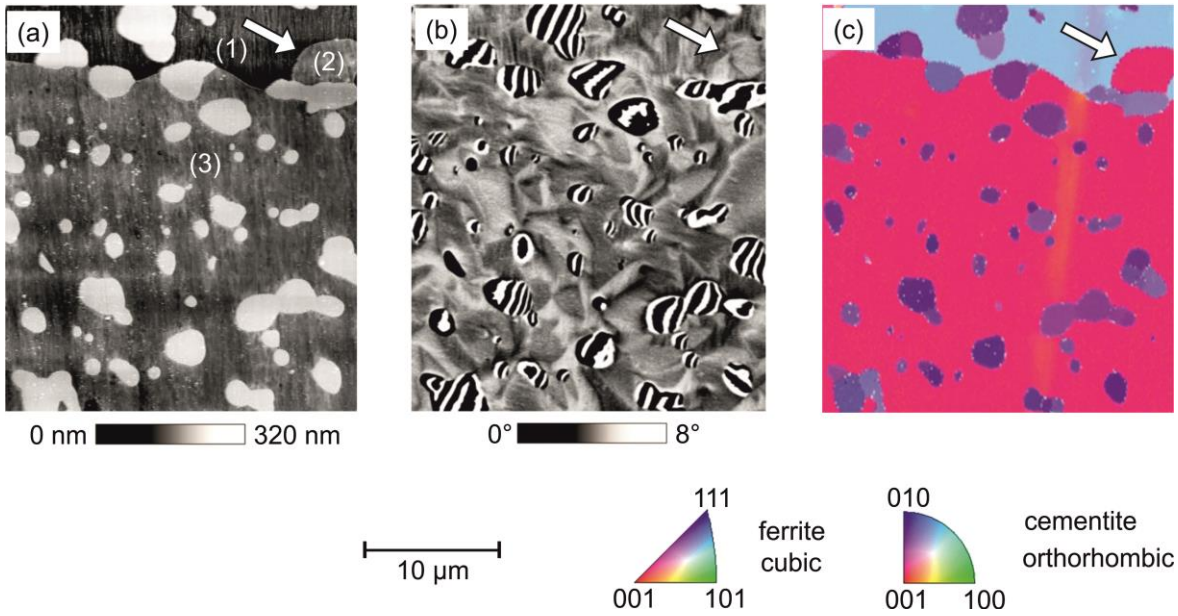

Figure 6. Topography (a) and MFM image (b) of the Fe-1.5%C sample with globular cementite taken with MFM. The corresponding IPF map (c) recorded in the SEM shows the crystals and their respective orientations. Three ferrite grains of different crystal orientation are marked by (1), (2), and (3).

Cementite is known to be a relatively hard magnetic material with high single crystal anisotropy constants ($K_1 = 118 \cdot 10^3$ Jm^{-3} and $K_2 = 394 \cdot 10^3$ Jm^{-3}) [31]. Since the contribution of the shape and stress anisotropies are reduced due to the globular form of the precipitates and the thermal annealing treatment performed on the samples, respectively, it is reasonable to assume that the crystal anisotropy is predominant, i.e. that the magnetic moments of the cementite in its demagnetized state are oriented along the easy axis of magnetization. In some cementite precipitates a complex branched magnetic structure is observed which can be explained by a high density of dislocations and thus a high density of stress fields which interact with the domain walls.

Fig. 7a-c show the topography, the magnetic microstructure and the IPF map of another region of the Fe-1.5%C sample. This surface section is a different area of the ferrite grain numbered (3) in Fig. 6 with only 9° misorientation relative to the (100) plane. In this area, single crystal cementite precipitates having a large misorientation with respect to the (010) plane, namely 82.5°, 85.6°, 78.8° and 78°, are present. These precipitates are labeled as (1), (2), (3) and (4) (Fig. 7c), they are oriented close to the (100) plane. The MFM phase shift measured in these particles is positive or negative over the entire precipitate surface (Fig. 7b and c, white arrows). However, the contrast is weaker, i.e. the phase shift is smaller in comparison to the bright or dark contrasts obtained in the precipitates which show a stripe

structure. The contrast of the MFM as explained in Fig. 5 leads to the conclusion that the magnetic moments of these precipitates are not perpendicular, but have a small angle (α) with respect to the sample surface.

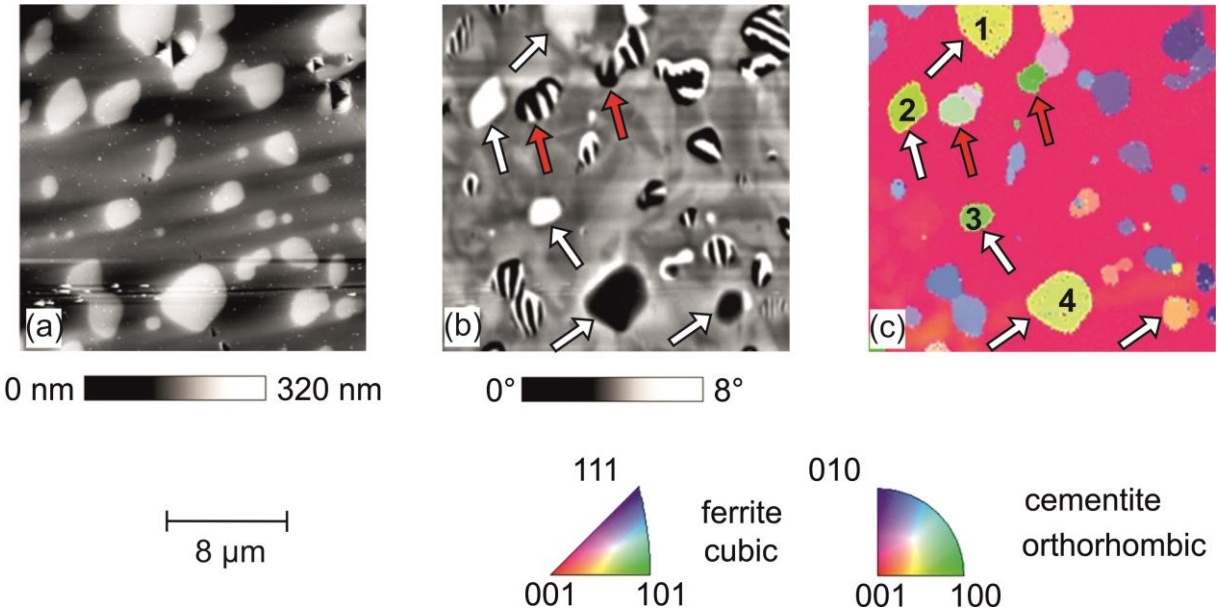

Figure 7. Topography (a) and MFM image (b) of the Fe-1.5%C sample with globular cementite taken with MFM. The corresponding IPF map (c) recorded in the SEM shows the crystals and their respective orientations.

It should be mentioned in addition that in the case for the precipitates which are not single crystals the domain structure may extend continuously from one grain to its neighbors (Fig. 7b and c, red arrows), which makes the analysis of the domain structure in such polycrystalline precipitates in correlation with their crystalline orientation more difficult.

A still different domain structure of globular cementite was detected in the area shown in Figs. 8a-c, which again show topography (Fig. 8a), magnetic image (Fig. 8b) and IPF map (Fig. 8c). The imaged area is located in one ferrite grain the surface of which is only inclined 3° with respect to the (101) plane. Contrary to cementite precipitates oriented in or close to the (010) plane in which a stripe structure was found, and contrary to precipitates which are oriented close to the (100) plane in which a weak dark or bright contrast were also observed, the cementite precipitates with orientation in or very close to the (001) plane, (indicated by white arrows in Fig. 8b), show a very weak and homogeneous magnetic contrast. Bright and dark areas with strong MFM contrast are visible along the edges of these precipitates. Such a magnetic contrast is indicating domains which are oriented in-plane with the sample surface. According to the IPF map (Fig. 8c) the large precipitate with orientation in or very close to the (001) plane is not a single crystal, but has a polycrystalline structure composed of four

grains with similar orientations. However the whole precipitate is misoriented less than 5°, and thus the magnetic contrast in all of its grains is similar. The orientation imaging software revealed that the long [010]- or b-axis of such cementite precipitates with low magnetic contrast lies in the surface plane and along the direction of the bright and dark edges (Fig. 8c) while their short [001]- or c-axis is oriented perpendicularly to the sample surface.

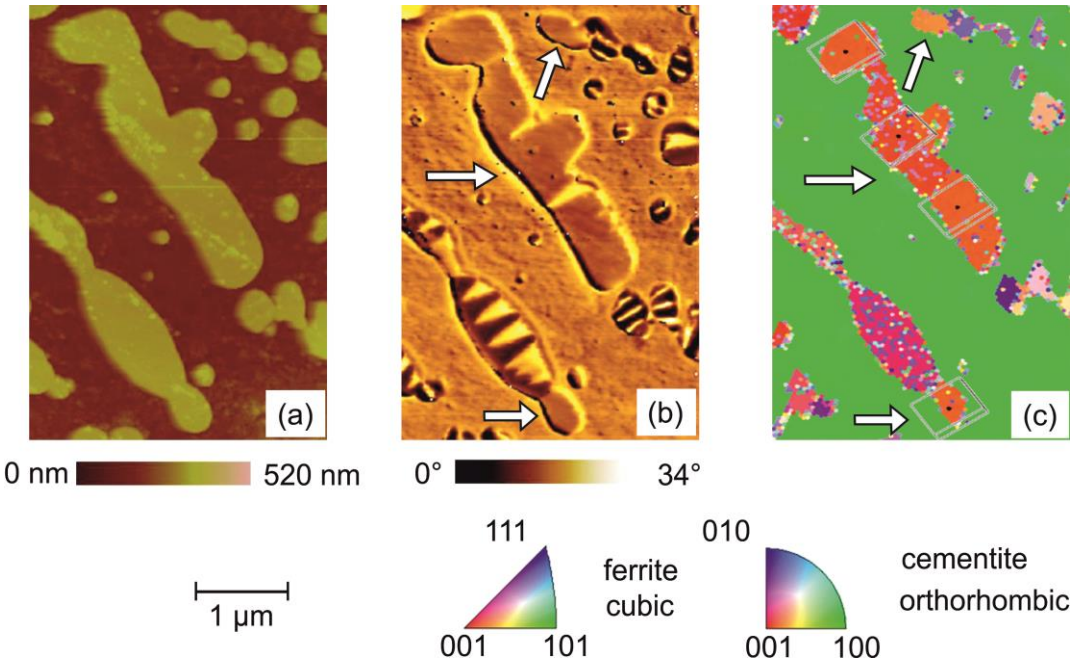

Figure 8. Topography (a) and MFM image (b) of the Fe-1.5%C sample with globular cementite taken with MFM. The corresponding IPF map (c) recorded in the SEM shows the crystals and their respective orientations. The long axes (here b-axes) of the orthorhombic cementite crystals indicated by the arrows are in the surface plane.

3.3 Domain structure in globular cementite in dependence of the size of the precipitates

As discussed in section 3.2, the domain structure in cementite precipitates is strongly correlated to their crystallographic axes. Furthermore, the influence of the size of the globular precipitates on the domain structure was investigated. The size (surface area in μm^2) of the precipitates was calculated directly from the topography images using the image processing software a4i Analysis (aquinto AG; Berlin-Landshut-Chicago) [32]. The domain structures, i.e. number of domains, were analyzed with the help of the NanoScope Analysis® software (Bruker AXS Inc., Madison, WI, USA). Figure 9 shows the number of domains as a function of the surface area of 177 randomly selected precipitates.

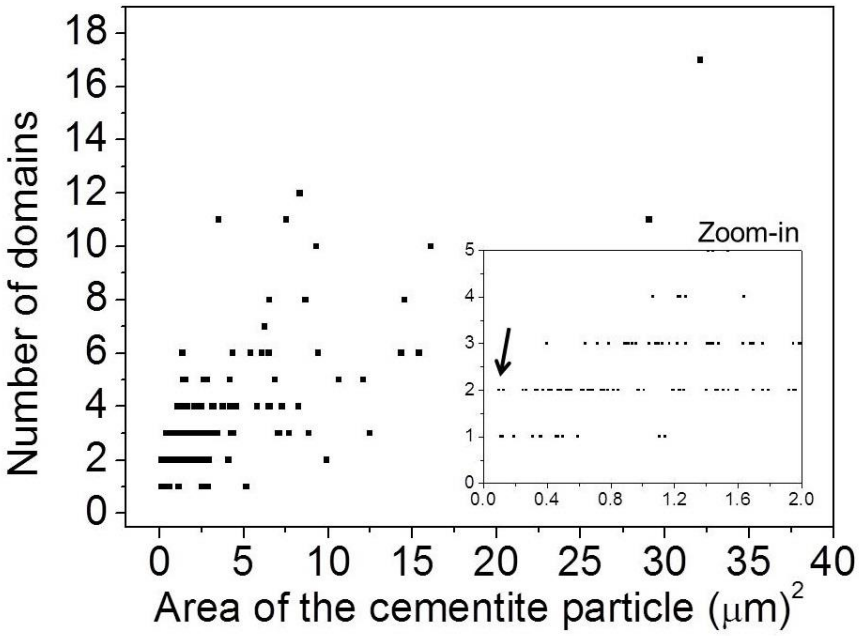

Figure 9. Plot of the number of domains as a function of the surface area of the cementite precipitates.

A clear trend can be realized: the larger the area, the higher is the number of domains. Very small precipitates (up to 5 μm^2) usually contain not more than 6 domains. Very large precipitates (> 20 μm^2), however, may contain more than 10 domains. Some large precipitates are not single crystals, but have a polycrystalline structure with different grain orientations. The software a4i analysis calculates the surface area of the whole precipitate without considering the individual grains separately. As the domain structure of such large precipitates often extends continuously from one grain to its neighbors, it is reasonable to treat a precipitate as one unit.

In the samples studied in this work, single-domains were observed in some spherical cementite precipitates. The single-domain state is energetically favored as long as the stray field energy is smaller than the wall energy needed for multi-domain formation. *Kronmüller and Fähnle* [33] estimated the critical size of a sphere of magnetic material for forming a single-domain state by

$$D_{crit}^{do} \approx \left(72\sqrt{AK_1}\right)/\mu_0 M_s^2, \qquad (1)$$

μ_0 [H/m] is the permeability of vacuum, M_s [A/m] is the saturation magnetization, A [J/m] is the exchange constant, and K_1 [J.m^{-3}] is the single crystal anisotropy. The material parameters of cementite from the literature, M_s = 9.8 x 10^5 A/m [34], K_1 = 1.18 x 10^5 J.m^{-3} [31] and A = 8.7 x 10^{-12} J/m [35], yield the critical diameter for single-domain state forming

D_{crit}^{do} = 60 nm. The size distribution and shape of the cementite precipitates depends mostly on the composition and the thermal treatment of the sample. As shown in the inset (zoom-in plot, black arrow) in Fig. 9, the smallest detected and analyzed precipitates have an area of 0.1 μm^2. They are composed of one or two domains. Assuming a spherical shape, their diameters are about 356.8 nm. These results confirm that, in agreement with theoretical predictions, even smaller precipitates must be considered in order to reach the critical diameter for single-domain state in cementite.

3.4 Determination of the easy axis in globular cementite

In order to determine the easy axis of cementite, forty cementite precipitates with similar size (~ 3 μm) and globular shape essentially containing parallel domains were analyzed with respect to their crystalline orientation. The averaged width of the striped domains was measured with the help of the NanoScope Analysis® software (Bruker AXS Inc., Madison, WI, USA). Fig. 10a shows in detail the domain structure of a cementite precipitate oriented close to the (010) plane. An MFM line scan across the domain structure (line indicated in Fig. 10a) is shown in Fig. 10b. The line scans clearly show the positive and negative phase shifts in the bright and dark imaged domains, respectively. The average width of the domains can be measured by evaluating sets of such line scans in selected areas.

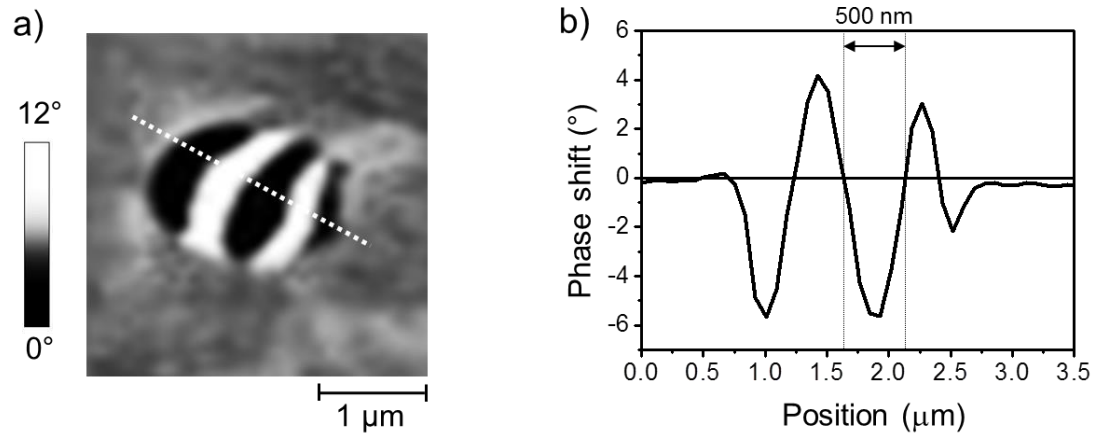

Figure 10. Enlarged section of Fig. 2e showing the domain structure of a cementite precipitate in the Fe-1.5%C sample; (b) line scan across the domain structure, line indicated in (a). The measured domain thickness in the indicated line scan is 500 nm.

Figure 11a shows a plot of the domain width versus the angle (α) between the [010] direction and the normal to the sample surface. In agreement with the results obtained by Keh and Johnson [16] using transmission electron microscopy studies on cementite thin foils of approximately 200 nm thickness, the domain width measured with the MFM shows a clear

dependence on the cementite crystalline orientation, i.e. the measured domain width increases with increasing inclination angle (α). This relation can be demonstrated by a schematic representation (Fig. 11b and c) of the magnetic moments with their respective stray fields. The measured domain width is smallest when the magnetic moments are oriented along the [010] direction and normal to the sample surface and increases as the [010] direction deviates by an angle (α) from the sample surface normal. This confirms that the magnetic moments of the cementite precipitates are oriented along the the long [010]- or b-axis.

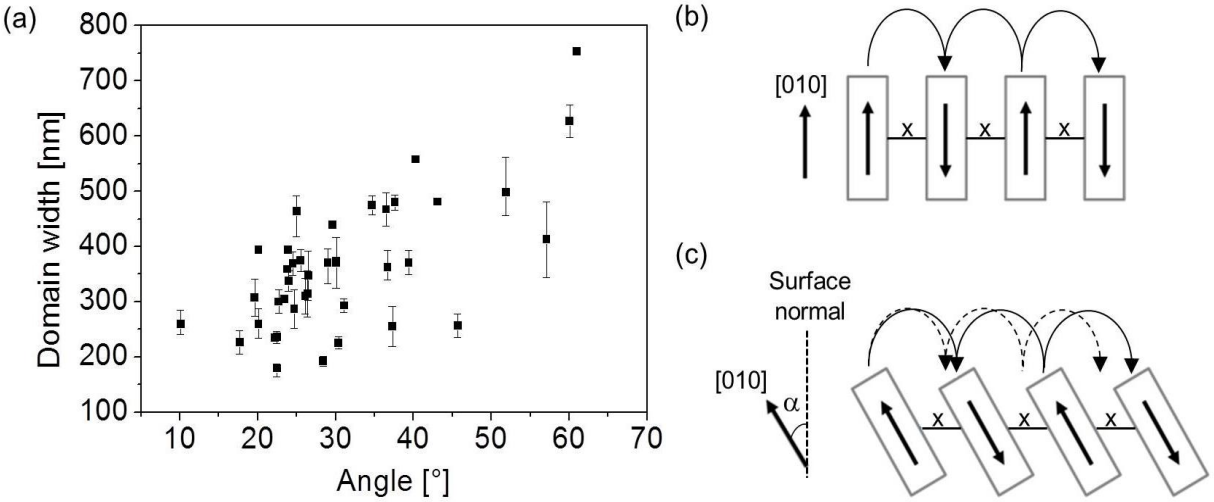

Figure 11. (a) Domain width as function of the angle between the surface normal and the [010] easy direction of cementite; (b) Schematic representation of the magnetic moments with their respective stray fields for a perfect orientation along the easy [010] direction (α = 0° to the surface normal) and (c) with an angle inclined (α > 0°). The error bars represent the arithmetic mean, minimum and maximum values of the measured domain widths for each cementite precipitate.

We can conclude that the [010] axis is the easy direction if we recall that cementite is hard magnetic material and that the crystal anisotropy is predominant, i.e. that the magnetic moments of the cementite in its demagnetized state are oriented along the easy axis of magnetization.

The observation that the easy axis of cementite is the long axis agrees with calculations [36] and experimental results obtained in thin foil samples [16] and in nanowires [37].

3.5 MFM images of lamellar pearlite

Figures 12a and b show the topography of the Fe-0.8%C sample containing lamellar pearlite and the corresponding magnetic microstructure in the demagnetized state, respectively. For lamellar cementite the determination of the crystalline orientations using electron diffraction techniques is very difficult because of its low structure factors [38,39]. Figures 13a and b show the phase distribution and the IPF map in one region of the Fe-0.8%C sample. The identification of the phases, ferrite and cementite, is possible as shown in the phase distribution map in Fig. 13a. However, the quality of the EBSD patterns (even by spot EBSD analysis) was insufficient to obtain accurate orientation of the lamellae cementite crystals (Fig. 13b).

The magnetic domain structures of the lamellar precipitates have similar features to those observed in the globular precipitates. Some lamellar cementite precipitates (Fig. 12b, arrow #1) exhibit parallel stripes with strong opposite magnetic contrasts which allows the conclusion that the magnetic moments of these precipitates are positioned alternately down- and upwards relative to the surface, and are therefore oriented in or close to the (010) plane. Other lamellar precipitates (Fig. 12b) show either a relatively strong dark and/or bright (arrow #2) or a very weak homogeneous magnetic contrast (arrow #3). For the relatively strong dark and/or bright magnetic contrast the domains are wide and their magnetic moments are inclined by an angle (α) with respect to the surface (see Fig. 11c). For the very weak and homogeneous magnetic contrast the magnetic moments are in-plane oriented. The lamellar cementite precipitates which show parallel stripes with strong opposite magnetic contrast, and therefore, oriented in or close to the (010) plane, exhibit higher topographic profiles (Fig. 12a) compared to the lamellae with other crystalline orientations. This observation can be explained by the fact that the grinding rate (material removal) during the polishing process of the surface depends on the material properties which vary not only with the kind of material, but also with its crystalline orientation. The investigations, therefore, reveal a distinct correlation of the magnetic domain structure as well as of the surface topography to the crystalline orientation.

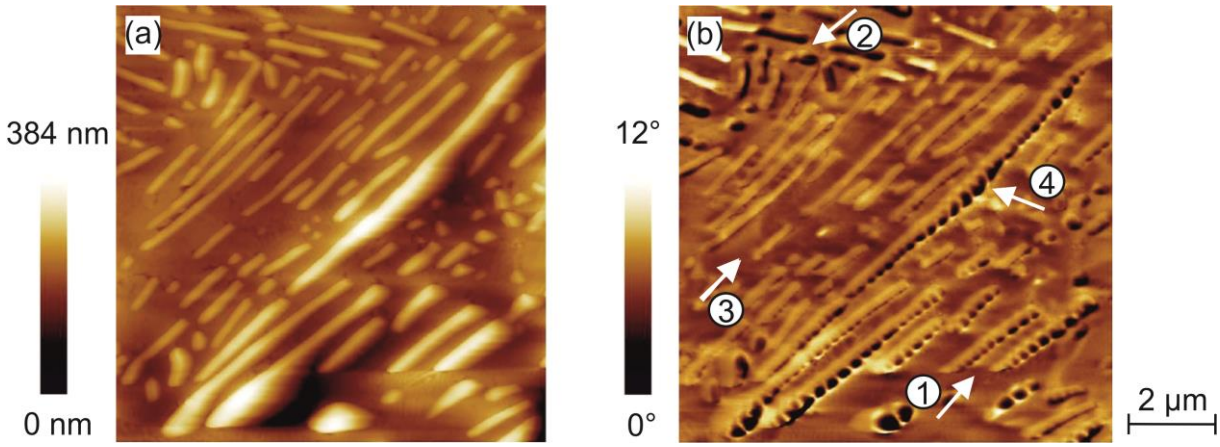

Figure 12. Topography (a) and MFM image (b) of the Fe-0.8%C sample with lamellar cementite taken by MFM.

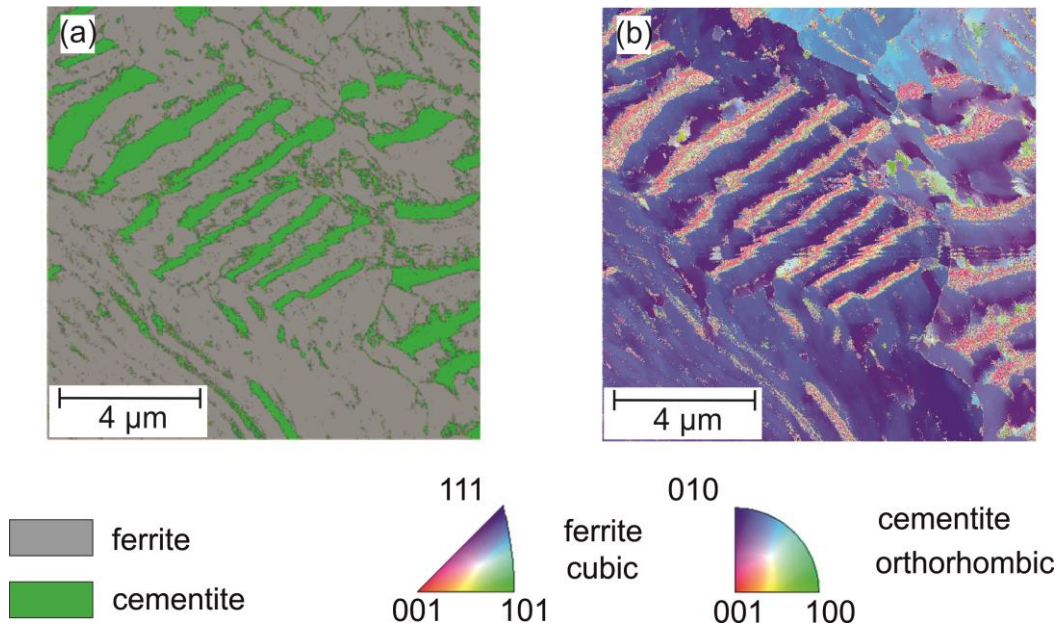

Figure 13. EBSD maps of the Fe-0.8%C sample with lamellar cementite: (a) phase distribution map displaying ferrite (gray) and cementite (green) phases and (b) inverse pole figure (IPF) map, displaying the crystal orientations.

For cementite lamellae with a very large aspect ratio, e.g. of 8 µm length and 300 nm width (Fig. 12b, arrow #4), the magnetic moments still are perpendicularly oriented with respect to the lamella axis. This observation confirms the high crystal anisotropy of cementite and that the magnetic domain formation is more dominated by the crystal anisotropy than by the shape anisotropy. Hence, if the magnetic easy axis is known, the analysis of the MFM images of the cementite lamellae only allows the estimation of their crystalline orientations.

4. SUMMARY

Unalloyed pearlitic steel samples containing globular and lamellar cementite in a ferrite matrix, respectively, were studied by means of MFM and EBSD techniques. MFM reveals the topographic and magnetic microstructure, EBSD the local crystalline orientations. Globular and the lamellar cementite precipitates in steels were chosen as examples to demonstrate the ability of the combination of MFM and EBSD results to determine the magnetic easy axes of micro- and nanoscopic precipitates in a bulk material.

In MFM measurements, the choice of an appropriate magnetic probe is crucial for each particular experiment. For the unalloyed pearlitic steels studied in this work the commercial MESP probe showed the best contrast and spatial resolution combination. The MESP probe did not influence the magnetic microstructure of the sample and vice-versa, and the observed contrast clearly revealed the magnetic microstructure in both phases, ferrite and cementite.

The combination of MFM and EBSD techniques enables the observation of associated local topographic, magnetic, and crystallographic microstructures. Bulk samples and compounds consisting of a matrix with embedded second phase particles can be studied. The MFM images (spatial resolution down to 50 nm) showed different orientations of the magnetic moments in the globular and in the lamellar cementite phase. The cementite domain structure in or around the (010) plane, i.e., the long easy [010]- or b-axis is oriented perpendicularly to the sample surface was found to consist of parallel stripes of strong opposite magnetic contrast. The magnetic moments of those precipitates are positioned alternately down- and upwards in relation to the surface and are separated by 180° domain walls. For the single crystal precipitates having a large misorientation with respect to the (010) plane, i.e. oriented close to the (100) plane, a weak dark or bright contrast was observed, which gives the conclusion that the magnetic moments of those precipitates are oriented with a small angle (α) with respect to the sample surface. The cementite precipitates oriented in or very close to the (001) plane showed a homogeneous contrast, i.e. very weak magnetic contrast, leading to the conclusion that their magnetic moments are oriented in-plane. By means of EBSD the long [010]- or b-axis of the precipitates was determined and correlated to the magnetic signal. Dark and bright imaged edges of the precipitates confirmed the in-plane and along the long [010]- or b-axis orientation of the magnetic moments. Additional MFM and EBSD analysis showed that the width of the domains in the surface is dependent on the cementite crystalline orientation relative to the surface. The width increases

with the angle between the easy [010] axis and the surface normal which confirms the observations that the magnetic moments are oriented along the long [010]- or b-axis.

In the case for the lamellar cementite precipitates, the EBSD measurements were not sufficiently accurate to determine the lamellae crystalline orientations. With the previous knowledge of the behavior of the magnetic domain structure with respect to the crystalline orientation of the globular precipitates, the crystalline orientation of the cementite lamellae can be estimated by simply observing the magnetic microstructure and the topographic profiles.

Finally, we may conclude that the combination of MFM and EBSD techniques allows determination of the magnetic easy axes of micro- and nanoscopic ferromagnetic precipitates in a bulk material requiring only relatively simple sample preparation.

REFERENCES

[1] M.T. Johnson, P.J.H. Bloemen, F.J.A. den Broeder, J.J. de Vries, *Reports on Progress in Physics* **59** (1996) 1409.

[2] N.P. Goss, *Electrical sheet and method and apparatus for its manufacture and test*, US Patent 1.965.559.

[3] N.P. Goss, *Transactions of the American Society of Metals* **23** (1935) 511.

[4] T. Hayashi, S. Hirono, M. Tomita, S. Umemura, *Nature* **382** (1996) 772.

[5] K.J. Kirk, *Contemporary Physics* **41** (2000) 61.

[6] R.C. Jacklevic, J.S. Lambe, A.H. Silver, J.E. Mercerau, *Physical Review Letters* **12** (1964) 159.

[7] R. Bergholz, U. Gradmann, *Journal of Magnetism and Magnetic Materials* **45** (1984) 389.

[8] P.J. Flanders, *Journal of Applied Physics* **63** (1988) 3940.

[9] S. Foner, *Journal of Applied Physics* **79** (1996) 4740.

[10] J.H.E. Giffiths, *Nature* **158** (1946) 670.

[11] H. Ebert, *Reports on Progress in Physics* **59** (1996) 1665.

[12] Z.Q. Ziu, S.D. Bader, *Review of Scientific Instruments* **71** (2000) 1243.

[13] J.W. Lau, J.M. Shaw, *Journal of Physics D: Applied Physics* **44** (2011) 303001.

[14] H. Matsuyama, K. Koike, *Journal of Electron Microscopy (Japan)* **43** (1994) 157.

[15] H. Boersch, H. Raith, *Naturwissenschaften* **46** (1959) 574.

[16] A.S. Keh, C.A. Johnson, *Journal of Applied Physics* **34** (1963) 2670.

[17] Y. Martin, H.K. Wickramasinghe, *Applied Physics Letters* **50** (1987) 1455.

[18] J.J. Saenz, N. Garcia, P. Grütter, E. Meyer, H. Heinzelmann, R. Wiesendanger, L. Rosenthaler, H.R. Hidber, H.J. Güntherodt, *Journal of Applied Physics* **62** (1987) 4293.

[19] U. Hartmann, *Annual Review of Materials Science* **29** (1999) 53.

[20] D. Dingley, *Journal of Microscopy* **213** (2004) 214.

[21] Q. Zhong, D. Inniss, K. Kjoller, V.B. Elings, *Surface Science* **290** (1993) L688.

[22] X. Zhu, P. Grütter, V. Metlushko, B. Ilic, *Journal of Applied Physics* **91** (2002) 7340.

[23] A. Alekseev, A. Popkov, A. Shubin, F. Pudonin, N. Djuzhev, *Ultramicroscopy* **136** (2014) 91.

[24] L. Yue, Z. Li, R. Kirby, D. Sellmyer, *Ultramicroscopy* 109 (2009) 1040.

[25] (2012). [Online]. Available: http://www.brukerafmprobes.com/.

[26] S. Wust, *Untersuchung der magnetischen Domänen in Stahlproben mittels Magnetkraftmikroskopie unter Anlegen eines externen Magnetfeldes*, Diploma thesis, Saarland University, IZFP report No.110126-TW, Saarbrücken (2011).

[27] *Diamond software* - Crystal and Molecular Structure Visualization, Crystal Impact, Bonn, Germany, http://www.crystalimpact.com/diamond.

[28] C. Jiang, S.G. Srinivasan, A. Caro, S.A. Maloy, *Journal of Applied Physics* **103** (2008) 043502.

[29] L. Batista, U. Rabe, S. Hirsekorn, *NDT & E International* **57** (2013) 58.

[30] L. Batista, U. Rabe, I. Altpeter, S. Hirsekorn, G. Dobmann, *Journal of Magnetism and Magnetic Materials* **254** (2014) 248.

[31] P. Blum, R. Pauthenet, *Comptes Rendus* **237** (1953) 1501.

[32] a4i Analysis, Version 5.10a; aquinto AG; Berlin-Landshut-Chicago http://www.aquinto.com.

[33] H. Kronmüller, M. Fähnle, *Micromagnetism and the Microstructure of Ferromagnetic Solids*, Cambridge University Press, Cambridge (2003).

[34] F. Stäblein, K. Schroeter, *Zeitschrift für anorganische und allgemeine Chemie* **174** (1928) 193.

[35] W. Lottermoser, A.K. Schaper, W. Treutmann, G. Redhammer, G. Tippelt, A. Lichtenberger, S.-U. Weber, G. Amthauer, *Journal of Physical Chemistry B* **110** (2006) 9768.

[36] A.K. Arzhnikov, L.V. Dobysheva, C. Demangeat, *Journal of Physics: Condensed Matter* **19** (2007) 9.

[37] U. Weissker, M. Löffler, F. Wolny, M.U. Lutz, N. Scheerbaum, R. Klingeler, T. Gemming, T. Mühl, A. Leonhardt, B. Büchner, *Journal of Applied Physics* **106** (2009) 054909.

[38] S. Zaefferer, S.I. Wright, D. Raabe, *Metallurgical and Materials Transactions A* **39A** (2008) 374.

[39] T. Takahashi, D. Ponge, D. Raabe, *Steel Research International* **78** (2007) 38.

V. CHARACTERIZATION OF THE MAGNETIC MICRO- AND NANOSTRUCTURE IN UNALLOYED STEELS BY MAGNETIC FORCE MICROSCOPY (PUBLICATION D)

L. Batista, U. Rabe, and S. Hirsekorn

AIP Conference Proceedings (2013) Vol. 1511; 1180-1187.

ABSTRACT. The formation of a cementite phase influences significantly the macroscopic mechanical and magnetic properties of steels. Based on a correlation between mechanical and magnetic properties, mechanical properties as well as the morphology and content of the cementite phase can be inspected by electromagnetic non-destructive testing methods. The influence of the carbon content on bulk magnetic properties of unalloyed steels is studied on a macroscopic scale by hysteresis loop and Barkhausen noise measurements. The micro- and nanostructure is investigated by atomic force microscopy and magnetic force microscopy. Surface topography images and magnetic images of globular cementite precipitates embedded in a ferrite matrix are presented. The size, shape, and orientation of the precipitates influence the domain configuration. Applied external magnetic fields cause magnetization processes mainly in the ferrite matrix: Bloch walls move and are pinned by the cementite precipitates. The correlation between the microscopic observations and macroscopic magnetic properties of the material is discussed.

Keywords: Atomic Force Microscopy (AFM), Magnetic Force Microscopy (MFM), Electron Backscattering Diffraction (EBSD), Steel, Microstructure, Nanostructure, Magnetic domains, Non-destructive testing

1. INTRODUCTION

Steels constitute the most widely used category of metallic materials because they provide a wide range of mechanical properties and can be manufactured relatively inexpensively in large quantities to very precise specifications [1]. Among all the phases or constituents that can be obtained by choosing the chemical composition, thermomechanical treatment, etc., two are frequently encountered in most of technical steels: ferrite and cementite. The volume fraction and morphology of the cementite phase controls directly the mechanical and magnetic properties of steels.

The bulk macroscopic magnetic properties of steels containing cementite embedded in a ferrite matrix have already been studied by many authors [2-5]. Even though several studies have been done using the magnetic Barkhausen noise (MBN) technique, a clear understanding on the individual influence of the cementite phase on the generation of the MBN has still not been well established. For example, the MBN activity profile in a microstructure containing cementite in a ferrite matrix has been observed as a single [4] as well as a double peak behavior [5].

All these macroscopic observations rely on a phenomenological description of the interactions of the magnetic domains with the microstructure. The microscopic magnetic domain structures can be imaged by different techniques. For example, domains in high-permeability materials were imaged by Kerr microscopy [6] and the domain configuration of a cementite thin foil was revealed by Lorentz electron microscopy [7]. Magnetic Force Microscopy (MFM) has been widely employed to map magnetic structures of surfaces [8-13]. In addition to its high local resolution in the range of 10 nm MFM has the ability to measure the topography and the magnetic microstructure simultaneously allowing the study of interaction between defects and magnetic properties.

In this paper, samples of a high purity polycrystalline iron and of two unalloyed steels (Fe-0.8%C and Fe-1.5%C) containing globular cementite embedded in a ferrite matrix were investigated. In the first part of this work, the macroscopic magnetic quantities, i.e. saturation magnetization, coercive field and maximum Barkhausen noise amplitude were measured and interpreted with respect to the microstructural state. In the second part, the magnetic microstructures were observed using a Magnetic Force Microscope. The MFM was coupled with an external coil providing a controlled in-plane magnetic field which allowed the observation of the dynamic behavior of the magnetic domains. Ferromagnetic domains were studied in the high purity polycrystalline iron sample and in the cementite and ferrite phases of the unalloyed steels. By means of Electron Backscatter Diffraction (EBSD) the crystalline

orientation of the cementite particles and the ferrite phase, respectively, were determined. The correlation between the macroscopic magnetic properties and the magnetic and crystallographic microstructure was examined.

2. MATERIALS AND METHODS

2.1 Unalloyed steels: Fe–C systems (Fe–Fe_3C)

Samples of high purity iron (99.99%) and of two unalloyed steels, Fe-0.8%C and Fe-1.5%C, containing globular cementite (Fe_3C) in a ferrite matrix were provided as-cast and machined in a cylindrical shape of 8 mm diameter and 50 mm length. Subsequently the samples were vacuum annealed at 600°C for 4h in order to remove all processing-induced residual stresses. The resulting microstructure has an average grain size of approximately 80 μm for all samples. The size of the cementite precipitates ranges from a few hundred nanometers to about 10 μm in diameter.

For AFM and MFM measurements small specimens (3 x 3 x 1 mm^3) were cut from the annealed cylindrical samples by spark erosion and mechanically polished by standard procedures. Directly before the measurements, the samples were slightly etched using Nital (95% Ethanol + 5% Nitric acid) in order to obtain reproducible surface conditions.

2.2 Bulk magnetic properties: hysteresis loop and Barkhausen noise signals

The hysteresis loop and Barkhausen noise measurements were performed inside an electromagnet with a bipolar power supply controlled by a function generator. The magnetic field strength was measured by a Hall probe. The cylindrical samples were magnetized along their axial direction reaching a maximum magnetic field strength of 110 A/cm at an excitation frequency of 0.5 Hz. The change in magnetic flux density and the inductive Barkhausen noise of the cylindrical samples were measured by a surrounding pick-up coil. The voltage induced by the noise signals was recorded as a function of the tangential field strength.

The magnetic hysteresis curves and the Barkhausen noise curves of the three samples are shown in figures 1a-c as dotted and continuous curves, respectively. The coercivity *Hc* increases with carbon content, while the relative permeability at the coercive field *Hc* and the saturation magnetization B_S at 100 A/cm decrease with increasing carbon content. This indicates that the magnetic hardness increases as the carbon content increases. The measured parameters are listed in Table 1. The Barkhausen noise curves are remarkably different in their shape (single and double peaks) and in their maximal amplitude values. High peaks (fig. 1a) close to the coercive field *Hc* are observed for the high purity iron sample showing

the easy irreversible domain wall movement (mostly 180° BWs) through the microstructure. The addition of 0.8 and 1.5 wt. % carbon, respectively, results in a microstructure with globular cementite precipitates embedded in a ferrite matrix with less than 0.008 wt. % of carbon in solid solution. A broadening of the Barkhausen noise peak and a decreasing peak height can be observed as shown in the continuous curves of figures 1b and c, respectively. This can be attributed to the interstitial carbon atoms in the ferrite matrix and the intra- and intergranular cementite precipitates. Furthermore, the Barkhausen noise signals of the samples with cementite precipitates clearly show double peaks. The lower field peak corresponds to the ferrite and the higher field peak to the cementite phase. The amplitude of the peaks seems to be proportional to the amount of each phase. Increasing the amount of carbon the ferrite peak decreases and the cementite peak increases (figs. 1b and c). This can be explained due to the fact that the magnetization and respective Barkhausen jumps in the cementite phase occur at higher fields.

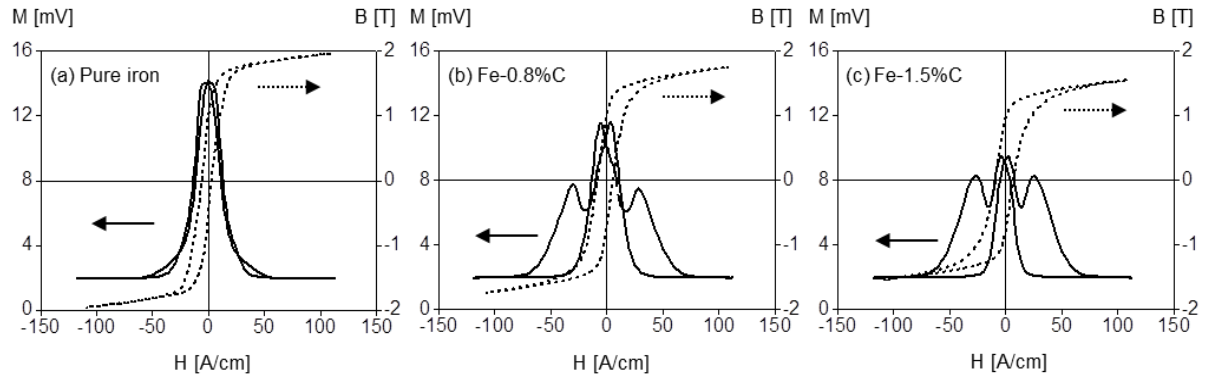

Figure 1. Hysteresis loop (dotted line) and Barkhausen noise (continuous line) curves for (a) pure Fe (99,99%) and two unalloyed steels containing different content of globular cementite (b) Fe-0.8%C and (c) Fe-1.5%C. The measurements were performed at 1.8 V and 0.5 Hz.

Table 1. Parameters deduced from the macroscopic measurements shown in figure 1.

Carbon content [wt%]	Coercive field H_C [A/cm]	Relative permeability at H_c	Saturation magnetization B_S [T]	Maximum Barkhausen noise amplitude M_{max} [mV]
0 (Pure Fe)	4.2	0.17	1.96	14.2
0.8	6.8	0.13	1.75	11.5
1.5	8.2	0.11	1.55	9.5

2.3 Local magnetic properties – magnetic force microscope (MFM) with a superposed external magnetic field

Atomic force microscopy (AFM) and MFM have been used to image the topography and the magnetic microstructure of the samples, respectively. The measurements were performed in tapping-lift mode using a commercial AFM/MFM instrument (Nanoscope III® multimode, Digital Instruments, Santa Barbara, CA, USA). The sensor tips were CoCr-coated with a coercivity of ~ 320 A/cm MESP, Bruker AXS Inc., Madison, WI, USA). A lift-height of 60 to 80 nm was chosen for all measurements reported here. In order to investigate the evolution of the magnetic microstructure and the resulting domain configuration, an external electromagnet was combined with the MFM as shown in figure 2. The pole shoes of the electromagnet were adjusted such that the sample inside the AFM was magnetized parallel to its surface. All magnetic images presented in this work are so-called phase images, i.e. the local phase shift was recorded as a function of position.

2.4 MFM images of the high purity bulk iron

Figure 3a shows the topography image obtained with the MFM of the high purity iron bulk sample revealing the grain structure having height differences up to about 100 nm. The corresponding magnetic microstructure is shown in fig. 3b. Each grain has its own domain structure depending mostly on the crystalline orientation and residual stress levels. For example, grain (1) shows large areas with an almost homogeneous grey level, while grain (2) displays a multitude of small areas with different magnetic contrast. The domain arrangement at the surface is primarily determined by the principle of flux closure which minimizes the total inner energy. Additionally, it is strongly dependent on the surface orientation relative to the easy directions. From the simplest case, i.e. a surface containing two easy axes, to strongly disoriented surfaces with no easy axis, the domain patterns become progressively more complicated [14]. The <001> directions are the easy directions for iron and therefore the (100) surface contains two mutually perpendicular easy directions. This allows us to conclude that the orientation of the grain (1) is close to the plane (100), and the orientation of the grain (2) strongly deviates from the plane (100). The domain patterns often face deviations from the ideal structure because of residual stresses and possibly induced anisotropies.

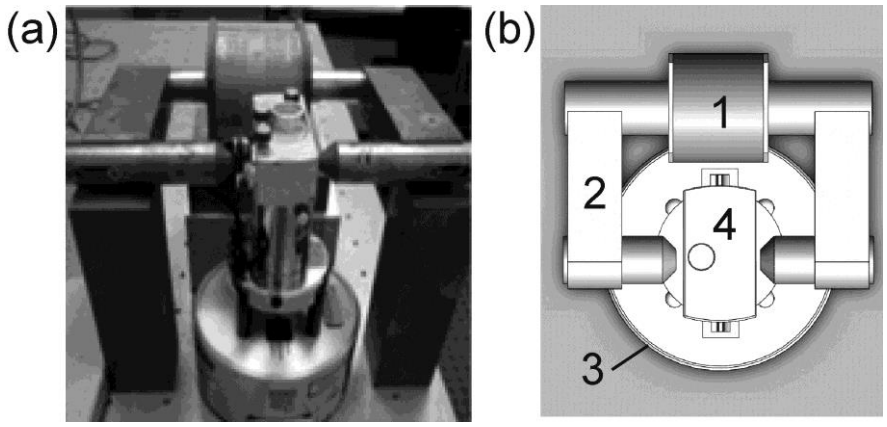

Figure 2. (a) Photograph of the experimental set-up for the MFM measurements coupled with an external coil providing a controlled in-plane magnetic field. (b) Corresponding drawing showing the coil (1), yoke (2), MFM base (3), and MFM head (4), respectively.

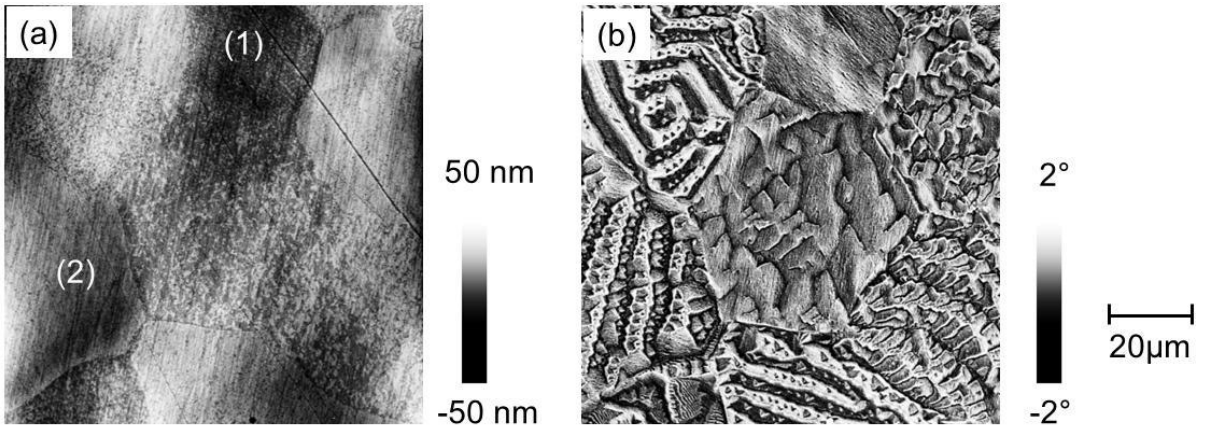

Figure 3. Topography (a) and MFM image (b) of the high purity bulk iron sample taken with MFM.

Figures 4 a-d demonstrate the evolution of the magnetic microstructure for the high purity iron sample in an external in-plane magnetic field. The imaged area is located in a grain oriented close to (100) surface. The image displays a few domains clearly separated by Bloch walls which can be detected as bright or dark lines in the MFM image (white arrows in fig. 4). At the remanence state, a domain wall will be in a position which minimizes the energy of the system formed by the wall itself and the adjoining domains and domain walls. Most domain walls are bulged possibly indicating the existence of defects and residual microstress, which is caused by crystal imperfections as e.g. dislocations [15].

When a magnetic field is applied, a change of position of the domains can be observed. For example a domain wall (dark line) indicated by a white arrow in figs. 4 moves downwards as the field strength increases. Another domain wall (bright line) also indicated by

a white arrow moves upwards. Accordingly, the supplementary domains between the black and white walls disappear.

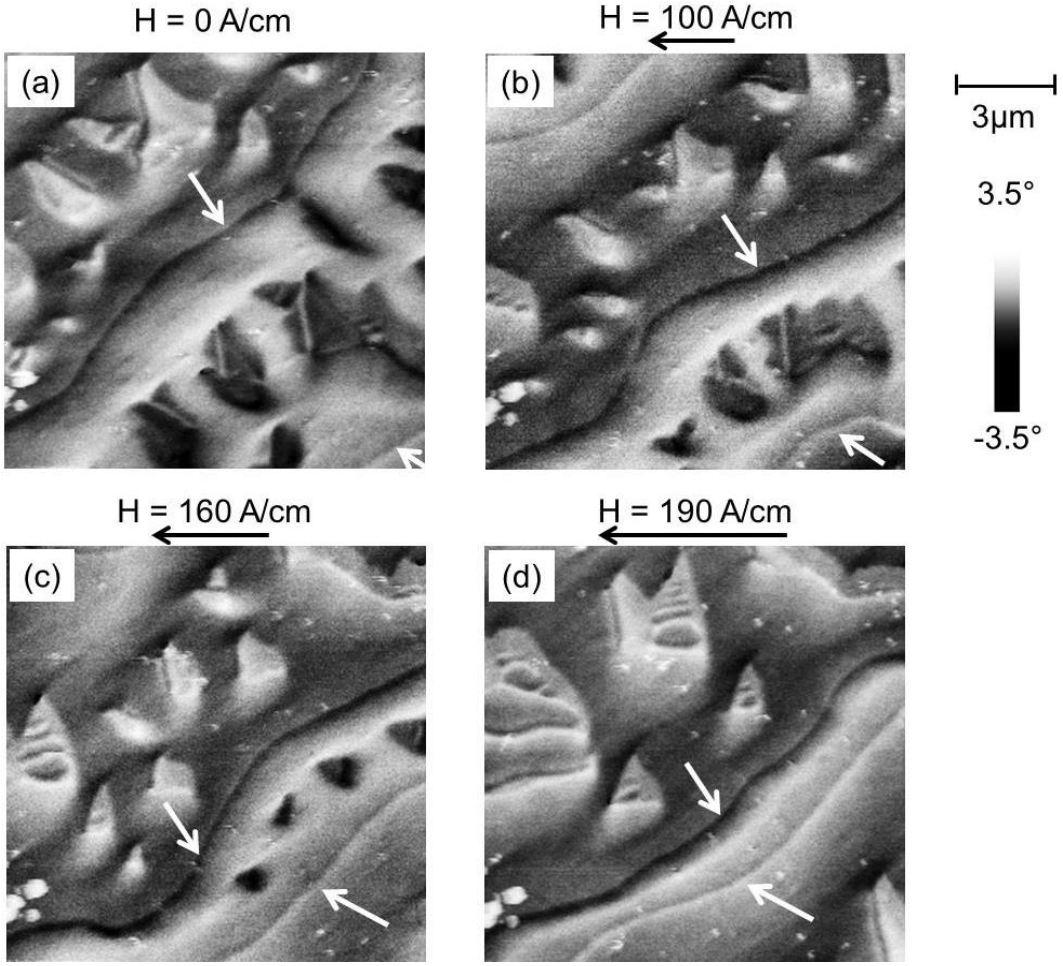

Figure 4. MFM images of the high purity iron sample (a) without external field and with an applied external field of (b) 100 A/cm, (c) 160 A/cm, and (d) 190 A/cm, respectively. The direction of the in-plane field is indicated by black arrows above the images.

2.5 MFM and EBSD images of samples containing globular cementite embedded in a ferrite matrix

The unalloyed steels Fe-0.8%C and Fe-1.5%C investigated in this work consist of a relatively hard magnetic cementite phase embedded in a soft ferromagnetic ferrite matrix. The cementite content is higher in the Fe-1.5%C sample than in the Fe-0.8%C-sample, but the basic behavior of the magnetic microstructure can be discussed by considering only the Fe-1.5%C as an example.

Figure 5a shows the topography obtained with the MFM of the Fe-1.5%C sample revealing the microstructure and surface roughness. The cementite precipitates appear higher than the ferrite matrix with an offset of about 400 nm maximum. Two grains with different

average height numbered (1) and (2) are visible in the ferrite matrix. The corresponding magnetic microstructure in the demagnetized state as well as the Electron Backscatter Diffraction (EBSD) map taken in the same area with a Scanning Electron Microscope, i.e. the Inverse Pole Figure (IPF), are shown in figs. 5b and 5c, respectively. The color code of the inverse pole figure represents the crystallographic orientation in the ferrite matrix (nearly pure b.c.c. iron, lattice constant a = 2.87Å), and in the cementite particles (orthorhombic symmetry, length of the three perpendicular axes a = 5.09Å, b = 6.74Å, c = 4.52Å). Using an orientation imaging software, the angles of inclination of the two ferrite grains (1) and (2) relative to the (100) plane were obtained as 9° and 15°, respectively. The ferrite matrix (fig. 5b) shows a complex domain configuration displayed by a multitude of small areas with different magnetic contrast. Spike domains [16] are formed on the cementite/ferrite interface, which can be attributed to stresses due to differences in thermal expansion coefficient of the two phases and reduction of the cementite magnetostatic energy. Orange arrows in fig. 5b point to a domain in the ferrite matrix, which is limited in size by a grain boundary on the right and by a cementite precipitate on the left side. It is well known that grain boundaries as well as precipitates contribute to increase the magnetic hardness of ferromagnetic materials by restricting the movement of domain walls.

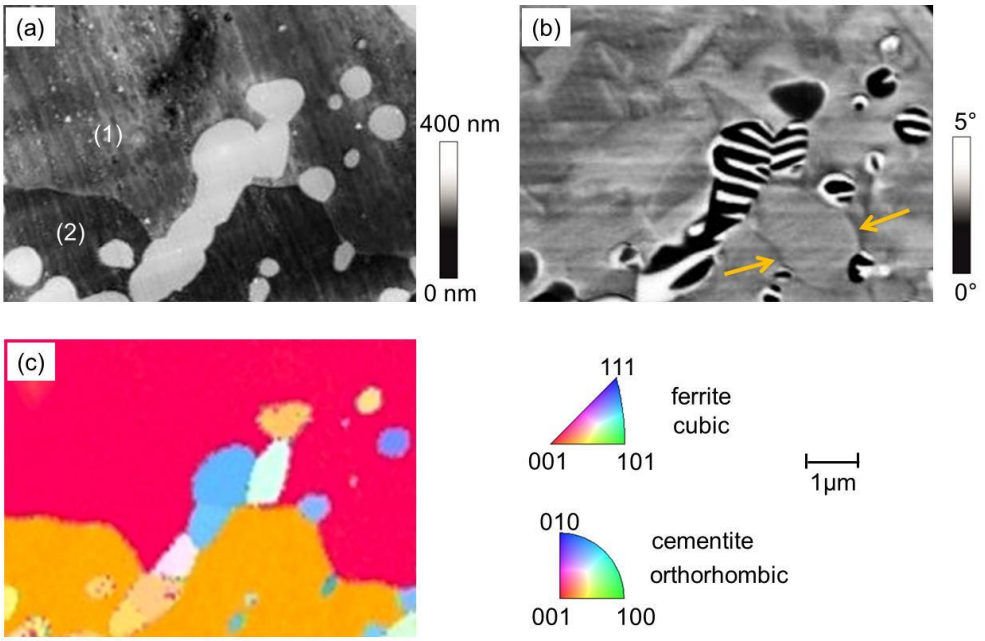

Figure 5. Topography (a) and MFM image (b) of the Fe-1.5%C sample taken with MFM. The corresponding IPF map recorded in the SEM shows the crystals and their respective orientations. Two ferrite grains with different crystal orientation are marked as (1) and (2) in the topography image.

The cementite precipitates show a much stronger magnetic image contrast than the ferrite matrix because cementite is magnetically harder than ferrite and thus causes stronger stray fields. The domains observed in the cementite precipitates range from 50 to 1000 nm in width depending on their crystalline orientation. The cementite precipitates in or around the (010) orientation presents always a stripe structure. Since the MFM tip senses the component of the stray field emerging perpendicularly from the surface, we may conclude that the magnetic moments of these precipitates are more or less parallel to the tip axis, i.e. perpendicular to the sample surface plane and oriented along the long axis (here [010]- or b-axis).

An example for a Barkhausen jump is shown in figures 6. Figure 6a shows the topography obtained with the MFM of the Fe-1.5%C sample, and the evolution of the magnetic microstructure under a superposed applied magnetic field is shown in figs. 6b and c. Figure 6b is recorded at the remanence state of the sample while fig. 6c displays the results with an applied magnetic field of 190 A/cm. Bright and dark lines are visible within the ferrite matrix, which can be identified as domain walls. Initially, if the magnetic field is smaller than the coercive field ($H < Hc$), the domain wall is attached to pinning points (fig. 6b). When $H > Hc$, the domain wall unpins, propagates and pins to the next precipitate (fig. 6c, white arrow). These microscopic observations make clear that an increase of the amount of carbon and consequently an increase of the amount of pinning sites can cause a decrease of the macroscopic initial permeability and an increase of coercivity.

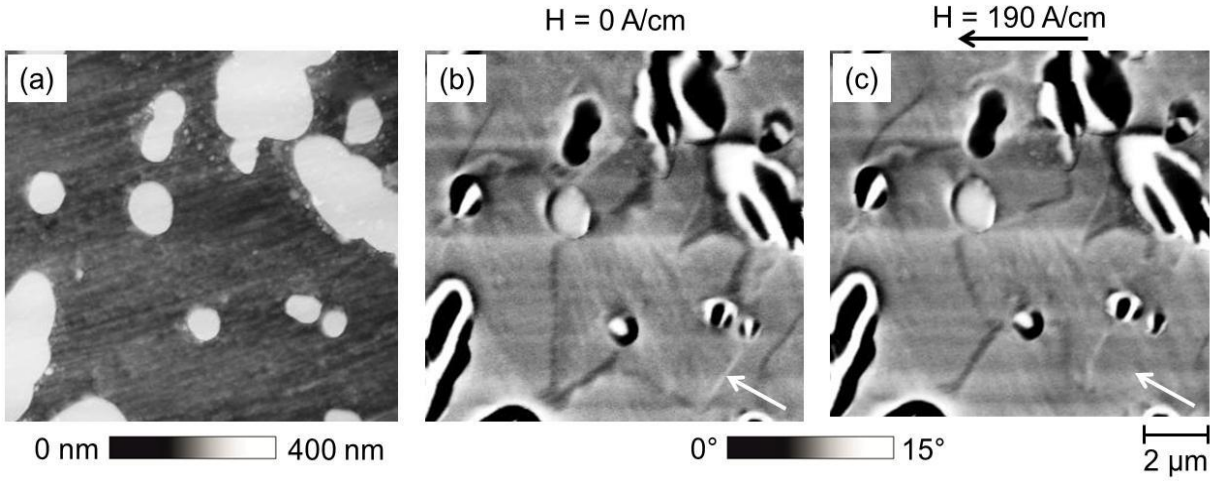

Figure 6. Topography (a) of the sample Fe-1.5%C containing globular cementite precipitates in a ferrite matrix, MFM images taken (b) without external magnetic field and with an applied field of (c) 190 A/cm. The direction of the in-plane field is indicated by a black arrow. The white arrows indicate a domain wall movement.

3. SUMMARY

The combination of AFM, MFM, and EBSD techniques with macroscopic magnetic measurements opens a new field for material development and design enabling the direct observation of magnetic micro- and nanostructures including the corresponding single crystal grain orientations. Samples of highly pure iron and the unalloyed steels Fe-0.8%C and Fe-1.5%C were characterized macroscopically by measuring hysteresis loops and Barkhausen noise signals. The magnetic hardness increases with increasing amount of carbon in form of globular cementite precipitates in the ferrite matrix. Besides, the Barkhausen noise amplitude decreases and becomes a double peak. The weaker field peak corresponds to the ferrite and the stronger field peak to the cementite phase.

MFM was shown to be a powerful tool for nondestructive magnetic microstructure imaging and characterization in the micro- and nanoscale of steels. In this work, MFM images with a local resolution of 50 nm have been achieved. The crystalline orientation of the ferrite and cementite phases were determined by EBSD and correlated to the domain structure. Ferromagnetic domain structures in highly pure iron and in cementite precipitates as well as their interaction were studied. Domain walls in the ferrite phase tend to intersect the cementite precipitates in order to minimize the magnetostatic and wall energy. By applying an external in-plane magnetic field the dynamic behavior of the magnetic domains and the interaction between domain walls and the cementite precipitates was observed and characterized.

REFERENCES

[1] ASM International Handbook (1990). ASM Handbook, Volume 1 - Properties and Selection: Irons, Steels, and High Performance Alloys, Materials Park, OH, ASM International, page 233.

[2] I. Altpeter, *Journal of Nondestructive Evaluation* **15** (1996) 45.

[3] I. Altpeter, G. Dobmann, M. Kröning, M. Rabung, S. Szielasko, *NDT&E International* **42** (2009) 283.

[4] M. Blaow, J.T. Evans, B.A. Shaw, *Acta Materialia* **53** (2005) 279.

[5] V. Moorthy, S. Vadyanathan, T. Jayakumar, B. Raj, *Journal of Magnetism and Magnetic Materials* **171** (1997) 179.

[6] R. Schäfer, *Journal of Magnetism and Magnetic Materials* **215-216** (2000) 652.

[7] A.S. Keh, C.A. Johnson, *Journal of Applied Physics* **34** (1963) 2670.

[8] P. Grütter, T. Jung, H. Heinzelmann, A. Wadas, E. Meyer, H.R. Hidberand, H.J. Güntherodt, *Journal of Applied Physics* **67** (1990) 1437.

[9] Y. Martin, H.K. Wickramasinghe, *Applied Physics Letters* **50** (1987) 1455.

[10] J.J. Saenz, N. Garcia, P. Griitter, E. Meyer, H. Heinzelmann, R. Wiesendanger, L. Rosenthaler, H.R. Hidber, H.J. Güntherodt, *Journal of Applied Physics* **62** (1987) 4293.

[11] S. Huo, J.E.L. Bishop, J.W. Tucker, M.A. Al-Khafaji, W.M. Rainforth, H.A. Davies, M.R.J. Gibbs, *Journal of Magnetism and Magnetic Materials* **190** (1998) 17.

[12] L. Batista, U. Rabe, S. Hirsekorn, "Micro- and Nanostructure Imaging and Characterization of Advanced Steels", *38th Annual Review of Progress in Quantitative Nondestructive Evaluation (QNDE)*, July 17-22, 2011, Burlington, Vermont, USA.

[13] L. Batista, U. Rabe, S. Hirsekorn, *Magnetic micro- and nanostructures of unalloyed steels: domain wall interactions with cementite precipitates observed by MFM*, in review.

[14] A. Hubert, R. Schäfer, *Magnetic Domains - The Analysis of Magnetic Microstructures*, Springer, Berlin (1998).

[15] B.D. Cullity, *Introduction to magnetic materials*, Addison Wesley, London (1972).

[16] H.J. Williams, *Physical Review* **71** (1947) 646.

VI. MICRO- AND NANOSTRUCTURE CHARACTERIZATION AND IMAGING OF TWIP AND UNALLOYED STEELS (PUBLICATION E)

L. Batista, U. Rabe, and S. Hirsekorn

AIP Conference Proceedings (2012) Vol. 1430; 1381-1388.

ABSTRACT. New design concepts for constructing light-weight and crash resistant transportation systems require the development of high strength and supra-ductile steels with enhanced energy absorption and reduced specific weight. TWIP steels combine these properties, a consequence of intensive mechanical twinning. To understand the mechanisms, related microstructures and local material properties are probed by AFAM, nanoindentation, and EBSD. The morphology of a cementite phase controls the macroscopic mechanical and magnetic properties of steels. Cementite embedded in a ferrite matrix is characterized by AFAM and MFM.

Keywords: Atomic Force Acoustic Microscopy, Imaging, Magnetic Force Microscopy, Microstructure, Nanostructure, Steel

1. INTRODUCTION

The current strong demand for vehicle lightening from the automobile sector requires flat carbon steel sheet manufacturers to develop new advanced grades capable of fulfilling the contradicting properties such as weight reduction and formability versus high stiffness and strength. Austenitic twinning induced plasticity (TWIP) steels have low to intermediate stacking fault energy and hence undergo extensive mechanical twinning during deformation, which in turn leads to an excellent combination of strength, ductility, and damage tolerance satisfying the requirements for automotive industries [1]. The main mechanical properties of these alloys have been investigated by many authors using standard destructive techniques [2-5]. The optimization of microstructures opens a new field for the design of new alloys. This requires the understanding of the macroscopic elastic and plastic properties in relation to the microstructure. In this contribution, the near-field technique atomic force acoustic microscopy (AFAM) [e.g. 6-11] which combines atomic force microscopy (AFM) [12] with ultrasound is used to image microstructures and probe material properties on the micro- and nanoscale. AFAM is a contact resonance spectroscopy technique with a spatial resolution down to the nm range and, similar to nanoindentation, sensitive to the local indentation modulus accounting for normal and shear deformation in the tip-sample contact zone.

In the second part of this work, an unalloyed steel Fe-0.8%C is studied by means of atomic force acoustic microscopy (AFAM) and magnetic force microscopy (MFM). Cementite (Fe_3C) is an important phase in steels because its morphology directly controls mechanical and magnetic properties. In contrast to its technological significance, the knowledge about the elastic properties of Fe_3C is quite limited. A large scatter on the value for the Young´s Modulus can be found in the literature [13-18]. The macroscopic magnetic properties of unalloyed steels have already been studied by many authors [e.g. 19,20]. Microstructure parameters such as lattice defects and grain and phase boundaries impede temporarily magnetic domain wall movements under magnetic load and thus reveal about mechanical material properties [21]. Therefore, a MFM coupled with an external coil providing an in-plane controlled magnetic field is employed to image the dynamic behavior of magnetic domains and related microstructures.

2. MATERIALS AND METHODS

2.1 Twinning-induced plasticity (TWIP) steels

Two different kinds of TWIP based 100% austenitic alloys are investigated. They were provided after hot-rolling, 50% cold-rolling, and annealing. The chemical composition (wt%) of the sheets are Fe-22Mn-0.6C-0.2V and Fe-20Mn-3Si-3Al with average grain sizes of 1 μm and 40 μm, respectively. Both sheets have a monomodal grain size distribution, a thickness of 1.2 mm, and show macroscopically isotropic material behavior. The elastic properties were measured by ultrasound in different directions. The isotropic plastic behavior was shown by tensile tests performed at small samples taken in rolling and in transverse direction. For AFAM and nanoindentation measurements small specimens were cut by spark erosion from the recrystallized and annealed steel sheets and mechanically polished by standard procedures. Directly before the measurements, in order to obtain suitably reproducible surface conditions, the samples were electropolished which removed a surface layer of about 1-2 μm. The AFAM and nanoindentation experiments were carried out with a Dimension 3000® from Digital Instruments (DI) and a Hysitron Triboscope® in conjunction with a DI Nanoscope II, respectively.

The microstructure evolution during tensile load of Fe-22Mn-0.6C-0.2V (wt%) TWIP alloy was monitored. The investigation was performed by an experimental set-up composed of an AFM (Dimension 3000®) and a tensile machine (UTS, electromechanical). In order to avoid residual stresses the bone-shaped tensile test samples were also cut by spark erosion. AFM observations and EBSD analysis require specific sample surface preparation. In order to observe very small deformation induced relief in the AFM images and to be able to probe local mechanical properties, the surfaces have to be perfectly plane. Thus, the sample was polished mechanically by standard procedures followed by electrochemical polishing. Suitable electrolyte as well as exposure time and voltage have to be identified and selected very carefully by series of experiments. After preparation, the surface roughness was evaluated statistically from AFM micrographs 3 μm x 3 μm in size. The best result obtained was a roughness of RMS < 1 nm. The sample was marked with a microindenter, and the grain orientations were determined by EBSD. The specimen was deformed with engineering plastic strains of ε_p = 3%, 6%, 10%, and 15%. After each deformation step the tensile test was interrupted and AFM images were taken in contact mode. The tests were carried out in air at room temperature.

2.2 Unalloyed steel (Fe-0.8%C)

The unalloyed steel Fe-0.8%C sample examined in this work was provided as-cast and annealed in a cylindrical shape of 8 mm diameter with a microstructure of globular cementite (Fe_3C) embedded in a ferrite matrix. From the cylindrical sample, a 1 mm thick disk shape was cut by spark erosion and prepared as described in the previous section.

2.3 Quantitative AFAM and nanoindentation compared to EBSD maps

In order to probe local elastic properties of the TWIP steels, AFAM as well as nanoindentation was applied. In AFAM, from measured local contact resonance frequencies of an AFM cantilever local indentation moduli of the sample surface are determined by calibration or by calculation via the Hertzian contact theory if the shape and the material properties of the cantilever and sensor tip are known well enough [e.g. 11].

Figure 1 shows EBSD maps and AFM topography images of nanoindents in the steels Fe-22Mn-0.6C-0.2V (Fig. 1a) and Fe-20Mn-3Si-3Al (Fig. 1b). To be able to probe the local mechanical properties in correlation to the grain orientation, the samples were previously marked by focused ion beam (Fig. 1a) and microindentation (Fig. 1b). In accordance to the ultrasonic measurements (see materials description above) the EBSD maps show no preferred grain orientation. The indentation moduli for different grain orientations are given in Table 1. All results show the same correct trend, i.e. stiffness in or around (111) direction is higher than in or around (101) direction which is higher than in or around (001) direction. The differences in AFAM and nanoindentation results might be caused by different tip shapes, different sizes of involved surface area, and inaccuracies in the AFAM calibration.

Figure 2 shows a series of AFM contact mode topography images of a surface area of the Fe22Mn0.6C-0.2V specimen for different plastic deformation levels revealing a typical evolution of the surface relief during a tensile test of TWIP steel. Fig. 2a presents the selected surface area before loading. It contains height differences up to about 100 nm and clearly reflects the grain structure (already imaged and confirmed by ArcelorMittal, who provided us with the samples). The grain boundaries appear higher than the grains itself, i.e. the preparation of the sample surface generates prominent grain boundaries. Such a relief is probably due to a preferential attack of grain interiors during electrolytic polishing. For 3% plastic strain, the AFM image already shows mechanical twinning in the austenite grains appearing as nearly equidistant straight lines (Fig. 2b). Increasing plastic strain (6, 10, and 15%) causes increasing twinning area fractions. Mechanical twinning creates a step the height of which can be accurately measured by AFM. Fig. 3 presents the height profiles in the area

pointed by a black arrow in Fig. 2 for the different plastic strain levels indicating an increase in step height with increasing plastic deformation. The EBSD map in Fig. 2f reveals the grain orientations in the sample surface at 15% deformation (see color code in the legend). The presence of twins is confirmed by the straight lines having different orientations than the austenite grain itself. AFM observations of the surface relief have already been reported, e.g. in 316L austenitic [22–24] and in duplex stainless steel [25]. However, the observation of surface relief due to mechanical twinning is presented for the first time. The determination of the involved slip planes during formation of the twins in relation to the surface relief is a topic of current work.

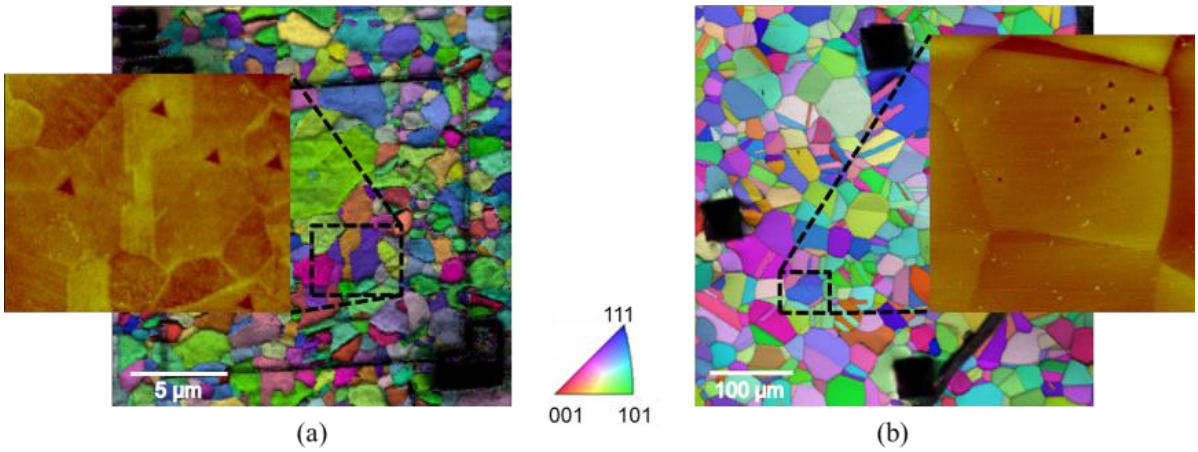

Figure 1. EBSD (Electron Backscattering Diffraction) images for single grain orientation determination and AFM topography images showing the nanoindentation marks in the austenitic TWIP steels: (a) Fe-22Mn-0.6C-0.2V, average grain size 1 µm and (b) Fe-20Mn-3Si-3Al, average grain size 40 µm.

Table 1. Indentation moduli (M) of the TWIP steels Fe-22Mn-0.6C-0.2V and Fe-20Mn-3Si-3Al with average grain sizes of 1 µm and 40 µm, respectively.

	M (GPa) from quantitative AFAM			M (GPa) from nanoindentation		
	(111)	(101)	(001)	(111)	(101)	(001)
FeMnC (V)	179	167	139	218	207	197
FeMnC (Al,Si)	171	142	113	160	134	131

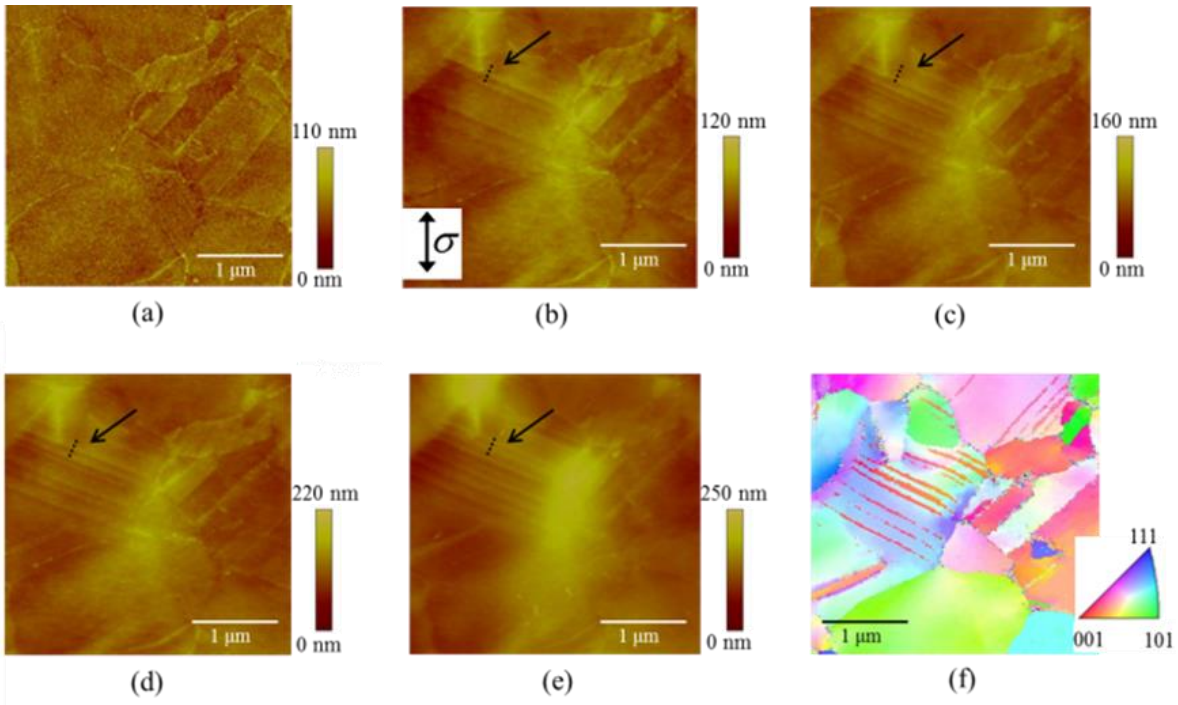

Figure 2. Series of AFM micrographs documenting the evolution of surface relief topography in Fe-22Mn-0.6C-0.2V TWIP steel during a tensile test: (a) before loading; (b, c, d and e) with plastic strains of 3%, 6%, 9%, and 15%, respectively; (f) EBSD map showing the grain orientations after 15% plastic stain. The loading direction is indicated in (b).

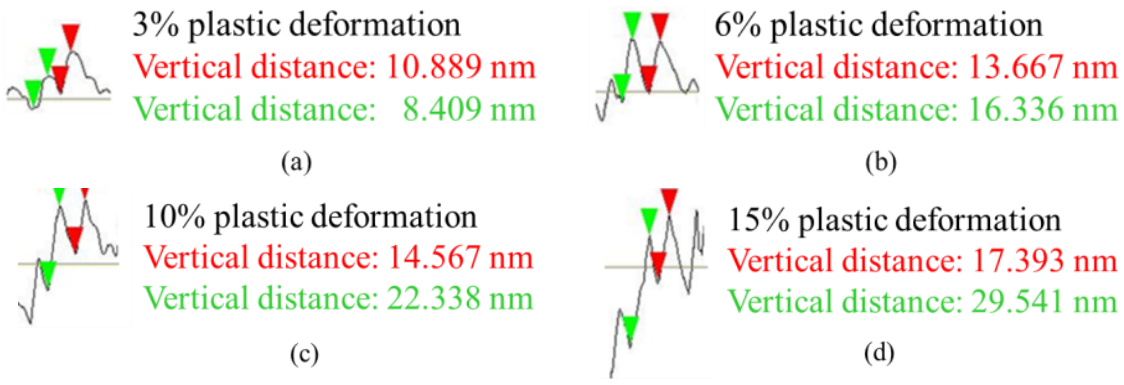

Figure 3. Series of AFM height profiles measured in Fe-22Mn-0.6C-0.2V TWIP steel with different plastic strain levels. The height profiles were measured in the same area as pointed by a black arrow in Fig. 2.

2.4 Magnetic force microscopy (MFM) combined with EBSD (sample Fe-0.8%C unalloyed steel)

AFM and MFM have been used to image the topography and the magnetic microstructure of the unalloyed steel Fe-0.8%C containing globular cementite embedded in a ferrite matrix. The measurements were performed in tapping-lift mode using a Nanoscope III®

multimode from DI and MESP CoCr-coated tips with a coercivity of ~ 400 Oe. The CoCr-coated tips are magnetized along the tip axis by a permanent magnet. A height of 60 to 80 nm above the sample surface was kept during measurement. The images acquired at the remanence and with a superposed magnetic field of different strength by means of an external coil reveal the magnetic microstructure and the evolution of the resulting domain configuration. In cubic crystals as in the case of the ferrite the domain patterns are determined by the surface orientation relative to the easy directions. From the simplest case, a surface with two easy axes, to strongly mis-oriented surfaces with no easy axis, the domain patterns become progressively more complicated [26]. The domain arrangement is primarily determined by the principle of flux closure which minimizes the total inner energy.

In ferrite the surface (100) contains two easy directions reducing the complexity for image interpretations. However, the domain patterns often face deviations from the ideal structure because of residual stresses and possible induced anisotropies. The domains in the ferrite matrix, generally in the form of closure domains, often appear to be unrelated to the domains in the cementite. The domains observed in the cementite particles range from 50 to 1000 nm in width depending on their orientation. The cementite particles in or around the (010) orientation present always a stripe structure showing perpendicular anisotropy. Supplementary domains can be seen at the interface between the ferrite and the cementite phases (white arrows in Fig. 4) which is typical for a pattern containing stresses. This can be explained by differences in the thermal expansion coefficient of the two phases creating residual stresses while cooling [20]. The MFM images show increasing size of supplementary domains with increasing in-plane magnetic field.

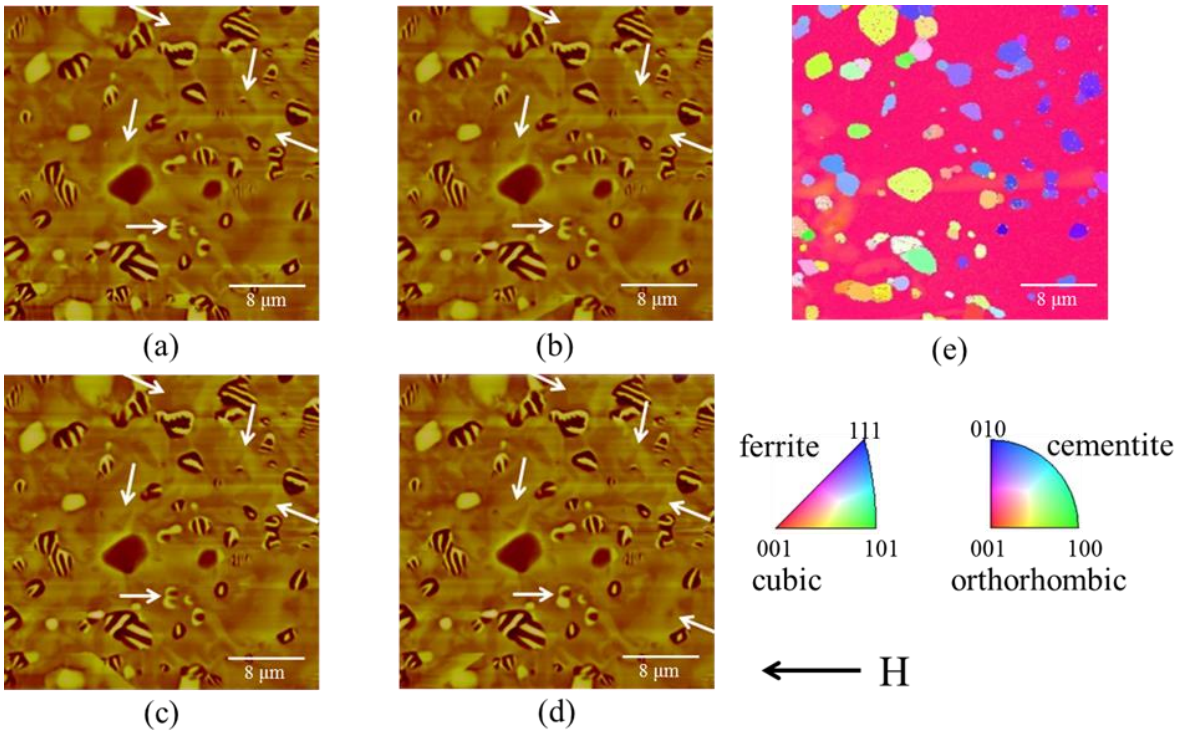

Figure 4. Series of MFM images taken at different applied field strengths in Fe-0.8%C unalloyed steel: (a) no external field, (b) to (d) external fiels of 13, 20, and 24 mT; (e) corresponding EBSD map showing the crystal orientations. The applied field direction (in-plane) is indicated by the black arrow.

A broadening of the stripe domain configuration in the cementite phase in or around the (010) orientation was observed by a sequence of MFM images (Fig. 5): the perpendicular anisotropy was progressively reduced by an external in-plane magnetic field.

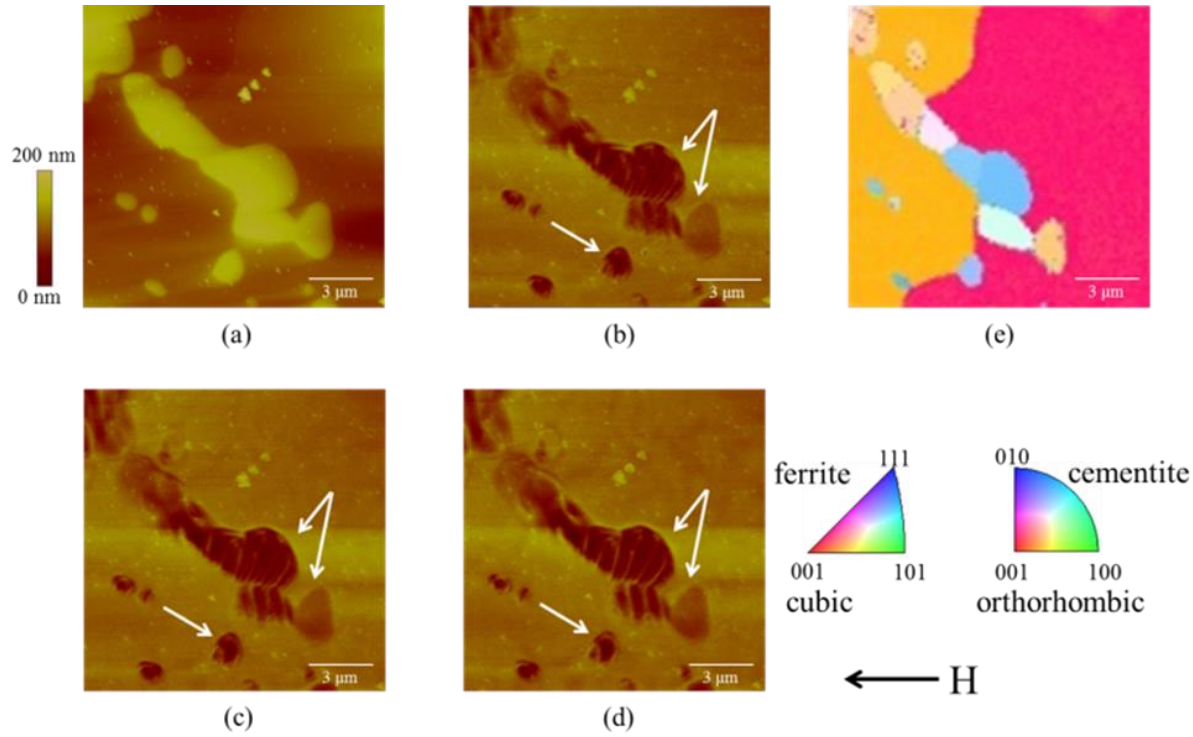

Figure 5. Series of images of Fe-0.8%C unalloyed steel showing the evolution of the cementite magnetic structure with an applied external magnetic field: (a) topography image; MFM images without (b) and with external field of (c) 13 mT and (d) 24 mT; (e) corresponding EBSD map showing the crystal orientations. The applied field direction (in-plane) is indicated by the black arrow.

2.5 In-situ elasticity mapping of cementite precipitates in Fe-0.8%C unalloyed steel

In this work, unalloyed steel Fe-0.8%C containing globular cementite was studied, i.e. cementite embedded in a ferrite matrix but not isolated cementite, which presents many difficulties during its preparation. Fig. 6a shows an optical micrograph of the steel. The topography (Fig. 6b) reveals microstructure and surface roughness. The cementite precipitates appear higher than the ferrite matrix with an offset of about 20 nm maximum.

AFAM amplitude images yield qualitative surface elasticity maps [e.g. 27]. While the sample surface is scanned the AFM cantilever is excited to vibrations at a fixed ultrasonic frequency close to a contact resonance. The cantilever vibration amplitude and thus the AFAM image contrast depends on the difference between the excitation frequency and the local contact resonance. Fig. 6c is recorded with a 622 kHz excitation, i.e. below the contact resonances of the specimen, and hence the cantilever vibration amplitude is higher on the more compliant phase, here cementite. Fig. 6d is recorded with an excitation frequency just above the contact resonances, 664 kHz, which causes contrast inversion in the AFAM image, i.e. the cantilever vibration amplitude is higher on the stiffer phase, here ferrite. The

resonance frequency spectra of the two phases are shown schematically in Fig. 6. Quantitative AFAM measurements for local indentation moduli determination on each single phase and for known grain orientation still have to be carried out.

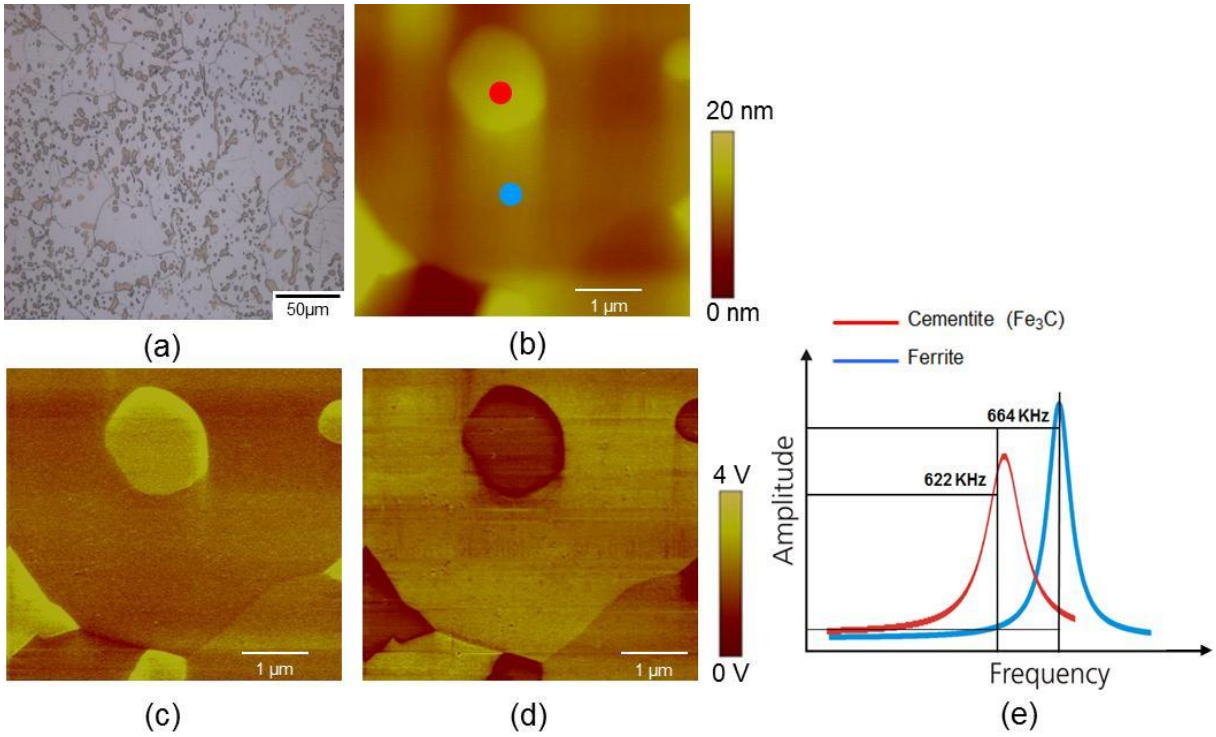

Figure 6. Unalloyed steel Fe-0.8%C with globular cementite: (a) optical micrograph; (b) AFM tapping-mode topography image; AFAM amplitude images at frequencies close to the contact resonance of the cementite phase with excitation at (c) 622 kHz and (d) 664 kHz, respectively; (e) contact resonance spectra measured on the cementite and ferrite phases (colors of spectra match the colors of the spots in the topography image) show different values depending on the local elastic properties. The images were recorded with the first bending mode of a silicon-NCL cantilever.

3. SUMMARY

AFAM was shown to be a powerful tool for nondestructive microstructure imaging and characterization as well as probing local material properties in the micro- and nanoscale of different steels if the sample surface is prepared appropriately. For AFM applications, mechanical polishing by standard procedures is not sufficient, but careful additional electrochemical polishing is required. The combination of AFM, AFAM, MFM, and EBSD techniques opens a new field for material development and design. Important insights in the deformation behavior of austenitic TWIP steels were provided via surface relief analysis by AFM during deformation. By means of MFM, ferromagnetic domain structures in cementite

particles and their interaction with a ferrite matrix was studied. The cementite domain structure was found to consist of parallel stripes alternatively down- and upwards directed in relation to the surface and without direct correlation to the ferrite domain structure. The crystalline orientation of the cementite particles was determined by EBSD and correlated to the domain structure. Finally, AFAM imaging showed that in the measured area on the unalloyed Fe-0.8%C steel ferrite is stiffer than globular cementite.

REFERENCES

[1] C. Scott, N. Guelton, S. Allain, M. Faral, *Proceedings of MS&T '05*, Sept. 26-28 2005, Pittsburgh, PA, USA.

[2] S. Allain, *PhD Thesis*, Ecole des Mines, Nancy, France, (2002).

[3] S. Allain, P. Cugy, C. Scott, J.P. Chateau, A. Rusineck, A. Deschamps, *International Journal of Materials Research* **99** (2008) 7.

[4] H. Idrissi, K. Renard, D. Schryvers, P.J. Jacques, *Scripta Materialia* **63** (2010) 961-964.

[5] D. Barbier, N. Gey, S. Allain, N. Bazzolo, M. Humbert, *Materials Science and Engineering A* **500** (2009) 196-206.

[6] U. Rabe, K. Janser, and W. Arnold, *Review of Scientific Instruments* **67** (1996) 3281-3293.

[7] K. Yamanaka and S. Nakano, *Applied Physics A* **66** (1998) 313-317.

[8] K. Yamanaka, H. Ogiso, and O.V. Kolosov, *Applied Physics Let*ters **64** (1994) 178-180.

[9] M. Kopycinska, U. Rabe, S. Hirsekorn, and W. Arnold, in *Int. Symp. Acoustical Imaging* **26**, ed. by R. Maev, Kluwer Acaademic Publishers, NY, (2002) 381-387.

[10] U. Rabe, M. Kopycinska, S. Hirsekorn, J. Muñoz-Saldaña, G.A. Schneider, W. Arnold, *Journal of Applied Physics D: Applied Physics* **35** (2002) 2621-2635.

[11] U. Rabe, "Atomic Force Acoustic Microscopy", in *Applied Scanning Probe Methods*, edited by H. Fuchs and B. Bhushan, Springer-Verlag, Berlin, (2006) 37-90.

[12] G. Binning, C.F. Quate, and Ch. Gerber, *Physics Review Letters* **56** (1986) 930-933.

[13] F. Laszlo and H. Nolle, *Journal of the Mechanics and Physics of Solids* **7** (1959) 193.

[14] B. Drapkin and B. Fokin, *Fizika Metallov i Metallovedenie* **49** (1980) 649.

[15] H. Mitsubayashi, S. Li, H. Yumoto, and M. Shimotomai, *Scripta Materialia* **40** (1999) 773.

[16] M. Umemoto, Y. Todaka, T. Takahashi, P. Li, R. Tokumiya, and K. Tsuchiya, *Journal of Metastable and Nanocrystalline Materials* **15** (2003) 607.

[17] M. Nikolussi, S.L. Shang, T. Gressmann, A. Leineweber, E.J. Mittemeijer, Y. Wang, and Z.-K. Liu, *Scripta Materialia* **59** (2008) 814-817.

[18] H. Ledbetter, *Materials Science and Engineering A* **527** (2010) 2657-2661.

[19] Altpeter, *Journal of Nondestructive Evaluation* **15** (1996) 45.

[20] Altpeter, G. Dobmann, M. Kröning, M. Rabung, S. Szielasko, *NDT&E International* **42** (2009) 283–290.

[21] G. Dobmann, "NDT – Do we have the potential to predict material properties as yield strength, tensile strength and fracture toughness on the component? A state of the art survey", 18th European Conference on Fracture, Dresden, 30.08.-03.09.2010.

[22] J. Man, K. Obrtlík, C. Blochwitz, J. Polák, *Acta Materialia* **50** (2002) 3767–3780.

[23] J. Man, K. Obrtlík, J. Polák, *Materials Science and Engineering A* **351** (2003) 123–132.

[24] J. Polák, J. Man, K. Obrtlík, *International Journal of Fatigue* **25** (2003) 1027–1036.

[25] S. Frechard, F. Martin, C. Clement, J. Cousty, *Materials Science and Engineering A* **418** (2006) 312–319.

[26] A. Hubert and R. Schaefer, *Magnetic Domains – The Analysis of Magnetic Micro-structures*, ISBN 3-540-64108-4, Springer Verlag Berlin Heidelberg New York (1998).

[27] S. Hirsekorn, U. Rabe, L. Batista, and L. Behl, "Microstructure characterization and imaging of fine-grained steel by microscopic ultrasonic techniques", *Review of Progress in Quantitative Nondestructive Evaluation (QNDE)* **30** (2011) 1097-1103.

VII. PIEZORESPONSE FORCE MICROSCOPY STUDIES ON (100), (110) AND (111) EPITAXIALLY GROWTH $BiFeO_3$ THIN FILMS (PUBLICATION F)

R. P. Fernandes, L. Batista, A. C. G. Castro, L. Salamanca-Riba, M. P. Cruz, F. J. Espinoza-Beltrán, S. Hirsekorn, U. Rabe, J. Muñoz-Saldaña, G. A. Schneider

MRS Proceedings (2012) Vol. 1477; 1097-1103.

ABSTRACT. Bismuth ferrite ($BiFeO_3$) is a magnetoelectric, multiferroic material with coexisting ferroelectric and magnetic orderings. It is considered as a candidate for the next generation of ferroelectric random-access memory devices because $BiFeO_3$, in contrast to industrial ferroelectrics used today, does not contain the toxic element lead. Furthermore, its polarization values are higher than those of lead-based ferroelectrics. The magnitude of the polarization of a $BiFeO_3$ film is dependent on its orientation and is related to the domain structure. This contribution presents and discusses the preparation of epitaxial $BiFeO_3$ (BFO) thin films grown on $SrRuO_3/SrTiO_3$ substrates by pulsed laser deposition (PLD) and their characterization, especially by piezo force microscopy (PFM) and atomic force acoustic microscopy (AFAM). The thickness of an individual BFO film varies between 100 and 200 nm. The epitaxial nature of films in the crystallographic (100), (110), and (111) directions was confirmed by x-ray diffraction (XRD). Thin $SrRuO_3$ layers, also prepared by PLD, were used as bottom electrode for the ferroelectric hysteresis measurements. Low frequency PFM measurements showed a monodomain structure for the as-grown (110) and (111) oriented samples. In BFO (100) films, different polarization variants were observed by ultrasonic piezo force microscopy (UPFM). The domain structure is reproduced from minimization of the electrostatic and elastic energies. Switching experiments using standard PFM as well as UPFM were carried out on the three samples with the objective of testing the coercive field and domain stability. The AFAM technique was used to map the elastic properties of the BFO thin-films at the micro- and nanoscale.

Keywords: Piezo response, Laser Ablation, Bismuth

1. INTRODUCTION

In the last decade, extensive research has been devoted to multiferroic materials, in particular to multiferroic magnetoelectrics [1,2,3]. This is due to the fascinating physics behind their response to external fields as well as to the potential applications for industry. More important than the usual ferromagnetism or ferroelectricity response is the coupling of the two effects which gives rise to a wide spectrum of new applications, e.g. memory elements with electric as well as magnetic data storage and media allowing data writing by an electric field and reading by the associated magnetic response [1].

Advances in the development of multiferroic magnetoelectrics are correlated with advances in the technology of thin film growth techniques. The availability of high quality thin films and advanced characterization tools have led to a better understanding of the phenomena of this class of materials [4]. Bismuth ferrite ($BiFeO_3$, BFO) is a room temperature, single-phase, magnetoelectric multiferroic with a high ferroelectric Curie temperature (T_C) of 1100 K and an antiferromagnetic Néel temperature (T_N) of 640 K [4]. The largest polarization value at room temperature reported so far is 100 μC/cm² for an epitaxial (111) oriented thin-film [5]. The ferroelectric domain structure and its control are described in [6,7], and the electrical control of the antiferromagnetic domains in bismuth ferrites at room temperature is reported in [8].

This work presents results on the growth and characterization of bismuth ferrite epitaxial thin films with different crystallographic orientations. The ferroelectricity and the domain structures are characterized by conventional PFM [9] and UPFM [10]. AFAM [10,11] was employed to investigate the local elastic properties of the films.

2. EXPERIMENTS, RESULTS AND DISCUSSIONS

BFO thin films were grown by PLD along the [100], [110] and [111] crystal orientations using $SrTiO_3$ substrates under the conditions outlined in Table 1. A $SrRuO_3$ buffer layer of less than 100 nm thickness was grown before deposition of the $BiFeO_3$. A $Bi_{1.1}FeO_3$ target was used to obtain the stoichiometry of the BFO thin films. An oxygen partial pressure of 100 mTorr was used to compensate for any deficiencies that may arise at the time of deposition. This oxygen pressure leads to a homogeneous thickness of ~ 200 nm.

Table 1. Pulsed laser deposition parameters.

Parameter	Value
Fluence	1.0 J/cm^2
Target-substrate distance	50 mm
Substrate Temperature	650 °C
Oxygen pressure	100 mTorr
Targets	$Bi_{1.1}FeO_3$, $SrRuO_3$
Deposition rate	6.5 nm/min (SRO) 10 nm/min (BFO)
Laser frequency	10 Hz
Substrates	$SrTiO_3$ (100), (110), (111)

Figure 1 shows the diffraction spectra of the $BiFeO_3/SrRuO_3/SrTiO_3$ samples deposited on different orientations on $SrTiO_3$ substrates. Epitaxial growth is clearly observed, and there are no traces of impurities, such as, iron oxides or bismuth oxides or other bismuth iron oxides with different stoichiometry than $BiFeO_3$ in the films. As expected, a shift to higher angles occurs between the peaks for each growth orientation due to the decrease in interplanar distance as they relate to different families having planar symmetry: namely, d (100) = 4.0614 Å, d (110) = 2.8319 Å, and d (111) = 2.3124 Å. The lattice parameters, both for the buffer layer and the BFO thin film remain approximately invariant in the different orientations, averaging 4.0058 Å, 3.9511 Å, and 3.9051 Å for BFO, SRO and STO, respectively.

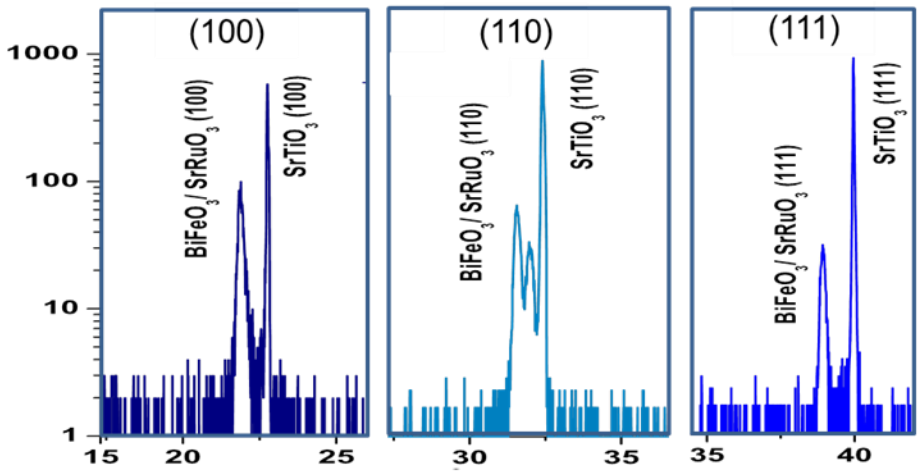

Figure 1. XRD spectra of $BiFeO_3/SrRuO_3$ thin films on $SrTiO_3$ oriented along the (100), (110), and (111) crystallographic planes.

To examine the elastic properties of the films, AFAM measurements were performed on all samples. AFAM amplitude images yield qualitative surface elasticity maps. While the

sample surface is scanned, the AFM cantilever is excited to vibrate at a fixed ultrasonic frequency close to a contact resonance. The cantilever vibration amplitude, and thus the AFAM image contrast, depends on the difference between the excitation frequency and the local contact resonance. The measurements were made with Pt-Ir coated tips (Nanosensors PPP-EFM, Neuchâtel, Switzerland) with the free resonance of the first bending mode around 70 kHz. A representative AFAM image along with the topographic AFM image of the BFO (100) sample are presented in Figure 2. The bright spots on Figure 2 are inclusions and are common in PLD prepared thin films.

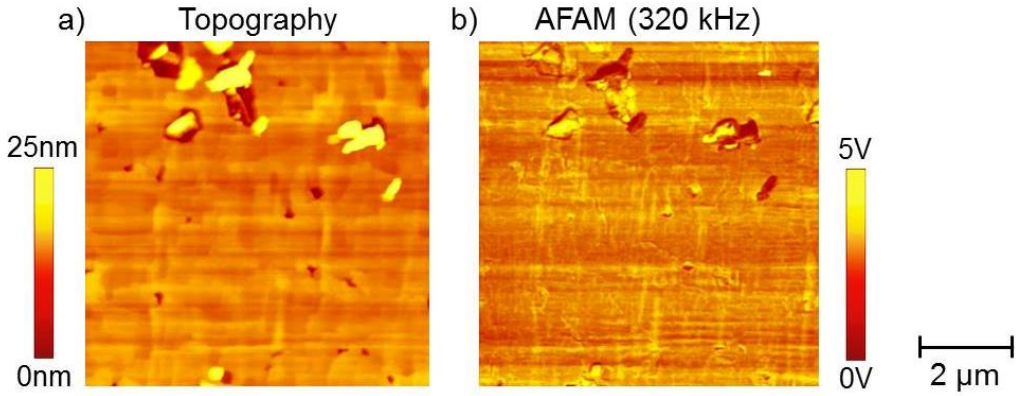

Figure 2. a) Topography and b) AFAM images from the BFO (100) sample at a frequency of 320 kHz, close to the contact resonance of the first bending mode of the cantilever. The elastic properties of the film are homogeneous with exception of the inclusions (bright contrast on the topography image).

The PFM experiments were performed using two different approaches: the conventional low frequency, in which the excitation frequency is well below the resonances of the cantilever, and the UPFM mode with excitation close to the contact resonance of the first bending mode of the cantilever which enhance the piezo-mode signal through resonance amplification [10]. Experiments done at the Technische Universität Hamburg-Harburg (TUHH) were carried out on a VEECO Dimension 3100 AFM with a Nanoscope IV controller, while a VEECO Dimension 3000 with a Nanoscope IIIA controller was used at Fraunhofer IZFP. Pt-Ir coated probes were used for all measurements. For the conventional PFM an excitation frequency of 10 kHz with amplitude of 3-5 V was applied to the tip. For the UPFM an excitation frequency around 320 kHz with an amplitude of 4 V was applied to the tip. In order to confirm ferroelectricity, poling experiments were carried out by applying a DC voltage to the tip while the bottom electrode (SRO) was grounded. In this way, the ferroelectric film below the tip switches its polarization direction. This method was applied to films with the three different growth directions and using both conventional PFM and UPFM,

for simplicity only selected images are shown is this work. In all films the presence of small amounts of inclusions was detected.

The images after the switching experiment with +22 V along with the topographic image for the BFO (110) sample are shown in Figure 3. The lateral components of the two polarization variants [4,5] are clearly observed in Fig. 3c, where the scanning (horizontal) direction is parallel to the <110> direction. The inclusions, visible as the bright spots in the topography image, do not show any piezoactivity and are visible in the VPFM and LPFM Signals as spots with color corresponding to 0 V.

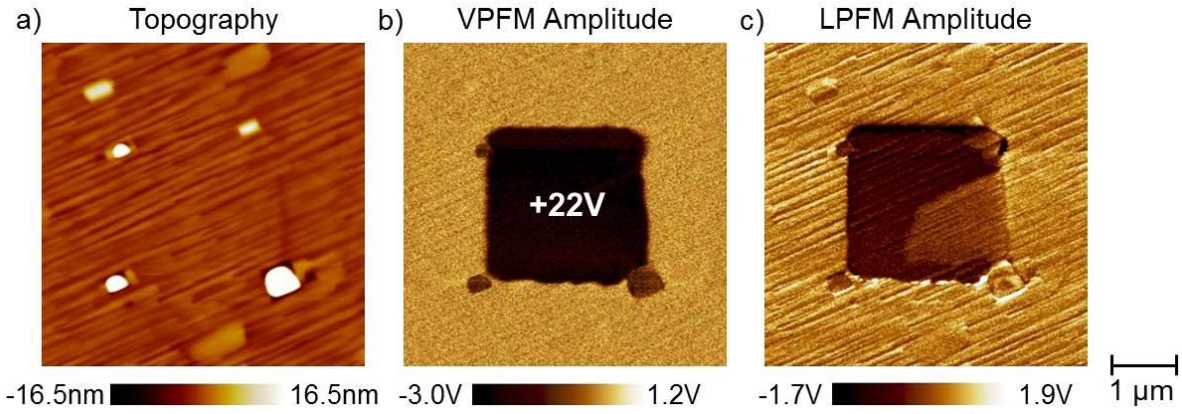

Figure 3. a) Topography, b) Vertical PFM (VPFM), and c) Lateral PFM (LPFM) of ferroelectric domains written on BFO (110) film by applying +22 V DC while scanning over a 3 x 3 μm^2 area of the sample. The polarization direction clearly changes (dark contrast) in the VPFM image and the LPFM image.

In the case of the BFO (111) sample, no lateral component of the PFM signal is expected. Figure 4 shows the results of the switching experiments for this sample. The first square was switched by applying +22 V over an area of 2 x 2 μm^2 and creates a dark contrast in the VPFM image. For the second switching, a voltage of -22 V was applied over an area of 1 x 1 μm^2 within the previously polarized area. The second switching led to a reversal of the polarization direction to the initial condition. For both samples the PFM signals were stable for up to 8 hours after the switching experiments; indicating that the expected quality of the film and behavior of the domain structure was achieved. The single- (mono-) domain state of the films can be explained by the strain in the films induced by the substrate as previously reported [1].

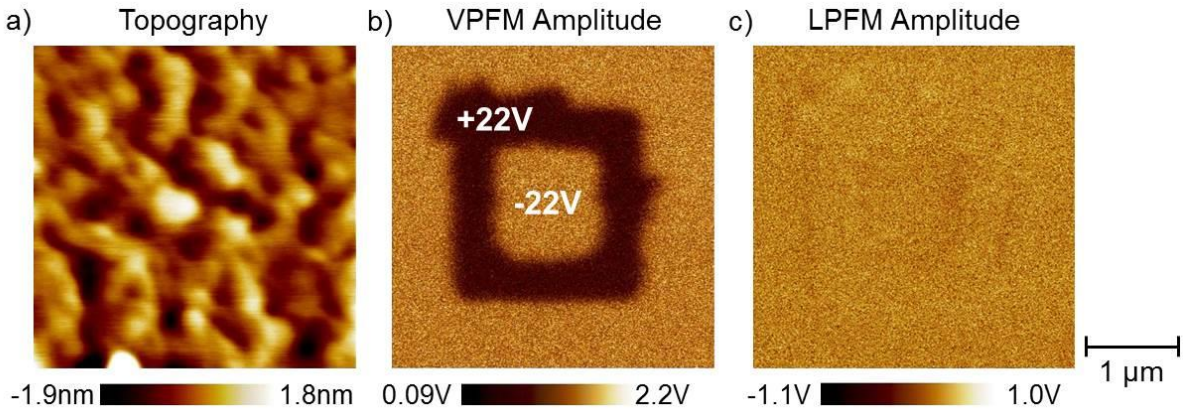

Figure 4. a) Topography and b) Vertical PFM images of ferroelectric domains written on BFO (111) film by applying +22 V DC while scanning over a 2 x 2 μm^2 area of the sample followed by an applied DC voltage of -22 V while scanning over a 1 x 1 μm^2 area within the already polarized area.

The BFO (100) sample is grown in a favorable direction for the visualization of the domain structure; therefore, it does not need local switching of the polarization direction in order to visualize the domains. Figure 5 shows the amplitude and phase signals of the vertical and lateral UPFM measurements for this sample. The UPFM images were recorded with a frequency close to the contact resonance (320 kHz) of the first bending mode of the cantilever. The observed striped domain structure correlates very well with other reports in the literature [1,4,12]. This indicates that the BFO (100) sample is of high quality and has the expected domain structure.

Finally, in order to quantify the piezoelectric activity of the BFO (100) sample, the PFM system was used to measure the deflection on the cantilever at different applied voltages. Figure 6 presents the measured data and the linear fit which yields $d_{33} = 39 \pm 2$ pm/V. This value is in line with those from literature: $d_{33} = 30\text{-}50$ pm/V [1,12].

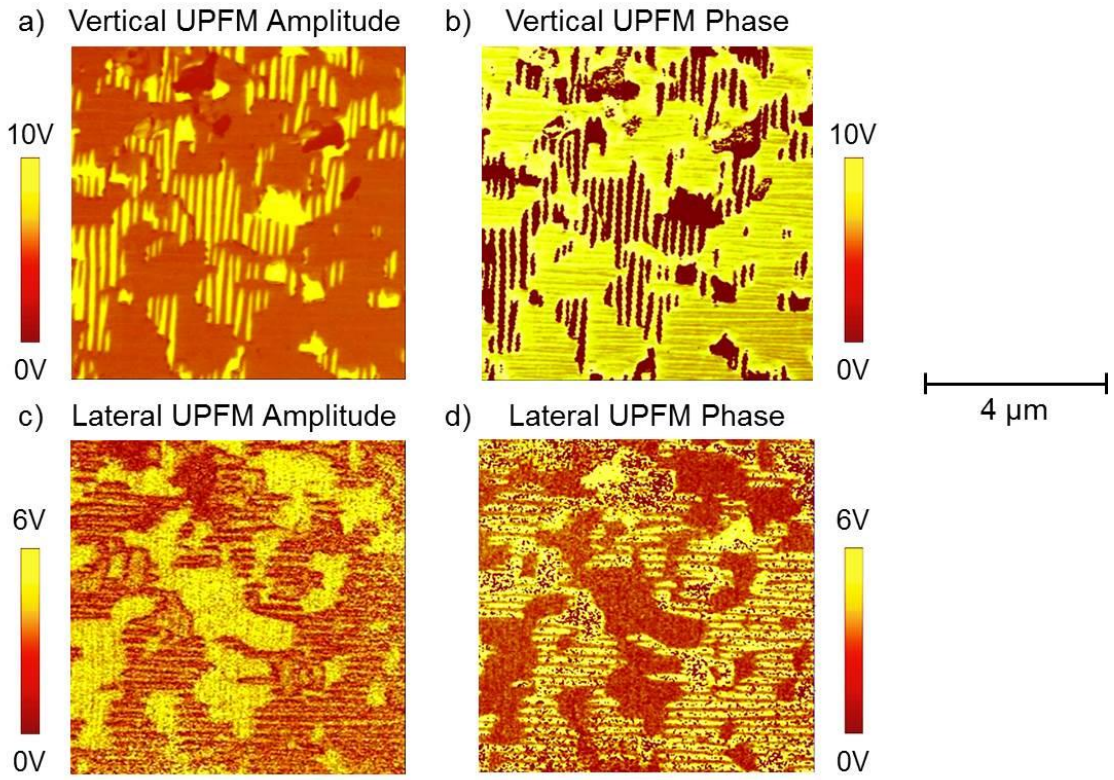

Figure 5. UPFM signals from BFO (100) film: Vertical UPFM a) amplitude and b) phase; Lateral UPFM c) amplitude and d) phase. The domain structure is visible without local switching.

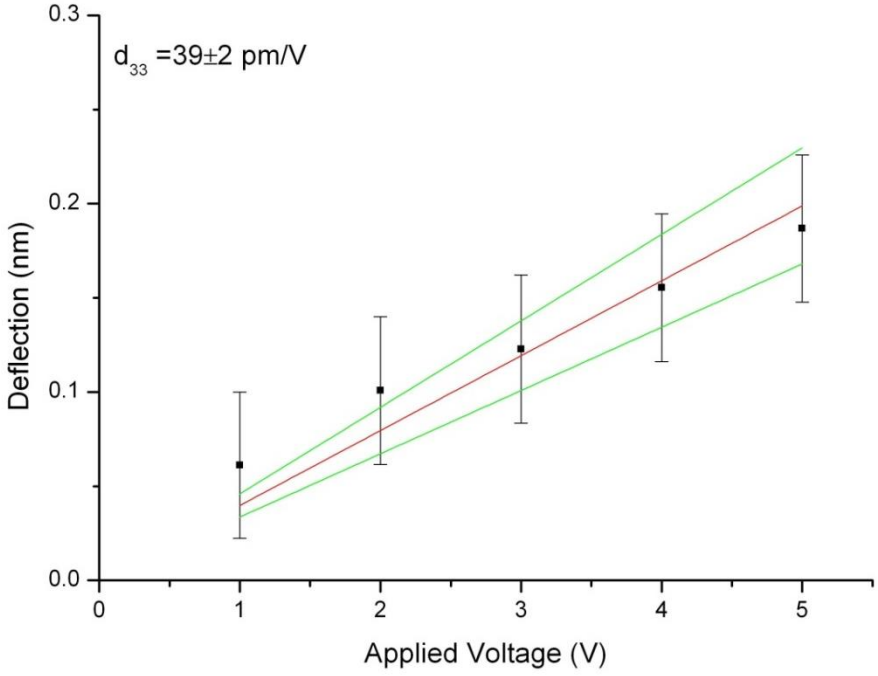

Figure 6. Piezoelectric constant d_{33} measured using the PFM system.

3. CONCLUSIONS

We successfully grew high quality bismuth ferrite (BFO) epitaxial thin films on (100), (110) and (111)-oriented $SrRuO_3/SrTiO_3$ substrates. The quality of the films was evaluated by XRD confirming the epitaxial orientation of the films and the absence of second phases. PFM and UPFM showed that the (111) and (110) oriented films are ferroelectric but are in a monodomain state and that the (100) film shows a striped domain structure, as already reported in the literature. The evaluation of the d_{33} piezoelectric constant for the (100) film yields a value of $d_{33} = 39 \pm 2$ pm/V, which is also in agreement with values already published in the literature. AFAM measurements showed the homogeneity of the elastic properties of all films.

REFERENCES

[1] N.A. Hill, *Journal of Physical Chemistry B* **104** (2000) 6694-6709.

[2] J. Wang, J. B. Neaton, H. Zheng, et al., *Science* **299** (2003) 1719.

[3] G. Catalan and J. F. Scott, *Advanced Materials* **21** (2009) 2463.

[4] R Ramesh, N.A. Spaldin, *Nature Materials* **6** (2007) 21-29.

[5] S.K Singh, H. Ishiwara, K. Maruyama, *Journal of Applied Physics* **100** (2006) 64102-64105.

[6] Y. Chu, M.P. Cruz, C. Yang, et al., *Advanced Materials* **19** (2007) 2662-2666.

[7] Y. Chu, Q. Zhan, L.W. Martin, et al., *Advanced Materials* **18** (2006) 2307-2311.

[8] T. Zhao, A. Scholl, F. Zavaliche, et al., *Nature Materials* **5** (2006) 823-829

[9] A. Gruverman, O. Auciello, and H. Tokumoto, *Annual Review of Materials Science* **28** (1998) 101.

[10] U. Rabe, M. Kopycinska, S. Hisekorn et al., *Journal of Applied Physics D: Applied Physics* **35** (2002) 2621.

[11] U. Rabe, K. Janser, W. Arnold, *Review of Scientific Instruments* **67** (1996) 3281-3293.

[12] F. Zavaliche, S.Y. Yang, T. Zhao, et al., *Phase Transitions* **79** (2006) 991-1017.

VIII. CHARACTERIZATION OF MATERIAL PROPERTIES AND FUNCTIONALITIES OF LEAD-FREE BISMUTH-BASED CERAMICS (PUBLICATION G)

L. Batista, U. Rabe, S. Hirsekorn

Part of the FP7-NMP-2010 EU-Mexico BisNano 263878 report, workpackage 9 (WP9), January (2014).

ABSTRACT. Ferroelectric materials are widely used in many applications as sensors, actuators, transducers, and memories. Most of these materials are however based on toxic elements, as e.g. lead (Pb), which can create hazards during materials processing and also disposal. With the new European regulations restricting the use of such toxic elements, the need arises for new materials which provide the same or better functional properties. These properties such as piezoelectric constants and high electromechanical coupling factors are mostly determined by the microstructure and the arrangement of the ferroelectric domains. In the framework of a European-Mexican project, lead-free Bismuth-based bulk ceramics like $Bi_{0.5}Na_{0.5}TiO_3$ (BNT), $0.94Bi_{0.5}Na_{0.5}TiO_3$-$0.06BaTiO_3$ (BNT-BT), Mn-doped BNT-BT, and Sr-doped BNT-BT were investigated and evaluated by different operating modes of an atomic force microscope (AFM), especially dynamic modes in the ultrasonic range such as atomic force acoustic microscopy (AFAM) and ultrasonic piezoelectric force microscopy (UPFM). Macroscopic properties of the above mentioned lead-free, bismuth-based, polarized bulk samples were also examined. Their piezoelectric activity was characterized by impedance and 3D laser vibrometer measurements. Mechanical properties such as Young's and shear moduli were determined by measuring longitudinal and transverse sound wave velocities and the density. Using these data and the geometrical parameters of the samples, the first thickness and radial resonance frequencies were calculated and compared to experimental spectra. In the end, the most promising lead-free ceramic samples were then successfully tested as ultrasonic transducer materials.

1. INTRODUCTION

The work presented in this chapter is a part of the FP7-NMP-2010 EU-Mexico BisNano 263878 report, workpackage 9 (WP9). The general objective of the BisNano project [1] is the acquisition of fundamental knowledge on bismuth-based nanostructures, as a new class of materials towards the development of value-added bismuth-based products and devices. One of the specific objectives, which is included in WP9, is the evaluation of the functionalities of the bismuth-based materials for a variety of applications, as e.g. lead (Pb)-free piezoelectrics.

In this context, lead-free bulk ceramic samples from different partners (UPJV, CINVESTAV and TUHH, see Table 1) have been sent to IZFP for materials characterization, in WP9 especially for piezo-response characterization.

Table 1. BisNano partners who worked with IZFP in WP9.

Institution	Location
Université de Picardie Jules Verne (UPJV)	Amiens, France
Centro de Investigación y Estudios Avanzados (CINVESTAV)	Querétaro, Mexico
Technische Universität Hamburg-Harburg (TUHH)	Hamburg, Germany

2. BULK SAMPLES FROM UPJV AND COMMERCIAL REFERENCE MATERIAL

In order to characterize the macroscopic piezoelectric and elastic properties of the lead-free bulk ceramic samples produced in our consortium, impedance, 3D laser vibrometer and ultrasound measurements were performed. The samples were coated with electrodes if necessary and polarized. Impedance measurements before and after polarization showed whether the samples were macroscopically active. Using a laser vibrometer, the resonance frequencies of the samples were detected, and the maximal surface vibration amplitudes were measured quantitatively.

A bulk BNT sample and a bulk BNT-BT sample (circular plates with a thickness of 2.8 mm and 2.7 mm, and a diameter of 12 mm and 11.1 mm, respectively, were provided by UPJV. The composition of the investigated materials is shown in Table 2.

Table 2. Composition of the investigated lead-free ceramic samples.

Abbreviation	Chemical composition
BNT	$(Bi_{0.5}Na_{0.5})TiO_3$
BNT-BT	$0.94(Bi_{0.5}Na_{0.5})TiO_3$-$0.06BaTiO_3$

The sample surfaces were sputtered with a thin gold electrode layer. By means of impedance measurements no activity was found for both samples (Figs. 1a and b) in their initial not polarized state.

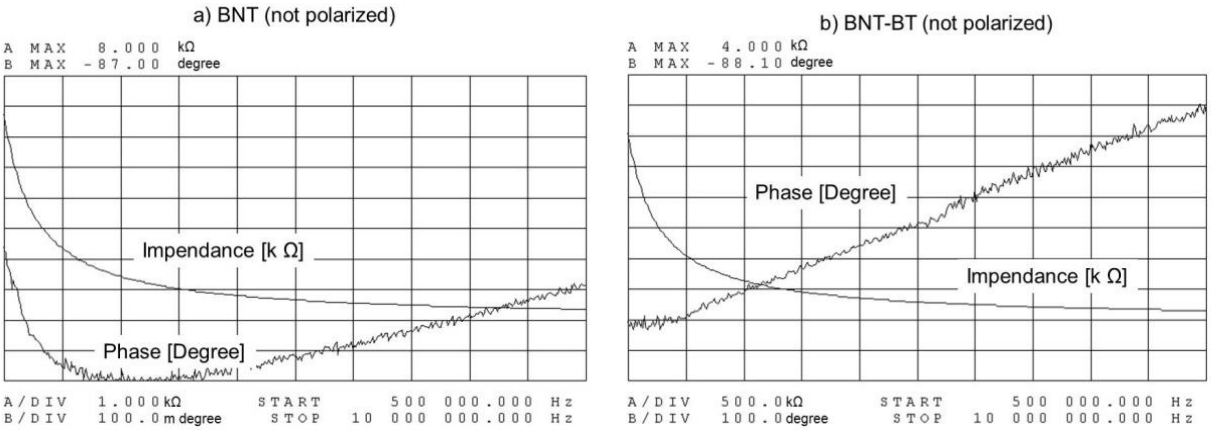

Figure 1. Impedance measurements on the samples (a) BNT and (b) BNT-BT in their initial state before polarization.

Then, in order to polarize the samples, a DC voltage of 7.5 kV was applied first at the BNT-BT sample. It was interrupted after 2 min because of extreme heating of the sample. Nevertheless, the sample showed very small piezoelectric activity (Fig. 2) after this polarization. In order to avoid the heating, both samples were immersed in an electronic fluid (3M Fluorinert FC-770) which cooled the samples.

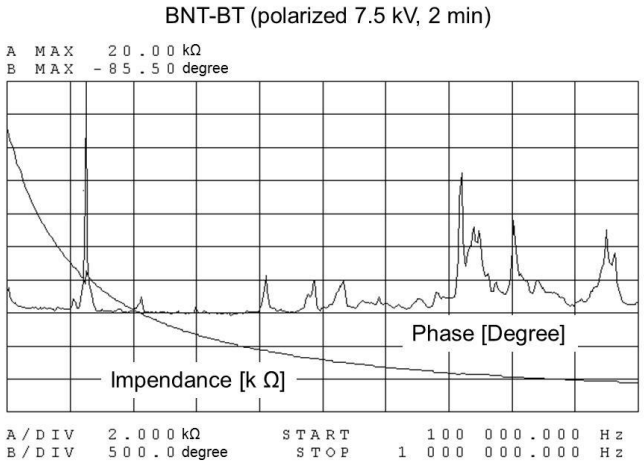

Figure 2. Impedance measurements on the sample BNT-BT polarized by 7.5 kV during 2 minutes.

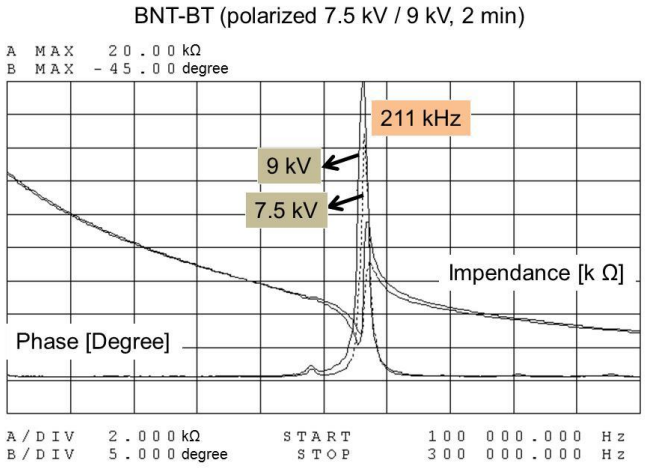

Figure 3. Impedance measurements on the sample BNT-BT after being polarized for 2 minutes at 7.5 kV and 9 kV, respectively.

Using this set-up, a voltage of 7.5 and 9 kV, respectively, was applied for 2 minutes. After this treatment, the BNT sample still was inactive, but on the BNT-BT sample piezoelectric activity was clearly detectable, and the frequencies of thickness and radial resonances and anti-resonances have been measured (Fig. 3).

The procedures described above damaged the gold electrodes. Therefore, the samples were coated with a thin layer of a conductive adhesive. In order to evaluate the piezoelectric activity, an AC voltage of 20 V was applied to both samples while the frequency was swept from 100 kHz to 1 MHz within 200 ms. The resulting surface vibrations of the samples were measured by a 3D laser vibrometer. The set-up of the laser vibrometer and the sample are shown in Fig. 4. The BNT sample did not show surface vibrations. On the BNT-BT sample, amplitudes of up to 17 pm only were measured. The frequency spectrum of the BNT-BT sample vibration detected by the vibrometer is shown in Fig. 5.

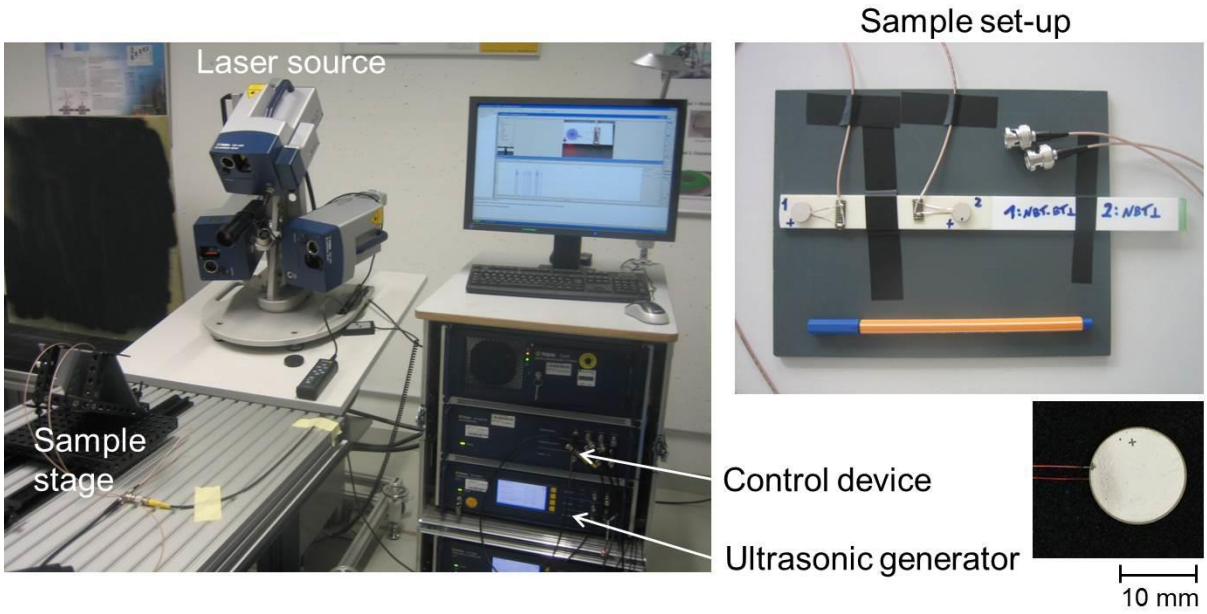

Figure 4. Set-up for the 3D laser vibrometer measurements.

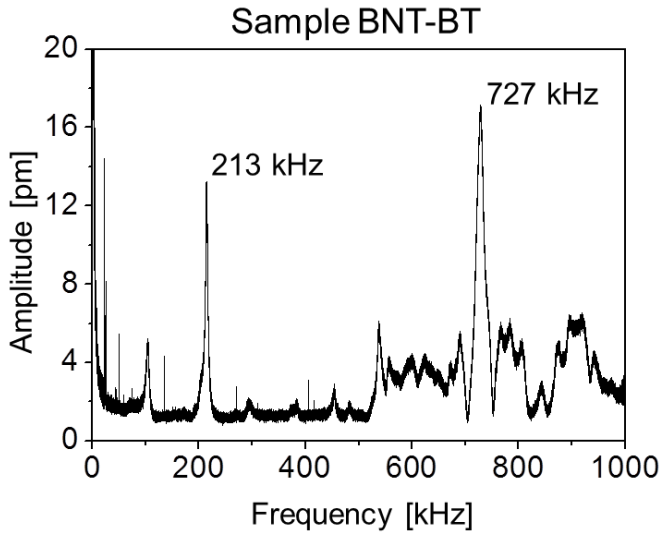

Figure 5. Frequency spectrum obtained by laser vibrometer measurement on the sample BNT-BT. Resonances were detected at 213 kHz and at 727 kHz as indicated in the figure.

As a reference, bulk lead-free piezoelectric ceramic samples from a commercial company have been ordered by IZFP (circular plates with a thickness of 1 mm and a diameter of 10 mm, coated with electrodes, PIC 700, PI Ceramic GmbH, Lederhose, Germany). The ceramic samples are based on Bismuth Sodium Titanate (BNT) and are still at a laboratory production level. The piezoelectric activity of these samples was checked by means of impedance measurements and 3D laser vibrometer. The results were compared with a standard PZT sample (PZ 29, Ferroperm Piezoceramics A/S, Kvistgard, Denmark) and with the results from the bulk ceramic sample BNT-BT received from UPJV. The objective was to

compare the macroscopic piezoelectric activity of a commercial lead-free piezoelectric ceramic sample with the samples produced in our consortium.

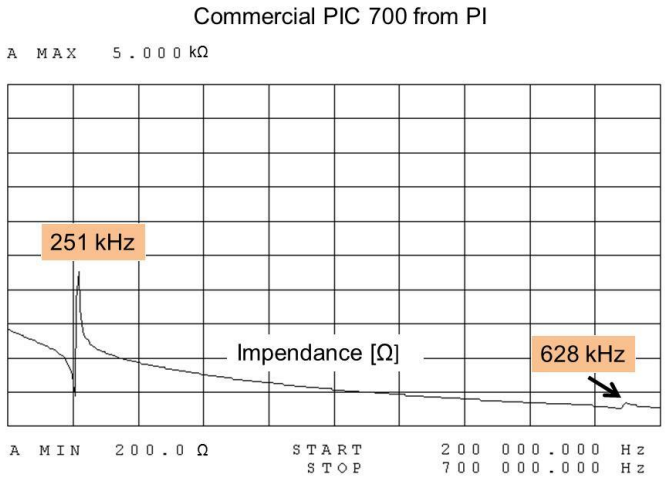

Figure 6. Impedance measurements on the commercial lead-free piezoceramic PIC 700.

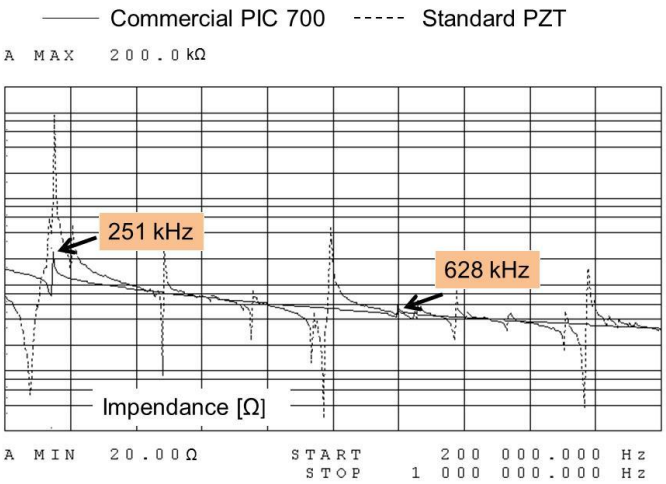

Figure 7. Impedance measurements on the commercial lead-free piezo-ceramic PIC 700 (continuous line) and on a standard PZT (PZ 29) from Ferroperm Piezoceramics A/S (dotted line).

Figure 6 shows the impedance curve of a PIC 700 sample. It is macroscopically active displaying impedance maxima at 251 kHz and 628 kHz. In order to compare the activity of the PIC 700 sample with a standard PZT, the impedance curves of both samples were plotted in Fig. 7. The PZT sample shows a much larger activity. The piezoelectric coupling factors of BNT and BNT-BT components are lower than those of conventional PZT materials.

3. BULK SAMPES FROM CINVESTAV AND TUHH

Further bulk samples were produced in the BisNano consortium, BNT-BT and Mn-doped BNT-BT were provided by CINVESTAV and Sr-doped BNT-BT was provided by TUHH. These samples were the most promising bulk lead-free piezoelectric materials for ultrasonic transducer applications. The commercial lead-free ceramic PIC 700 mentioned in the previous chapter was taken for comparison. The composition of the investigated materials is shown in Table 3.

Table 3. Composition of the investigated lead-free ceramic samples.

Abbreviation	Chemical composition
BNT-BT	$0.94(Bi_{0.5}Na_{0.5})TiO_3$-$0.06BaTiO_3$
Mn-doped BNT-BT or BNT-BT + 0.005Mn or BNT-BT-Mn	$0.995(0.94(Bi_{0.5}Na_{0.5})TiO_3$-$0.06BaTiO_3)$-0.005Mn
Sr-doped BNT-BT or BNT-BT-ST or BNT-BT-Sr	$(0.85(Bi_{0.5}Na_{0.5})TiO_3$-$0.12BaTiO_3$-$0.03SrTiO_3)$

3.1 Macroscopic measurements with the bulk samples from CINVESTAV and TUHH

For the samples in Table 3, the bulk ultrasound longitudinal and transverse wave velocities were measured at a frequency of 5 MHz. The Young's (E) and the shear (G) moduli were determined from the measured densities and sound velocities, the first thickness and radial resonances of the samples were calculated from the sound velocities and the geometrical parameters (Table 4). The results indicate that the Sr-doped BNT-BT (BNT-BT-Sr) sample has the highest E and G moduli. The direct comparisons of elastic properties should be carefully analyzed since the samples have different densities, which also influence the elastic properties. Thus the results may be misinterpreted.

Table 4. Parameters obtained by measurement in IZFP (geometry, density, elastic constants, resonant frequencies) of the samples in Table 3.

	BNT-BT	BNT-BT-Mn	BNT-BT-Sr	PIC 700
Thickness *t* [mm]	1.43	1.51	1.24	0.99
Diameter *d* [mm]	12.35	12.21	11.6	12
Density ρ [g/cm^3]	5.18	5.46	5.64	5.69
Long. sound velocity v_L [mm/µs] (5 MHz)	4.85	5.21	5.18	5.02
Trans. sound velocity v_T [mm/µs] (5 MHz)	2.77	2.98	2.97	2.82
Young´s modulus *E* [GPa]	99.9	121.6	125.1	114.9
Shear modulus *G* [GPa]	39.7	48.3	49.9	45.2
First long. thickness resonance [kHz]	1692	1720	2078	2539
First long. radial resonance [kHz]	196	213	223	209

In order to examine whether the samples are macroscopically active, impedance measurements were performed. First, all lead-free ceramic samples were poled by applying an electric field of 38 kV/cm for 2 min. For this purpose, the samples were sputtered with a thin gold electrode layer. The impedance curves for the BNT-BT and Mn-doped BNT-BT samples are shown in Fig. 8 (a), those of the Sr-doped BNT-BT and PIC 700 samples in Fig. 9 (a).

By means of impedance measurements the activity of the samples was confirmed, and the radial and thickness resonances for all samples were identified. From the resonance (f_r) and anti-resonance (f_a) peaks the planar and thickness coupling coefficients K_p and K_t, respectively, were calculated (Table 5) using the following equations:

$$K_p = \sqrt{2.51\frac{f_a - f_r}{f_a} - \left(\frac{f_a - f_r}{f_a}\right)^2}. \quad (1)$$

$$K_t = \sqrt{\frac{\pi}{2}\frac{f_r}{f_a} * cot\left(\frac{\pi}{2}\frac{f_r}{f_a}\right)}. \quad (2)$$

Please note that at higher frequencies, the resonance and anti-resonance peaks of the BNT-BT and BNT-BT-Mn samples were not very clear (indicated by red and black ellipses in Fig. 8a). Therefore the coupling factor K_t of those samples is only an approximation.

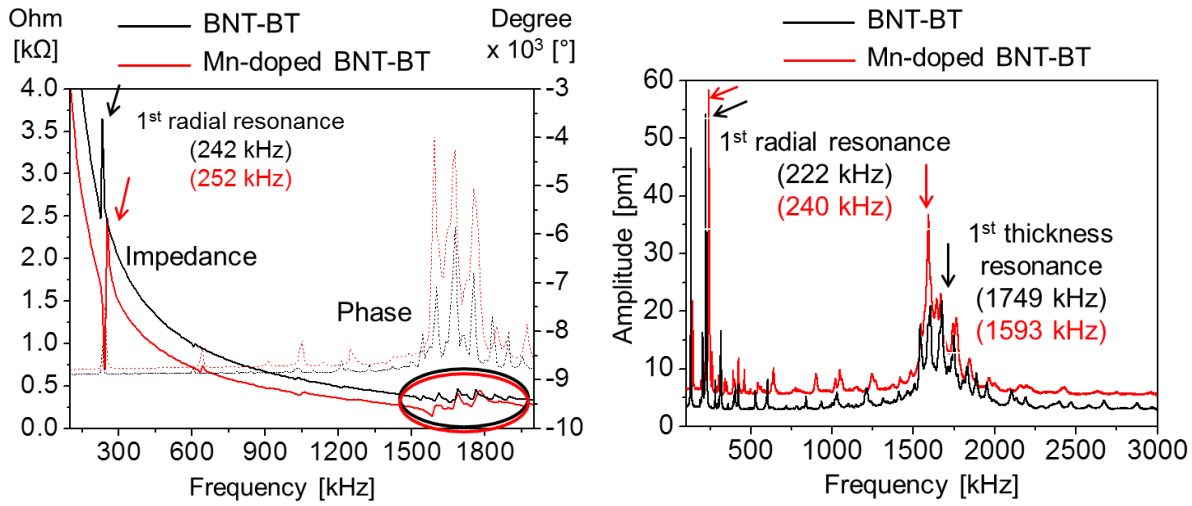

Figure 8. (a) Frequency plot of the electrical impedance and phase angle for the BNT-BT and Mn-doped BNT-BT samples. (b) Laser vibrometer measurement on the BNT-BT and Mn-doped BNT-BT samples showing clearly the amplitude vibrations at their respective resonances.

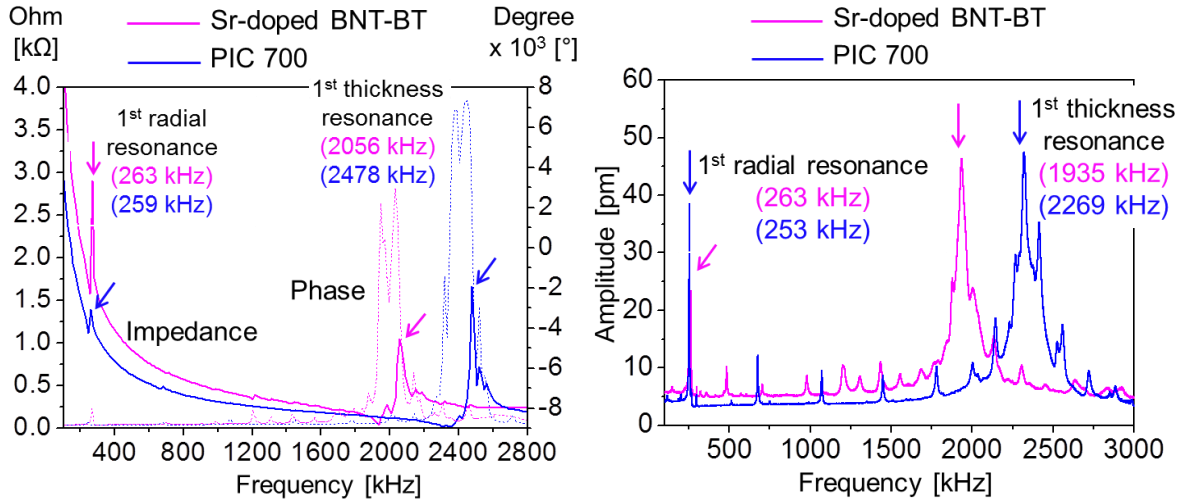

Figure 9. (a) Frequency plot of the electrical impedance and phase angle for the Sr-doped BNT-BT and PIC 700 samples. (b) Laser vibrometer measurement on the Sr-doped BNT-BT and PIC 700 samples showing clearly the amplitude vibrations at their respective resonances.

The impedance curves reveal that the Sr-doped BNT-BT and the commercial PIC 700 samples show much higher resonance and anti-resonance peaks at higher frequencies than the BNT-BT and Mn-doped BNT-BT samples.

Using the 3D laser vibrometer, the radial and thickness resonances of all samples were again identified. An AC voltage of 20 V was applied while the frequency was swept from 100 kHz to 3 MHz within 10 ms. Fig. 8 (b) shows the amplitude versus frequency plot for the BNT-BT and Mn-doped BNT-BT samples, and Fig. 9 (b) shows the amplitudes of the Sr-

doped BNT-BT sample and the PIC 700 sample. The first radial and thickness resonances of all samples are indicated in the figures. The results for the radial and thickness resonances using calculations based on bulk ultrasonic velocities (Table 4), impedance and the laser vibrometer (Figs. 8 and 9) measurements are in a good agreement.

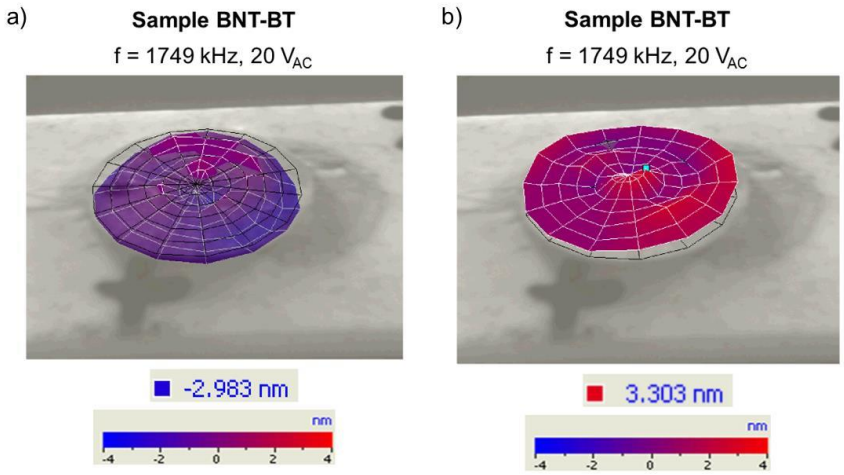

Figure 10. Local surface displacement obtained by laser vibrometry measurements on the BNT sample. An AC voltage of 1749 kHz frequency was applied. The images show the surface displacement at the negative maximum (a) -20 V and at the positive maximum (b) 20 V of the AC voltage.

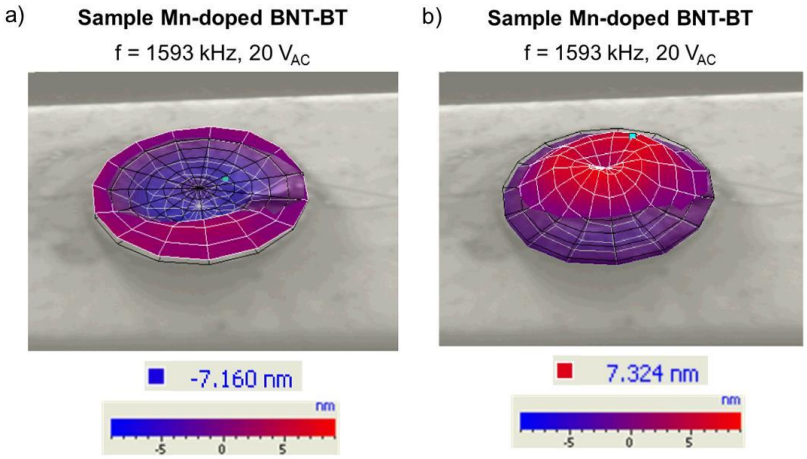

Figure 11. Local surface displacement obtained by laser vibrometry measurements on the Mn-doped BNT-BT sample at (a) -20 V and (b) 20 V. An AC voltage of 1593 kHz frequency was applied.

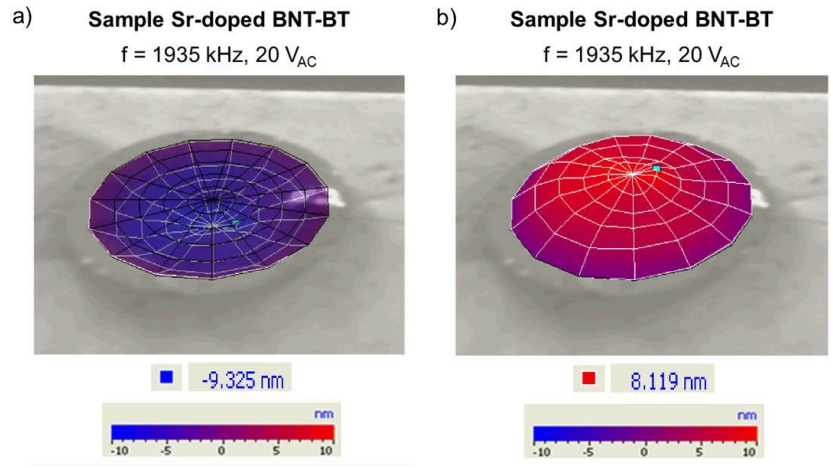

Figure 12. Local surface displacement obtained by laser vibrometry measurements on the Sr-doped BNT-BT sample at (a) -20 V and (b) 20 V. An AC voltage of 1935 kHz frequency was applied.

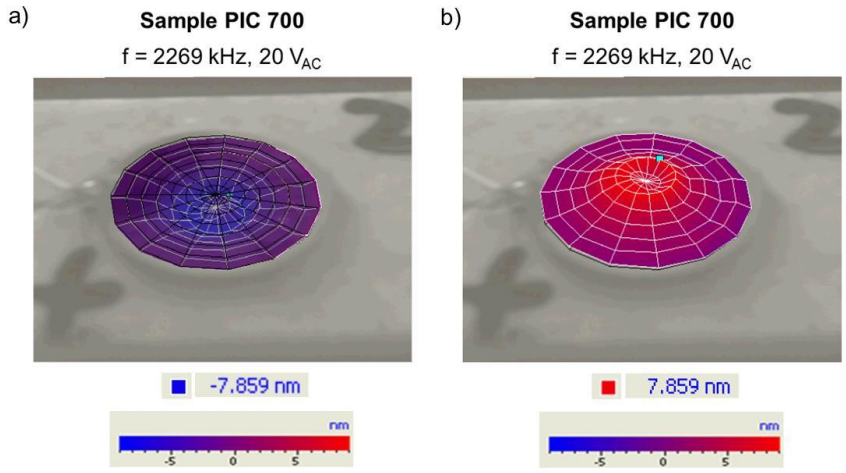

Figure 13. Local surface displacement obtained by laser vibrometry measurements on PIC 700 sample at (a) -20 V and (b) 20 V. An AC voltage of 2269 kHz frequency was applied.

In order to measure the maximal surface vibration amplitudes, the samples were scanned at their respective thickness resonance frequencies using again the laser vibrometer technique. All measurements were performed by applying an AC voltage of 20 V. Figure 10 shows the laser vibrometer displacement measurements on the BNT-BT sample at 1749 kHz. The maximal vibration amplitude measured close to the center point of the sample yields 6 nm. On Mn-doped BNT-BT the laser vibrometer displacement measurements show at 1593 kHz a 14 nm amplitude (Fig. 11). The same measurements were performed on the Sr-doped BNT-BT and the PIC 700 samples as shown in Figs. 12 and 13, respectively. On the Sr-doped BNT-BT sample the measurement was performed at 1935 kHz, on the PIC 700 at

2269 kHz. The maximal vibration amplitudes are similar for both samples (about 18 nm). The summary of the results can be found in Table 5.

Table 5. Summary of the measured properties using laser vibrometry and impedance techniques.

	BNT-BT	BNT-BT-Mn	BNT-BT-Sr	PIC 700
Thickness resonance [kHz] (Laser vibrometer)	1749	1593	1935	2269
Maximal surface vibration amplitude measured at the thickness resonance [nm]	6	14	18	18
Planar coupling coefficient (K_p)	0.32	0.31	0.33	0.37
Thickness coupling coefficient (K_t)	0.20	0.27	0.37	0.35

3.2 Scanning probe measurements with the bulk materials from CINVESTAV and TUHH

In addition to the macroscopic measurements, IZFP used micro- and nanoscopic techniques to characterize the bulk samples provided by the project partners. In order to investigate the micro- and nanoscopic piezoelectric properties of the lead-free bulk ceramic samples produced in our consortium, AFM, AFAM and UPFM measurements were additionally performed. The surface of the samples was carefully prepared using standard polishing procedures. At IZFP, the PFM (Piezoresponse Force Microscopy) is combined with ultrasonic techniques enabling the piezo-mode signal being enhanced through resonance amplification. This technique is called Ultrasonic Piezoresponse Force Microscopy (UPFM) [2]. The AFM, AFAM and UPFM investigations were performed using an Electrical Force Microscopy (EFM)-cantilever (silicon cantilever coated with a Pt/Ir layer, PPP-EFM, NanoWorld AG, Neuchâtel, Switzerland). The static spring constant of this type of cantilever is in the range of 1-5 N/m. Prior to the AFAM and UPFM investigations the conventional AFM contact mode was used to examine the surface topography of the sample surfaces, their roughness and cleanness. The topography mode is furthermore active simultaneously to the ultrasonic operation modes. Additional ultrasonic equipment is used in combination with the commercial AFM for the AFAM and UPFM modes (chapter I, section 2 and 3). AFAM amplitude images yield qualitative surface elasticity maps. In the UPFM mode, either amplitude or phase images are taken for information about the sample's piezo activity.

Qualitatively, an increased contrast in the UPFM amplitude image corresponds to an increased piezo activity. Similar to the vertical and lateral low frequency PFM modes, a vibration of the cantilever in bending mode vertical to the sample surface corresponds to out-of-plane sample surface activity (vertical UPFM), while a torsional vibration of the cantilever corresponds to an in-plane sample surface activity (lateral UPFM). In this work, only UPFM was performed. The ferroelectric properties of the samples were further examined by local polarization experiments. A DC voltage of variable amplitude and poling direction was applied between the tip and the sample while the sample surface was scanned. Afterwards the same area was imaged in the UPFM mode to see whether the PFM contrast was changed locally. The negative or positive DC voltage was increased stepwise from 5 V to 20 V until the domain writing was successful. The first free flexural frequency of the type of cantilever used here is found in the frequency range of 50-100 kHz and the corresponding first flexural contact resonance frequency is found in the frequency range of 300-700 kHz.

Figure 14 (a) shows the contact-mode topography image of the BNT-BT bulk sample produced by CINVESTAV. The vertical UPFM amplitude image is shown in Fig. 14 (b). Very fine ferroelectric domains are observed mostly close to grain boundaries. In order to confirm ferroelectricity of the BNT-BT bulk sample local switching experiments were performed as shown in the vertical UPFM amplitude and phase images, respectively. The switching experiment was performed by applying -20 V DC while scanning an area of 1.5 x 1.5 μm^2 which created a dark contrast in the vertical UPFM amplitude and phase images (Figs. 14 (c) and (d)). For the second switching, a voltage of +20 V DC was applied while scanning an area of 0.5 x 0.5 μm^2 within the same area which caused a reversal of the polarization direction, i.e. a bright contrast (Figs. 14 (c) and (d)).

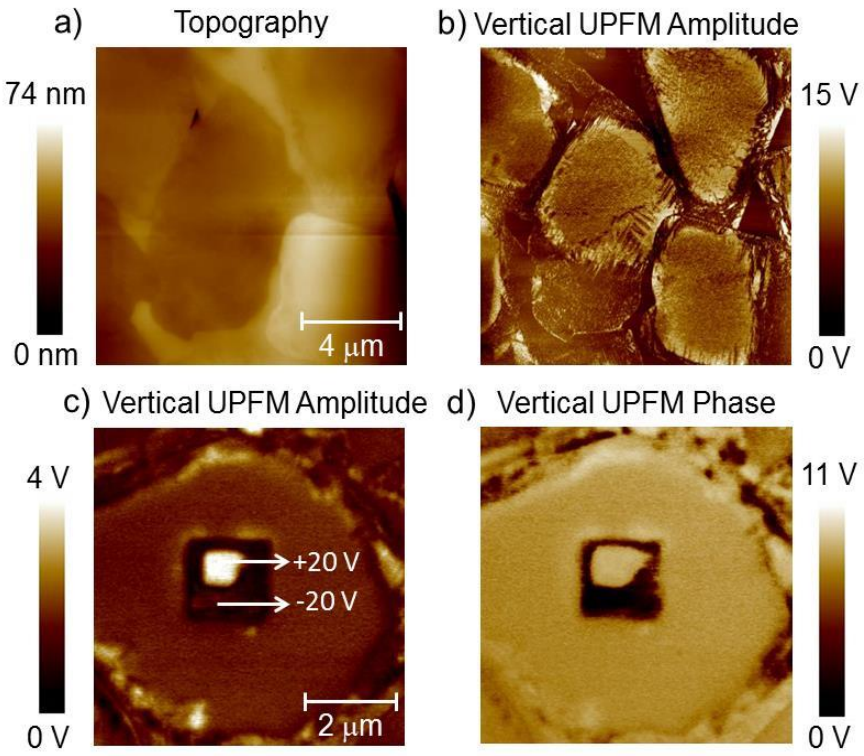

Figure 14. Topography (a) and vertical UPFM amplitude image (b) of the BNT-BT bulk sample. (c) and (d) show vertical UPFM amplitude and phase images, respectively, of ferroelectric domains written in a selected grain of the sample by applying -20 V DC while scanning over a 1.5 x 1.5 μm^2 area of the sample followed by an applied DC voltage of +20 V while scanning 0.5 x 0.5 μm^2 within the same area (scan rate 2 Hz) [3].

Figure 15 (a) shows the topography image of the bulk Mn-doped BNT-BT sample also produced by CINVESTAV. The vertical UPFM amplitude image is shown in Fig. 15 (b). A higher piezo-activity is found in the center of the grains but no defined domain structure is observed. Second-phase inclusions are detected on the grain boundaries as shown in the topography image (Fig. 15 (c)). Those inclusions show no contrast in the UPFM amplitude image (Fig. 15 (d)), and therefore, we may conclude that they do not show piezo-activity.

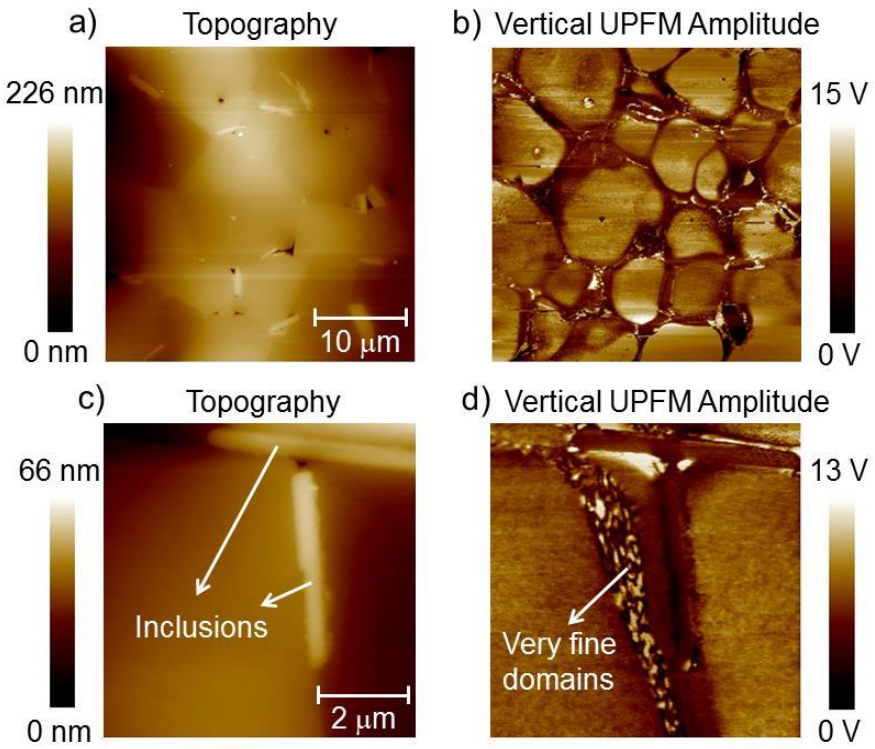

Figure 15. Contact-mode topography (a) and vertical UPFM amplitude (b) images of the Mn-doped BNT-BT bulk sample. Higher resolution contact mode topography (c) and vertical UPFM amplitude (d) images show inclusions which do not show piezo-activity [3].

The bulk Sr-doped BNT-BT sample was produced by TUHH by sintering at 1150°C for 2h. It has obtained 97% of the theoretically possible density. Macroscopic polarization and strain curves were measured at TUHH (P_s ~ 40 μC/cm, E_c ~ 3 kV/mm, and d_{33} ~ 180 pm/V). Contact-mode topography, UPFM, and AFAM images (Figs. 16 (a), (b) and (c)) were taken. The topography in Fig. 16 (a) provides information about the microstructure and the surface roughness. In Fig. 16 (b), the presence of ferroelectric domains is confirmed. Large domains as well as very fine small domains (~ 20 nm) are observed. The AFAM image (Fig. 16 (c)) gives information of the elastic properties of the surface. Some grain and domain boundaries which have different elastic properties compared to the grain interior are visible.

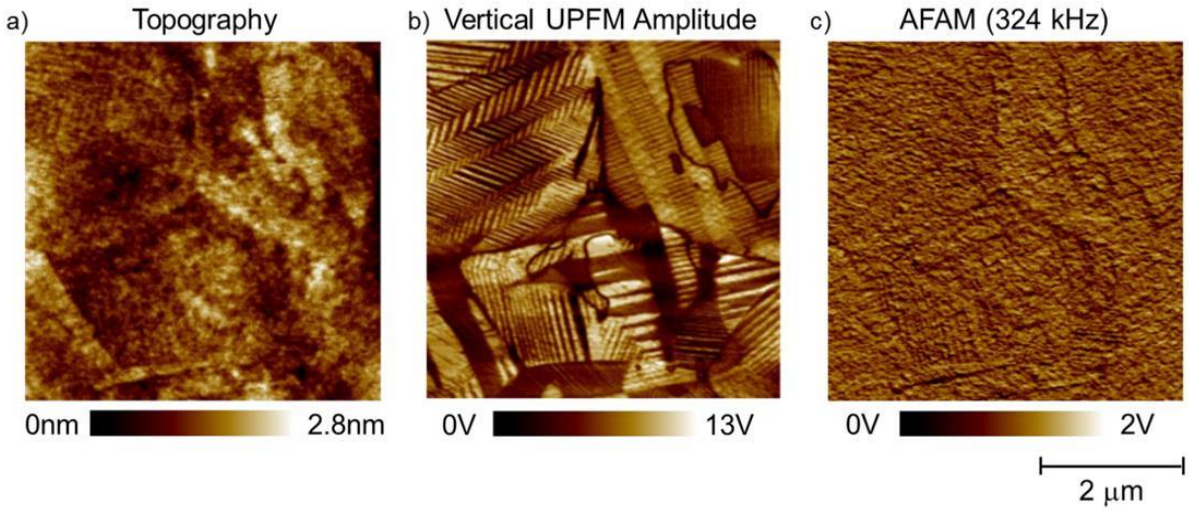

Figure 16. Contact-mode topography (a), vertical UPFM amplitude (b) and AFAM (c) images of the Sr-doped BNT-BT bulk sample. The images were recorded at a frequency of 324 kHz close to the contact resonance of the first bending mode of the cantilever.

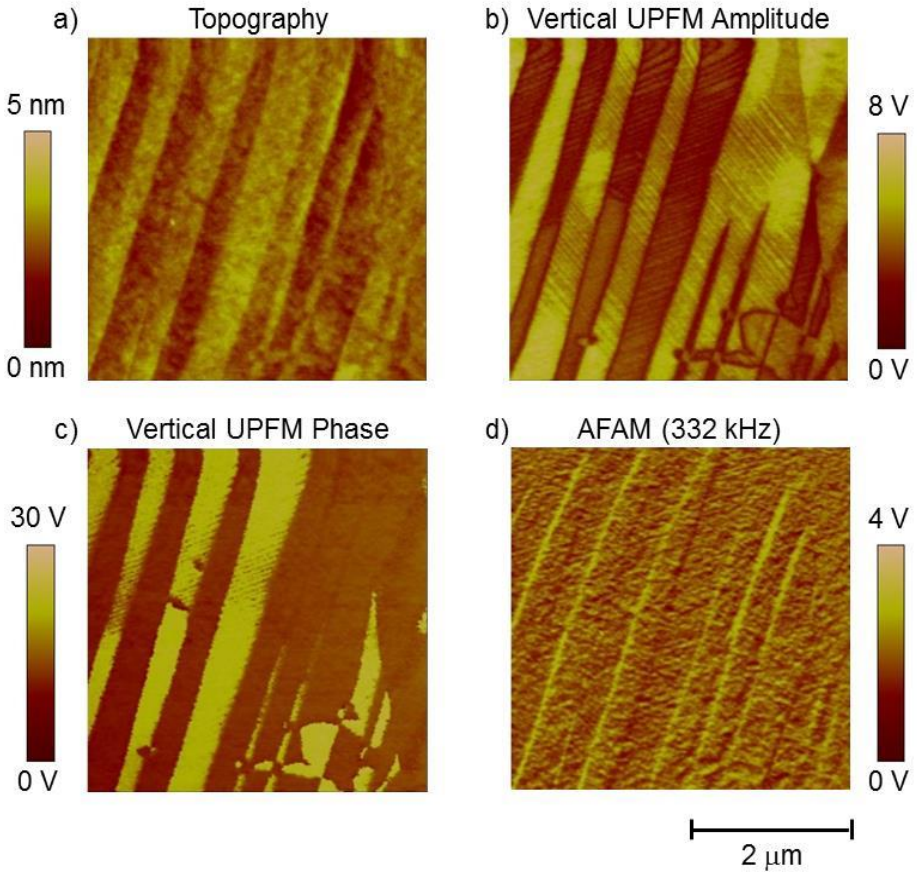

Figure 17. Contact-mode topography (a), vertical PFM images: (b) amplitude and (c) phase, and AFAM (d) images of the Sr-doped BNT-BT bulk sample. The images were recorded at a frequency of 332 kHz close to the contact resonance of the first bending mode of the EFM-cantilever [3].

Figure 17 shows another region of the Sr-doped BNT-BT sample. The topography image (Fig. 17 (a)) reveals height differences which correspond to the large domains in the UPFM image. Very fine ferroelectric domains are observed inside the large domains as shown in the UPFM amplitude (Fig. 17 (b)) and phase (Fig. 17 (c)) images. The AFAM image (Fig. 17 (d)) shows that the domain boundaries exhibit different elastic properties compared to the interior of the domains.

We can summarize the macroscopic and the microscopic properties of the lead-free bulk ceramic samples produced in our consortium as follows:

Macroscopic properties

- Sr-doped BNT-BT presents the highest E and G moduli.
- BNT-BT, Mn-doped BNT-BT, Sr-doped BNT-BT and PIC 700 become piezoelectrically active after poling (38 kV/cm during 2 min).
- Using calculations based on bulk ultrasonic velocities, impedance, and laser vibrometer measurements, the radial and thickness resonance frequencies of the ceramic bulk samples were clearly identified.
- BNT-BT shows the lowest maximal vibration amplitude (6 nm). The Mn-doped BNT-BT sample shows an intermediary maximal vibration amplitude (14 nm). The Sr-doped BNT-BT and commercial PIC 700 samples show the largest maximal vibration amplitudes (18 nm). The measurements were performed at the respective thickness resonances of the samples by applying 20 V AC.

Microscopic properties

- BNT-BT shows grains with different piezo-activities. Some nano-domains close to the grain boundaries were observed.
- Mn-doped BNT-BT shows higher piezo-activity in the center of the grains, no defined domain structure was found. Second phase inclusions were characterized on the grain boundaries, they do not present piezo-activity.
- Sr-doped BNT-BT displays large as well as very fine striped domains (~ 20 nm) over the whole measured sample surface.
- Local polarization switching was possible in all bulk samples by applying -20 V DC between the tip and the sample.

4. CORRELATIONS

From all bulk lead-free ceramic samples produced in our consortium the Sr-doped BNT-BT sample showed the most stable ferroelectric domain structure. The Mn-doped BNT-BT sample presented an additional phase (inclusions) which do not show piezo-activity. Macroscopic measurements using laser vibrometry showed that the Sr-doped BNT-BT sample presents the largest surface vibration amplitudes. Hence, for ultrasonic transducer applications, it is the most promising lead-free ceramic sample investigated in this work.

5. APPLICATIONS

Figure 18 (a) shows a set-up to test the most promising lead-free ceramic materials produced in our consortium for ultrasonic transducer applications. A Polymethylmethacrylate (PMMA) block with a thickness of 6 cm is used, on top of which the ceramic materials coated with top and bottom electrodes and their respective electric contacts are glued. The thickness of the PMMA block was chosen to be about twice the acoustic near-field length to avoid interferences.

A standard ultrasonic pulse generator/receiver instrument was used for signal excitation and reception. The generator sends a spike pulse with –125 V amplitude to the transducer materials. All ceramic materials under test provided clear ultrasonic signals. Examples of back wall echoes generated by the Mn- and Sr-doped BNT-BT samples, respectively, are shown in Fig. 18 (b). The receiver amplification was set to 28 dB and 38 dB, respectively. The normalized spectra of the received pulses are shown in Fig. 18 (c). The spectrum of the spike signal used for excitation is also shown for comparison. The center frequencies of the pulses generated by the BNT-BT-Mn and -Sr disks correspond well to the resonance frequencies detected by laser vibrometry as presented in Figs. 11-13. Further measurements are ongoing at IZFP to compare in detail the materials produced in this project (Sr- and Mn-doped BNT-BT) to a commercial lead-free ceramic, PIC 700, and a standard lead zirconate titanate ceramic material, PZ 29.

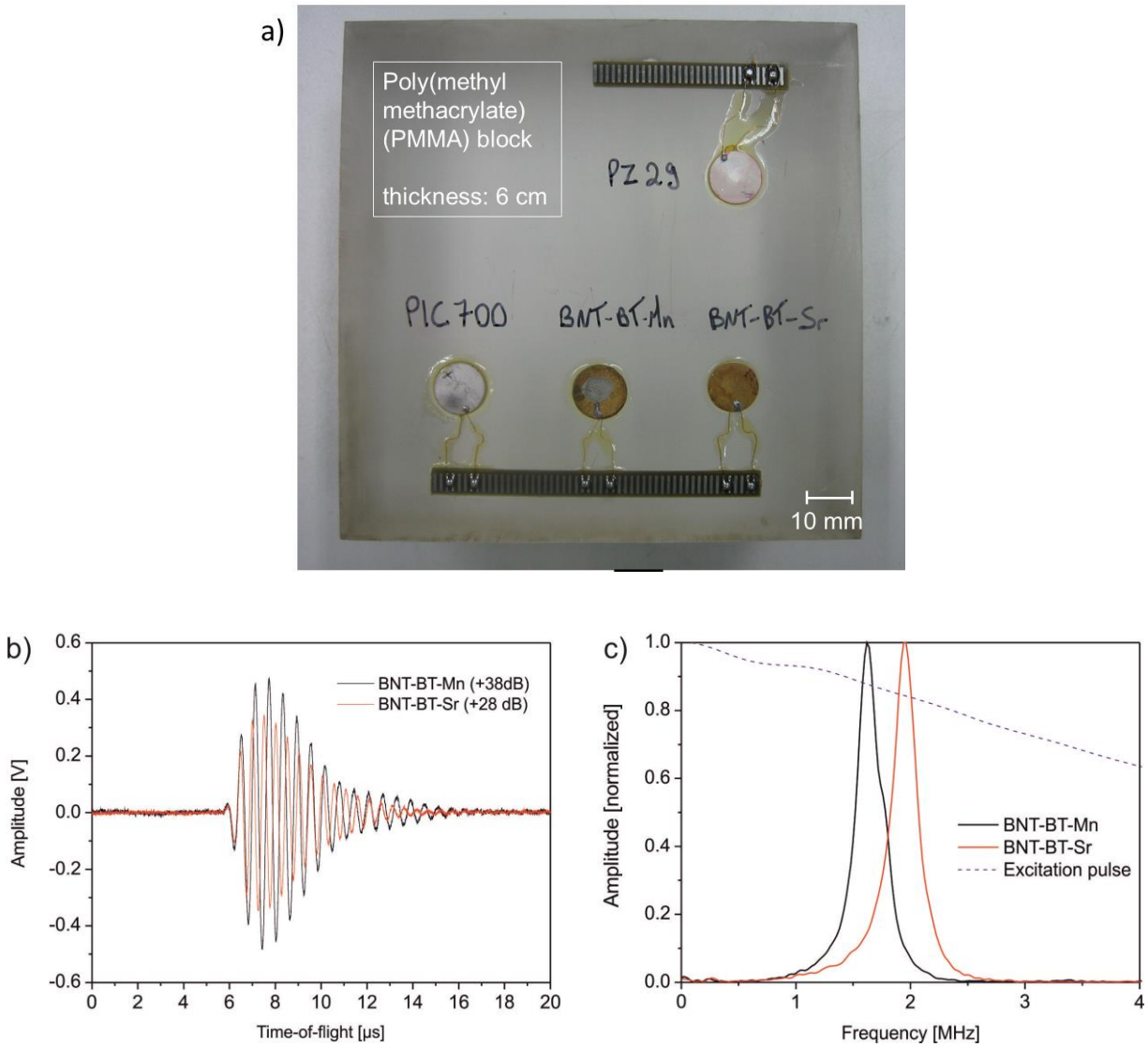

Figure 18. Set-up used for ultrasonic testing of the lead-free piezoelectric ceramics produced in this project (a). Ultrasonic pulses obtained using a conventional ultrasonic pulser/receiver instrument in combination with the test set-up (b), Frequency spectra of the pulses (c).

REFERENCES

[1] EC-FP7 Call: NMP.2010.1.2-4 Adding Value to mining at the Nanostructure level, Project: Functionalities of Bismuth-based nanostructures (BisNano) 263878.

[2] U. Rabe, M. Kopycinska, S. Hirsekorn, J. Muñoz-Saldaña, G.A. Schneider, W. Arnold, *Journal of Physics D: Applied Physics* **35** (2002) 2621.

[3] M. Rank, *Charakterisierung Bismut-basierter bleifreier Piezokeramiken mit Ultraschall-Kraftmikroskopie und Ultraschall-Piezomode*. Saarbrücken: Bachelor thesis, Science and Technical Faculty III, Saarland University and IZFP report No. 130123-TW, 2013.

IX. SUMMARY AND OUTLOOK

1. Structural steels

With the overall motivation to support the developments of nondestructive electromagnetic and micromagnetic methods for material characterization and evaluation, the first and larger part of this work explored and finally interpreted the micro- and nanoscopic origin of the electromagnetic and micromagnetic output signals of one of the most extensively studied material, pearlitic steel, by various SFM-electron microscopy combined studies. It was shown that the detailed analysis of microstructural magnetic property relationships by means of macroscopic magnetic measurements like hysteresis loop and MBN in combination with micro- and nanoscopic imaging techniques like high resolution MFM and EBSD allows a clear interpretation of magnetization processes in steels containing different phases responsible for the macroscopic electromagnetic and micromagnetic measurement signals.

Samples of a high purity polycrystalline iron and of two unalloyed pearlitic steels (Fe-0.8%C and Fe-1.5%C) containing globular cementite precipitates embedded in a ferrite matrix were investigated. The samples were characterized macroscopically by measuring hysteresis loops and MBN profiles. It was found that experimental conditions such as magnetization frequency, magnetization amplitude, signal pick-up, band width, sample surface condition, etc. play a crucial role on the measured results. Macroscopic magnetic quantities like saturation magnetization, coercive field, and maximum Barkhausen noise amplitude were measured and interpreted with respect to the microstructural state.

On the high purity iron sample large Barkhausen noise amplitudes were obtained at all measured frequencies. This is attributed to the easy irreversible motion of domain walls (mostly 180° BWs) in the annealed pure iron the microstructure of which presents low densities of dislocations and lattice defects. In contrast, within the unalloyed pearlitic steel samples, the 180° and 90° BWs in the ferrite interact with the cementite precipitates and with the interstitial carbon atoms in the ferrite matrix. By optimizing the measured hysteresis loop and MBN parameters the relative proportion and contributions of the cementite and ferrite phases in the unalloyed pearlitic steels were determined. For the magnetic Barkhausen noise, the choice of the frequency of the applied field plays a crucial role in the detection of the cementite phase and the nondestructive evaluation of its proportion in unalloyed pearlitic steels. At sufficiently high frequency (about 0.5 Hz), two peaks are observed. The observation of two peaks in the MBN profiles of unalloyed pearlitic steels agrees with previous work [1] performed at Fraunhofer IZFP.

The behavior of the hysteresis loops and MBN measurement signals originate from the underlying magnetic domains and their interactions with the microstructure. Most helpful in correlating the macroscopic behavior with the microstructure and better understanding of the above mentioned macroscopic measurement signals is the possibility to image the magnetic micro- and nanostructure of macroscopic bulk (thick) sample surfaces. The magnetic microstructures of the investigated samples and their dynamics were observed and characterized using a magnetic force microscope. It was shown that the MFM technique not only has a high spatial resolution and allows a relatively low cost implementation, but also has a tremendous advantage for magnetic micro- and nanostructure imaging in steels because local and collective magnetization switching behavior of large area scans (~ 100 μm^2) can be recorded. The MFM was coupled with an external coil providing a controllable in-plane magnetic field which allows the observation of the dynamic behavior of magnetic domains and their interactions with the microstructure. It was shown that the choice of an appropriate magnetic probe plays a crucial role on the quality and reliability of the MFM images. For the samples studied in this work, the commercial CoCr coated probe (MESP) with a coating of about 40 nm thickness showed the best contrast/resolution combination. The MESP probe did not influence the magnetic microstructure of the investigated samples and vice-versa, and the observed contrast clearly revealed the magnetic microstructure of the high purity iron and the ferrite and cementite phases in the unalloyed pearlitic steel samples. Using the EBSD technique, the crystalline orientation of both phases, cementite and ferrite, were determined and correlated to the magnetic domain structure.

The domain arrangement at the surface is primarily determined by the principle of flux closure which minimizes the total inner energy. Additionally, it is strongly dependent on the orientation of the easy directions of the grains relative to the sample surface. In the simplest case of pure iron, <001> is the easy direction, and therefore, a (100) surface contains two mutually perpendicular easy directions. With increasing misoriention relative to the surface till it contains no easy axis anymore, the domain patterns become progressively more complicated. In order to observe domain wall dynamics (micromagnetic events) in the high purity iron as well as in the ferrite phase of the unalloyed pearlitic steel samples, grains oriented with its (100) plane in or close to the sample surface were chosen. In the high purity iron sample, reversible and irreversible movements mainly of 180° domain walls were easily demonstrated.

For the unalloyed pearlitic steel samples, the magnetic domain structure is more complicated. The microstructure is composed of two phases, the soft ferromagnetic ferrite

matrix and the cementite precipitates. An increasing amount of carbon in form of globular cementite precipitates enhances the pinning of domain walls in the ferrite matrix due to the presence of the second phase and its stress fields. Furthermore, the cementite phase increases the magnetic hardness of steels because cementite is magnetically harder than ferrite. The cementite precipitates have their own domain structure, and in order to reduce the magnetostatic energy, spike domains are often formed at the interface between the two phases. In general, the cementite precipitates showed a much stronger magnetic contrast than the ferrite matrix. This is attributed to the stray fields which are stronger when emanating from cementite compared to ferrite. Domain walls in the ferrite phase tend to intersect the cementite precipitates in order to minimize the magnetostatic and wall energy, and they are hindered in their movement by large and small precipitates. The wall width measured in the ferrite phase ranges from 140 nm to about 500 nm, which is in the same order of magnitude as the literature values, e.g. around 100 nm in iron. Analysis of MFM line scans across walls in ferrite demonstrate average magnetic moments inside the walls either pointing out or into to the surface plane.

Successively recorded MFM images with different strengths of the applied external magnetic field elucidated reversible and irreversible break-free of domain walls in the ferrite matrix from the cementite precipitates, which is interpreted as local Barkhausen events or jumps. Measuring the curvature of a bowed 180° domain wall in the ferrite matrix demonstrated the ability for local stress estimation. When an external magnetic field was applied, the magnetization process in ferrite sets in already at low fields via the 180° and 90° domain walls. In the ferrite matrix, 180° domain walls are mainly located in the center of grains whereas 90° domain walls are mainly observed in connection with the closure domains in the proximity of phase and grain boundaries. The activation of domain wall movements in cementite required considerably stronger external fields, which is due to the high single crystal anisotropy and the high density of defects (e.g. dislocations) and reflects the higher magnetic hardness of cementite compared to ferrite. This microscopic observation correlates qualitatively with the increase of magnetic hardness with increasing amount of cementite and with the emergence of a second peak in the MBN signal due to the cementite phase at higher external fields. The peak amplitude at the lower field corresponds to the amount of ferrite and that one at the higher field to the amount of the cementite phase, respectively. This explains the physical origin of the second peak in MBN profiles in unalloyed pearlitic steels containing globular cementite in a ferrite matrix, which is discussed since years. The analysis of the MFM images confirmed the observed macroscopic nondestructive electromagnetic signals.

Contrary to the already existing data in the literature where the observation of domain wall dynamics in steels required specially prepared (transparent to electrons) thin foils, it was shown that also in macroscopic bulk (thick) samples, which are more relevant when considering correlations with macroscopic NDT methods, domain wall dynamics can be observed.

With the combination of MFM and EBSD techniques a new method to determine the magnetic easy axes of micro- and nanoscopic ferromagnetic precipitates embedded in a bulk material was demonstrated. Globular and lamellar cementite precipitates embedded in a ferrite matrix in unalloyed steels were taken as examples. The MFM and EBSD techniques were used for the visualization of the magnetic and crystallographic microstructures, respectively. It was shown that the domain structures of cementite precipitates are strongly correlated to their crystalline planes. MFM images with a local resolution down to 50 nm revealed differently oriented magnetic moments in the cementite phase. The cementite domain structure in a (010) crystal plane (at least almost) parallel to the sample surface, i.e. the long easy [010]- or b-axis is (at least almost) perpendicular to this surface, was found to consist of parallel stripes of strong opposite magnetic contrast. The magnetic moments of those precipitates are positioned alternately down- and upwards perpendicularly to the surface and are separated by 180° domain walls. The width of the domains at the sample surface is dependent on the inclination of the (010) crystal plane relative to the surface and increases with the angle between the easy [010] axis and the surface normal. The cementite precipitates oriented with their (001) plane in or close to the surface plane showed a weak and homogeneous contrast in the image leading to the conclusion that their magnetic moments are oriented in-plane. By means of EBSD, the long [010]- or b-axis of these precipitates was determined and correlated to the magnetic signal. Dark and bright imaged edges of the precipitates confirmed the in-plane orientation of the magnetic moments along the long [010]- or b-axis. The combined MFM and EBSD studies allow to conclude that the easy direction of magnetization in cementite is the long [010]-axis. For the lamellar cementite precipitates, the acquisition of EBSD patterns in order to determine their crystalline orientation is very difficult. It was shown that the crystalline orientation of the cementite lamellae can be estimated by simply imaging the magnetic and the topographic microstructure.

The combined application of micro- and nanoscopic imaging techniques allowed a correlation between microstructure and macroscopic material behavior and thus a better understanding of the macroscopic electromagnetic NDT&E methods. Theoretical models

based on microstructural magnetic property relationships in complex multiphase steels which correlate the amount, size, and shape of precipitates, grain size and shape, etc. to important macroscopic properties such as, for example, the magnetic hardness, can now be confronted and developed by observing the microstructure and the magnetization dynamics directly on the surface of macroscopic thick (bulk) samples. Additionally, parameters like depinning fields, domain wall mobilities, etc. can be measured and used in micromagnetic simulation software tools, e.g. 3D EMicroM [2], in order to study the evolution of macroscopic magnetic signatures as function of changes in defect concentrations and/or the magnetic field.

Even though of high technological significance, the elastic constants of cementite are still subject of debate. Atomic force acoustic microscopy was used to probe the local elastic properties of the unalloyed steel samples with a spatial resolution down to 10 nm. Qualitative AFAM surface elasticity maps indicated that in the measured area of the investigated unalloyed Fe-0.8%C steel, ferrite is stiffer than cementite. To obtain quantitative elastic moduli data, it is suggested to perform quantitative AFAM as well as nanoindentation measurements on areas of each phase with known grain orientations. In this work, topographic, magnetic, and elastic properties of the unalloyed pearlitic steel samples were correlated.

Elastic properties of newly developed high strength steels were also investigated at the nanoscale. AFAM, nanoindentation, and EBSD techniques were employed in order to evaluate the local elastic properties as function of crystalline grain orientation of two different austenitic twinning induced plasticity steels, Fe-22Mn-0.6C-0.2V and Fe-20Mn-3Si-3Al, with average grain sizes of 1 μm and 40 μm, respectively. Even though the values measured using nanoindentation were higher than those obtained by AFAM, the results from both techniques presented the same trend, i.e. when comparing grains with similar crystalline orientations, the steel Fe-22Mn-0.6C-0.2V showed higher stiffness than the steel Fe-20Mn-3Si-3Al, and for both steels, the stiffness of grains in or around the (111) plane is higher than the stiffness of grains in or around the (101) plane which is higher than the stiffness of grains in or around the (001) plane. Finally, AFM contact mode was used to monitor local deformation behavior in the Fe-22Mn-0.6C-0.2V steel. A series of topography images acquired for different plastic deformation levels revealed an increase in step height with increasing plastic deformation, which correlated with the formation of deformation twins, as was later confirmed by EBSD.

2. Functional lead-free ferro- and piezoelectric ceramics

In the context of the European-Mexican collaborative project (BisNano) the objective of which was the acquisition of fundamental knowledge on bismuth-based nanostructures towards the development of products and devices, different lead-free bismuth based alloys were synthesized in form of bulk samples as well as thin films in order to discover new lead-free ferro- and piezoelectric materials for industrial applications.

Ferroelectric epitaxial thin films of bismuth ferrite ($BiFeO_3$) were grown on (100), (110) and (111)-oriented $SrRuO_3/SrTiO_3$ substrates. The thickness of the films varied between 100 and 200 nm. The quality of the films with regard to their epitaxial orientation and absence of second phases were confirmed using XRD. AFM contact mode topography images showed a flat surface (low range of the height scale, max. 33 nm). The homogeneity of the elastic properties of all films was confirmed using AFAM. To study the influence of the crystallographic orientation of the films on the ferroelectric domain patterns, low frequency (standard) as well as ultrasonic piezoresponse force microscopy were used. By combining the vertical and the lateral piezoresponse data, it was shown that the (111) and (110) oriented films are ferroelectric, but are in a mono-domain state and that the (100) film presented a striped domain structure. Local polarization switching was possible in all films by applying 22 V DC between the AFM tip and the sample. Analysis of the lateral PFM signal acquired on the (110) and (111) oriented films after the polarization switching shows a lateral component on the (110) film, but no contrast on the (111) film. The results are in accordance to the literature data in which the (100), (110), and (111)-oriented films have 4-, 2-, and 1-polarization variants, respectively, because of the symmetry of the rhombohedrally distorted perovskite $BiFeO_3$ structure. Finally, the measurement of the d_{33} piezoelectric constant of the (100) film with the PFM system yielded a value of $d_{33} = 39 \pm 2$ pm/V. The high polarization and piezoelectric response in thin $BiFeO_3$ films suggest a possibly environmentally acceptable alternative to Pb-based ferroelectrics. However, further comprehensive investigations of the processes related to ferroelectric fatigue are still necessary. In addition, large ferroelectric coercive field and high leakage currents are considered as further limitations in utilizing $BiFeO_3$ for commercial device applications.

Not only thin films, but also bulk ceramic samples were investigated. Promising candidates for lead-free piezoelectric materials like $Bi_{0.5}Na_{0.5}TiO_3$ (BNT), $0.94Bi_{0.5}Na_{0.5}TiO_3$-$0.06BaTiO_3$ (BNT-BT), Mn-doped BNT-BT and Sr-doped BNT-BT were synthesized in bulk form by different BisNano partners. A commercial lead-free ceramic based on BNT, called PIC 700, was taken for comparisons. The samples were investigated

and evaluated at different scales. The samples BNT-BT and Mn-doped BNT-BT provided by the *Centro de Investigación y Estudios Avanzados* and Sr-doped BNT-BT provided by the *Technische Universität Hamburg-Harburg* were the most promising bulk lead-free piezoelectric materials produced in the BisNano consortium for industrial applications. The density of the samples was measured using the so-called Archimedes method. The Sr-doped BNT-BT and the PIC 700 samples exhibit the largest densities ($\rho = 5.64$ g/cm^3 and $\rho = 5.69$ g/cm^3, respectively), which corroborate the AFM topographic and optical images, where much lower porosity levels were observed in these samples compared to the other ones.

Macroscopic mechanical and piezoelectric properties were characterized using ultrasonic, impedance, and 3D laser vibrometer measurements. The bulk ultrasound longitudinal and transverse wave velocities were measured at a frequency of 5 MHz. Mechanical properties such as Young's and shear moduli were determined by measuring longitudinal and transverse sound wave velocities and the density. The sample Sr-doped BNT-BT showed the largest Young's and shear moduli (E = 125.1 GPa and G = 49.9 GPa, respectively). Before the impedance and the 3D laser vibrometer measurements, the samples were sputtered with a thin conductive electrode layer and poled by applying an electric field of 38 kV/cm for 2 min. By means of impedance measurements the activity of the samples was confirmed, and the radial and thickness resonances of all samples were identified. From the resonance (f_r) and anti-resonance (f_a) peaks the planar and thickness coupling coefficients K_p and K_t, respectively, were calculated. The sample Sr-doped BNT-BT presented the largest thickness coupling coefficient ($K_t = 0.37$), whereas the sample PIC 700 showed the largest planar coupling coefficient ($K_p = 0.37$). Using a laser vibrometer, the resonance frequencies of the samples were detected, and the maximal surface vibration amplitudes measured at their thickness resonances were obtained quantitatively. All measurements were performed by applying an AC voltage of 20 V. The measured thickness resonance frequencies of all samples ranged from 1749 to 2269 kHz. The maximal vibration amplitudes were measured close to the center point of the samples. The BNT-BT sample showed the lowest maximal vibration amplitude (6 nm), the Mn-doped BNT-BT sample displayed a medium maximal vibration amplitude (14 nm), and the maximum in vibration amplitudes were found on the Sr-doped BNT-BT and commercial PIC 700 samples, both samples yielded 18 nm.

The above mentioned macroscopic properties of the ceramic samples are mostly determined by the microstructure and the arrangement of the ferroelectric domains. AFM was used to image the surface micro- and nanostructures. Surface elastic properties and ferroelectric domains were imaged at a nanoscale in all samples using AFAM and UPFM,

respectively. Grains with different piezo-activities were observed on the BNT-BT sample, and some nanodomains were detected close to the grain boundaries. The Mn-doped BNT-BT sample showed higher piezo-activity in the center of the grains. However, no defined domain structure was found. Additionally, second phase inclusions which did not present piezo-activity were detected at the grain boundaries. A well-defined high-contrast domain structure was observed on the Sr-doped BNT-BT sample. Large as well as very fine striped domains (~ 20 nm) over the whole measured sample surface were detected. Local polarization switching was possible by applying 20 V DC between the AFM tip and the sample.

Finally, the most promising lead-free bismuth-based bulk ceramic samples produced in the BisNano consortium were successfully tested as ultrasonic transducer material. A testing setup was built, and together with a conventional ultrasonic pulser/receiver instrument, ultrasonic pulses were obtained. The results indicated that the Sr-doped BNT-BT sample exhibited the best performance, which confirms the previously measured macroscopic and micro- and nanoscopic properties, i.e. the Sr-doped BNT-BT sample presented the highest density, the highest E- and G moduli, the largest thickness coupling coefficient, and the most distinct and stable ferroelectric domain structure. Therefore, the Sr-doped BNT-BT material has high potential to be applied in ultrasonic transducers as an alternative to lead-based piezoelectric materials.

REFERENCE

[1] I. Altpeter, *Spannungsmessung und Zementitgehaltsbestimmung in Eisenwerkstoffen mittels dynamischer magnetischer und magnetoelastischer Meßgrößen*, Dissertation, Saarland University, Saarbrücken (1990).

[2] Stéphane Labbé and Pierre Leca, EMicroM, *Simulation de l'évolution de l'aimantation dans les matériaux ferromagnétiques*, ONERA, numéro APP: IDDN.FR.001.320023.R.P.1998.000.31235 (1998).

X. LIST OF PUBLICATIONS

Papers in Journals:

L. Batista, U. Rabe, S. Hirsekorn, "*Magnetic micro- and nanostructures of unalloyed steels: Domain wall interactions with cementite precipitates observed by MFM*", *NDT & E International* **57** (2013) 58–68.

L. Batista, U. Rabe, I. Altpeter, S. Hirsekorn, G. Dobmann "*On the mechanism of nondestructive evaluation of cementite content in steels using a combination of magnetic Barkhausen noise and magnetic force microscopy techniques*", *Journal of Magnetism and Magnetic Materials **254*** (2014) 248–256.

L. Batista, U. Rabe, S. Hirsekorn, "*Determination of the easy axes of small ferromagnetic precipitates in a bulk material by combined magnetic force microscopy and electron backscatter diffraction techniques*", *submitted to Ultramicroscopy*.

R. P. Fernandes, L. Batista, A.D.G. Castro, L. Salamanca-Riba, M.P. Cruz, J. Muñoz-Saldaña, F. Espinoza-Beltran, S. Hirsekorn, U. Rabe, G.A. Schneider, "*Piezoresponse force microscopy studies on (100), (110) And (111) epitaxial growth of BiFeO3 thin films*", *MRS Proceedings* **1477** (2012) doi:10.1557/opl.2012.1701.

M. Bousquet, L. Batista, J. L. Dellis, A. Boulle, U. Rabe, O. Durand-Drouhin, Y. Gagou, L. Dupont, V. Viallet, A. Zeinert, S. Hirsekorn, N. Lemée, "*Structural and electrical properties of $Bi_{0.5}Na_{0.5}$ TiO_3 based superlattices grown by pulsed laser deposition*", *to be submitted to Journal of Applied Physics*.

Conferences:

L. Batista, U. Rabe, S. Hirsekorn, "*Characterization of the magnetic micro- and nanostructure in unalloyed steels by magnetic force microscopy*", Review of Progress in Quantitative Nondestructive Evaluation (QNDE), 39th Annual Meeting, 16th-20th July (2012), Denver, Colorado, USA, Vol. **32**, *AIP Conference Proceedings* **1511** (2013) 1180–1187.

L. Batista, U. Rabe, S. Hirsekorn, "*Micro- and nanostructure characterization and imaging of twip and unalloyed steels*", Review of Progress in Quantitative Nondestructive Evaluation (QNDE), 38th Annual Meeting, 17th-22th July (2011), Burlington, Vermont, USA, Vol.**31**, *AIP Conference Proceedings* **1430** (2012) 1381–1388.

S. Hirsekorn, U. Rabe, L. Batista, L. Behl, "*Microstructure characterization and imaging of fine-grained steel by microscopic ultrasonic techniques*", Review of Progress in Quantitative Nondestructive Evaluation (QNDE), 37th Annual Meeting, 18th-23th July (2010), San Diego, California, USA, Vol. **30A**, *AIP Conference Proceedings* **1335** (2011) 1097–1103.

L. Batista, U. Rabe, S. Hirsekorn, "*Cementite Content in Steel: Magnetic Barkhausen Noise and Visualization of Domain Wall Movement by Magnetic Force Microscopy*" *(poster),* Symposium: Crackling noise and intermittency in condensed matter, 22th–24th May (2013), Göttingen, Germany.

U. Rabe, L. Batista, S. Hirsekorn, "*Magnetic micro- and nanostructures of steels imaged by magnetic force microscopy: Is it possible to observe a local Barkhausen jump?*", Symposium: Crackling noise and intermittency in condensed matter, 22th–24th May (2013), Göttingen, Germany.

L. Batista, U. Rabe, S. Hirsekorn, "*Magnetic micro- and nanostructures of unalloyed steels observed by magnetic force microscopy*" *(poster),* Materials Science and Engineering (MSE), 25th–27th September (2012), Darmstadt, Germany.

L. Batista, U. Rabe, S. Hirsekorn, "*Micro- and Nanostructure Characterization and Imaging of TWIP and Unalloyed Steels*", "NDT in Progress", 10th–12th October (2011), Prague, Czech Republic.

L. Batista, U. Rabe, S. Hirsekorn, "*Darstellung von Mikro- und Nanostrukturen in perlitischen Stählen mittels elektromagnetischer zfP-Verfahren*" *(in german),* DGZfP-Jahrestagung 6th–8th May (2013), Dresden, Germany.

L. Batista, U. Rabe, S. Hirsekorn, "*Characterization of Lead-Free Bismuth-Based Ceramics by Bulk Ultrasound and Ultrasonic Operation Modes of Atomic Force Microscopy*" *(poster),* EuroNanoforum (ENF), 18th–20th June (2013), Dublin, Ireland.

L. Batista, U. Rabe, S. Hirsekorn, "*Micro- and Nanostructure Characterization Imaging of TWIP Steels*", Deutsche Physikalische Gesellschaft (DPG-Jahrestagung) 13th–18th March (2011), Dresden, Germany.

L. Batista, U. Rabe, S. Hirsekorn, M. Bousquet, N. Lemée, O. Durand-Drouhin, A. Zeinert, E.J. Herrera-Jiménez, A.C. Garcia-Castro, F.J. Espinoza-Beltrán, J. Muñoz-Saldaña, "*Characterization of bismuth-based ceramics using bulk ultrasonics and ultrasonic modes of atomic force microscopy*", XXI International Materials Research Congress (IMRC) 12th–17th August (2012), Cancún, Mexico.

L. Batista, U. Rabe, S. Hirsekorn, "*Characterization and Investigation of Material Properties and Functionalities of Bismuth-Based Nanostructures*", VI International Conference on Surfaces, Materials and Vacuum (ICSMV) 23th–27th September (2013), Mérida, Mexico.

U. Rabe, L. Batista, S. Hirsekorn, "*Application of Atomic Force Acoustic Microscopy and Ultrasonic Piezoelectric Force Microscopy to Characterization of Bismuth-Based Piezoelectric Ceramics*", IEEE International Ultrasonics Symposium (IUS), 21st–25th July (2013), Prague, Czech Republic.

L. Batista, U. Rabe, S. Hirsekorn, "*Materialcharakterisierung und Anwendung von bleifreien Keramiken auf Bismut-Basis*" *(in german),* DGZfP-Jahrestagung 26th–28th May (2014), Potsdam, Germany.

L. Batista, U. Rabe, S. Hirsekorn, "*Investigation of the mechanical and piezoelectric properties of Bismuth-based ceramics on the macro- and nanoscales*", Nanobrücken-Nanomechanical Testing Workshop, 26th–28th March (2014), Saarbrücken, Germany.